SPECTROSCOPIC STUDIES OF NOBLE-GAS MONOHALIDES.

by

AGUST KVARAN

PhD

UNIVERSITY OF EDINBURGH

1979

ACKNOWLEDGEMENTS.

A number of people have helped me to achieve the personal goal which is culminated in the completion of this dissertation. I wish to use this opportunity to thank these people.

I would like to express my sincere gratitude to my supervisors, Dr. Robert J. Donovan and Dr. Michael F. Golde, for their great help and understanding during my graduate studies in Edinburgh and Pittsburgh. Their inspiration, encouragement and critical evaluation in all aspects of this work are greatly acknowledged. I cannot thank them enough.

I wish to thank the members of Dr. Donovan's group during my stay in Edinburgh for their many assistances and for providing a healthy atmosphere in the lab. A special thanks go to Dr. Costas Fotakis for many stimulating discussions.

My thanks are due to Mr. Bruce Berquist at the University of Pittsburgh for kindly providing a computer program for nonlinear least square analysis.

A special note of thanks go to Dr. Kristján Árnason for proof-reading the final manuscript.

In addition I wish sincerely to thank my mother-in-law, Ingibjörg Eyþórsdóttir, for her support, both emotional and financial.

I would like to express my appreciations to my wife, Edda who contributed directly to this thesis by

typing it and indirectly, by showing a great patience and understanding and thus to provide a great emotional support, during the years.

Financial support for my graduate studies from the following sources is greatly acknowledged: A British Council scholarship, the Petroleum Research Fund, administered by the American Chemical Society, the Research Corporation and the Royal Society.

ABSTRACT.

Vacuum-UV emission spectra were obtained in a discharge flow system for reactions of bromine-, chlorine- and iodine containing reagents with metastable argon atoms ($Ar^{*}(^{3}P_{2,0})$). Halogen atomic lines were observed for many of these spectra. Noble gas halide spectra were identified for the reactions of the bromine- and chlorine- containing reagents (ArBr- and ArCl- spectra). HCl and DCl spectra were observed for the reactions of these reagents.

The pressure- and temperature- dependence behaviour of some of the argon halide spectra as well as their structure was studied, and the spectra were analysed by simulation calculations. Detailed studies of the effect of the various parameters on the calculated spectra were carried out for the simulation of the ArBr spectra. This showed that important information on the various parameters could be derived from the simulation calculations.

Spectral contributions due to three different bound-free transitions (B-X, C-A(3/2) and B-A(1/2)) and the spectral ranges of these were identified for some ArBr spectra. Only the very lowest vibrational levels in the excited states were found to emit due to an efficient predissociation of high vibrational levels. The occurrence of a collision induced crossing between the emitting states (B and C) and a vibrational relaxation

in these states was observed. Estimates were made of relative rates of collisional deactivation processes and population distributions in the emitting states (B and C) for some of the spectra. Approximate potential curves (X, A(3/2), B and C) were obtained and the transition moments for the transitions B-X and C-A(3/2) were found to vary rapidly with internuclear distance.

Analyses of some ArCl, MC spectra made it possible to estimate the population distribution in the ArCl B-state and the occurrence of a rapid vibrational relaxation in the B-state was observed. Approximate potential curves (X,B) were also obtained.

CONTENT.

1. INTRODUCTION.

1.1 Chemiluminescent reactions of excited noble gas atoms.

The chemistry of atoms and molecules in excited states can be very different from that of the ground states.[1] The contrast between the chemical behaviour of ground and excited state species is perhaps nowhere more marked than in the noble gases.[2,3] While the ground state noble gas atoms are virtually inert, the first excited states are highly reactive.

The physical and chemical properties of these species show a close similarity to that of the alkali atoms. Thus a noble gas atom in its first excited states has polarizability,[4,5] ionization potential [2] and shows reactivity[14] and elastic scattering[6,7] similar to the closest alkali atom in the periodic table.

The quenching of the excited noble gas atoms has been observed to occur by a variety of channels.[2] Collisional excitation and deactivation is important in pure or mixed noble gases and can be

represented as

$$Ng^* + Ng' \longrightarrow Ng^{**} + Ng' \qquad (1)$$

where Ng and Ng′ represent noble gas atoms and the asterisks denote electronic excitation. Two - and three - body recombination,

$$Ng^* + Ng \longrightarrow Ng_2^* \qquad (2)$$

and

$$Ng^* + 2Ng \longrightarrow Ng_2^* + Ng \qquad (3)$$

are important in pure noble gases. Chemiionization of a reagent can occur by different reaction channels to form various ionic species. Dissociation reactions of a reagent BC can lead to formation of neutral species

$$Ng^* + BC \longrightarrow Ng + B + C \qquad (4)$$

or species in excited states

$$Ng^* + BC \longrightarrow Ng + B^* + C \qquad (5)$$

A number of electronic - to - electronic (E - E) energy transfer reactions

$$Ng^* + BC \longrightarrow Ng + BC^* \qquad (6)$$

have been identified.

Chemiluminescent reactions of the metastable excited states, $^3P_2$ and $^3P_0$ of the heavy noble gas atoms, is the most recently discovered channel,

$$Ng^*(^3P_{0,2}) + RX \longrightarrow NgX^* + R \qquad (7)$$

$$NgX^* \longrightarrow h\nu + Ng + X \qquad (8)$$

which was first identified by Golde and Thrush[8] in 1974. They observed the chemiluminescence in vacuum - UV due to a transition from a bound upper state of

ArCl, ArO and KrO to a repulsive lower state when metastable Ar- and Kr- atoms reacted with O- and Cl-containing reagents. A halogen atomic emission was observed in some of these spectra. Excited halogen atoms are thought to be formed at least partly due to predissociation of the excited noble gas halides

$$NgX^* \longrightarrow Ng + X^* \qquad (9)$$

$$X^* \longrightarrow h\nu + X \qquad (10)$$

Soon after the discovery of the chemiluminescent reactions a laser action on the noble gas halide transitions was suggested by Setser and his co-workers.[13,14]

Since then, lasing has been achieved in ArF[32] (193nm), $ArCl$[33] (175nm), $KrCl$[34] (222nm), KrF[29] (248nm), XeF[30] (352nm), $XeCl$[29] (308nm) and $XeBr$[35] (282nm), with electron - beam and discharge techniques to produce electronically excited noble gas atoms. Principally because of this very rapid development of high power pulsed lasers, an intense interest has arisen in these noble gas halide systems.

In the last few years these systems have been studied extensively, both experimentally and theoretically, in order to obtain a better understanding of the spectroscopy and the various kinetic processes in these systems. Various experimental techniques have been utilized for this purpose.

The initial identification of the chemiluminescent channel was made by recording the vacuum - UV emission

spectra in a discharge flow system at low pressures[8] (typically 0.5 - 10 torr)*. Such low pressure spectra have now been identified and published for a number of noble gas halides, such as ArF,[9] ArCl,[8] ArBr,[10] KrF,[9] KrCl,[9] KrBr,[9] KrI,[10] XeF,[16] XeCl,[14] XeBr,[14] and XeI.[28] High pressure emission spectra (P > 300 torr)* have been obtained from high energy electron beam excitation of noble gas/halogen mixtures for the xenon-halides[23,27,28,38-41] and KrF.[27] Absorption spectra for XeF have been recorded in gas phase in flash photolysis experiments.[42] Emission and absorption spectra for the xenonhalides[43-46] and KrF[43,45] have also been studied by the matrix isolation technique. ESR spectrum of XeCl in matrices has been recorded.[47]

Total quenching rate constants have been measured for reactions of the metastable noble gas atoms with various halogen containing reagents, and the rate of formation of excited noble gas halides has been measured for some systems. These kinetic studies have been made by Setser and his coworkers in discharge flow systems.[2,15,16] Molecular beam studies have been made to obtain the excitation function of the reaction of metastable Xe ($^3P_{0,2}$) with Br_2.[48] The radiative life-time of a particular excited state of XeF (B - state) has been measured by various methods i.e. by utilizing electron beam dissociation excitation of XeF_2[31,49]

* 1 torr = 133.322 Nm^{-2}

and ArF - laser photodissociation of XeF_2,[50] and most recently by the laser induced fluorescence technique.[51] Quenching rate coefficients for the excited state of XeF and various gases have been determined by use of the resonance fluorescence[19] and laser induced fluorescence techniques.[50]

Various spectroscopic calculations have been done on these systems. Spectral simulation calculations have been carried out to interpret the main features of the low pressure spectra and to obtain information on the emitting potentials[9] or population distribution.[21] Several high pressure spectra have also been simulated.[40] Ab initio, configuration interaction calculations have been made for the noble gas fluorides [52-54, 56-57] (NgF for Ng = Ne, Ar, Kr, Xe) and xenon halides[55-56] (XeX for X = F, Cl, Br, I). These calculations were made in order to obtain the various potential curves for these noble gas halide molecules as well as transition moments. From these calculation results, the various experimentally observed radiative transitions were assigned. Krauss has derived perturbation expressions for potential curves, and dipole- and transition moments for KrF.[59] Krauss and Liu have done theoretical calculations on the ground state of XeF.[60] The electron gas model[61] has been utilized to obtain potential curves for KrF.[58] A self - consistent-field potential energy curve for the ground state of ArCl has also been calculated.

The work which is presented in this thesis started in the early days of the studies of the noble gas monohalides, the year after Golde's and Thrush's discovery of the chemiluminescent reactions.[8] The aim of the project was to learn more about the noble gas halide systems in general by studying the vacuum - UV spectra obtained from reactions of $Ar^*(^3P_{0,2})$ with halogen containing reagents in a flow system.

In the following two sections of this chapter other people's results on the noble gas halide systems which are most relevant to the work presented in this thesis will be reviewed.

1.2 Spectroscopy of the noble gas monohalides.

The first spectroscopic evidence for the noble gas monohalides came from ESR - spectra of gamma - irradiated crystals of XeF_4[62] and KrF_2[63] in 1963 and 1964. These spectra were assigned to XeF- and KrF - radicals. In 1964 Kuznetsova et al[64] announced their observation of emission bands in the UV region from discharge of XeF_2 vapour, which they assigned to XeF - species.

In 1971 and 1973, self - consistent - field (SCF) calculations concluded that the KrF^-[65] and XeF^-[66] molecules have repulsive ground states which predicts the nonexistence of XeF and KrF as chemically bound species. More recent experimental and theoretical evidence , however, suggest that the ground state of XeF is bound. The ground state of XeCl is also found to be bound, while for most of the other noble gas halides it is found to be repulsive with a slight Van der Waals minimum at long range.

The early recorded UV - spectra were ignored until very recently, or until after the discovery of the chemiluminescent reactions[8] (reaction (7)).

Noble gas halide spectra obtained in discharge flow systems at low pressures are shown in figures 1.1 and 1.2 for XeI and KrBr respectively. The main feature of such noble gas halide spectra is the so - called "main continuum"(MC) - a continuous spectrum

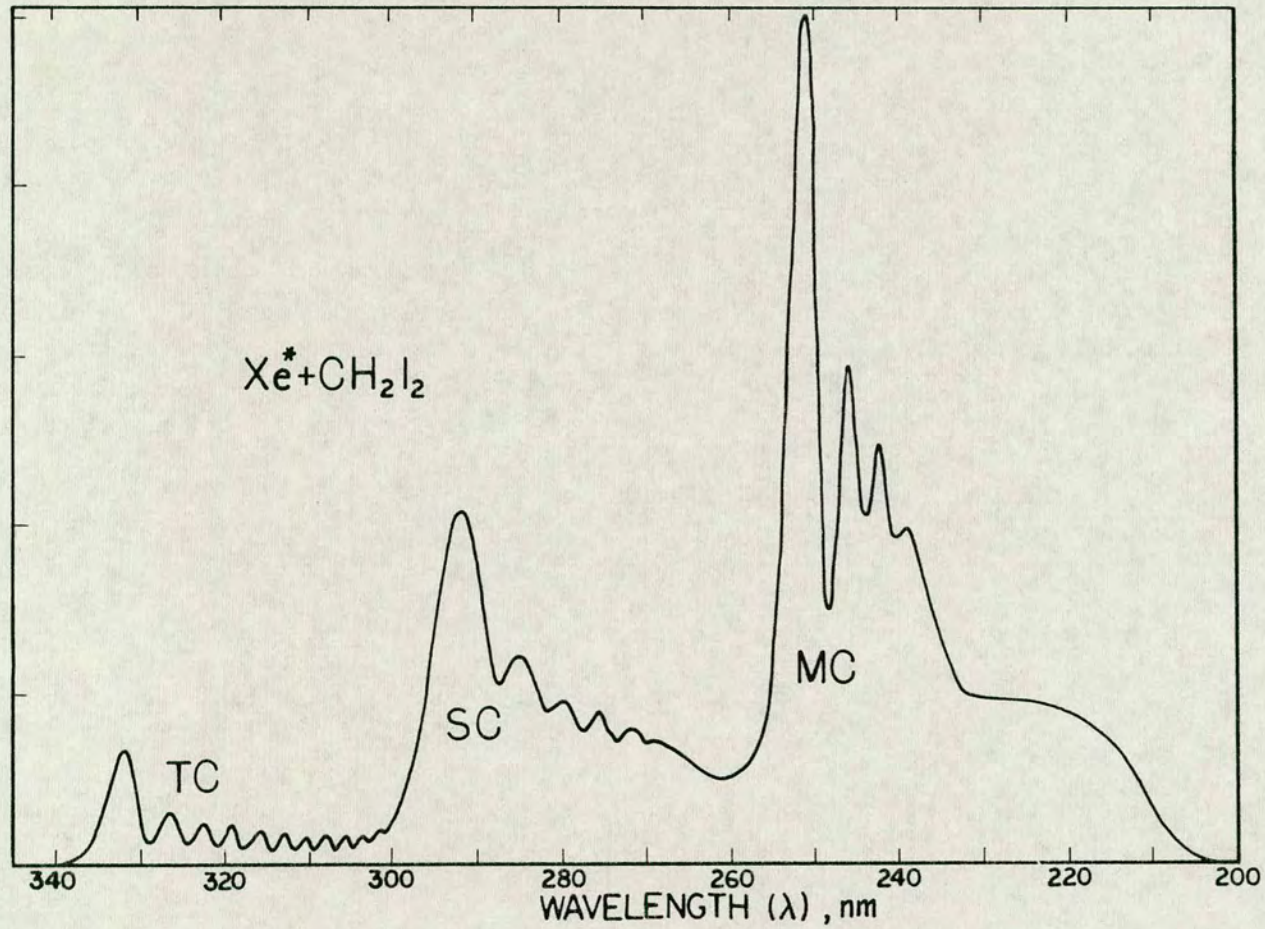

Fig. 1.1 XeI spectrum generated by $Xe^{*} + CH_2I_2$. Total pressure : 0.8 torr ($107 Nm^{-2}$) (after M.F. Golde.[10]).

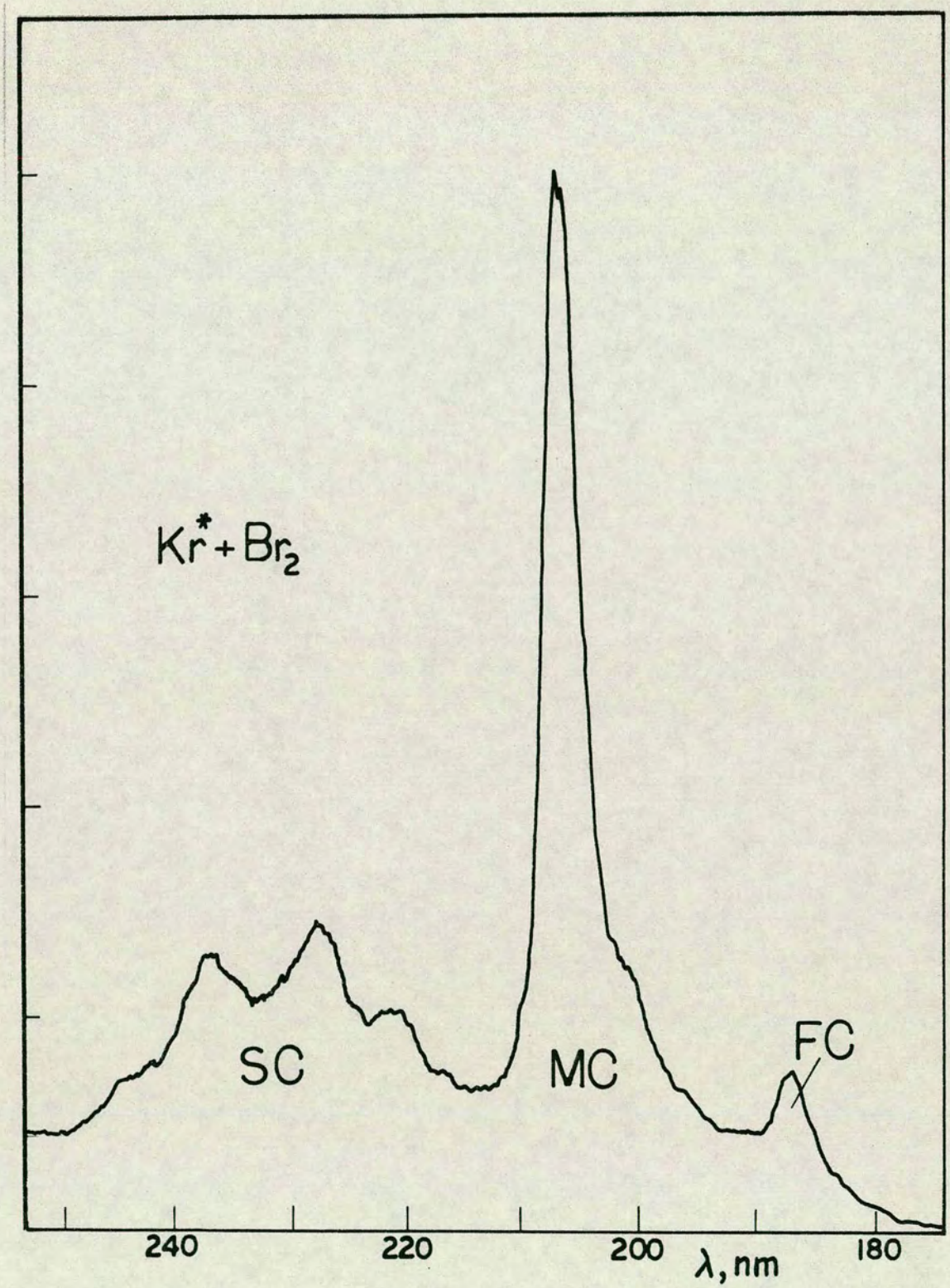

Fig. 1.2 KrBr spectrum generated by $Kr^* + Br_2$ (after M.F. Golde).

displaced to the long wavelength side of a spectrum from noble gas excimer- and atomic- transitions

$$Ng_2^* \longrightarrow 2Ng + h\nu \qquad (11)$$

$$Ng^* \longrightarrow Ng + h\nu \qquad (12)$$

The MC shows an increase in the intensity from a short wavelength threshold to a broad peak at long wavelength. Most spectra show subsidiary peaks to the short wavelength of the strongest peak, which together form a broad, oscillatory pattern. The positions of the strongest peak in the MC are tabulated in table 1.1 for the various spectra.

Table 1.1

Positions (in wavelengths (nm)) of strongest MC peak in low pressure spectra obtained in discharge flow systems for the various noble gas halides.

Ng \ X	F	Cl	Br	I
Ar	193	175	165.5	-
Kr	248	222	206	190
Xe	352	308	282	251

On the long wavelength side of the MC a weaker "secondary continuum" (SC) is found. It is more irregular in shape, and shows broader structure than the MC.

A weak "third continuum" (TC), to even longer wavelength, has been identified in a number of spectra

(figure 1.1) by M.F. Golde, M.P. Casassa and myself.[10] (see appendix 1).

Some of the noble gas halide spectra show a separate low intensity continuum in the MC region to shorter wavelength than the strongest MC peak,[16] which I will call the "fourth continuum" (FC) (figure 1.2).

Each of the different spectral contributions, MC, SC, TC and FC have been assigned to different electronic transitions.

Three emitting states have been identified. These are the ionic states, $B(^2\Sigma^+)$ and $C(^2\Pi_{3/2})$ (or B III ($\Omega=1/2$) and C II ($\Omega=3/2$) in Hunds case c), which correlate diabatically with $Ng^+(^2P_{3/2}) + X^-(^1S)$, and $D(^2\Pi_{1/2})$ (or D IV ($\Omega=1/2$)), which correlates with $Ng^+(^2P_{1/2})$ and $X^-(^1S)$. Three low lying states have been identified, $X(^2\Sigma^+)$ ($X(\Omega=1/2)$) and $A(^2\Pi_{3/2})$ ($AI(\Omega=3/2)$), which correlate with the neutral species $Ng(^1S)+X(^2P_{3/2})$, and $A(^2\Pi_{1/2})$ ($AII(\Omega=1/2)$), which correlates with $Ng(^1S) + X(^2P_{1/2})$. A schematic diagram of these potentials is shown in figure 1.3.

These potentials have been calculated by ab initio calculations for the various noble gas halides.[52-56] The B- and the C- states are found to be very close in energy, while the D-state is higher in energy by approximately the magnitude of the spin orbit splitting in the positive noble gas ion.[16] The calculations

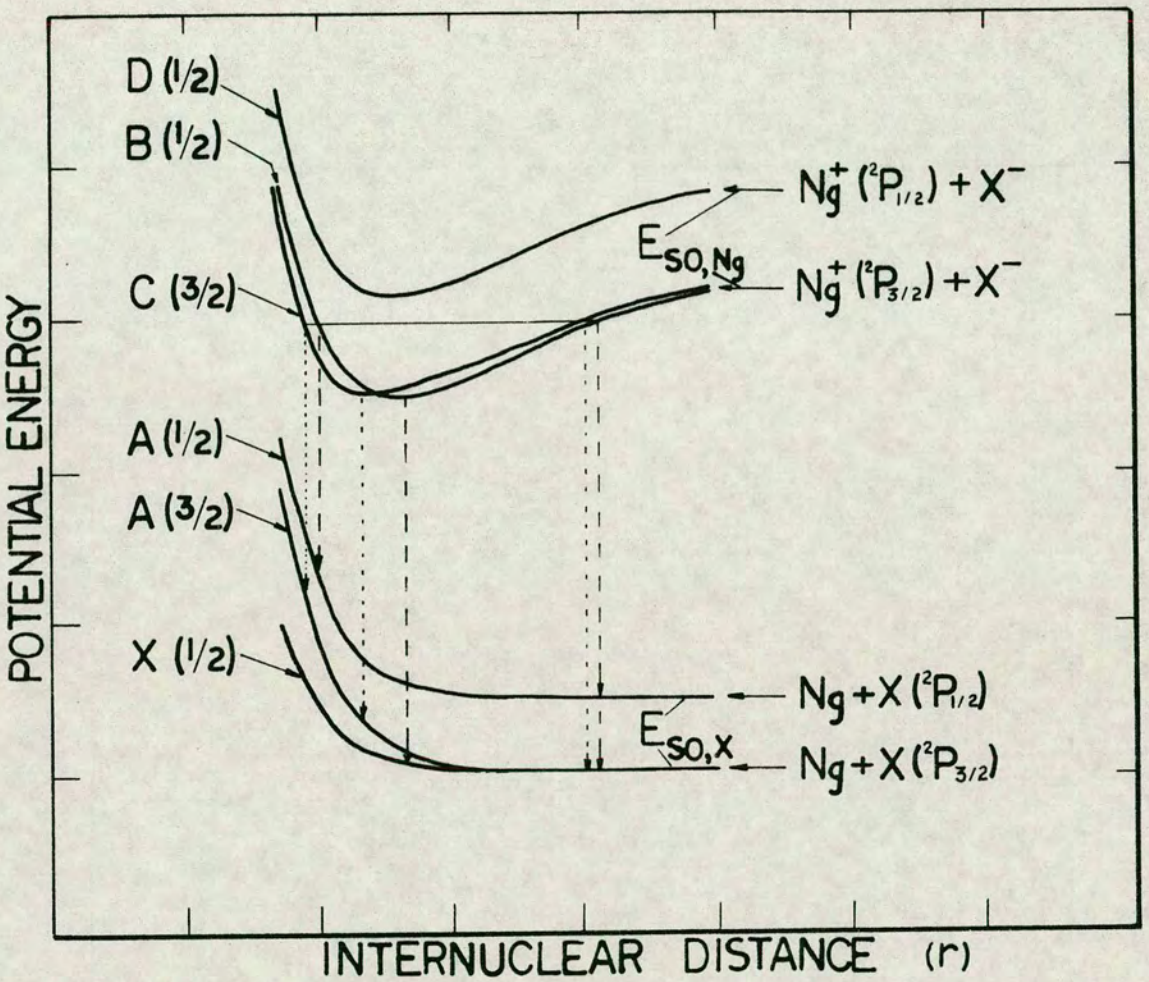

Fig. 1.3 Schematic potential curves for the noble gas halides, NgX. $E_{SO,Ng}$ (cm^{-1}) : Ar : 1432; Kr : 5371; Xe : 10537. $E_{SO,X}$ (cm^{-1}) : Cl : 881; Br : 3685; I : 7603. - - - Transitions from B(1/2), . . . transitons from C(3/2). $1 cm^{-1} = 11.963$ J $mole^{-1}$.

predict that the C-state lies slightly higher in energy than the B-state and has slightly shorter equilibrium internuclear distance (r_e) (see tables 1.2 a and b). Experimental results, however, suggest that the B-state lies above the C-state.[25]

The calculated ionic potentials closely resemble the ground state of the alkalihalides in that they have similar bond strength, vibrational frequency and equilibrium internuclear distance, as shown in table 1.2. A characteristic difference is noticed, however, as the vibrational frequency and bond strength for the noble gas halide ionic states are slightly less than for the alkali halides. The equilibrium internuclear distance is slightly greater, however (see figure 1.4 a). This is understandable since the interaction of the negative ion X^- with Ng^+ with nonclosed shell configuration and unpaired electron is expected to be more repulsive than with an alkali ion (M^+) which has a closed shell configuration.[53] Orbital diagrams for the electronic states of $Ng^+ + X^-$ ($^2\Sigma^+$ and $^2\Pi$) for heavy noble gas atoms and ground state $M^+ + X^-$ are shown in figure 1.4 b.

The oscillatory structure of the MC spectra was interpreted in terms of transitions from high vibrational levels in a strongly bound upper state to a flatter region of the ground state.[8,9] A semiclassical analysis of these spectra suggests that the emitting states have comparable or slightly less

Table 1.2

Spectroscopic constants obtained from theoretical calculations for the ionic excited states for the noble gas halides (NgX) (ab initio - calculations), the B (III (1/2))-states (a.), and the C (II (3/2))-states (b.) (see references 52 - 56). The constants in c. are obtained from Perturbation theoretical calculations for the ground states of the alkalihalides (MX) (see reference 140). ω_e is the vibrational frequency in cm^{-1}, D_e is the bond strength of the ionic states (correlating with the ionic species) in cm^{-1} and r_e is the equilibrium internuclear distance in nm.

a. B- states (NgX)

X / Ng	F ω_e	F $D_e x10^{-4}$	F r_e	Cl ω_e	Cl $D_e x10^{-4}$	Cl r_e
Ne	541	5.13	0.201			
Ar	390	4.43	0.239			
Kr	339	4.28	0.251			
Xe	303	4.09	0.268	188	3.40	0.322

X / Ng	Br ω_e	Br $D_e x10^{-4}$	Br r_e	I ω_e	I $D_e x10^{-4}$	I r_e
Xe	133	3.24	0.338	107	3.06	0.362

b. C- states (NgX)

X / Ng	F ω_e	F $D_e x10^{-4}$	F r_e	Cl ω_e	Cl $D_e x10^{-4}$	Cl r_e
Ne	539	5.05	0.200			
Ar	392	4.33	0.233			
Kr	346	4.20	0.243			
Xe	321	4.06	0.256	188	3.34	0.314

X / Ng	Br ω_e	Br $D_e x10^{-4}$	Br r_e	I ω_e	I $D_e x10^{-4}$	I r_e
Xe	132	3.19	0.331	106	2.99	0.357

Cont. table 1.2

c. X- states (MX)						
X /	F			Cl		
M(Ng)	ω_e	$D_e x10^{-4}$	r_e	ω_e	$D_e x10^{-4}$	r_e
K(Ar)	426	4.87	0.217	283	4.13	0.267
Rb(Kr)	373	4.67	0.227	233	3.97	0.279
Cs(Xe)	353	4.56	0.235	214	3.93	0.291
X /	Br			I		
M(Ng)	ω_e	$D_e x10^{-4}$	r_e	ω_e	$D_e x10^{-4}$	r_e
K(Ar)	219	3.97	0.282	187	3.71	0.305
Rb(Kr)	169	3.81	0.294	139	3.56	0.318
Cs(Xe)	150	3.80	0.307	119	3.54	0.332

$1 cm^{-1} = 11.963\ J\ mole^{-1}$.

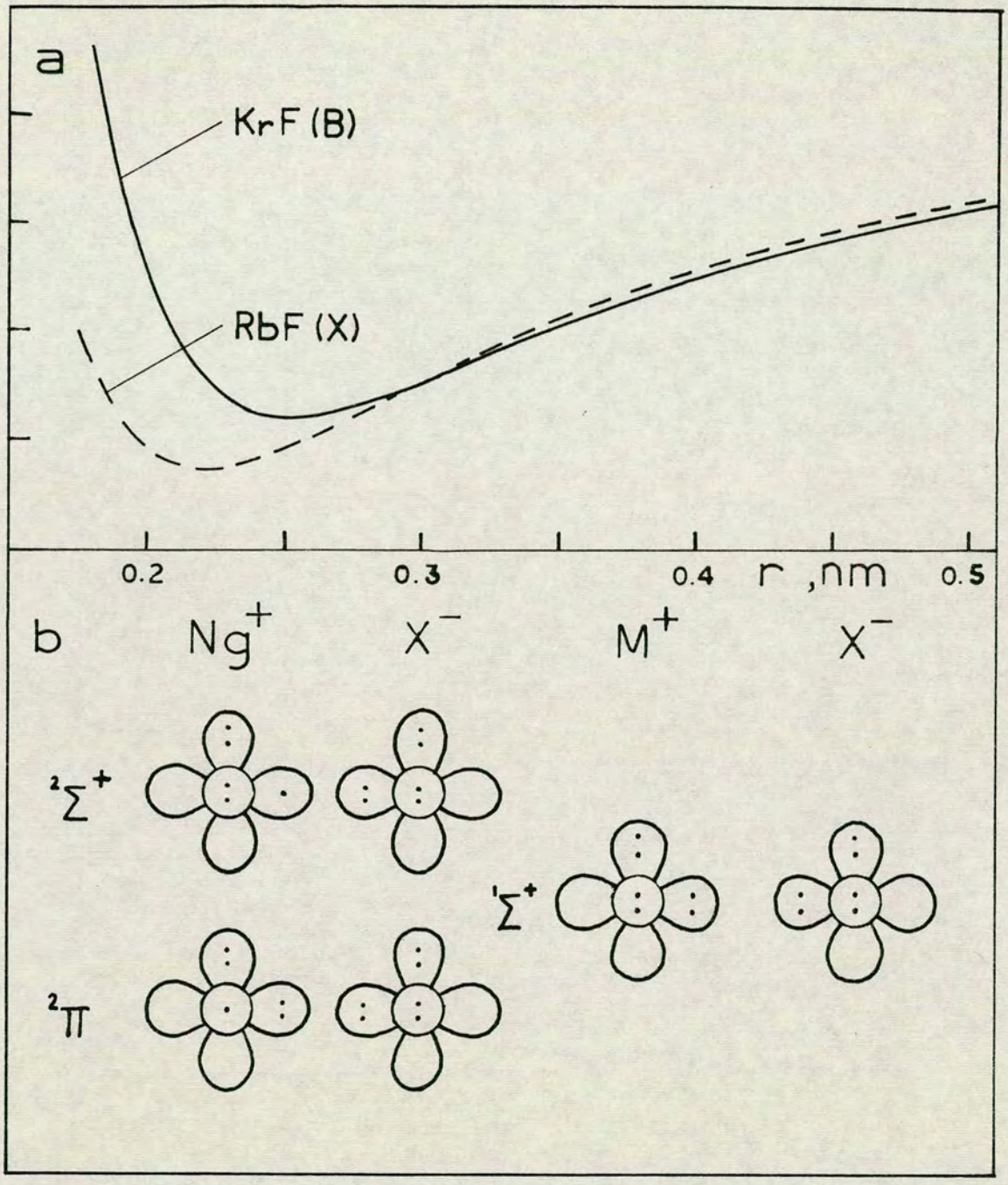

Fig. 1.4 Ionic potential curves and orbital diagrams for ground state alkalihalide- (M^+X^-) and excited state noble gas halide- (Ng^+X^-) molecules. a. Rittner potentials for $RbF(X\,^1\Sigma^+)$[140] and $KrF(B\,^2\Sigma^+)$[59]. b. Orbital diagrams for Ng^+X^-, $^2\Sigma^+$- and $^2\Pi$ - states and for M^+X^- $^1\Sigma^+$- ground state.

bond strength and vibrational frequencies than the ionic ground states of the corresponding alkalihalides.

The structure and pressure dependence behaviour of the SC, which differ from that of the MC, suggests that it represents a radiative transition where both electronic states (upper- and lower-states) differ from those for the MC.[9,15] The intensity of the SC shows a decrease relative to the intensity of the MC with pressure suggesting that a collision intersystem crossing is occurring between two states of close energy,[15] the C- and B- states. Ab initio calculations predict the most probable radiative transitions from these states to be the B - X and C - A(3/2) transitions (see table 1.3) which were assigned to the MC and SC respectively.

Table 1.3

Estimated reciprocal values of the transition probabilities for the various electronic transitions ($1/A_{nm}$, nsec) for the noble gas fluorides and the xenonhalides, obtained from ab initio calculations. (see references 52 - 56).

Electronic transitions	NgX					
	ArF	KrF	XeF	XeCl	XeBr	XeI
B-X	4.2	6.7	12	11	12	12
D-X	22	12	9.5	9.6	8.8	8.6
C-A(3/2)	48	63	113	120	120	110
D-A(1/2)	62	77	75	180	730	610
B-A(1/2)	221	195	340	140	51	44

The TC show similar pressure dependence behaviour as the MC and judging from the wavelength at which these appear, these were assigned to the B-A(1/2) transition.[10]

The FC are found to be similar in shape to the MC and are found to be positioned at a characteristic distance from the strongest peak of the MC - almost equal to the spin orbit splitting of the Ng^+ ion. This suggests that these can be assigned to the D-X transition.[16]

Although the various spectral regions have been assigned to specific electronic transitions, it is clear that various other transitions, which have not been mentioned, can also occur and will appear in the same region. Theoretical calculations, however, predict that the probability for other transitions is small compared with those which have already been mentioned. It has also been shown by M.F. Golde, M.P. Casassa and myself that those transitions which mainly contribute to the noble gas halide spectra can overlap.[10] Thus, the short wavelength tail of the C-A(3/2) spectrum in some systems is found to overlap with the B-X spectrum in the MC region.[10]

Spectra recorded at high pressure from electron beam excitation of gas mixtures differ from the low pressure spectra, indicating the importance of relaxation processes in these systems. Virtually no emission is observed from the C-state due to a rapid

collision induced crossing from the C - state to the B - state. The MC reflects transitions from the lowest vibrational levels in the B - state where the population is Boltzmann distributed.

Spectra of XeF[23,27,39,41] and XeCl[27,38] show band structure due to bound - bound transitions. These spectra have been analysed to yield spectroscopic constants and approximate potentials for the B- and the X- states.[38,39]

The MC spectra of XeBr, XeI, and KrF show an oscillatory structure which is less broad and has many more peaks than observed in the corresponding low pressure spectra.[40] These spectra closely resemble the structure observed in the low pressure ArBr spectrum obtained from HBr + Ar^* (see figure 3.6 in chapter 3) for reasons which will be discussed later. This type of structure is characteristic for bound - free transitions from a number of lowest vibrational levels in the bound state, where the number of peaks indicates the number of emitting vibrational levels. Similar spectra have been found for other systems such as Mg_2.[67] These noble gas halide spectra have been analysed by simulation calculations and approximate potentials have been obtained.[40] The assumption was made that the transition moment does not vary significantly with internuclear distance in the FC - region and that the excited molecules thermalize before they radiate. Calculated spectral contributions due to transitions from individual

vibrational levels are found roughly to mirror the radial probability distribution for these showing an oscillatory structure and illustrating the reflection principle neatly. The strongest peak in the experimental spectra on the long wavelength end is shown to be made up of contributions from a number of vibrational levels corresponding to transitions in the region of the inner turning points. The oscillatory structure to shorter wavelength is due to the characteristic oscillatory structure in the v′ contributions. Calculated ArBr spectra presented in this thesis agree with this (see figures 5.4 and 5.5). A number of different systems have been studied where radiative transitions are found to obey the reflection principle. See, for example, references 68 - 72.

Ab initio calculations by Dunning and Hay[52-55] show rapid changes in the transition moments, with internuclear distance for the various radiative transitions for the noble gas fluorides and the xenon halides. These are shown in figures 1.5 and 1.6 for the transitions B-X and C-A(3/2). All the calculated transition moments have a maximum value at a shorter internuclear distance than the equilibrium internuclear distance (r_e), but fall off rapidly to a longer internuclear distance to an asymptotic value corresponding to that for the long lived metastable states of the noble gas atoms.

The importance of taking account of the transition

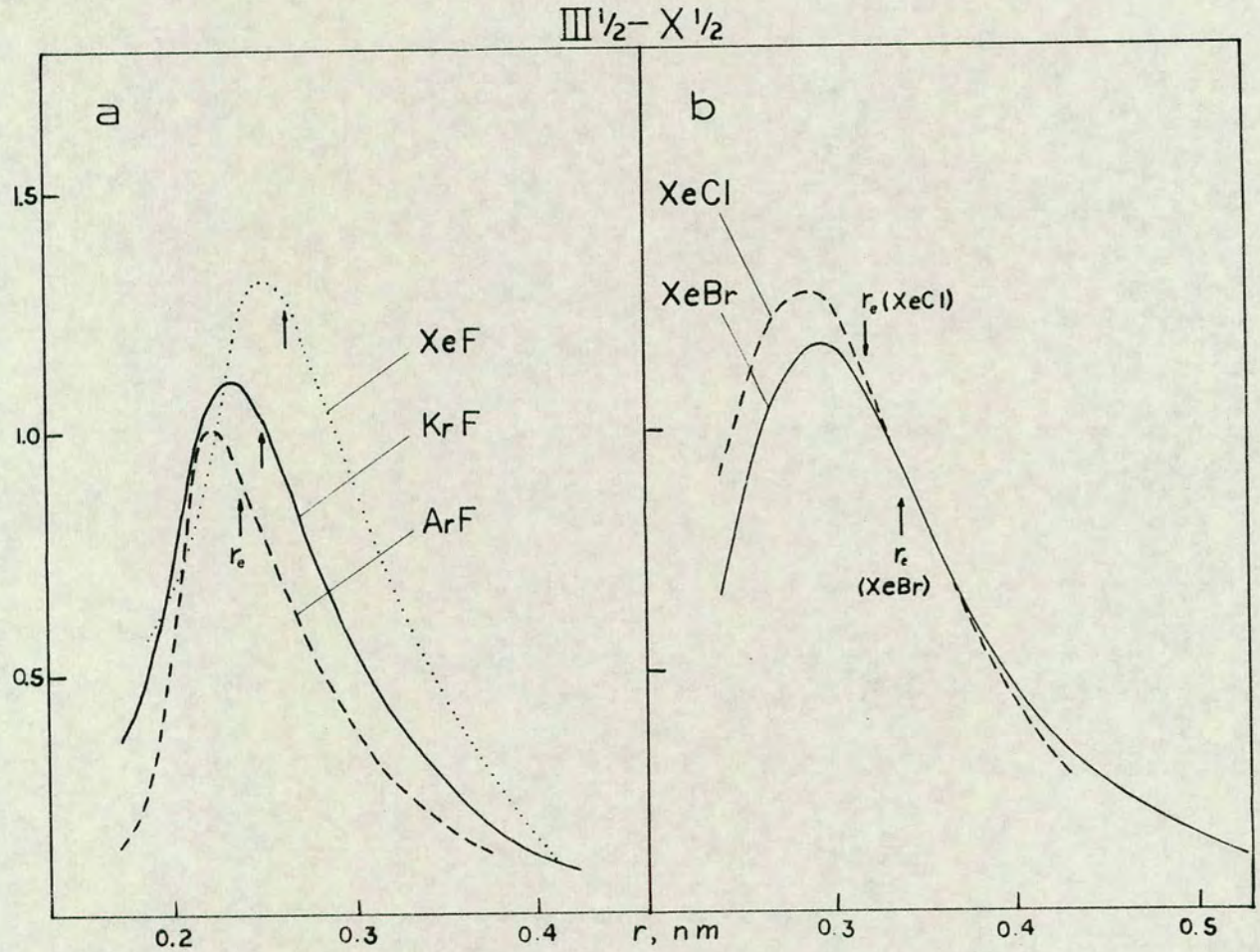

Fig. 1.5 Electronic transition moments for the transition B III(1/2)-X(1/2) for the noble gas fluorides (a) and the xenonhalides (b) obtained from ab initio calculations by Dunning and Hay.[52-56] The arrows show the equilibrium internuclear distance (r_e) for the B-state.

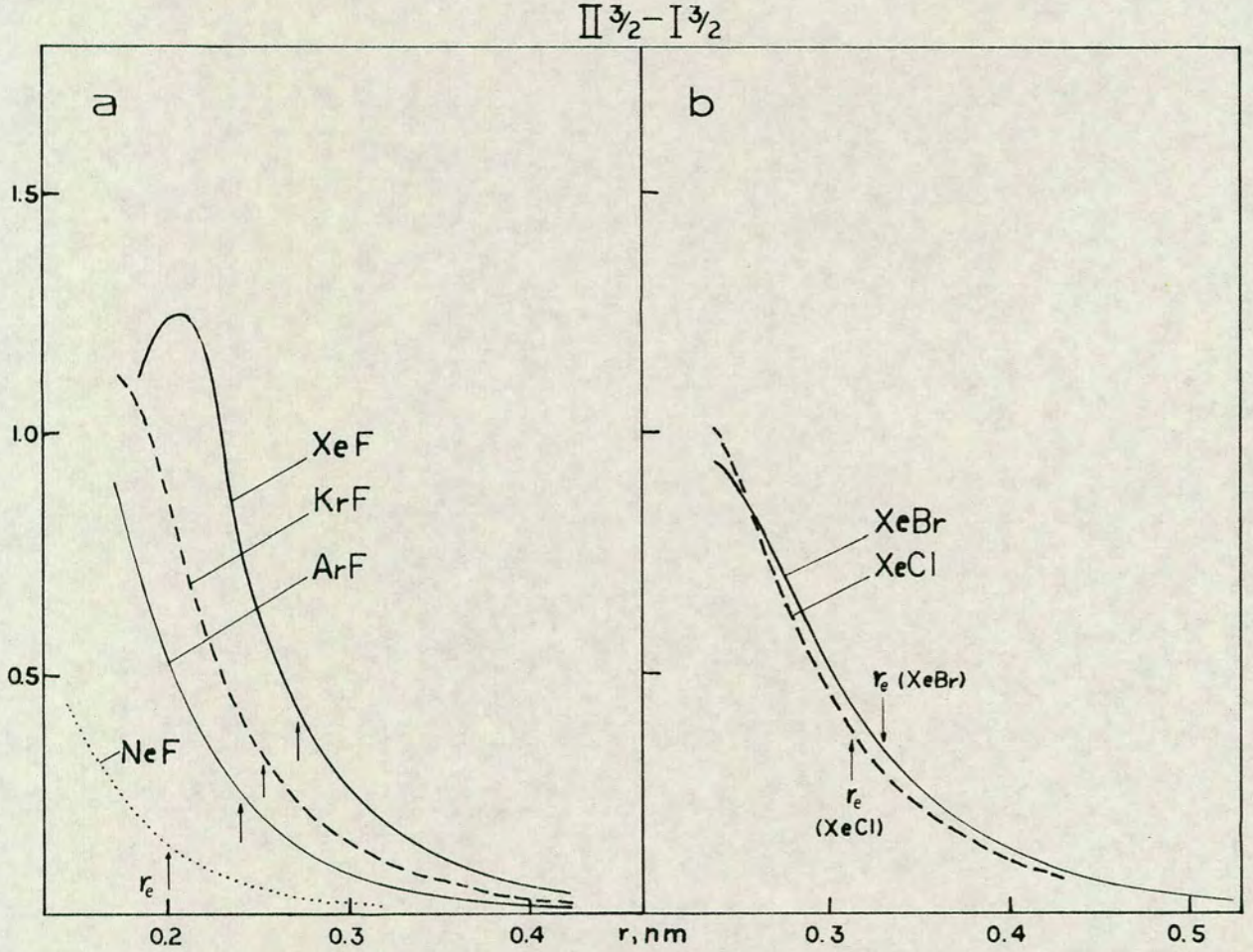

Fig. 1.6 Electronic transition moments for the transition C II(3/2)-A I(3/2) for the noble gas fluorides (a) and the xenonhalides (b) obtained from ab initio calculations by Dunning and Hay.[52-56] The arrows show the equilibrium internuclear distance (r_e) for the C-state.

moments in simulation calculations for noble gas halide spectra is therefore clear. It is especially so for spectra which involve transitions from high vibrational levels which span over a long range of internuclear distance, such as some low pressure spectra. This has been illustrated in simulation calculations for KrF spectra.[21] Later in this thesis (chapter 5) it will be shown to be a critically important factor in the simulation of the ArBr spectra, where only the very lowest v′ levels are emitting.

Setser et al use potential curves and transition moments calculated by Dunning and Hay for KrF in the simulation calculations of the MC and SC obtained from low pressure spectra. These simulation calculations yield estimates of initial and steady state population distributions in the B- and the C- states from reactions of Kr^* with different fluorine containing reagents. This shows a broad distribution over a wide range of vibrational levels from v′= 0 to levels close to the threshold energy for the reactions (see figures 12 and 15 in reference 21). It is necessary to weigh the population in the lowest vibrational levels significantly less than in the higher ones, in simulations of the SC, in order to obtain fits to the experimental spectra - more so than in the simulation of the MC.

Halogen atomic emission is observed in many of the

spectra for reactions of metastable noble gas atoms with halogen containing reagents. Excited halogen atoms are believed to be formed by predissociation of the excited ionic states by low lying, repulsive molecular states which correlate with $Ng(^1S)$ and X^*. Other reaction channels can possibly also account for the formation of excited halogen atoms.[15] The low lying molecular states are lower in energy for heavy halogen atoms than light ones. The ionic potentials are of higher energy for light noble gas atoms than heavy ones. Predissociation is therefore especially important in systems of light noble gas atoms and heavy halogen atoms where a number of low lying Rydberg states cross high energy ionic states. Thus, no ArI emission has been observed due to complete predissociation of the ionic states as will be shown later in this thesis (chapter 3). Only the lowest vibrational levels in $ArBr^*$ and KrI^* can emit while the higher ones are predissociated. Predissociation is also found but to a less extent in $ArCl^*$, $KrBr^*$ and XeI^*.

1.3 Kinetics of the noble gas halide systems.

The close similarity of physical and chemical properties between the metastable noble gas atoms and the ground state alkali atoms, and of the potential curves of the excited noble gas halides and the ground states of the alkali halides has been taken to imply analogies between reaction (1) and the alkali atom reaction

$$M + RX \longrightarrow MX + R \qquad (13)$$

These reactions are thought to occur by the electron jump mechanism[73-77] (harpoon mechanism), the basic features of which have been developed in a theoretical study by Magee in 1940.[76-77]

According to this model, the Rydberg electron of the metastable noble gas atom jumps to the halogen containing reagent, as the species approach. This occurs at a characteristic separation (R_c) corresponding to the crossing point of the covalent entrance channel and the ionic ($Ng^+ RX^-$) surface (figure i).

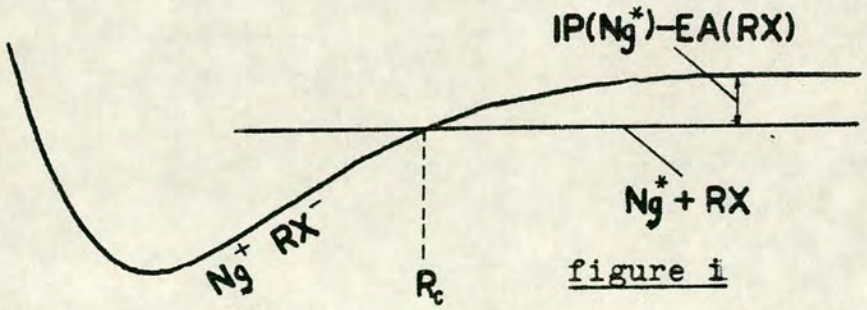

figure i

If the ionic potential surface is characterized by the dominant coulomb attraction (e^2/r), R_c is given by the expression

$$IP(Ng^*) - EA(RX) = e^2/R_c \qquad (1.1)$$

where IP is the ionization potential of the metastable noble gas atom and EA is the vertical electron affinity of RX. If the probability of the electron jump and the subsequent reaction is unity, the reaction cross - section is simply πR_c^2.

The electron jump mechanism has been used to explain the large cross section found for the reactions of the alkali atoms with the halogens, with high efficiency of conversion of the reaction exothermicity into vibrational energy in the MX product molecules. The total cross-section and the branching ratio for the formation of the excited noble gas halides (approximately unity) from reactions of the metastable noble gas atoms with the halogens is close to that found for the reactions of the alkali atoms with the halogens.

The low pressure spectra obtained from the reactions, $Ng^* + X_2$, where predissociation does not occur, give an indication of an emission from vibrational levels in the ionic states which are close to the threshold energy.

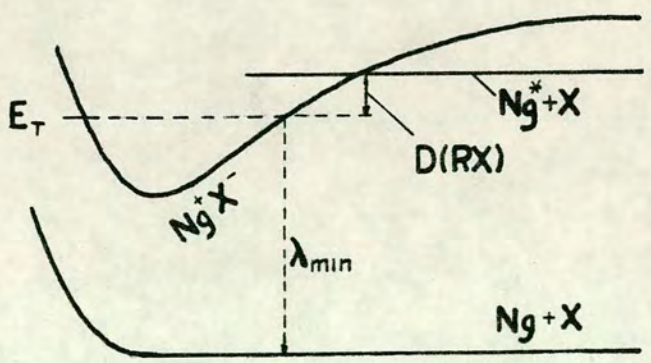

figure iii

The threshold energy (E_T) is determined by the bond strength of the reagent molecule, D(RX), and the

electronic energy of the metastable noble gas atom, $E(Ng^*)$, and is approximately

$$E_T = E(Ng^*) - D(RX) \qquad (1.2)$$

The majority of the excited state species is in the $^3P_2$ - state while some ($\sim$ 10 - 15%) are in the $^3P_0$ - state[7,20] so Ng^* are commonly assumed to be $Ng^*(^3P_2)$. The low wavelength limit (λ_{min}) of the low pressure spectra gives a direct indication of the threshold energy, assuming that the energy of the ground state is zero in the region of the outer turning points[8] (see figure ii). More detailed analyses of these spectra suggest that the efficiency of the conversion of the reaction - exothermicity into vibrational energy is indeed very high.[9,21]

Studies of reactions of metastable noble gas atoms with polyatomic molecules show lowering in the fraction of quenching collisions which yield NgX^* from that for reactions with the halogens. A shift in the initial vibrational distribution below the maximum energetically attainable is also observed. This is in agreement with observations that a larger fraction of the exothermicity goes into translational energy for the reactions of the alkali atoms with polyatomic halogen containing reagents than with the halogens. A suggestion has been made that some reactions of the metastable noble gas atoms with the halogen containing reagents occur via complex formations.[15,16]

Low pressure spectra indicate that rapid

vibrational relaxation processes are occuring in the excited states of the noble gas halides in rare gas media.[9,10,15] This has been further verified by simulation calculations for KrF spectra.[21]

The disappearance of the SC spectra followed by enhancement of the MC, is assumed to indicate that a collision induced crossing is occuring from the C-state to the B-state.

Rate constants for transfer between the B- and the C- states have been estimated for the noble gas fluorides and argon quenching gas

$$NgF^*(B) + Ar \xrightarrow{k^B_{Ar}} NgF^*(C) + Ar \qquad (14)$$

$$NgF^*(C) + Ar \xrightarrow{k^C_{Ar}} NgF^*(B) + Ar \qquad (15)$$

These are found not to differ greatly for the different noble gas fluorides. k^B_{Ar} and k^C_{Ar} are found to be 54 ± 20 and $97 \pm 30 \times 10^{-11}$ cm^3 molecule^{-1} s^{-1}. [25]

The quenching of the excited ionic states to lower lying states is found to be unimportant for the noble gases relative to other processes like the transfer processes between the B- and the C- states or radiative transition.[26]

1.4 Content of chapters 2 - 5.

Chapters 2 to 5 of this thesis contain detailed descriptions of spectroscopic studies of vacuum - UV spectra obtained from reactions of Ar^* with Br-, Cl- and I- containing reagents in a low pressure discharge flow system. Most of the work, which will be described here, was done at the University of Edinburgh, UK, while some of it was done at the University of Pittsburgh, USA, (the least square analysis of the spectra, described in chapters 4 and 5).

A special emphasis was on the study of ArBr spectra, which were observed from reactions of a number of bromine containing reagents. The ArBr spectra proved to be especially useful for deriving information on the spectroscopy and the kinetics of the noble gas halide systems in general. Most low pressure spectra which have been recorded in discharge flow systems are hard to analyse, due to their complexity, because of the great number of emitting vibrational levels. The ArBr spectra were shown to represent radiative transitions from the lowest vibrational levels in the ionic states only, while the high vibrational levels are predissociated. These spectra are therefore easier to analyse than most other low pressure spectra. The ArBr MC resembles those observed in high pressure spectra for other noble gas halide systems, which have proved to be relatively easy to analyse. The absence of SC

in the high pressure spectra makes these spectra of limited use for studying the collision induced crossing between the B- and the C- states. The low pressure ArBr spectra, on the other hand, show SC with relatively strong intensity. One particular advantage of the ArBr system proved to be the appearance of bromine atomic lines close to the ArBr spectra, which could be used as an internal standard against which changes in the intensities of the ArBr spectra could be studied.

In addition to that of identifying the MC and the SC in these spectra a weak continuum on the long wavelength side of the SC was also found in some of these and was assigned to the B-A(1/2) transition (TC) which had not been identified in other spectra before.

The wavelength ranges of the spectral contributions corresponding to the individual electronic transitions were estimated in some of the spectra. The B-X and the C-A(3/2) spectra were found to overlap in the MC region and the C-A(3/2) and the B-A(1/2) spectra to overlap in the SC region. This showed that overlap of spectral contributions due to different electronic transitions can be of significant importance in the noble gas halide spectra.

Rapid vibrational relaxation processes were found to occur in the C- and the B- states, as well as a collision induced crossing between these.

A relative rate constant for the collision

induced crossing from the C state to the B state was obtained.

Simulation calculations for the various B-X and C-A(3/2) spectra were carried out. A semiclassical uniformized WKB method was used for evaluating calculated intensities. The use of this method was preferable to that of the more commonly used numerical methods, due to the use of much less computer time in evaluating the WKB wavefunctions than the numerical wavefunctions. A method was developed for evaluating uniformized WKB wavefunctions for repulsive potentials.

It was shown, despite very limited information on potential curves and transition moment, that valuable information, especially on the population distributions in the emitting states, can be obtained from such simulation calculations for bound – free transitions, such as those which are occuring in the ArBr system, if the number of emitting v′ levels is known.

Chapter 2 contains a description of the experimental set up and other necessary details concerning obtaining the experimental results.

In chapter 3 the experimental spectra are presented and interpreted. ArBr- and ArCl- spectra are shown, as well as changes in intensities of these with pressure. The effect of changing the temperature in

the reaction vessel on the ArBr spectrum obtained from $HBr+Ar^*$ is also dealt with.

All the $RBr+Ar^*$ spectra show strong bromine atomic lines but chlorine atomic lines were only identified in Cl_2+Ar^*.

Spectra from $HCl+Ar^*$ and $DCl+Ar^*$ show spectra due to electronic transitions in HCl and DCl respectively.

No ArI emission was observed from reactions of Ar^* with iodine containing reagents, but only iodine atomic emission was observed. This is due to a very efficient predissociation in this system.

Chapter 4 contains a description of the semiclassical WKB approximation method.

The simulation calculations for the various ArBr- and ArCl- spectra are described in chapter 5.

The MC and the SC spectra obtained from $HBr + Ar^*$ and $DBr + Ar^*$ and the SC obtained from $CH_2Br_2+Ar^*$ were simulated, and the structure of these spectra was interpreted. Information on population distributions in the emitting states (C- and B- states) was obtained from these simulation calculations for spectra obtained at various pressures. Out of various analytical potential curves which were used in the simulation calculations, potentials were selected to represent the B,C,X and A(3/2) states respectively.

The MC ArCl spectra from Cl_2+Ar^*, CCl_4+Ar^* and $HCl+Ar^*$ were simulated. Qualitative information on

population distributions in the B-state were obtained. Analytical repulsive potential curves which were used in the simulation calculations were compared with a calculated (SCF) potential curve for the X-state.

2. EXPERIMENTAL.

2.1 Apparatus.

2.11 Discharge flow system.

Experiments were made using a discharge flow system. It followed closely the design of Setser and coworkers.[3] The discharge region and the observation vessel are shown schematically in figure 2.1 a.

A flow of purified argon of between 250 and 300 μmole s^{-1} passed through the system at pressures between 0.6 and 4 torr*. Excited state argon atoms were produced in a low power hollow cathode dc discharge between molybdenum electrodes operating at 200 V, to give approximately 1mA electric current through the gas. A Woods horn light trap was placed between the discharge and the reaction vessel to prevent stray light from the discharge from reaching the observation vessel. The glasstubing in this region was 7 cm long, with 0.8 cm i.d. and made of pyrex. A linear flow velocity at about 1 torr* was typically 80 ms^{-1}. The lifetime of the metastable noble gas atoms exceeds 1 sec. A loss of these excited states

* 1 torr = 133.322 Nm^{-2}

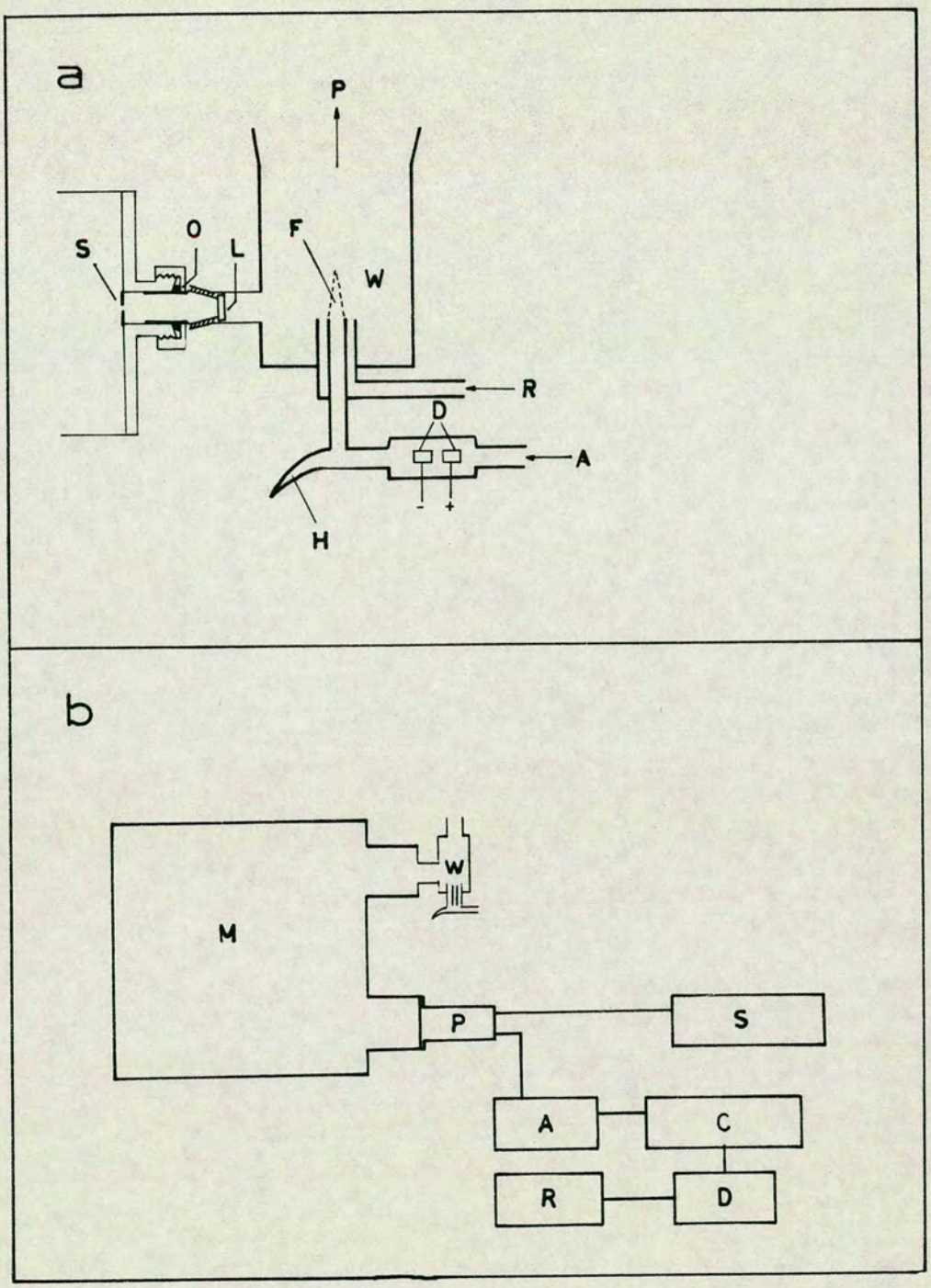

Fig. 2.1 Schematic figure of the experimental apparatus. a. The discharge region and the observation vessel, A : Ar - flow; D : Discharge; H : Wood's horn; R : Flow of reagents; F : Flame; W : Reaction vessel; P : To the pump; L : LiF - window; O : O - rubber ring; S : Entrance slit b. The detection system, W : Reaction vessel; M : Monochromator; P : Photomultiplier; S : Power supply; A : Amplifier; C : Counter; D : Digital/analoge converter; R : Pen recorder.

by radiative transitions is therefore not of great importance. These states can be quenched by recombination reactions and by collisions with the glass walls, of which the latter process is especially critical at low pressures, when the excited state species can diffuse rapidly to the walls. The length of the tubing between the discharge and the observation vessel (7cm) was therefore made as short as possible to minimize wall loss of Ar^*. The major excited species reaching the vessel are expected to be the long lived metastable states $Ar^* 3p^5 4s\ ^3P_2$ and $^3P_0$ with a production of about 10^{-4} - 10^{-5}%.[17]

Reagents were added to the argon flow through a coaxial tube at the inlet to the reaction vessel. Typical flow rates were about 1 μmole s^{-1}.

The gases flowed from the reaction vessel through a wide pyrex tube to an Edwards "Speedivac" 1SC900 pump, with a capacity of 1110 litres/min. The pumping rate was controlled by a regulating stopcock, attached to the pump. Gas flows were controlled by Edwards fine control needle valves (models LB1B or LB2B).

The flow rates were measured by observing the pressure drop across calibrated capillaries at a known backing pressure. The backing pressure for argon was measured by a mercury manometer and usually maintained at about latm ($1.01 \times 10^5 Nm^{-2}$). The backing pressure for the reagents was measured by a calibrated glass spiral manometer, suitable for measuring low pressures of the

order of a few torr[†]. The pressure inside the reaction vessel, as well as the pressure drop across the capillaries, was measured by using silicone oil manometers.

The reaction vessel was made of 4 cm i.d. pyrex tube with a side tube as shown in figure 2.1 a. A LiF window (22 mm in diameter, 4 mm thick) was cemented on a cone which fitted to this side arm, as well as to a brass holder on the monochromator in front of the entrance slit. For such a design of the reaction vessel the major emission from chemiluminescent reactions occurs from a flame of conical shape, whose height and shape depend on the flow rates of the reagents and the total pumping rate. Maximum height of slits (20 mm) on the monochromator was used in order to observe as much of the flame as possible. The mean distance ($\bar{x}$) diffused by an argon atom in one residence time (t_c) is about[145]

$$\bar{x} = (2Dt_c)^{1/2} \qquad (2.1)$$

where D is the diffusion coefficient. In a typical experiment, where the total pressure inside the reaction vessel is about 1 torr[‡], the mean distance is negligible during the short residence time in the reaction vessel ($\bar{x}$ = 1-2 mm), and the shape of the argon flow (Ar and Ar*) deviates only slightly from

† 1 torr = 133.322 Nm^{-2}.

that of being like a cylinder (figure i a). Due to this small diffusion the chemiluminescent reactions which occur when the reagent flow is switched on happen at points within the region of this gas - cylinder which gradually approach the center axis in the direction of the flow as the distance from the inlet tubes increases, while the outermost Ar^* atoms in the flow cylinder are quenched first due to the geometry of the inlet tubes. Thus a flame of conical shape is formed. As the flow of the reagent increases the Ar^* atoms are quenched faster, and the height of the flame decreases. This is illustrated in figures i b-d.

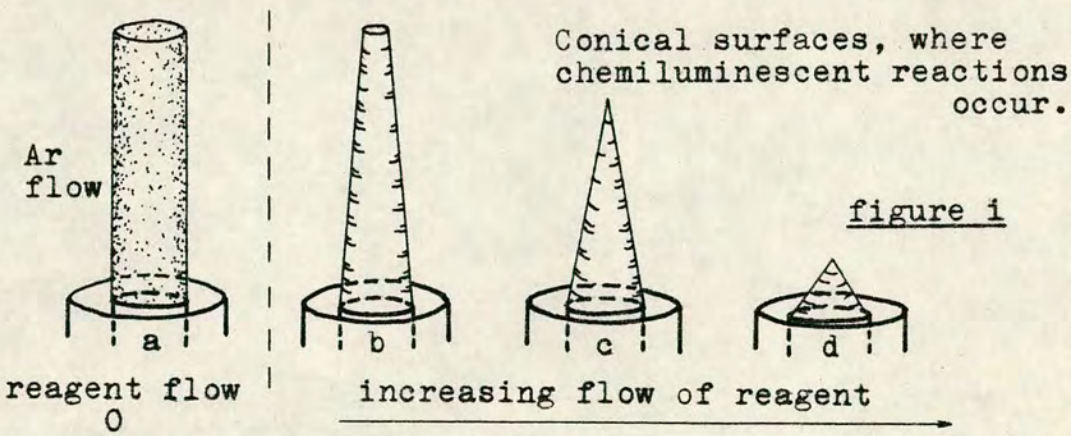

figure i

2.12 Detection system.

A vacuum - UV emission from the reaction vessel was detected by an EMR 542G "solar blind" photomultiplier, after being dispersed by a Hilger E766 one meter normal - incidence vacuum monochromator (figure 2.1b).

The monochromator was maintained at pressures

below 10^{-5} torr*, measured on a Penning gauge, by means of an Edwards oil vapour diffusion pump, model E04, backed by a rotary pump (ES200). The grating (1200 lines/mm blazed at 120 nm) was coated with aluminum, and magnesium fluoride. The reciprocal linear dispersion was 0.42nm/mm. Slit widths in the range 250 - 1500 μm were used. Most commonly a slit width of 500 μm was used, with a resolution of 0.21nm.

The photomultiplier was placed in front of the exit slit, inside a metal housing. It was operated at a voltage of about 3kV. obtained from a stabilized power supply (Brandenburg 507R) and was used in the photon counting mode. A schematic drawing of the photomultiplier and the circuit used in the photon counting mode is shown in figure ii.

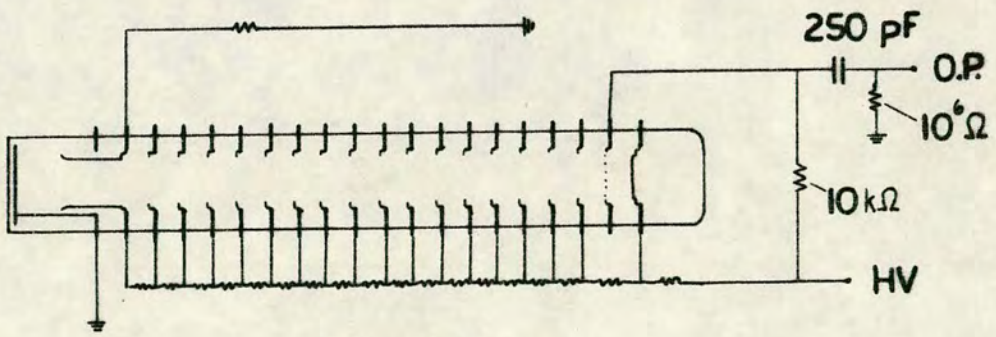

figure ii

The signals were fed through a pulse amplifier and displayed on a Timer Counter, SM201, or a pen recorder via a digital/analoge converter. The electronic dark current was typically 1 count s^{-1} and signals of

* 1 torr = 133.322 Nm^{-2}

between 20 and 1×10^5 counts s^{-1}, which corresponded to a range over which the photomultiplier showed a linear response with number of incident photons.

Spectra were obtained by scanning over the relevant wavelength range and accumulating counts over a period of 1 second or 10 seconds. Intensities at particular wavelengths were obtained by recording the signal at that wavelength for a suitable period of time. In certain cases spectra were obtained by the latter technique, advancing the monochromator setting manually. A background signal measured either at 100 nm or 196 nm was subtracted. At 100 nm the light was absorbed by the LiF window.[78] The sensitivity of the photomultiplier for light at 196 nm is very low.

In order to minimize scattered light from bromine atomic lines for studying some ArBr spectra, a spectrosil window (25 mm in diameter, 2 mm thick) was placed between the exit slit of the monochromator and the photomultiplier. The short wavelength transmission limit for a spectrosil window (synthetic fused quartz) is about 160 nm[78] (see figures 2.3 and 2.4).

2.2 Spectral response calibration.

The relative quantum efficiency of the detection system as a function of wavelength can be obtained from v''- progressions in electronic spectra of diatomic molecules with known transition probabilities.[10,15] The ratio of the relative quantum efficiencies, at the wavelengths, $\lambda_{v'v_1''}$ and $\lambda_{v'v_2''}$, where the two bands, $v'v_1''$, and $v'v_2''$, are found is expressed as

$$\frac{R(\lambda_{v'v_1''})}{R(\lambda_{v'v_2''})} = \frac{A_{v'v_2''}}{A_{v'v_1''}} \cdot \frac{S_{v'v_1''}}{S_{v'v_2''}} \qquad (2.2)$$

where $S_{v'v''}$ is the detected integrated intensity (counts s^{-1}) of the $(v'v'')$ band, $R(\lambda_{v'v''})$ is the relative quantum efficiency, and $A_{v'v''}$ is the transition probability for spontaneous emission.

Spectra from $H_2(B^1\Sigma_u^+ - X^1\Sigma_g^+)$ and $CO(A^1\Pi - X^1\Sigma^+)$ obtained from the reactions $Ar^* + H_2$, $Ar^* + COS$ and $N_2^* + CO$ were used. These are known to give rather simple spectra in the vacuum - UV region,[12,24,79] due to transitions from few vibrational levels. These spectra are shown in figure 2.2 and are similar to those seen by others.[15,79]

The H_2(B-X) emission occurs after a collision excitation of H_2 by trace quantities of the resonance state $Ar^*(^3P_1)$.[79] A weak emission, due to transitions from v'=3 in the B - state, were obtained for relatively

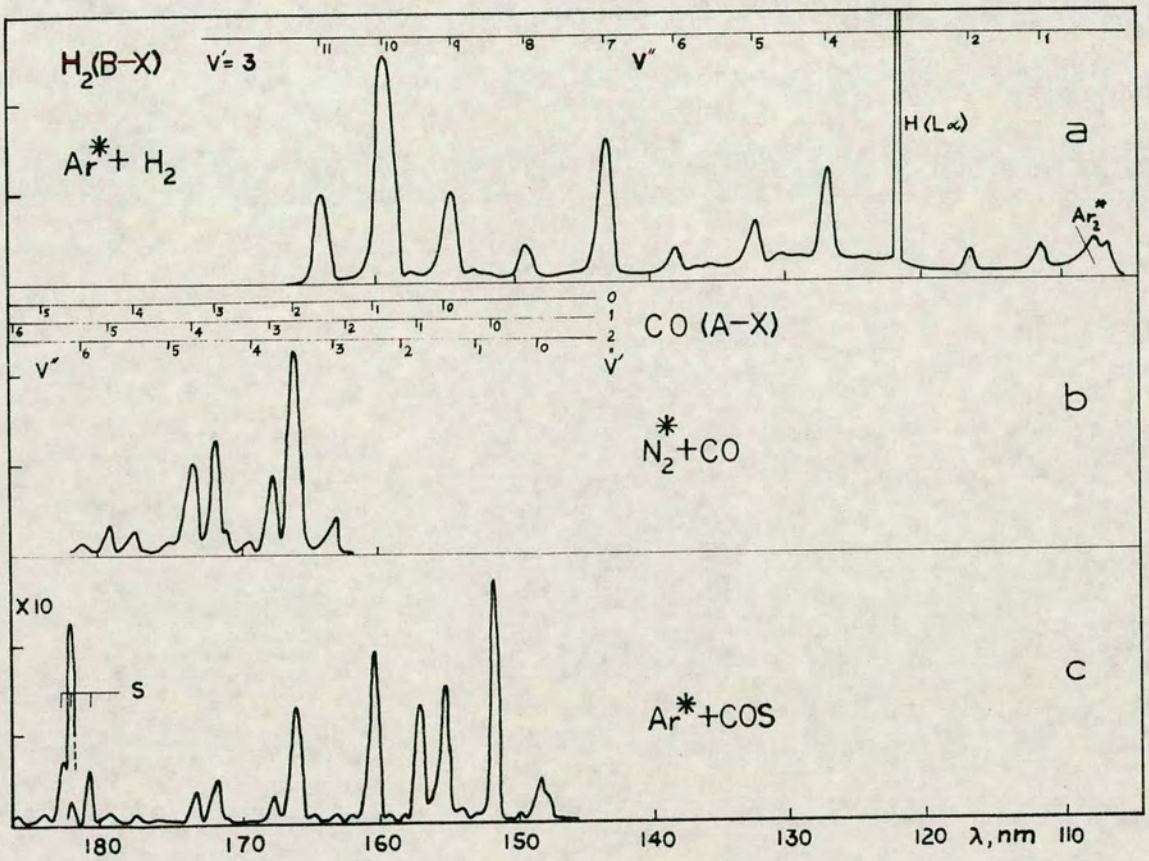

Fig. 2.2 Band spectra used to obtain the relative quantum efficiency of the detection system.
a. $H_2(B^1\Sigma_u^+ - X^1\Sigma_g^+)$ spectrum from Ar^*+H_2. Progression from $v'=3$ is indicated as well as $H(L_\alpha)$ and Ar_2^* transitions. Slit width 750μm.
b. and c. $CO(A^1\Pi - X^1\Sigma^+)$ spectra from N_2^*+CO and Ar^*+COS respectively. Progressions from $v'=0$ - 2 as well as $S(^3S - ^3P)$ transitions are indicated. Slit widths: b. 500 μm, c. 400 μm.

high flow of H_2 and 750 μm slit width in the region 110 nm to 165 nm. These hydrogen bands sit on top of the Ar_2 continuum, extending from a short wavelength limit near 107 nm. A hydrogen atomic line (L_α) at 121.56 nm overlapping with the (3,3) - H_2 band is also observed. The relative quantum efficiencies were derived from the relative integrated intensities of these bands, and the transition probabilities were obtained from ab initio calculations[80] (see table 2.1).

The CO spectrum from $Ar^* + COS$ shows emission bands due to transitions from $v' = 0$ and 1 in the A - state in the wavelength region between 147 nm and 190 nm (figure 2.2c). Some sulphur atomic lines are also found. The $N_2^* + CO$ spectrum shows the same CO bands as found in the $Ar^* + COS$ spectrum, as well as weak bands due to transitions from $v' = 2$. By use of the relative intensities of these bands and the transition probabilities obtained by Mumma,[81] the relative quantum efficiencies were obtained (table 2.1). These results, as well as those obtained from the H_2 spectrum, are plotted in figure 2.3. Average values obtained for the same bands from the $Ar^* + COS$- and $N_2^* + CO$- spectra are plotted. The solid curve is a least square fit curve to these points.

The relative quantum efficiency, when a spectrosil window was placed in front of the photomultiplier, was obtained from change in the continuous spectrum of ArCl from $Cl_2 + Ar^*$ (figure 2.4) and compared with the

Table 2.1

Spectral response calibration.

a. $H_2(B^1\Sigma_u^+ - X^1\Sigma_g^+)$ from $Ar^* + H_2$

v′,v″	λ(nm)	$R(\lambda_{v',v''})$ (arbitrary units)
3,1	111.4	0.12
3,2	116.4	0.25
3,4	127.0	0.62
3,5	132.8	0.76
3,6	138.1	0.74
3,7	143.5	0.91
3,8	148.8	1.00
3,9	154.3	0.85
3,10	159.0	0.66
3,11	163.6	0.57

b. $CO(A^1\Pi - X^1\Sigma)$ from $Ar^* + COS$ and $N_2^* + CO$

		$R(\lambda_{v',v''})$ (arbitrary units)	
v′,v″	λ(nm)	$COS + Ar^*$	$N_2^* + CO$
0,0	154.4	0.93	
0,1	159.7	0.72	
0,2	165.3	0.58	0.665
0,3	171.2	0.40	
0,4	177.5	0.20	
0,5	184.2	0.11	0.065
1,0	151.0	1.00	
1,1	156.0	0.83	
1,3	167.0	0.66	0.610
1,4	173.0	0.39	
1,5	179,3	0.17	0.150
1,6	186.0	0.06	0.041
2,3	163.0		(0.730)
2,4	168.7		0.540
2,6	181.1		0.140

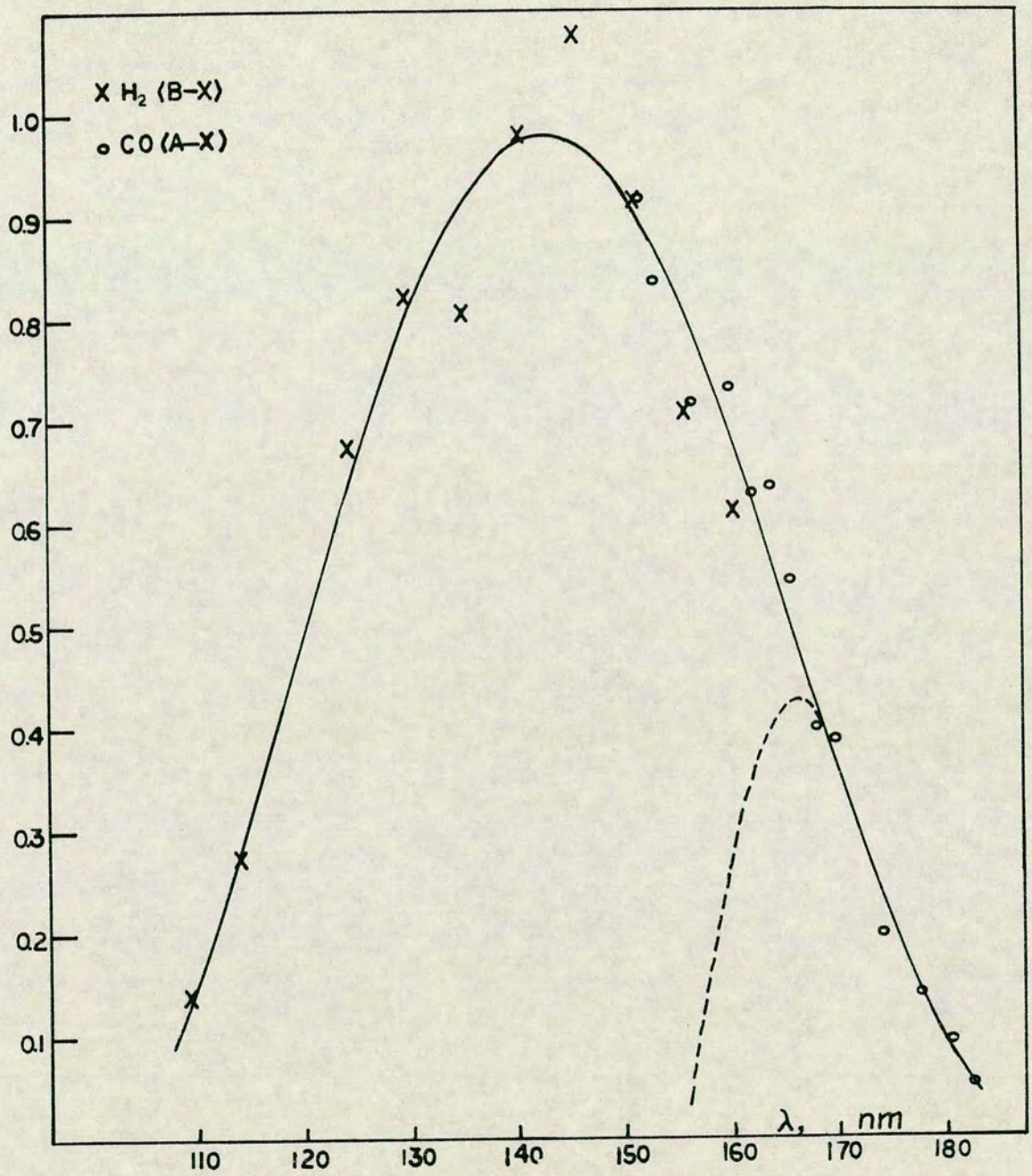

Fig. 2.3 Relative quantum efficiency as a function of wavelength (λ). × H_2(B-X); o CO(A-X). The full line is a smoothed least square fit to the points. The broken line represents the relative quantum efficiency when a spectrosil window was placed in front of the exit slit (obtained from the change in intensity of the ArCl MC spectrum as shown in figure 2.4).

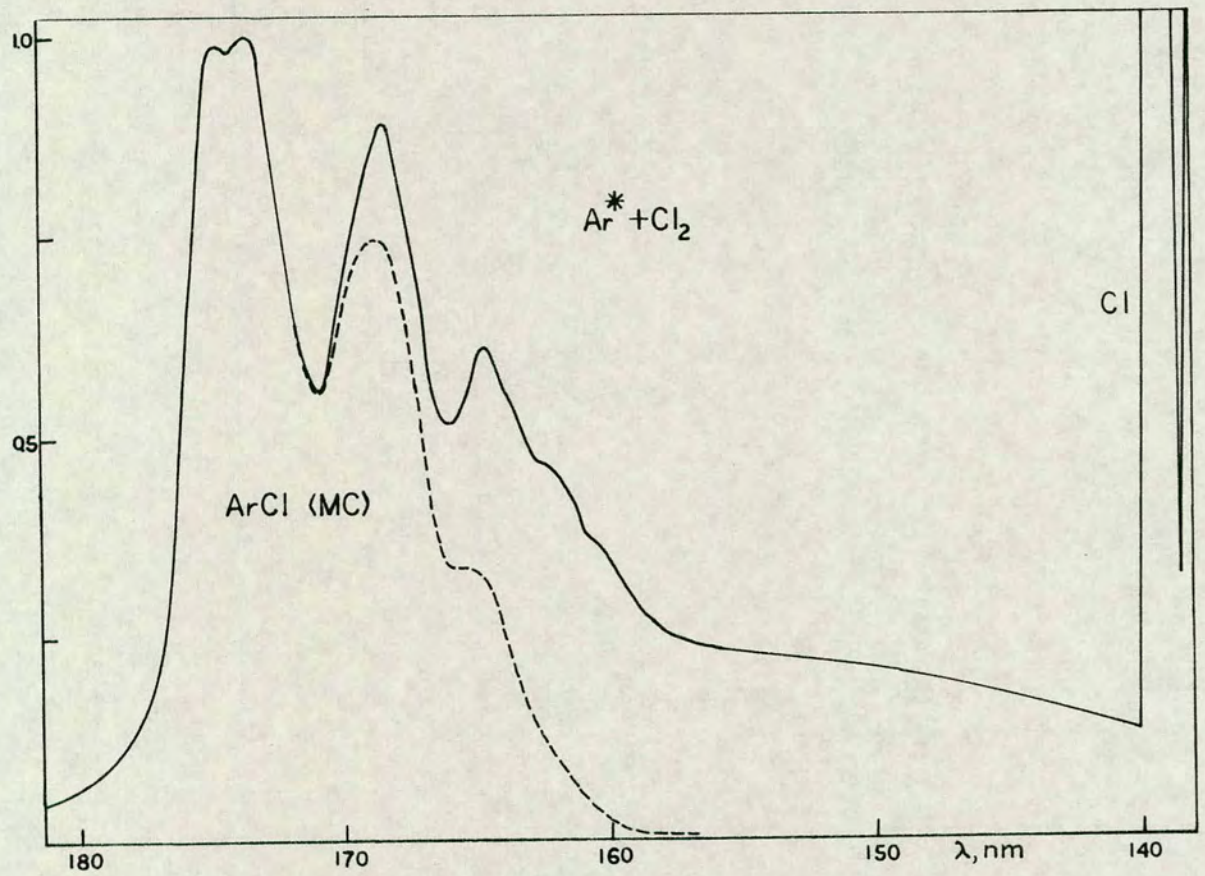

Fig. 2.4 ArCl, MC spectrum uncorrected for spectral response. The broken curve shows the spectrum obtained when spectrosil window was placed in front of the exit slit. The intensity is normalized such that the value for the strongest MC peak is 1. Total pressure : 1.56 torr (208 Nm^{-2}). Slit width: 500 μm.

relative quantum efficiency without spectrosil window in,

$$R_\lambda' = R_\lambda \cdot S_\lambda'/S_\lambda \qquad (2.3)$$

where R_λ' and S_λ' are the relative quantum efficiency and intensity (counts s^{-1}) at a particular wavelength λ with the spectrosil window in, but R_λ and S_λ are the corresponding quantities without the spectrosil window in. A least square fit curve to such a plot is shown in figure 2.3.

2.3 Purification and handling of reagents.

BOC - standard argon (99.996%) was purified by passing it through a Cu - furnace at about 1000°K, 1 atm. ($1.01 \times 10^5 Nm^{-2}$) pressure, to remove traces of O_2. The furnace was made of a quartz tube filled with copper turnings and heated by nichrome wire. The gas was then passed through a silica gel trap maintained at 196°K by a mixture of dry ice and isopropanol, to remove traces of CO_2 and H_2O. In the low pressure part of the flow tube the argon was passed through a liquid nitrogen trap before the discharge.

Those halogen containing reagents which are gases at room temperature were transferred to 5 liter bulbs on the vacuum line and degassed several times, to remove possible O_2- and N_2- impurities.

A special care was taken in handling the deuterium halides, DBr and DCl. The part of the vacuum line through which these reagents were passed was first deuterated. D_2O was allowed to evaporate and expand into that part of the vacuum line and left on the line foracouple of days. The line was pumped thoroughly before the deuterium halides were transferred into it.

DBr was obtained from a BOC - cylinder. An infrared spectrum taken of a sample of DBr, showed some HBr impurities (an upper limit of about 20% was estimated). A DCl sample was borrowed from the inorganic laboratory and was found to have significant amount of HCl impurities (an upper limit of about 40%

was estimated).

CNCl was synthesised in the laboratory by reacting NaCN with Cl_2 as described in reference 82. Cl_2 impurities were separated from the sample on the vacuum line, until no Cl atomic lines (from $Ar^* + Cl_2 \rightarrow Cl^*$) appeared from adding the gas to Ar^* in the vacuum - UV spectrum.

Other gases which were used were transferred from cylinders (standard grades). These are tabulated in table 2.2.

Table 2.2

Gas reagents, their origin and purity.		
Comp.	Cylinder from	Purity
HBr	BOC	99.8%
CF_3Br	Cambrian Chemicals Ltd.	99.0%
CF_2ClBr	Imperial Chemicals Industries Ltd.	
Cl_2	BOC	
HCl	BOC	
N_2	BOC	standard grade
H_2	BOC	standard grade
COS	BOC	97.5%
CO	BOC	

Liquid reagents were used without further purification (see table 2.3) and kept in traps connected to the vacuum line. CH_2Br_2 and CCl_4 were kept in traps

connected to the line on the high pressure side of the needle valve and cooled with an ice bath. The pressure on that part of the line was determined by the vapour pressure of the reagent at that temperature, and the flow was controlled with a needle valve. Br_2 and $CHBr_3$ have significantly lower vapour pressures and could therefore not be handled in the same way. Instead, these reagents were kept in a cooled trap on the low pressure side of the needle valve, directly connected to the inlet tube to the reaction vessel. The flow of these reagents was then controlled by the pumping rate and the temperature of the trap. The trap was cooled with a mixture of isopropanol and dry ice ($T \geq 196$°K). A steadier flow could be obtained by passing a small flow of argon over the trapped reagents.

Table 2.3

Liquid reagents, their origin and purity.		
Comp.	Cylinder from	Purity
Br_2	British Drug Houses Ltd.	99.0% Br
$CHBr_3$	Aldrich Chemical Company Inc.	96.0%
CCl_4	Fisons Scientific Apparatus.	Analytical reagent.

For studying the effect of changing the temperature in the reaction vessel, measurements were made at room temperature and at undefined temperatures

obtained by covering the reaction vessel and the inlet tubes with dry ice.

3. EXPERIMENTAL RESULTS.

Experimental results will be presented and discussed in this chapter. Spectra from reactions of the various bromine- chlorine- and iodine-containing reagents (RBr, RCl, RI) with $Ar^*(^3P_{0,2})$ were recorded for different pressures and resolutions. The greatest emphasis was put on studying the spectra obtained from reactions of the bromine containing reagents.

3.1 RBr + Ar^*

Vacuum-UV spectra were generated by reactions of CH_2Br_2, HBr, DBr, Br_2, CF_3Br, PBr_3, CF_2ClBr and $CHBr_3$ with $Ar^*(^3P_{0,2})$. All these spectra showed atomic lines which were assigned as radiative transitions from excited states of bromine. These were found between 131 nm and 164 nm superimposed on weak Ar_2 continua. Weak continua with an oscillatory structure were found in the region 158 - 187 nm for all these reagents and were assigned as ArBr spectra. In addition the spectrum for CF_2ClBr showed a weak ArCl spectrum peaking

at 175.4 nm.

The spectra for the reactions of the first six bromine containing reagents listed above will now be discussed while those for the reactions of the CF_2ClBr and $CHBr_3$ will not be discussed further.

3.11 Br atomic lines and relative intensities of Br- and ArBr- spectra.

Spectra obtained from reactions of the bromine containing reagents, HBr, Br_2, CH_2Br_2 and CF_3Br with Ar^* corrected for spectral response are shown in figures 3.1 and 3.2. These show the strong bromine atomic lines to be the dominant feature of the spectra. ArBr spectra for these reactions are shown in figures 3.5, 3.8 and 3.10 in next section.

The atomic lines shown in figures 3.1 and 3.2 were assigned as atomic transitions $Br^*(5s) \longrightarrow Br(^2P_{1/2,3/2})$, shown at the top of these figures.[85,86] Relative intensities of these atomic lines and the strongest ArBr peak at 165.4 nm are tabulated in table 3.1. The relative intensities of the bromine lines were not found to differ significantly with changes in pressure or flow rates. Table 3.2 contains ratios of the total bromine atomic intensities (I_{Br}) to the total ArBr intensities I_{ArBr} obtained from the spectra for these reactions (I_{Br}/I_{ArBr}). These ratios were found to be

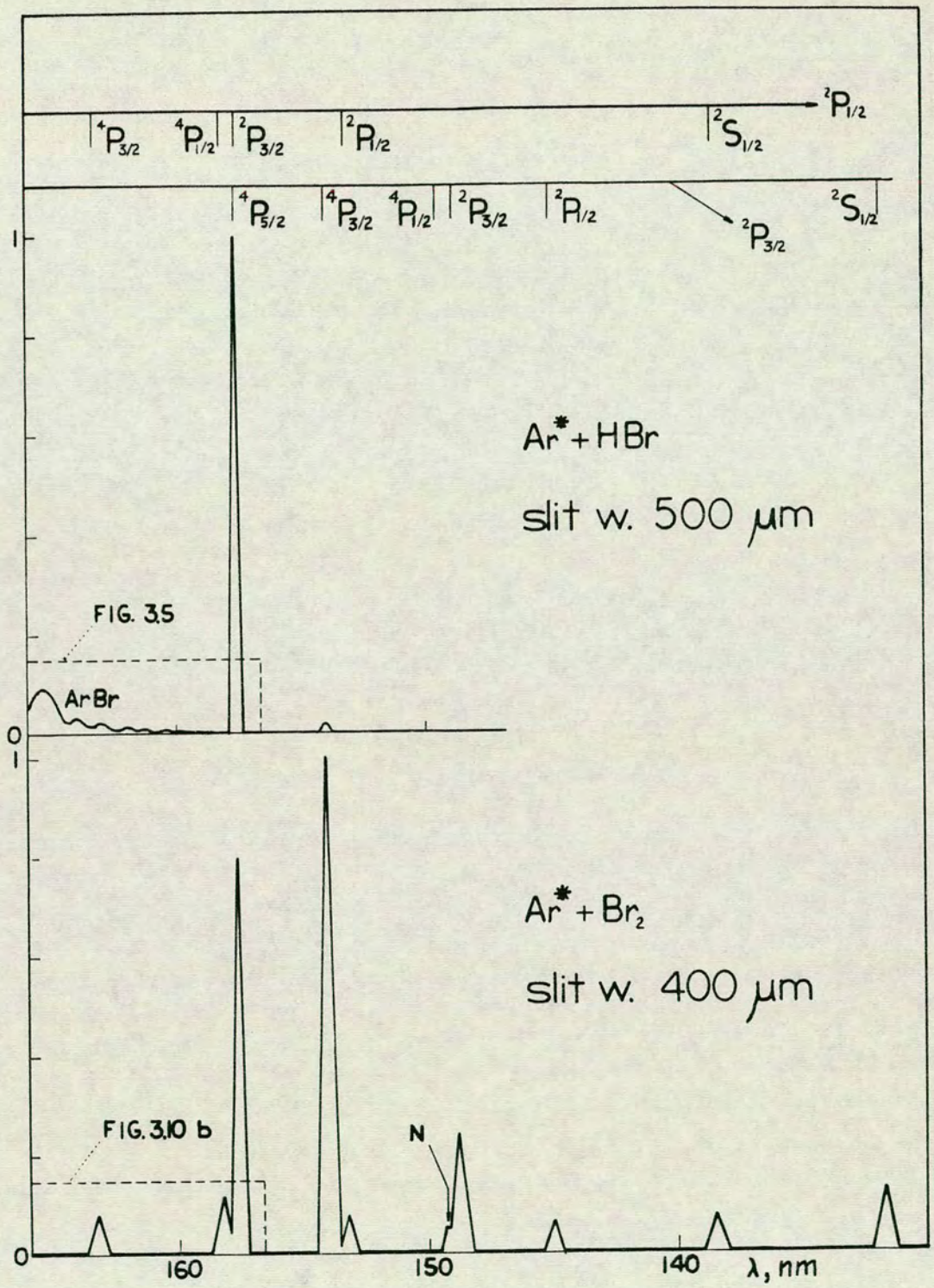

Fig. 3.1 Spectra obtained from reactions of HBr and Br_2 with $Ar^*(^3P_{2,0})$ showing strong bromine atomic lines and weak ArBr spectra. The bromine lines are assigned to transitions from $Br^*(5s)$ atoms as indicated. Figures where ArBr spectra are shown on amplified scales are indicated.

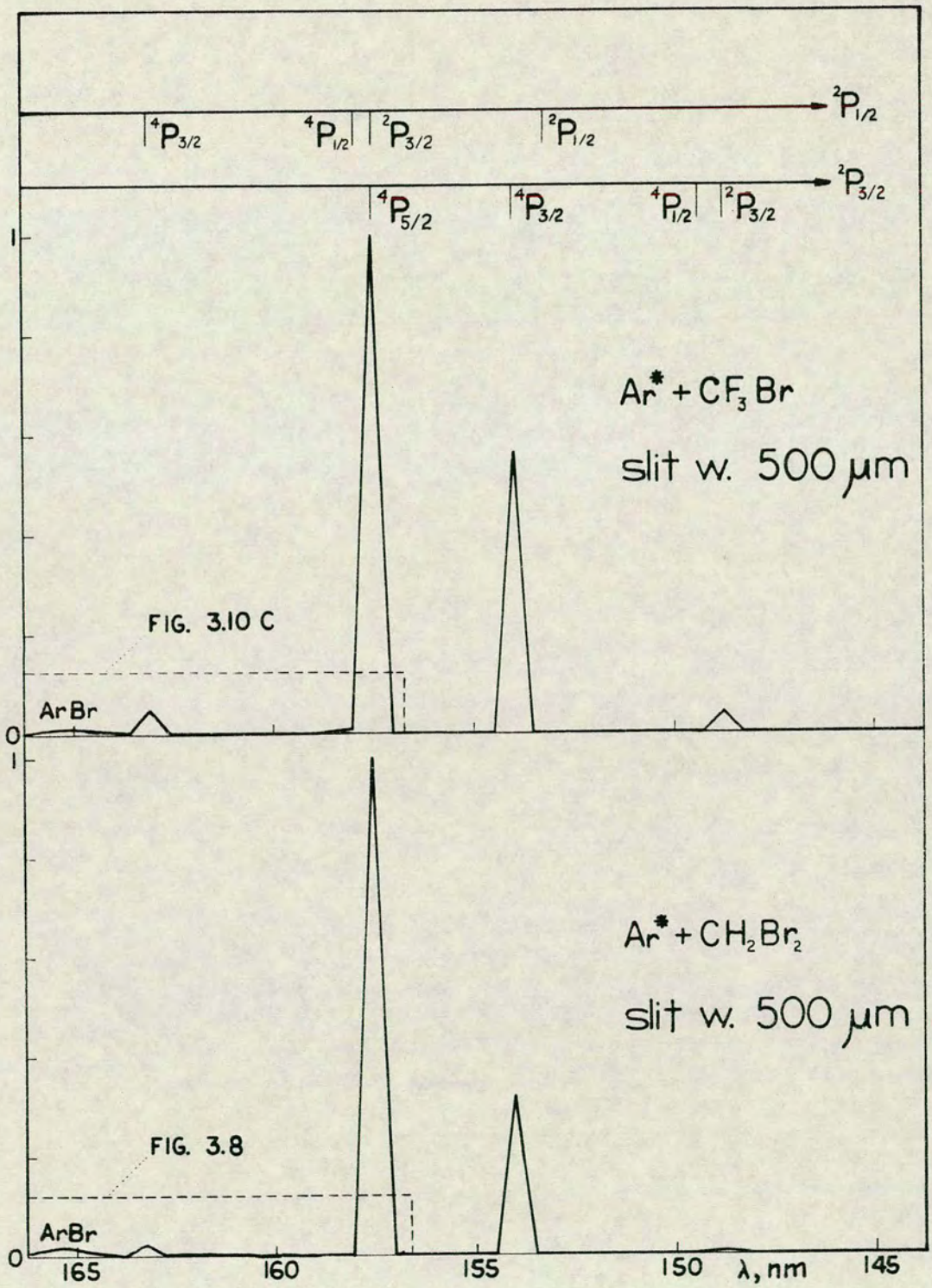

Fig. 3.2 Spectra obtained from reactions of CF_3Br and CH_2Br_2 with $Ar^*(^3P_{2,0})$ showing strong bromine atomic lines and weak ArBr spectra. The bromine lines are assigned to transitions from $Br^*(5s)$ atoms as indicated. Figures where ArBr spectra are shown on amplified scales are indicated.

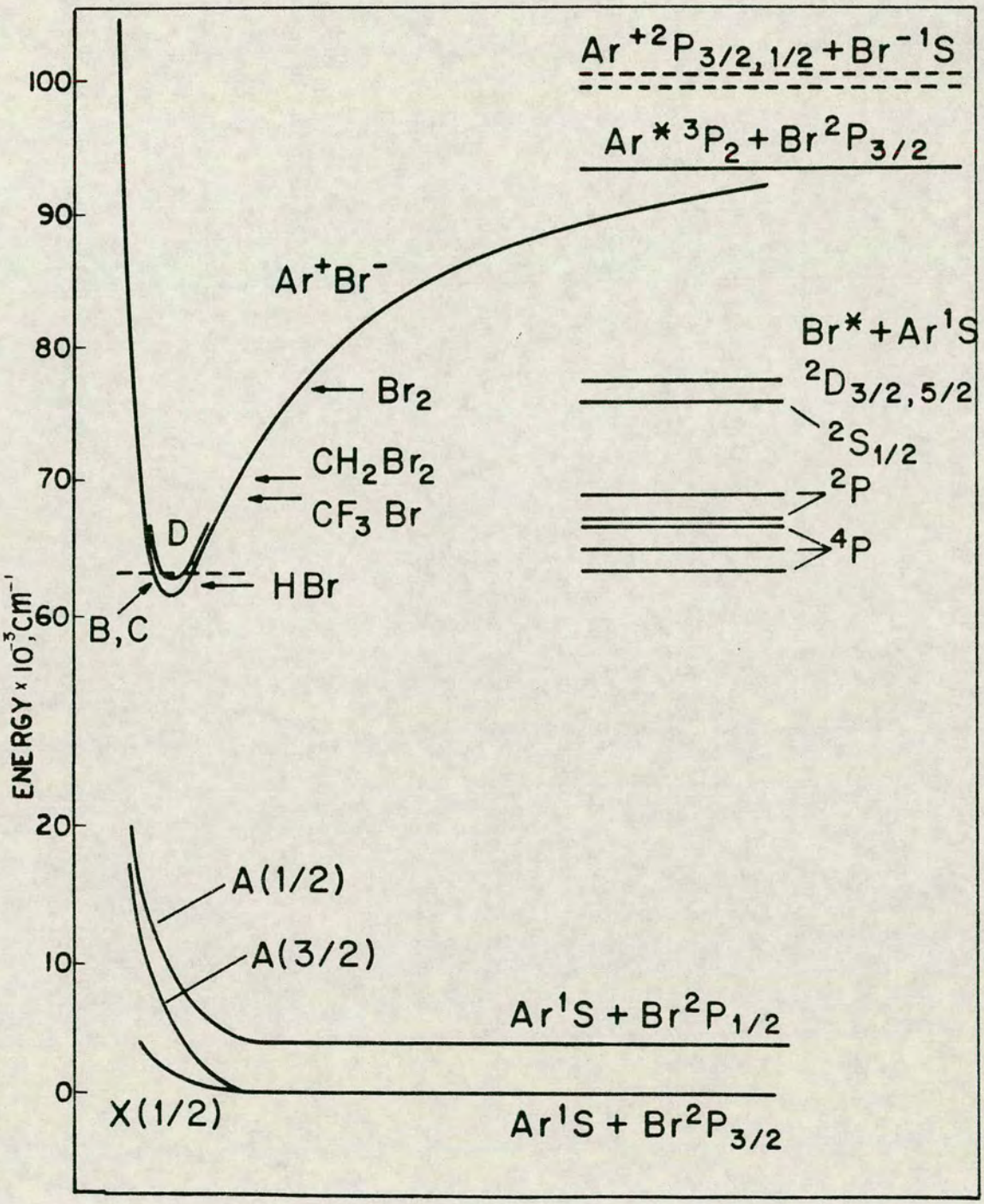

Fig. 3.3 Schematic potential curves for the ArBr- states correlating diabatically with $Ar(^1S) + Br(^2P_{3/2,1/2})$ and $Ar^+(^2P_{3/2,1/2}) + Br^-(^1S)$, and asymptotic energies for Rydberg states which correlate with $Br^*(5s)+Ar(^1S)$. Threshold energies for the various RBr reagents are indicated by arrows. $1cm^{-1} = 11.963\ J\ mole^{-1}$.

unchanged with changes in pressure for constant flows of the reagents. The bromine intensity was found to be less relative to the ArBr intensity for DBr+Ar^* than for HBr+Ar^* ($I_{Br}/I_{ArBr} < 1.8$).

Table 3.1

Relative intensities of bromine atomic lines and the strongest ArBr peak at 165.4 nm at 0.6 torr (80 Nm^{-2}) total pressure (500 μm slit width) in spectra for reactions of the various bromine containing reagents (RBr) with Ar^*.

Transitions	λ(nm)	HBr	CH_2Br_2	CF_3Br	PBr_3	Br_2
$^2S_{1/2} \rightarrow {}^2P_{1/2}$	138.5					7.34
$\rightarrow {}^2P_{3/2}$	131.8					12.9
$^2P_{1/2} \rightarrow {}^2P_{1/2}$	153.2			0.08	2.34	7.62
$\rightarrow {}^2P_{3/2}$	145.0		$\leqslant$0.04		1.61	6.2
$^2P_{3/2} \rightarrow {}^2P_{3/2}$	148.9		0.45	4.1	17.1	23.4
$^4P_{1/2} \rightarrow {}^2P_{1/2}$	158.3		$\leqslant$0.05	0.7		11.5
$^4P_{3/2} \rightarrow {}^2P_{1/2}$	163.4		2.77	4.2	7.11	7.81
$\rightarrow {}^2P_{3/2}$	154.1	2	31.5	56	100	100
$^4P_{5/2} \rightarrow {}^2P_{3/2}$	157.7	100	100	100	84.4	79.8
ArBr peak	165.4	9	1.6	1.1	0.3	0.3

Figure 3.3 shows a potential curve diagram for ArBr. The B- and the C- states are assumed to be

Table 3.2

Ratios of the total bromine atomic intensities to the ArBr intensities (I_{Br}/I_{ArBr}) for reactions of the various bromine containing reagents (RBr) with Ar^*.	
RBr	I_{Br}/I_{ArBr}
HBr	1.8
CH_2Br_2	5.2
CF_3Br	15
Br_2	66

indistinguishable and identical with the Rittner potential for the ground state for KBr[140] adjusted to the $Ar^+(^2P_{3/2})+Br^-(^1S)$ asymptotic limit. The minimum of the D-state is placed above the minimum of the B- and the C- states by the same magnitude of energy as the $Ar^+(^2P_{1/2}-{}^2P_{3/2})$ spin orbit splitting (1432 cm^{-1}, 17440 J $mole^{-1}$). The asymptotic energy levels for low lying Rydberg states which equal the energy of the excited Br^* atomic lines are also shown. The shape of these low lying Rydberg states at short internuclear distances is uncertain and thus are not drawn in figure 3.3 but most of these potentials are expected to be repulsive.[15] The low lying states, X(1/2), A(3/2) and A(1/2) are drawn schematically.

The number of bromine atomic lines and

identified excited states were found to increase with increasing threshold energy for the reactions

$$Ar^* + RBr \rightarrow Br^* + Ar + R \qquad (1)$$

The threshold energy is given approximately by the expression

$$E_T = E(Ar^*(^3P_2)) - D(RBr) \qquad (3.1)$$

where $E(Ar^*(^3P_2))$ is the electronic energy of the $Ar^*(^3P_2)$ state (=93144 cm^{-1}).[2,3] D(RBr) is the bond strength of R-Br. Bond energies and threshold energies for CH_2Br_2, Br_2, CF_3Br and HBr are listed in table 3.3 (page 52). The threshold energies for reagents are shown by arrows in figure 3.3.

Transitions from all bromine atomic states of lower energies than the threshold energies were identified from the spectra. Transitions from the closest energy levels above the threshold energies defined by equation 3.1 were also identified from spectra for HBr+Ar*, DBr+Ar* and CF_3Br+Ar* ($^4P_{5/2,3/2}$ for HBr and DBr and $^2P_{1/2}$ for CF_3Br). These are formed from reactions with greater total energy than $E(Ar^*(^3P_2))$ such as from reactions of $Ar^*(^3P_0)$ and/or from reactions of species with a great thermal energy. The formation of the excited atomic states can be explained as being due to an efficient predissociation of the ionic states by low lying Rydberg states which cross the ionic

states below or slightly above the threshold energies defined by equation 3.1. The fact that no ArBr emission was observed on the short wavelength side of the bromine atomic line at 157.7 nm, which corresponds to the energy of the lowest excited state of bromine, the transition $^4P_{5/2} \rightarrow {}^2P_{3/2}$, suggests that the high vibrational levels are completely predissociated. However, it should be noted that the excited states could also be formed by other unknown reaction channels such as by predissociation of electronically excited RBr molecules, previously formed by energy transfer reactions.[15]

The measured relative intensity of a bromine line, centered at the wavelength λ (I^{λ}_{Br}), is a measure of the rate of formation of the excited state (R^{λ}_{Br})

$$I^{\lambda}_{Br} \propto R^{\lambda}_{Br} \qquad (3.2)$$

Because of the uncertainty as to how the excited states of the bromine atoms are formed the relative intensities of the bromine lines are not easily interpreted (table 3.1).

The fact that the total bromine line intensity is greater than the ArBr intensity in a spectrum for HBr+Ar* is surprising (table 3.3). The formation reaction for $Br(^4P_{5/2})$ is endothermic for $Ar^*(^3P_2)$.

The formation of all the excited state atoms which are emitting, cannot be explained as being solely due to predissociation, since that would mean that the rate of formation of the ArBr molecules with energy in the endothermic region is greater than for molecules with lower energy. It is therefore likely that another formation mechanism is also responsible for the formation of Br^*.

The spectra for RBr = Br_2, CH_2Br_2, CF_3Br and PBr_3 showed a decreasing atomic line intensity with decreasing total angular momentum quantum number (J) for the emitting states (with the exception of the $^4P_{5/2}$ and $^4P_{3/2}$ states for $Ar^* + Br_2$ and $Ar^* + PBr_3$). Thus the intensity was found to change as $^4P_{5/2} > {}^4P_{3/2} > {}^4P_{1/2}$ and $^2P_{3/2} > {}^2P_{1/2}$.

According to Wigner's and Witmer's correlation rules,[106] a combination of the excited bromine atoms with $Ar(^1S)$ will result in a different number of molecular states, depending on the total angular momentum quantum number. Thus a combination of $Br^*(^4P_J)$ and $Ar(^1S)$ which can result in four $^4\Pi$ - and two $^4\Sigma$ - substates, will give three molecular states if J = 5/2, two if J = 3/2 and one if J = 1/2. Thus, there is a greater number of predissociation channels available which can result in formation of excited bromine atoms with high J values than with low J values. This may partly explain the difference in the intensities of the bromine

atomic lines.

Br_2 and PBr_3 have the lowest bond energies of those bromine containing reagents which were tried (see table 3.3 for $D(Br_2)$) and therefore the greatest threshold energies (see figure 3.3 for Br_2). This suggests that the exceptions from the regular trend in intensity vs angular momentum quantum number mentioned above are connected with populations in relatively high vibrational levels. Thus, for example the higher vibrational levels may be predissociated especially efficiently by higher lying molecular states such as those which correlate with $Ar(^1S) + Br^*(^4P_{3/2})$ resulting in greater rate of formation of $Br^*(^4P_{3/2})$ than $Br^*(^4P_{5/2})$ for the reactions of Br_2 and PBr_3.

The high vibrational levels close to the threshold energies are in fact expected to be populated quite efficiently. Molecular beam studies of the reactions of Br_2 and phosphorus trihalides with the alkali atoms show that these reactions occur with high efficiency of conversion of the reaction exothermicities into internal energy in the alkalihalides.[143,150] It has been suggested that these reactions, resemble the corresponding reactions of the metastable noble gas atoms, as mentioned previously (section 1.3). Results of the simulation calculations for ArCl spectra generated by $Cl_2 + Ar^*$, which are presented in

chapter 5, suggest that a broad initial vibrational population distribution is obtained in the argon halide molecules for the reactions of the halogen molecules (see section 5.21).

Generally, the initial population distribution in the vibrational levels in the ionic states of $ArBr^*$ is expected to affect the population in the bromine states due to the predissociation and therefore to affect the relative intensities of the bromine atomic lines.

The reaction exothermicity is found to be converted less efficiently into internal energy in KBr for the reaction CH_2Br_2+K[144] than for Br_2+K.[143] Similar effects are expected for the corresponding reactions of Ar^*. This, together with the fact that the threshold energy for $CH_2Br_2+Ar^*$ is lower than for Br_2+Ar^*, possibly explaines the significant difference in the relative intensities of the bromine lines for these two systems as well as the great difference in the ratios of the total bromine atomic intensities to the ArBr intensities shown in table 3.2.

It is of interest to compare the bromine atomic line intensities for $CH_2Br_2+Ar^*$ and CF_3Br+Ar^* (figure 3.3 and table 3.1). Intensities of the atomic lines relative to the strongest one ($^4P_{5/2} \rightarrow {}^2P_{3/2}$) are greater for CF_3Br+Ar^* than for $CH_2Br_2+Ar^*$. Using similar arguments as above it may be suggested that this is due to

relatively greater initial population in the higher vibrational levels than in the lower ones in $ArBr^*$ for the former reaction than for the latter reaction. The ratios of the total bromine atomic intensity over the total ArBr intensity obtained from spectra for these two reactions, differ significantly (table 3.2). This is consistent with that relatively greater initial population is in those vibrational levels which predissociate (high ones) for Ar^*+CF_3Br than for $Ar^*+CH_2Br_2$.

High efficiency of conversion of the exothermicity into internal energy is associated with a significant importance of the electron jump mechanism.[73-77] There are many examples in the literature of a greater importance of this mechanism for a reaction of an alkali atom with a halogen containing reagent, where the group to which the halogen atom is connected is very electronegative than with reagents where the corresponding group is less electronegative.[144,149] The CF_3 group is more electronegative than the CH_2Br group which might in fact suggest that the efficiency of conversion of the exothermicity into vibrational energy is greater for CF_3Br+Ar^* than for $CH_2Br_2+Ar^*$.

The fact that the ratio I_{Br}/I_{ArBr} is less for $DBr+Ar^*$ than for $HBr+Ar^*$ is understandable if it is assumed that the bromine states are partly populated by reactions of thermally excited species

since the thermoneutral limit (threshold energy) is lower for DBr+Ar* than for HBr+Ar* (see table 3.3).

Weak light intensity wings were observed on both sides of bromine lines due to scattered light. The intensity of these decreased with increasing distance from the bromine lines. The scattered light associated with the bromine line at 157.7 nm was measured for different slit widths, as shown in figure 3.4, where the intensity of the bromine line (at 157.7 nm) has been normalized to the value of 1000. These wings overlapped with the ArBr spectra. For spectra such as those for Br_2+Ar* and PBr_3+Ar*, where the intensities of the bromine lines are relatively much greater than the ArBr intensity (see tables 3.1 and 3.2), these wings made significant contributions to the intensity in the region of the ArBr spectrum. In other spectra such as for HBr+Ar*, DBr+Ar* and CH_2Br_2+Ar*, where I_{Br}/I_{ArBr} is low, this contribution was found to be minor.

Table 3.3

Bond strengths for the various bromine containing compounds (R-Br) and threshold energies (E_T) for Ar($^3P_2$) RBr.

RBr	Bond energies $x10^{-4}(cm^{-1})$	$E_T x10^{-4}$ (cm^{-1})	reference numbers for bond energies
HBr	3.025	6.289	88
DBr	3.035	6.279	87
CH_2Br_2	2.27	7.044	92
CF_3Br	2.43	6.88	91
Br_2	1.6206	7.6938	89,90
KBr	3.1791		89,90

$1cm^{-1} = 11.963$ J $mole^{-1}$.

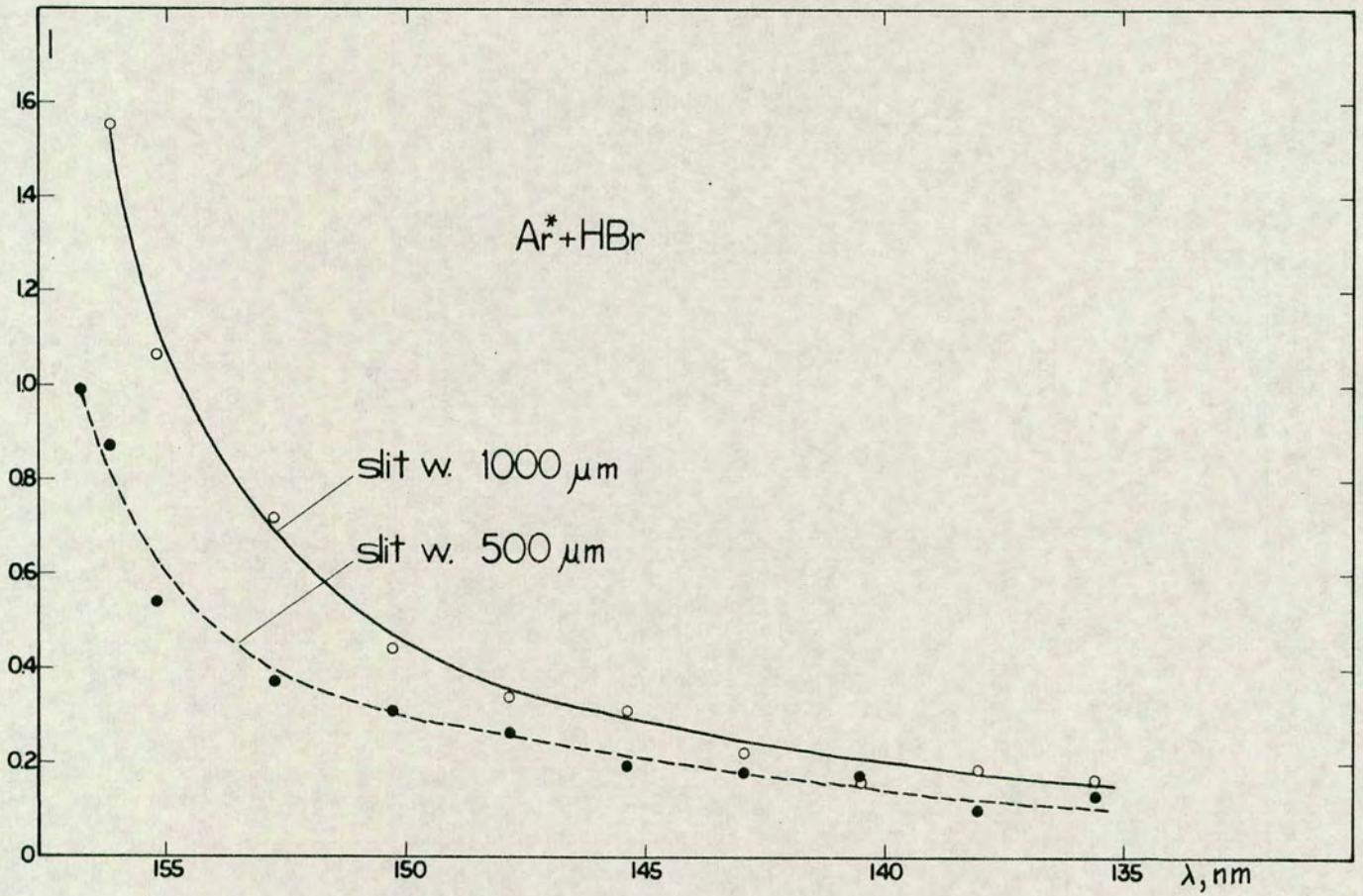

Fig. 3.4 Scattered light associated with the bromine atomic line at 157.7 nm vs wavelength for the intensity of the bromine line normalized to the value of 1000.

3.12 ArBr spectra.

The ArBr spectra will be discussed in this section. The structure of these spectra was found to differ a lot for the use of different bromine containing reagents. Relative intensities were found to change with pressure and temperature. Valuable information was derived from experimental studies of these spectra. Various radiative transitions were identified and the corresponding spectral ranges determined. Collision induced crossing between two excited states was found to occur as well as vibrational relaxation in these states. An attempt was made to estimate an upper limit of the minimum of the B state from temperature experiments.

3.121 Structure.

The ArBr spectra which were studied in the greatest detail are those which were obtained from the reactions of CH_2Br_2, HBr, DBr, Br_2 and CF_3Br with Ar^*. Spectra from these reactions are shown in figures 3.5 - 3.10. These spectra have been corrected for spectral response and scattered light associated with the bromine lines has been subtracted.

All the ArBr spectra show a peak at 165.4 nm. On the short wavelength side of this peak the intensity falls off to a short wavelength limit near 158.0 nm. This short wavelength part of the spectra

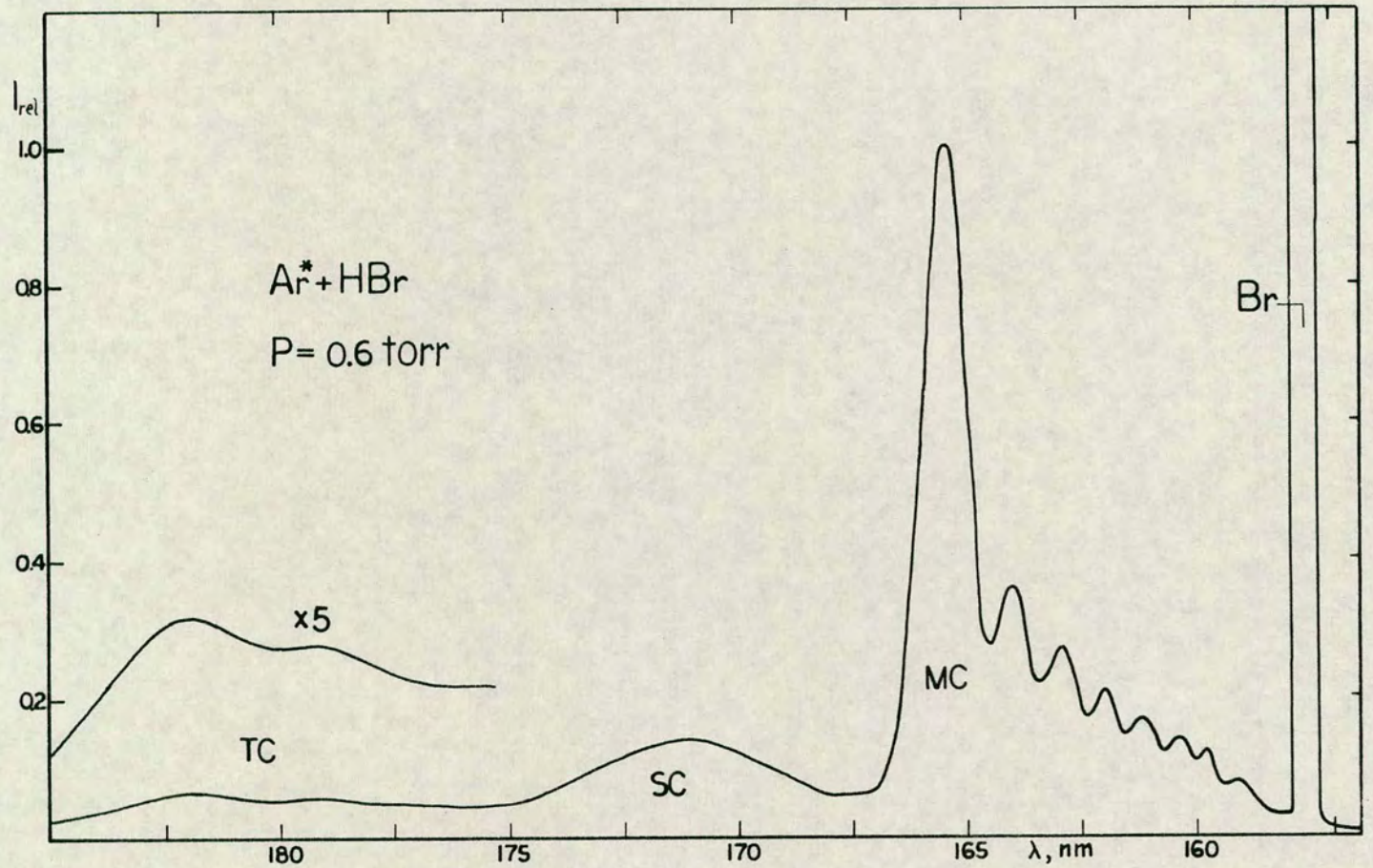

Fig. 3.5 ArBr spectrum generated by Ar^*+HBr. The MC was obtained for 250 μm slit width, the SC for 500 μm slit width and the TC for 1500 μm slit width. Intensities are normalized such that the intensity at 165.4nm is 1.
1 torr = 133.322 Nm^{-2}.

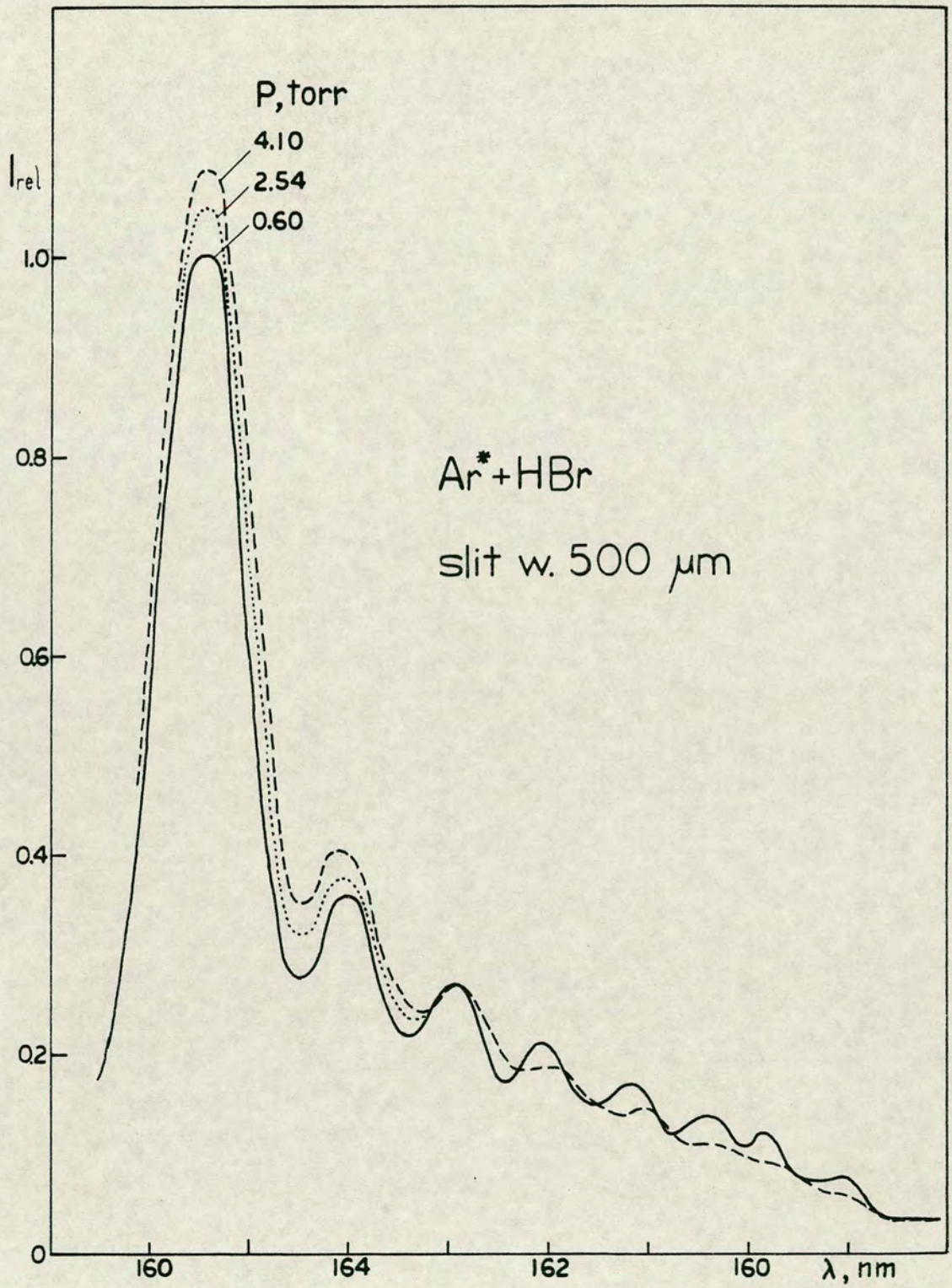

Fig. 3.6 ArBr , MC spectra generated by Ar^*+HBr at three different total pressures. Relative intensities are normalized such that the relative intensity at 165.4nm, 0.6 torr (80 Nm^{-2}) is 1. 1 torr = 133.322 Nm^{-2}.

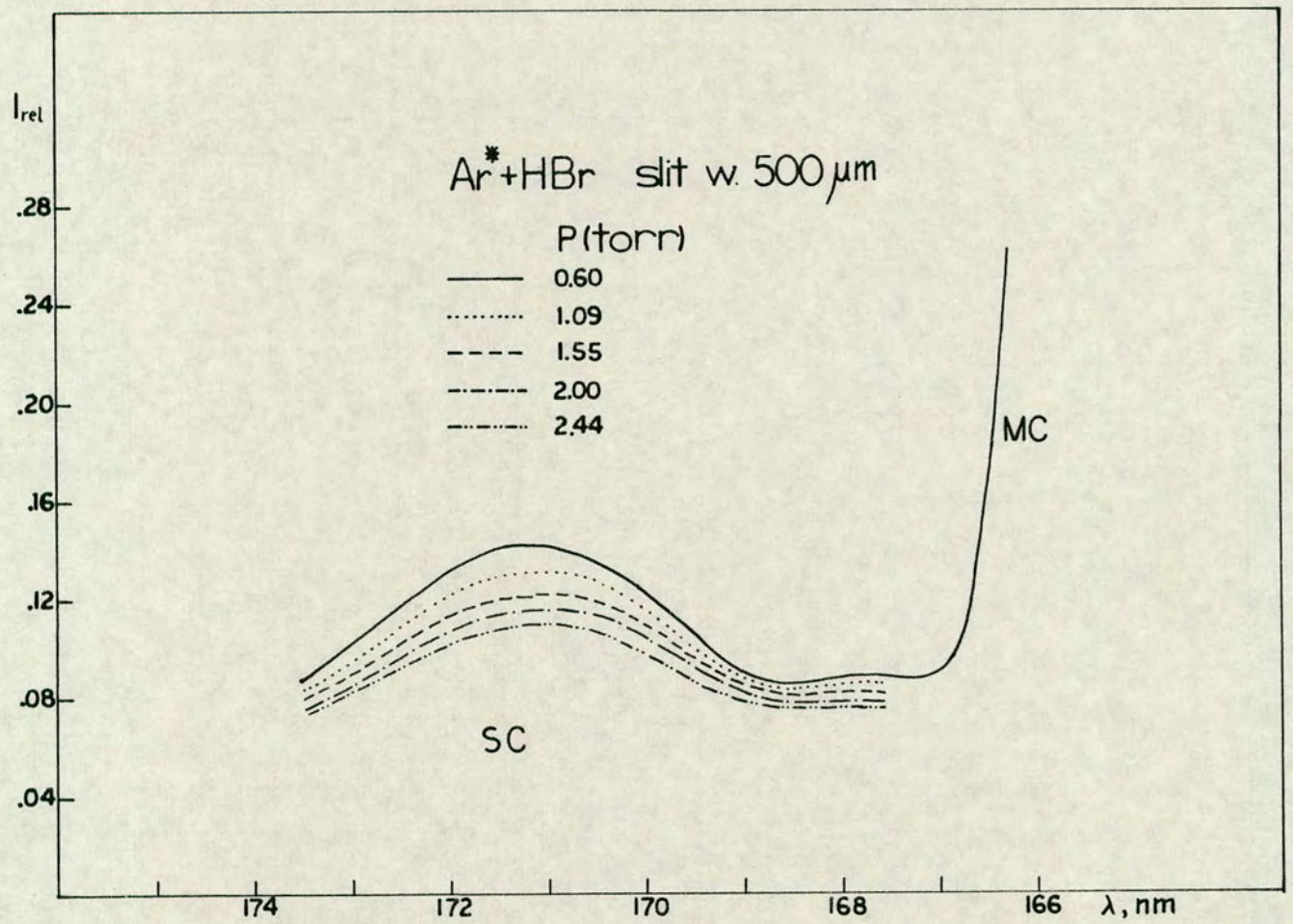

Fig. 3.7 ArBr , SC spectra generated by Ar^*+HBr at five different total pressures. Relative intensities are normalized such that the relative intensity at 165.4 nm, 0.6 torr (80 Nm^{-2}) is 1. 1 torr = 133.322 Nm^{-2}.

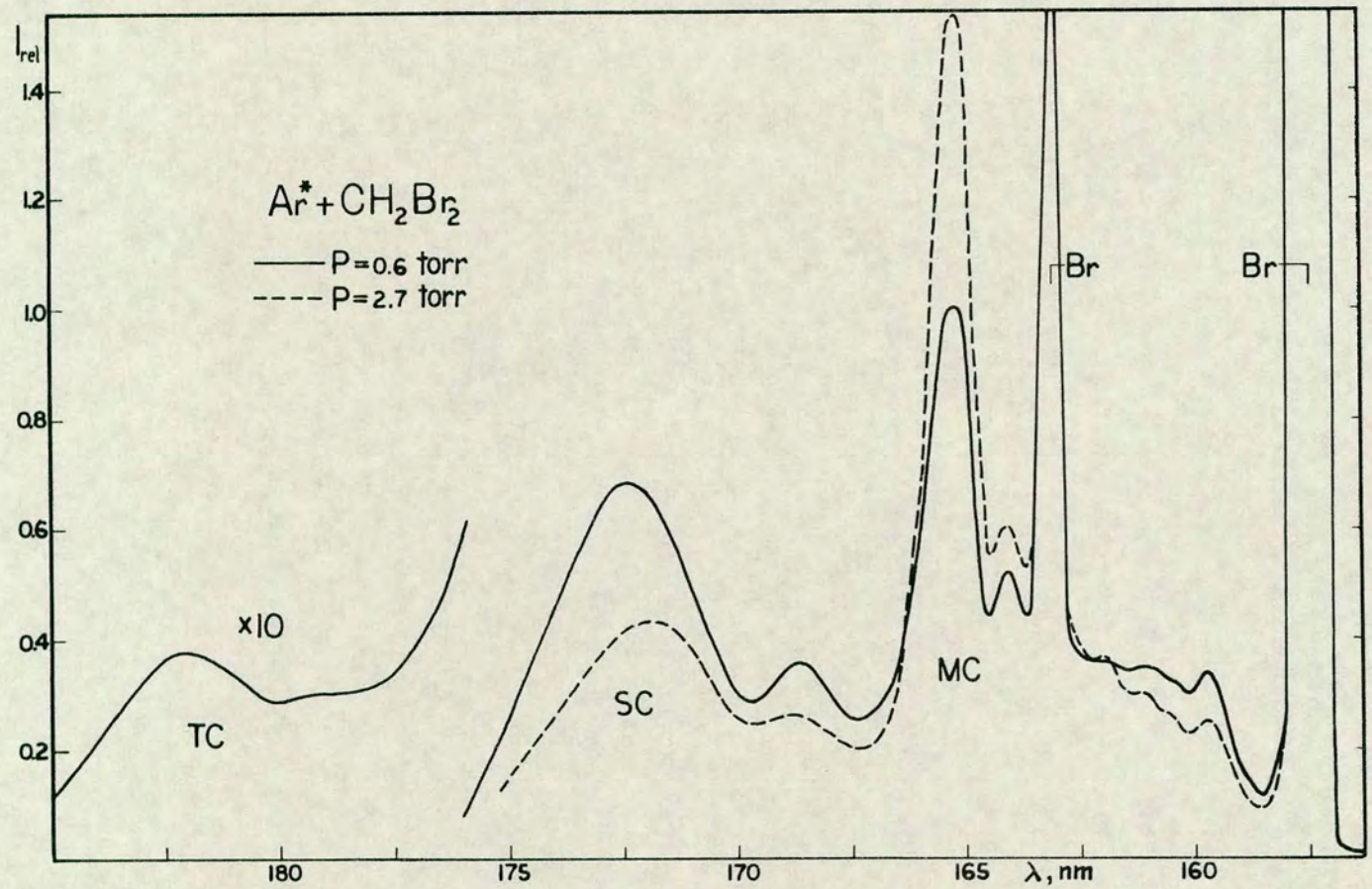

Fig. 3.8 ArBr spectrum generated by $Ar^* + CH_2Br_2$ at two different total pressures. The MC and the SC were obtained for 500 μm slit width and the TC for 1500 μm slit width. Relative intensities are normalized such that the relative intensity at 165.4 nm, 0.6 torr (80 Nm^{-2}) is 1. 1 torr = 133.322 Nm^{-2}.

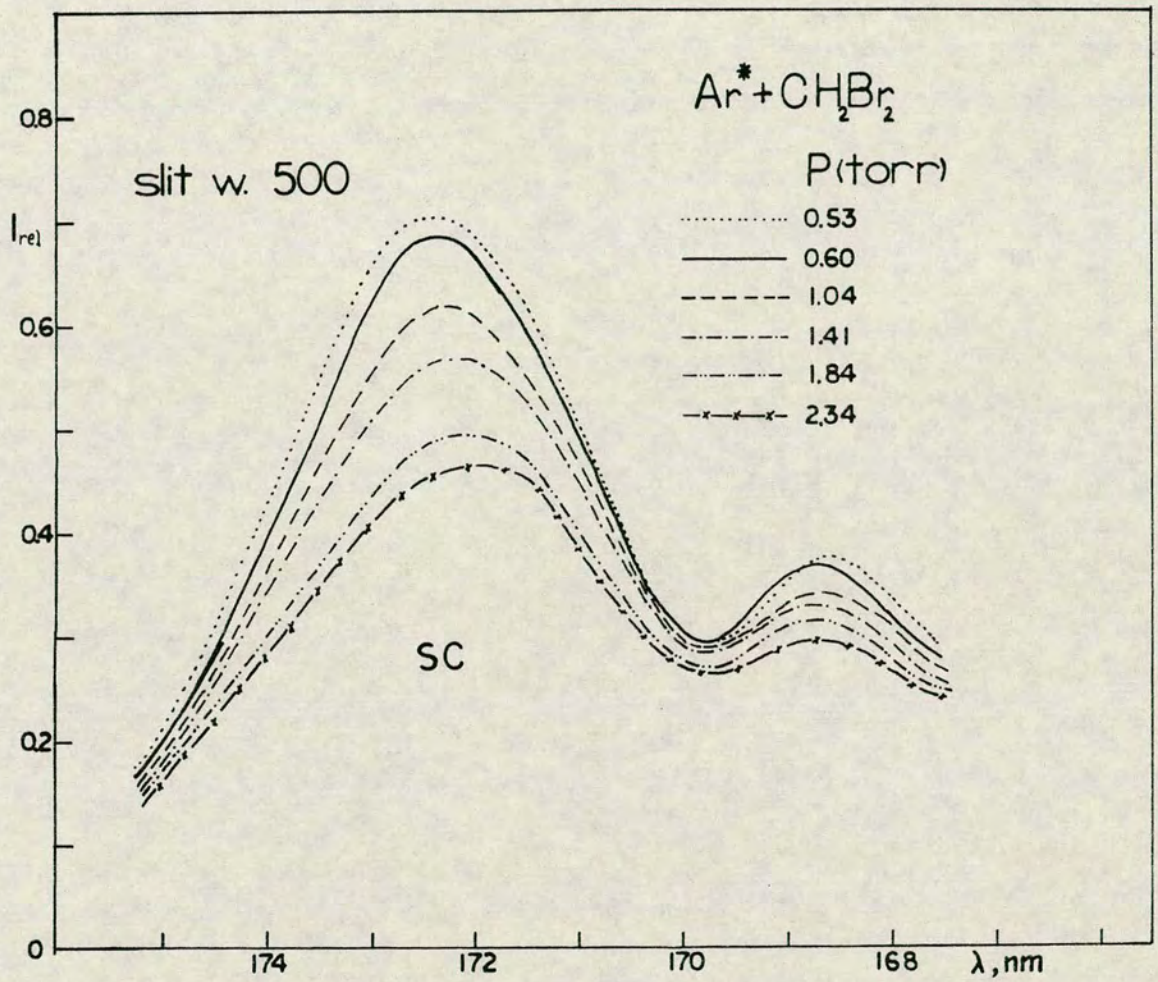

Fig. 3.9 ArBr , SC spectra generated by $Ar^* + CH_2Br_2$ at six different total pressures. Relative intensities are normalized such that the relative intensity at 165.4nm, 0.6 torr (80 Nm^{-2}) is 1. 1 torr = 133.322 Nm^{-2}.

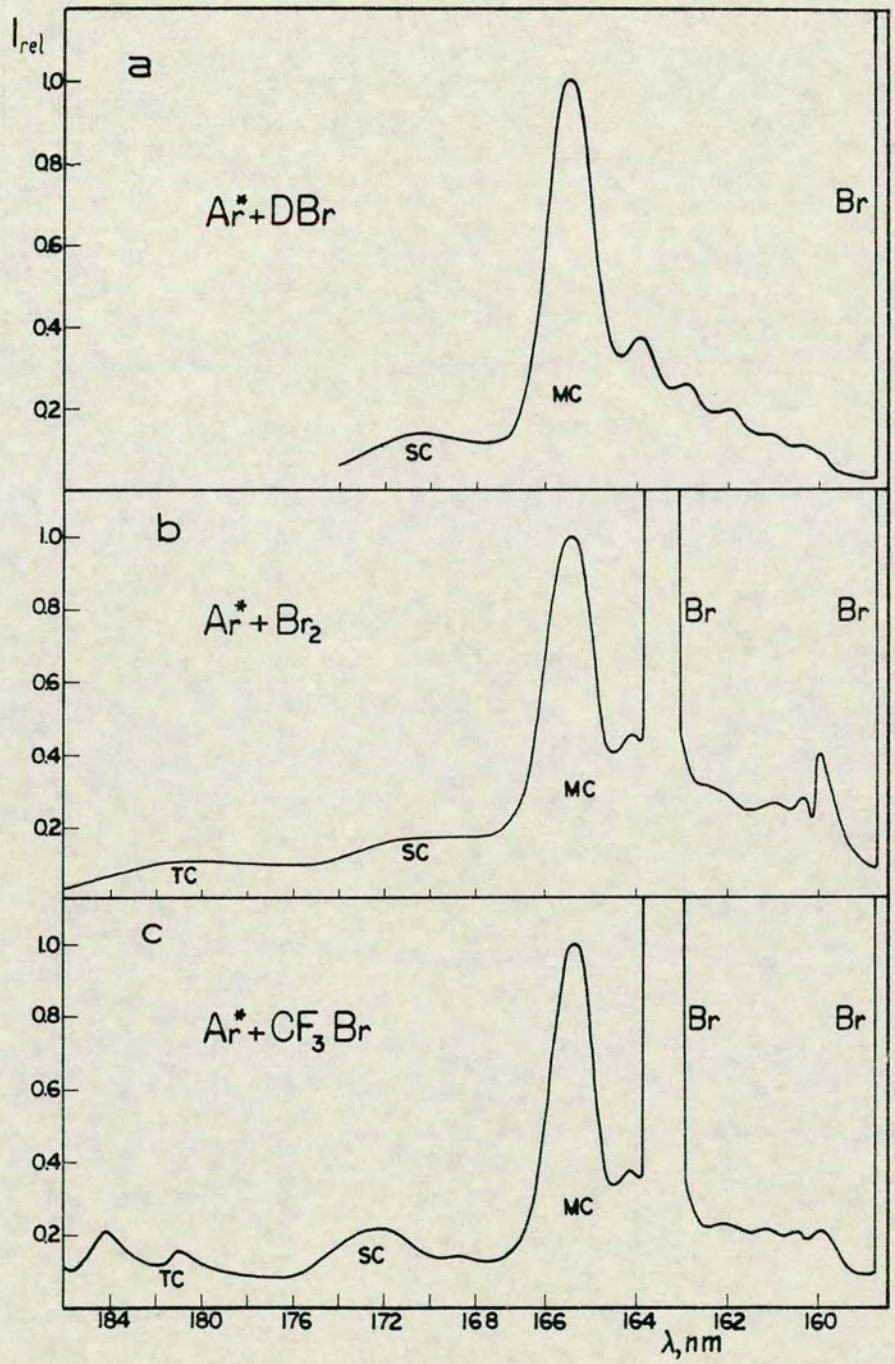

Fig. 3.10 ArBr spectra generated by reactions of DBr (a.), Br_2 (b.) and CF_3Br (c.) with Ar^*. a. Slit width : 500μm, pressure : 0.78 torr (104 Nm^{-2}). b. Slit width : 400μm for the MC and the SC, 1500μm for the TC, pressure : 0.6 torr (80 Nm^{-2}). c. Slit width : 500μm for the MC and the SC, 1500μm for the TC, pressure : 0.6 torr (80 Nm^{-2}). Relative intensities are normalized such that the relative intensities at 165.4nm, 0.6 torr (80 Nm^{-2}) are 1.

shows an oscillatory structure, most clearly shown in the HBr+Ar* and DBr+Ar* spectra (figures 3.5, 3.6 and 3.10). In these spectra the spacing between peaks decreases slightly to shorter wavelength as shown in table 3.4

Table 3.4

Positions of peaks in the ArBr spectrum for HBr+Ar* (MC) and the spacing between these.

λ(nm)	E(cm^{-1})	ΔE(cm^{-1})
165.4	60440	540
164.0	60980	390
163.0	61370	350
162.0	61720	320
161.2	62040	320
160.4	62360	210
159.8	62570	320
159.0	62890	

$1 cm^{-1} = 11.963$ J $mole^{-1}$.

The oscillatory structure is not quite as clearly resolved in the other spectra. The bromine atomic line at 163.4 nm which appears in these spectra is in this region, and part of the peak at 159.9 nm is a ghost line associated with the strong bromine atomic line at 157.7 nm. It will be shown later that this region of the spectra consists of spectral contributions due to the two different electronic transitions, B-X and C-A(3/2), one of which is responsible for the characteristic oscillatory structure (B-X). In a

spectrum like the one from $CH_2Br_2+Ar^*$ the C-A(3/2) contribution is relatively greater than in the $HBr+Ar^*$- and the $DBr+Ar^*$- spectra and causes a distortion of the structure in the B-X spectrum. However, four peaks were identified at the same positions as in the spectra for the reactions of HBr and DBr in the spectra for the reactions of CH_2Br_2, Br_2 and CF_3Br at 164.0, 162.0, 161.2 and 160.4 nm (see figures 3.8 and 3.10). On the short wavelength side of the 163.4 nm bromine line a slight shoulder was found, corresponding to the 163.0 nm peak. The 159.8 nm peak could not be resolved from the ghost line at 159.9 nm.

The spectra on the long wavelength side of the 165.4 nm peak show great changes in structure and intensities for the different reagents. These spectra will be shown to be due to two different radiative transitions (C-A(3/2) and B-A(1/2)) where the spectrum between 166.6 nm and 176.4 nm is mostly due to the C-A(3/2) transition, but the spectrum between 176.4 nm and 186.0 nm is mostly due to the B-A(1/2) transition.

The spectra in the 166.6 nm - 176.4 nm region show two broad peaks at about 172.3 nm and 168.6 nm in the spectra for the reactions of CH_2Br_2 and CF_3Br, a single broad peak in the spectra for the reactions of HBr and DBr and a steadily decreasing intensity to longer wavelength for Br_2+Ar^*. The total

integrated intensity in this region was found to be relatively greatest in the $CH_2Br_2+Ar^*$ spectrum. This can be seen in figure 3.11, where the various spectra obtained at the same total pressure (0.6 torr, 80 Nm^{-2}) are drawn for the intensity of the peak at 165.4 nm, normalized to a value of 1 for all the spectra.

The structure in the long wavelength region between 176.4 and 186.0 nm is not very well established since the sensitivity of the detection system was very low for light of that wavelength and a big slit width was used. The spectra for the reactions of CH_2Br_2, Br_2 and HBr all show a decreasing intensity from about 182.0 nm to longer wavelength. The $HBr+Ar^*$ and $CH_2Br_2+Ar^*$ spectra both show peaks at 182.0 nm, and the $HBr+Ar^*$ spectrum also shows a peak at about 178.0 nm.

The structure in this region for the CF_3Br+Ar^* spectrum looks different from the others. It shows sharp bands at 184.3 nm and 181.1 nm. Also the integrated intensity in this region is greater relative to the integrated intensity of the total ArBr spectrum than for any other spectra.

3.122 Pressure dependence.

As mentioned before (section 3.11) the ratio I_{Br}/I_{ArBr} for a particular spectrum was found to be constant with changes in the pressure for a constant flow of the reagent. The change in the total

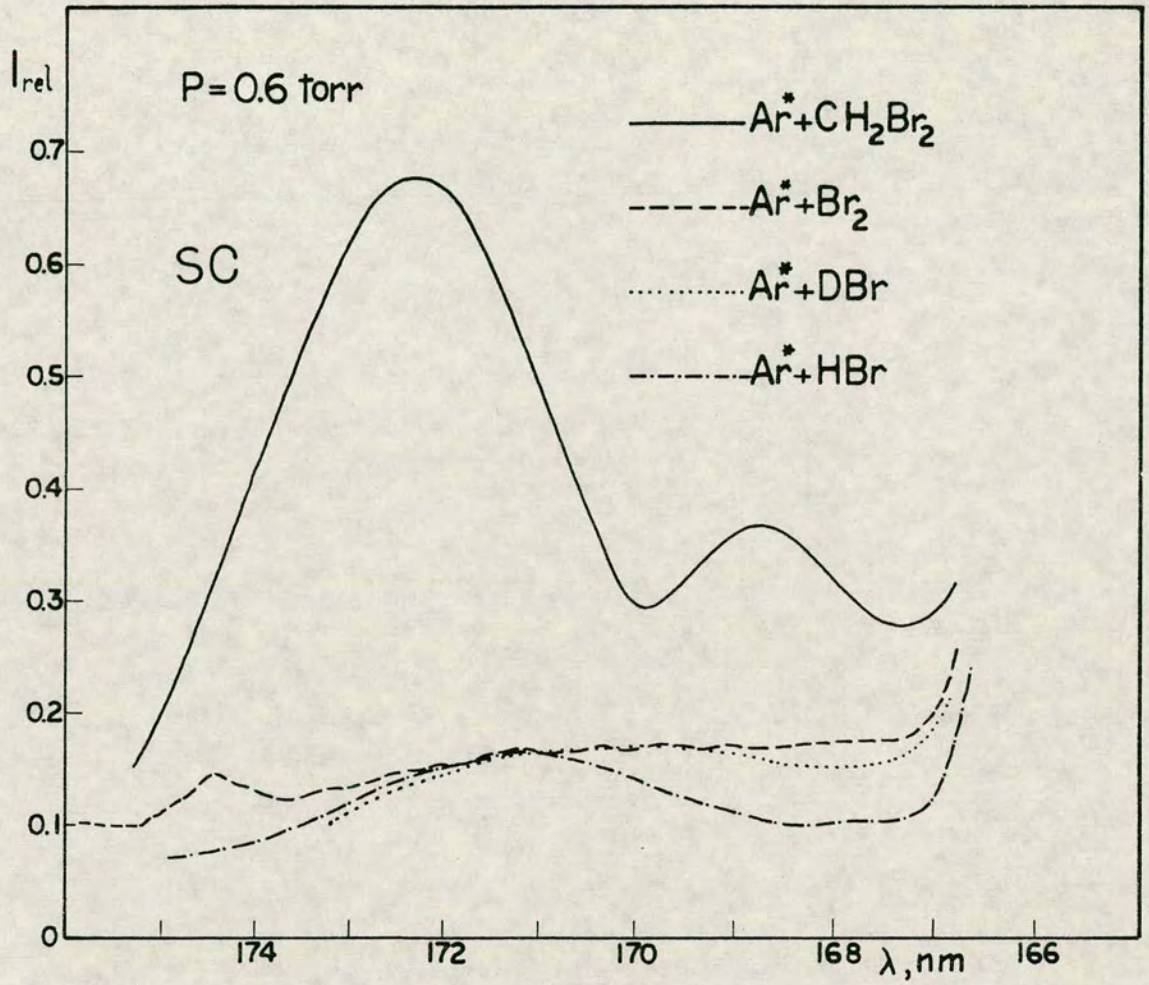

Fig. 3.11 ArBr , SC spectra generated by reactions of the various bromine containing reagents with Ar^*. The spectra from the reactions of HBr, DBr and Br_2 were obtained for 1000 μm slit width but CH_2Br_2 for 500 μm slit width. Relative intensities are normalized such that the relative intensities at 165.4nm, 0.6 torr (80 Nm^{-2}) are 1.

measured intensity of a particular ArBr spectrum is therefore analogous to the change in the total measured bromine intensity which was typically found to increase slightly with pressure from about 0.6 torr (80 Nm^{-2}) to a maximum for slightly greater pressure than 1 torr (133 Nm^{-2}) and to decrease with further increase in pressure as shown for $CH_2Br_2+Ar^*$ in figure 3.12 (solid curves).

The total ArBr intensity depends on the number of excited state $ArBr^*$ molecules formed in the reaction vessel which depends on the flow of Ar^* and the flow of the bromine containing reagent as mentioned previously (chapter 2). Electronic quenching of $ArBr^*$ by Ar to lower states would involve a transfer of a very large amount of energy to the Ar and is therefore unlikely to occur. It is not found to be an important quenching channel in other noble gas halide systems. Among other possible secondary reactions which might be occurring are quenching of $ArBr^*$ by vibrational excitation followed by predissociation and formation by recombination of Ar and Br^*. However, if such reactions were of great importance one might expect to observe significant changes in the ratio I_{Br}/I_{ArBr} with pressure, this, however, is not the case. Such secondary reactions are therefore not expected to affect the pressure dependence behaviour significantly.

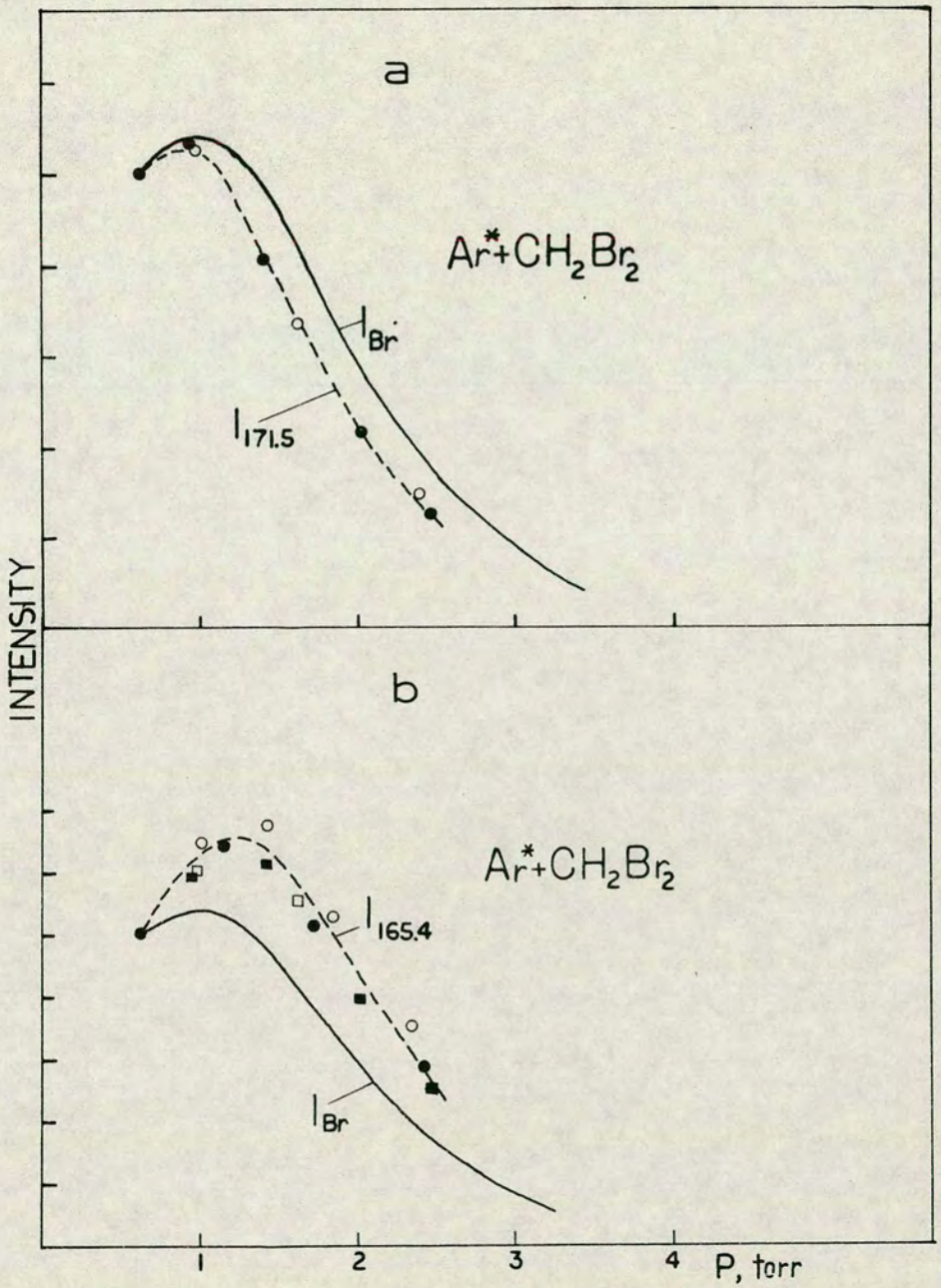

Fig. 3.12 Light intensities from $Ar^* + CH_2Br_2$ as a function of pressure. The solid curves show the variation of the light intensity from the bromine atomic lines. The dots represent intensities at the wavelengths a. 171.5 nm and b. 165.4 nm. Different types of dots represent values from independent experiments. The dashed curves are smoothed fits to the points. The intensities are normalized such that the intensity from the various experiments at 0.6 torr is the same. Slit width : 500 μm. 1 torr = 133.322 Nm^{-2}.

The pressure dependence behaviour of the total ArBr intensity is therefore mainly expected to reflect the change in flow of Ar^* into the reaction vessel rather than the effect of some secondary reactions of $ArBr^*$. The flow of Ar^* is greatly pressure dependent as mentioned in chapter 2. Thus the total ArBr intensity (I_{ArBr}) is directly proportional to the rate of formation of $ArBr^*$ (R_{ArBr}) in the reaction vessel

$$I_{ArBr} \propto R_{ArBr} \qquad (3.3)$$

The major processes of concern are formation reactions and radiative transitions

$$Ar^* + RBr \longrightarrow ArBr^* + R \qquad (2)$$

$$ArBr^* \rightarrow Ar + Br + h\nu \qquad (3)$$

The rapid fall off in the intensities with pressure puts severe limitations on the range of pressure over which studies of changes in the intensities at various wavelengths could be made. For higher pressure than about 4.0 torr (533 Nm^{-2}) intensities were found to be almost unmeasurable except by using very big slit widths (low resolution). In a typical experiment on HBr+Ar^*, using 500 μm slit width, the intensity of the 165.4 nm peak dropped from a maximum value of 1600 counts s^{-1} at a total pressure of 1.2 torr (160 Nm^{-2}) to about 80 counts s^{-1} at

4 torr (533 Nm^{-2}). The HBr+Ar^* reaction gave the strongest ArBr emission of the reactions which were studies. The lower limit of the pressure range was determined by the maximum pumping rate for a fixed flow rate, and was found to be typically about 0.6 torr (80 Nm^{-2}).

The pressure dependence behaviour of the intensities was found to vary with wavelength. At some wavelengths the intensities were found to reach maxima at lower total pressure and fall off more rapidly with further increase in pressure than observed for the Br- or total ArBr- intensities, as observed at 171.5 nm for CH_2Br_2+Ar^* (figure 3.12 a). At other wavelengths the intensities were found to fall off less rapidly with pressure, as found for the 165.4 nm peak for CH_2Br_2+Ar^* (figure 3.12 b). Since the ArBr intensity depends on the number of emitting species in the observation vessel, it is clear that the number of $ArBr^*$ molecules which emit at these wavelengths ($ArBr^*_\lambda$) changes differently with pressure than the total number of $ArBr^*$ molecules. This characteristic change must be due to some secondary reactions other than those which were considered above. Secondary reactions which can account for this characteristic difference are vibrational and rotational deactivation reactions and electronic quenching or collision induced crossing between

electronic states of close energy. Such quenching and formation reactions can be expressed as

$$ArBr^{*}_{\lambda} + Ar \xrightarrow{k_c^{\lambda}} ArBr^{**} + Ar \qquad (4)$$

$$ArBr^{**} + Ar \longrightarrow ArBr^{*}_{\lambda} + Ar \qquad (5)$$

where $ArBr^{**}$ represents excited state molecules with different energy from $ArBr^{*}_{\lambda}$ and which emit at different wavelengths.

The pressure dependence behaviour of the intensity at $\lambda = 171.5$ nm for $CH_2Br_2 + Ar^{*}$ (fig. 3.12 a) indicates that the $ArBr^{*}_{171.5}$ molecules are being quenched by some secondary reactions.

By ignoring any possible formation reactions but assuming that the $ArBr^{*}_{\lambda}$ molecules are being quenched by collisions with Ar, the intensity at λ (I^{λ}_{ArBr}) can easily be derived from analysis of reaction (4) and the following reactions

$$Ar^{*} + RBr \longrightarrow ArBr^{*}_{\lambda} + R \qquad (6)$$

$$ArBr^{*}_{\lambda} \xrightarrow{k_r^{\lambda}} Ar + Br + h\nu \qquad (7)$$

to result in

$$I^{\lambda}_{ArBr} \propto \frac{R^{\lambda}_{ArBr}}{1 + \frac{k_c^{\lambda}}{k_r^{\lambda}} [Ar]} \qquad (3.4)$$

where R^{λ}_{ArBr} is the rate of formation of $ArBr^{*}_{\lambda}$.

Pressure dependence behaviour as observed at 165.4 nm for $CH_2Br_2+Ar^{*}$ (fig. 3.12 b) indicates that $ArBr^{*}_{165.4}$ molecules are formed by secondary reactions. Analysis of the reactions (5), (6) and (7) yields

$$I^{\lambda}_{ArBr} \propto R^{\lambda}_{ArBr} + c'[Ar] \qquad (3.5)$$

where c′ is a positive value proportional to the number of $ArBr^{**}$ molecules in the observation vessel.

The [Ar] containing terms in equations 3.4 and 3.5 determine the characteristic deviation in the pressure dependence behaviour of I^{λ}_{ArBr} from the pressure dependence behaviour of I_{ArBr} (or I_{Br}). However, it is more likely that <u>both</u> secondary quenching- and formation- reactions are occuring for $ArBr^{*}$ in which case the pressure dependence of I^{λ}_{ArBr} reflects which processes are dominant and

$$I_{ArBr} \propto \frac{R^{\lambda}_{ArBr} + c'[Ar]}{1 + \frac{k^{\lambda}_{c}}{k^{\lambda}_{r}} \cdot [Ar]} \qquad (3.6)$$

is derived. The behaviour of I^{λ}_{ArBr} with [Ar] is not obvious from equation 3.6 but it is determined by the relative sizes of the pressure dependent terms (which include [Ar]).

Because the deviation of the pressure dependence of I^{λ}_{ArBr} from that of I_{ArBr} (and I_{Br}) reflects the

importance of secondary reactions of $ArBr^*$ the same will be true for the ratios $I^{\lambda}_{ArBr}/I_{ArBr}$ and $I^{\lambda}_{ArBr}/I_{Br}$. It should be noted that equally useful information is obtainable from the pressure dependence of $I^{\lambda}_{ArBr}/I_{ArBr}$ and $I^{\lambda}_{ArBr}/I_{Br}$, because of the simple relationship between I_{ArBr} and I_{Br} (see section 3.11).

$$I_{Br}/I_{ArBr} = c \tag{3.7}$$

therefore

$$I^{\lambda}_{ArBr}/I_{ArBr} = c \; I^{\lambda}_{ArBr}/I_{Br} \tag{3.8}$$

where c is a constant (see table 3.2) for specific reactions. Expressions for $I^{\lambda}_{ArBr}/I_{ArBr}$ and $I^{\lambda}_{ArBr}/I_{Br}$ can be obtained by combining expressions for I^{λ}_{ArBr} like equations 3.4, 3.5 and 3.6 and equations for I_{ArBr} (eq. 3.3) or I_{Br} (eq. 3.2).

Particularly simple expressions can be derived from the intensity ratios by ignoring any secondary formation reactions (reaction (5)) such as by combining equations 3.4 and 3.2

$$I_{Br}/I^{\lambda}_{ArBr} \propto \alpha_{\lambda}[Ar] + \beta_{\lambda} \tag{3.9}$$

for

$$\alpha_{\lambda} = \beta_{\lambda}(k^{\lambda}_{c}/k^{\lambda}_{r}) \tag{3.10}$$

and

$$\beta_\lambda = (R_{Br}/R^{\lambda}_{ArBr}) \qquad (3.11)$$

where β_λ is a constant. A special version of expression (3.9) will be utilized later in this chapter. More complicated expressions are derived for other combinations of equations.

Intensities in the ArBr spectra will frequently be expressed as relative intensities (I_{rel}) in the rest of this chapter, where

$$I_{rel} = I_{ArBr}/I_{Br} \quad (\text{or } I^{\lambda}_{rel} = I^{\lambda}_{ArBr}/I_{Br}) \qquad (3.12)$$

Furthermore the relative intensities were normalized so that the value for the strongest MC peak was set equal to one for 0.6 torr (80 Nm^{-2}) total pressure.

The relative intensities (I^{λ}_{rel}) at 171.5 nm and 165.4 nm are plotted for various pressures for CH_2Br_2+Ar^* and HBr+Ar^* in figures 3.13 and 3.14. A definite decrease in I^{λ}_{rel} was found at 171.5 nm while an increase was found at 165.4 nm for both these reactions.

The magnitude of changes in the relative intensities varies for different reagents. The greatest variation was found for CH_2Br_2+Ar^*. At most wavelengths the relative intensity was either found to decrease steadily, as at 171.5 nm, or to increase steadily, as at 165.4 nm, with pressure over the pressure range which was studied, 0.6 - 4 torr, (80 - 533 Nm^{-2}).

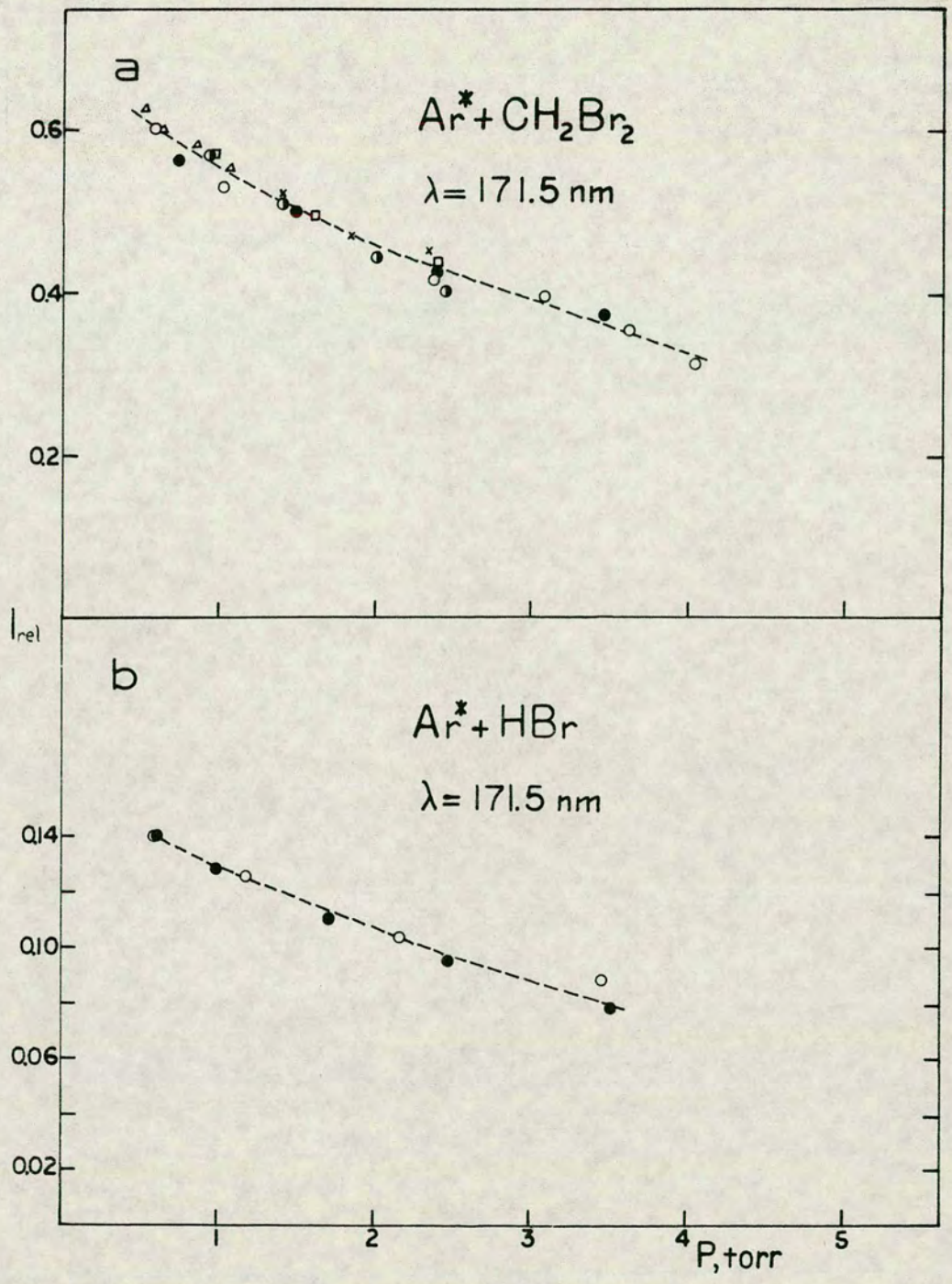

Fig. 3.13 Relative intensities at the wavelength (λ) 171.5nm (I_λ/I_{Br}) for various pressures, for a. $Ar^*+CH_2Br_2$ and b. Ar^*+HBr. Different types of dots represent values from independent experiments. The dashed curves are smoothed fits to the points. Relative intensities are normalized such that the relative intensity at 165.4nm, 0.6 torr is 1.
1 torr = 133.322 Nm^{-2}.

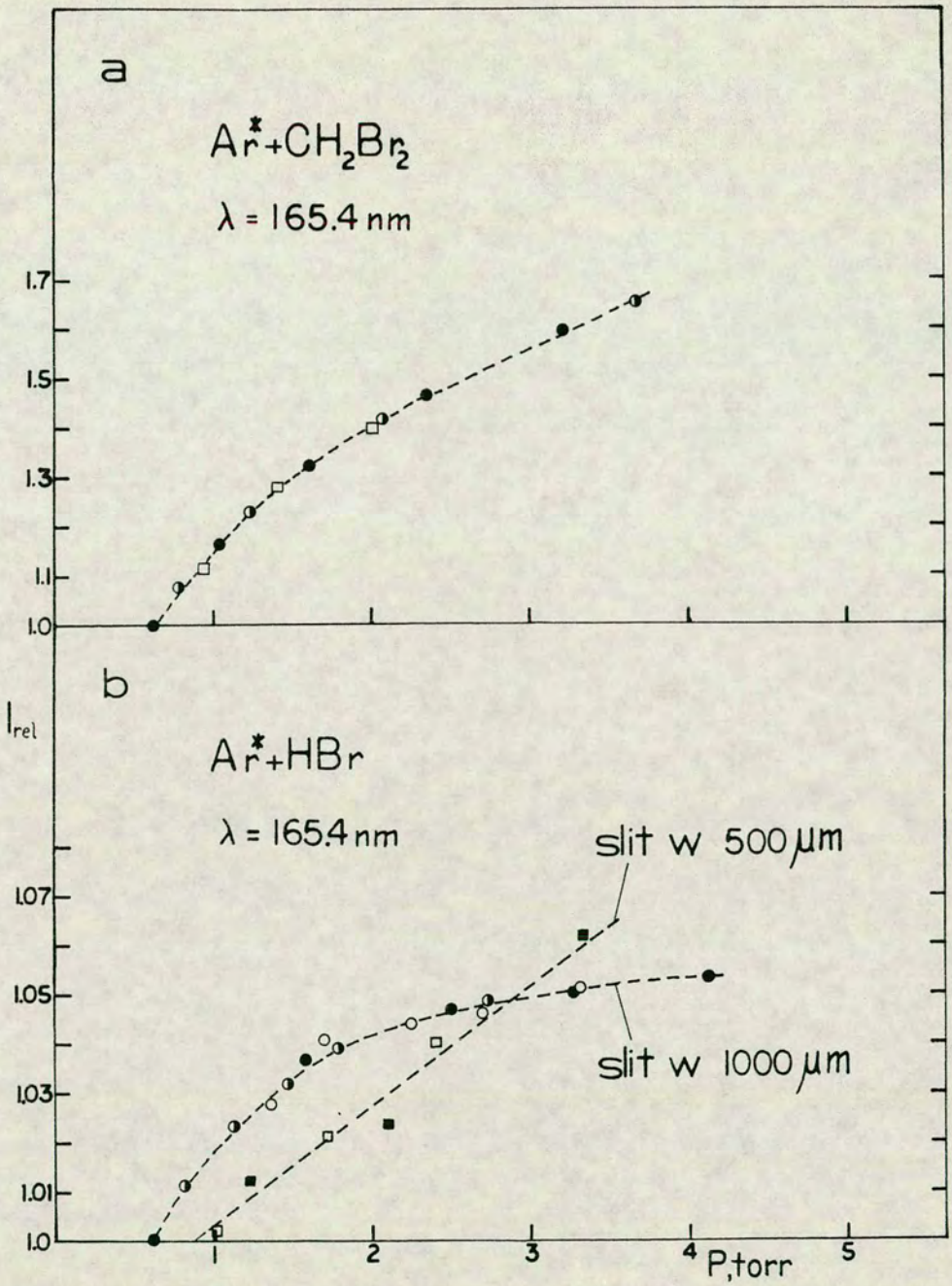

Fig. 3.14 Relative intensities at the wavelength (λ) 165.4nm (I_λ/I_{Br}) for various pressures for a. $Ar^* + CH_2Br_2$ and b. $Ar^* + HBr$. Different types of dots represent values from independent experiments. Square dots represent relative intensities found for 500 μm slit width while circles were found for 1000 μm slit width. The dashed curves are smoothed curves to the points. Relative intensities are normalized such that the relative intensity at 165.4nm, 0.6 torr is 1. 1 torr = 133.322 Nm^{-2}.

(see figures 3.13 and 3.14). Thus a particular spectrum could be separated into parts in which the relative intensities showed either negative or positive pressure dependence. Spectral ranges which showed a given pressure dependence were found to be very much the same for the different reactions.

The spectra for $HBr+Ar^*$ and $CH_2Br_2+Ar^*$ shown in figures 3.6, 3.7, 3.8 and 3.9 for various pressures represent relative intensities vs wavelength (normalized to constant bromine atomic intensity). A negative pressure dependence behaviour was basically found to occur between 159 - 161.5 nm and 166 - 176 nm and a positive pressure dependence behaviour between 162 - 166 nm and 176 - 185 nm (see appendix 1 figure 5, for the pressure dependence behaviour between 176 - 185 nm).

More data on the pressure dependence of the relative intensities for $CH_2Br_2+Ar^*$, $HBr+Ar^*$ and $DBr+Ar^*$ are tabulated in tables 3.5 to 3.10. These relative intensities have been corrected for background due to total photon scattering and photomultiplier dark current. The data on the pressure dependence in the 166.0 - 176.0 nm region (SC) for $CH_2Br_2+Ar^*$ as well as at 165.9, 164.9 and 164.4 nm were obtained with a spectrosil window in front of the photomultiplier detector to minimize scattered light associated with the bromine atomic lines.

Table 3.5

Relative intensities in the MC for $CH_2Br_2 + Ar^*$. Relative intensities are normalized such that the value at 165.4 nm at 0.6 torr is 1.

a. slit width 1000 μm

P(torr) \ λ(nm)	166.1	165.9	165.4	164.9	164.4
0.60	0.681	0.835	1.000	0.793	0.576
0.79			1.069		
0.88	0.715		1.104		
0.93			1.121		
1.02			1.153		
1.05			1.164		
1.09		0.823	1.178	0.897	0.617
1.24			1.223		
1.41			1.271		
1.45	0.802		1.280		
1.48			1.290		
1.55			1.306		
1.58			1.313		
1.62		1.050	1.322	0.990	0.642
1.79			1.359		
2.00			1.400		
2.03			1.406		
2.09		1.094	1.416	1.042	0.683
2.27			1.446		
2.36	0.865		1.460		
2.63			1.498		
2.90			1.535		
2.92			1.538		
3.19		1.199	1.575	1.161	0.748
3.21		0.911	1.579		
3.34			1.602		
3.67			1.656		

1 torr = 133.322 Nm^{-2}

Cont. Table 3.5 a. slit width 1000 μm

P(torr) \ λ(nm)	162.2	161.9	161.6	160.5
0.60	0.409	0.405	0.405	0.372
0.79			0.405	
0.93		0.405		
1.02			0.406	
1.05	0.419		0.410	0.360
1.24			0.401	
1.41	0.420			
1.45			0.403	
1.48	0.423			0.345
1.55		0.410		
1.58			0.399	
1.79	0.416			
2.00		0.402		
2.03			0.391	
2.09			0.390	
2.27	0.414			0.325
2.36	0.416			
2.63		0.403	0.377	
2.90	0.418			
2.92	0.418			0.309
3.34	0.428			
3.67			0.370	

b. slit width 500 μm

P(torr) \ λ(nm)	165.4	162.2	160.5
0.60	1.000	0.398	0.364
0.94	1.122	0.405	
1.22	1.215		0.345
1.39	1.264	0.410	
1.87	1.374	0.417	0.328
2.46	1.472	0.413	
2.66	1.501		0.310
2.83	1.523	0.425	
3.32	1.592	0.427	

Table 3.6

Relative intensities in the SC for $CH_2Br_2 + Ar^*$.
Relative intensities are normalized such that the value at 165.4 nm at 0.6 torr is 1.

a. slit width 500 μm

λ(nm) / P(torr)	175.2	173.5	173.0	172.7	172.5	172.0
0.53		0.540	0.650	0.666	0.715	0.695
0.60	0.176	0.498	0.621	0.665	0.670	0.684
0.86		0.495	0.581	0.617	0.647	0.628
1.00	0.160			0.597		
1.07		0.463	0.537	0.594	0.612	0.605
1.41	0.150			0.542		
1.84	0.147			0.471		
2.34	0.159			0.436		

λ(nm) / P(torr)	171.5	171.0	170.5	170.3	170.0	169.5
0.53	0.633	0.501	0.379	0.362	0.306	0.302
0.60	0.606	0.495	0.377	0.348	0.301	0.307
0.86	0.586	0.484	0.373	0.354	0.298	0.316
0.94	0.598					
0.98	0.603					
1.00	0.572			0.341		
1.04	0.558					
1.07	0.557	0.476	0.368	0.351	0.303	0.261
1.41	0.531			0.328		
1.44	0.522					
1.84	0.474			0.299		
2.02	0.467					
2.34	0.456			0.297		
2.40	0.462					
2.45	0.423					

1 torr = 133.322 Nm^{-2}

Cont. Table 3.6 a. slit width 500 μm

P(torr) \ λ(nm)	169.1	168.6	168.1	167.8	167.6	166.6
0.53	0.323	0.378	0.343	0.313	0.231	
0.60	0.348	0.367	0.326	0.311	0.269	0.336
0.86	0.332	0.361	0.318	0.294	0.266	
1.00	0.330			0.288		0.324
1.07	0.328	0.336	0.307	0.293	0.268	
1.41	0.320			0.271		0.325
1.84	0.304			0.252		0.315
2.34	0.284			0.257		0.315

b. slit width 1000 μm

P(torr) \ λ(nm)	171.5
0.60	0.670
1.01	0.627
1.50	0.557
2.40	0.475
3.46	0.417

c. slit width 1250 μm

P(torr) \ λ(nm)	171.5
0.60	0.708
1.04	0.534
2.38	0.418
3.09	0.398
3.63	0.358

Table 3.7

Relative intensities in the MC for HBr + Ar^*.
Relative intensities are normalized such that the value at 165.4 nm at 0.6 torr is 1.

a. slit width 1000 μm

λ(nm) / P(torr)	166.1	165.9	165.4	164.9	164.7	164.4	164.2
0.60	0.567	0.775	1.000	0.678	0.480	0.350	0.331
0.80			1.009				
0.87			1.012		0.493		
0.97		0.780	1.016	0.691		0.363	0.358
1.00	0.584		1.017				
1.25			1.022				
1.32			1.028		0.507		
1.37		0.794	1.029	0.698		0.373	
1.40			1.030				
1.47			1.032				
1.50			1.032				0.367
1.59			1.035				
1.72	0.594		1.037				
1.75		0.801	1.038	0.713		0.381	
1.78			1.038		0.505		
2.00			1.042				0.372
2.17			1.043				
2.23		0.798	1.044	0.705		0.387	
2.50	0.596		1.046		0.538		0.377
2.73			1.048				
2.82		0.808	1.048	0.718		0.388	
2.95			1.049				
3.23			1.049		0.549		
3.27			1.049				0.384
3.25		0.810	1.050	0.738		0.401	
3.42			1.050				
3.51	0.587		1.050				
3.70			1.050				
4.00			1.051				0.386

1 torr = 133.322 Nm^{-2}

Cont. Table 3.7 a. slit width 1000 μm

λ(nm) / P(torr)	163.9	163.7	162.9	162.2	161.6	160.5
0.60	0.336	0.308	0.261	0.215	0.187	0.141
0.80					0.185	
0.97		0.308	0.261			
1.00						0.139
1.25					0.184	
1.40	0.350					
1.47					0.181	
1.59				0.213		
1.72						0.134
1.75		0.318	0.261		0.178	
2.17	0.352				0.178	
2.23					0.176	
2.50		0.323	0.262			0.126
2.73					0.171	
2.95	0.357				0.169	
3.35					0.166	
3.42		0.325	0.260	0.205		
3.51						0.122
3.70	0.362				0.166	

b. slit width 500 μm

λ(nm) / P(torr)	166.1	165.9	165.4	164.9	164.7	164.4	164.2
0.60	0.431	0.701	1.000		0.338	0.280	0.342
1.22	0.428	0.709	1.015	0.549	0.351	0.294	0.352
1.87	0.432	0.701	1.030	0.625	0.374	0.302	0.360
2.54	0.436	0.706	1.047	0.621	0.385	0.320	0.361
3.16	0.447	0.715	1.062	0.641	0.394	0.331	0.373
4.04	0.467	0.733	1.084	0.667	0.430	0.353	0.398

λ(nm) / P(torr)	163.9	163.7	162.9	161.7	161.6	160.5
0.60	0.350	0.283	0.280	0.187	0.174	0.156
1.22	0.360	0.290	0.280	0.184	0.174	0.149
1.87	0.359	0.292	0.280	0.181	0.174	0.147
2.54	0.366	0.306	0.279	0.179	0.166	0.142
3.16	0.384	0.304	0.284	0.182	0.162	0.140
4.04	0.386	0.313	0.295	0.179	0.162	0.131

Table 3.8

Relative intensities in the SC for $HBr + Ar^*$.
Relative intensities are normalized such that the value at 165.4 nm at 0.6 torr is 1.

a. slit width 500 μm

λ(nm) / P(torr)	173.5	173.0	172.7	172.5	172.0	171.5
0.60	0.087	0.102	0.110	0.116	0.133	0.140
1.09	0.083	0.095	0.103	0.109	0.122	0.129
1.20						0.127
1.55	0.079	0.090	0.095	0.103	0.114	0.120
2.00	0.076	0.085	0.091	0.097	0.105	0.114
2.17						0.110
2.44	0.073	0.081	0.087	0.092	0.103	0.104
2.77						0.101
3.46						0.097

λ(nm) / P(torr)	171.0	170.5	170.3	170.0	169.6
0.60	0.143	0.135	0.129	0.123	0.106
1.09	0.132	0.128	0.123	0.117	0.102
1.55	0.122	0.119	0.117	0.110	0.098
2.00	0.115	0.115	0.111	0.106	0.095
2.44	0.111	0.106	0.103	0.100	0.088

1 torr = 133.322 Nm^{-2}

Cont. Table 3.8 a. slit width 500 μm

λ(nm) / P(torr)	169.1	168.6	168.1	167.8	167.6
0.60	0.093	0.086	0.088	0.089	0.089
1.09	0.092	0.086	0.085	0.086	0.085
1.55	0.088	0.081	0.082	0.082	0.080
2.00	0.084	0.079	0.078	0.078	0.079
2.44	0.072	0.075	0.075	0.076	0.076

b. slit width 1000 μm

λ(nm) / P(torr)	171.5
0.60	0.181
1.00	0.169
1.71	0.150
2.48	0.134
3.51	0.117

Table 3.9

Relative intensities in the MC for DBr + Ar^*. Relative intensities are normalized such that the value at lowest measured pressure at 165.4 nm is 1.

a. slit width 1000 μm

λ(nm) / P(torr)	165.4	164.7	161.7	160.5
0.60	1.000	0.543	0.174	0.110
1.00	0.963			
1.28	0.980			
1.48		0.547	0.173	0.101
1.78	0.984			
2.06	1.000			
2.42		0.565	0.165	0.096

b. slit width 500 μm

λ(nm) / P(torr)	165.4
0.78	1.000
1.23	1.004
1.64	0.995
2.11	0.977
2.77	0.951

Table 3.10

Relative intensities in the SC for DBr + Ar^*. Relative intensities are normalized such that the value at 165.4 nm at 0.6 torr is 1. Slit width 1000 μm.

λ(nm) / P(torr)	172.7	171.5	170.3	169.1	167.8
0.60	0.126	0.157	0.174	0.162	0.152
1.18	0.110	0.140	0.160	0.154	0.134
1.52	0.101	0.130	0.152	0.137	0.131
1.95	0.101	0.116	0.143	0.134	0.125
2.41	0.096	0.118	0.140	0.131	0.124

1 torr = 133.322 Nm^{-2}

The importance of rovibrational relaxation and collision induced crossing in $ArBr^*$ has been mentioned. These secondary processes as well as the radiative decay of $ArBr^*$ will be discussed in the next three sections.

3.123 Radiative transitions.

The three ionic states, the B-, C- and D- states and the three lower states, the X-, A(3/2)- and A(1/2)- states have to be considered in order to assign the various spectral contributions to particular electronic transitions.

a. MC and SC.

The strong peak at 165.4 nm and the oscillatory structure on the short wavelength side of it resembles the main feature in other noble gas halide spectra, the "main continuum" (MC).[9,40] The oscillatory structure, however, shows a much closer spacing between peaks than is found in any other low pressure noble gas halide spectrum and resembles more the fine structure observed in the high pressure spectra,[27,28,40] which has been interpreted as being due to one particular electronic transition (B-X).

The pressure dependence behaviour in this region of the ArBr spectra resembles that observed for the MC of other noble gas halides.[9,15] The intensity shifts to long wavelength as shown clearly

for $CH_2Br_2+Ar^*$ in figure 3.8. While the relative intensity between 159.0 - 161.5 nm is depressed, the relative intensity between 162.0 - 166.0 nm is enhanced.

Analogous to the high pressure spectra, the ArBr spectra represent radiative transitions from the lowest vibrational levels in the emitting states, while high vibrational levels are predissociated. While the high pressure spectra represent radiative transitions for thermal population distributions (Boltzmann distributions), the population distributions in the emitting states of $ArBr^*$ are not likely to be thermal because of incomplete relaxations in the rovibrational levels and due to the great exothermicity in forming $ArBr^*$ for reactions like $CH_2Br_2+Ar^*$, CF_3Br+Ar^* and Br_2+Ar^*. The number of peaks in the high pressure spectra reflects the number of vibrational levels which are emitting. Correspondingly one might expect the number of emitting vibrational levels for the ArBr MC to be equal to the number of peaks in the MC, which are 8 (see figures 3.5 and 3.6).

For bound-free transitions, a particular vibrational level is expected to emit over a wide spectral range.[40,21] The width of a vibrational (v′) contribution increases with increasing vibrational quantum number. This will be shown in chapter 5. The analogy with the high pressure spectra suggests that the lowest v′ contributions are to be found in

the long wavelength region of the spectra, while the high level contributions extend over the same region as well as further to short wavelength.

The pressure dependence behaviour of the MC is thus consistent with relative decrease in contributions from the highest v′ levels and relative increase in contributions from the lowest v′ levels due to vibrational relaxation. However, because of an overlap of two spectra due to two different electronic transitions in the MC region, which will be discussed later, the pressure dependence behaviour in this region can not be interpreted as being due to vibrational relaxation only.

The analogy with the high pressure spectra suggests that a negligible contribution from the transition which is responsible for the structure in the ArBr MC (the "MC transition") is to be found on the long wavelength side of the 165.4 nm peak. The spectrum in that region must therefore be assigned to another transition. The spectrum between 166.6 - 176.0 nm was found to show a slight shift in intensity to short wavelength as the pressure was increased opposite to what was found in the MC. This is shown most clearly in the CH_2Br_2+Ar^* spectra (figures 3.8 and 3.9). The intensity on the long wavelength side of the peak at 172.5 nm (0.6 torr (80 Nm^{-2})) was found to be quenched more efficiently than on the short

wavelength side, as shown in figure 3.15. This pressure dependence behaviour is analogous to that found for the "secondary continuum" (SC) spectra in other low pressure noble gas halide spectra.[2,9,10,15] The much broader structure in this spectrum than that of the MC spectrum and the characteristic lowering in the relative intensities with pressure is also analogous to that found in other low pressure noble gas halide spectra.

If this pressure dependence behaviour of the ArBr SC for CH_2Br_2+Ar^* is to be interpreted as due to a vibrational relaxation, it indicates that the higher v′ levels are emitting to longer wavelength and the lower v′ levels are emitting to shorter wavelength opposite to what was found for the MC.

The analyses by Tellinghuisen et al. of the high pressure MC spectra[40] showed the structure of the v′ contributions to illustrate the reflection principle neatly, as mentioned before (section 1.2). The vibrational contributions showed a characteristic oscillatory structure where the outermost peaks at the maximum and the minimum wavelengths of the spectra (λ_{max} and λ_{min}) are associated with vertical transitions from the turning points in agreement with the FC principle (see figure 3.16 a). For a particular bound upper state the position and the broadness of the peaks in the v′ contributions and

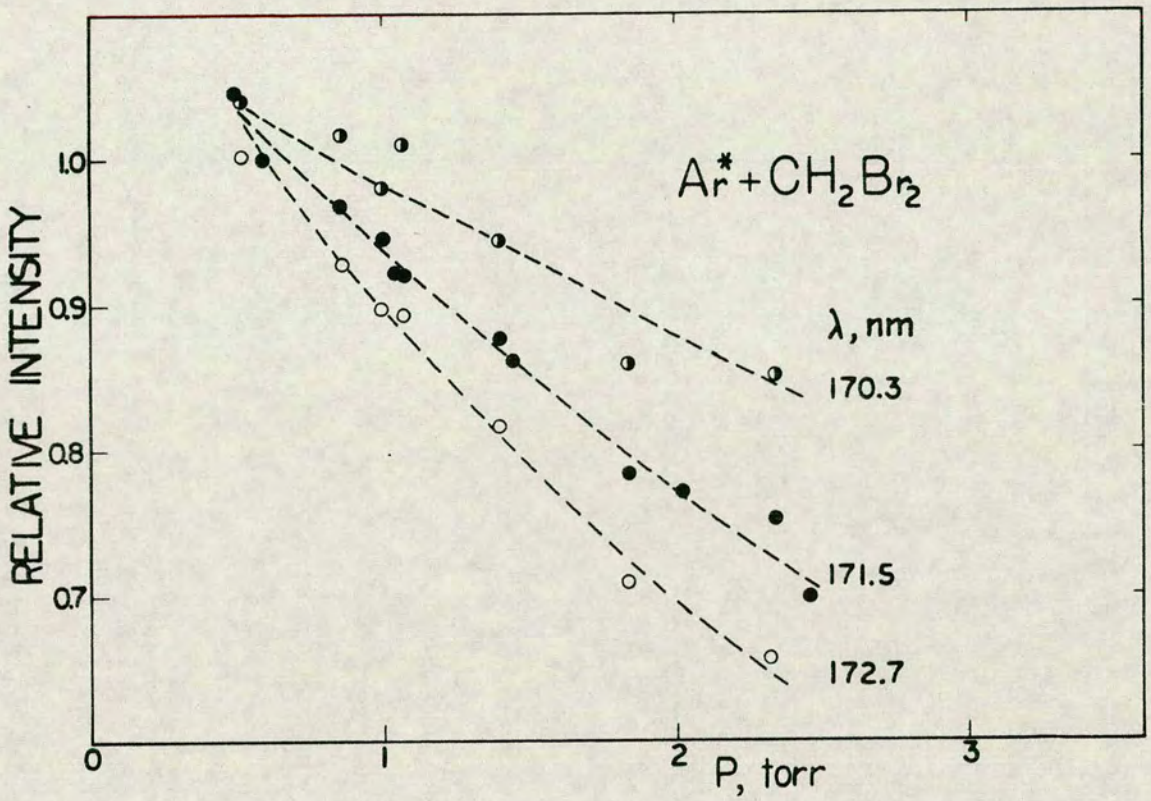

Fig. 3.15 $Ar^* + CH_2Br_2$. Relative intensities at the wavelengths 170.3, 171.3 and 172.7 nm (I_λ / I_{Br}) for various pressures. The relative intensities are normalized such that the relative intensities at 0.6 torr are 1. Dashed curves are smoothed fits to the points. 1 torr = 133.322 Nm^{-2}.

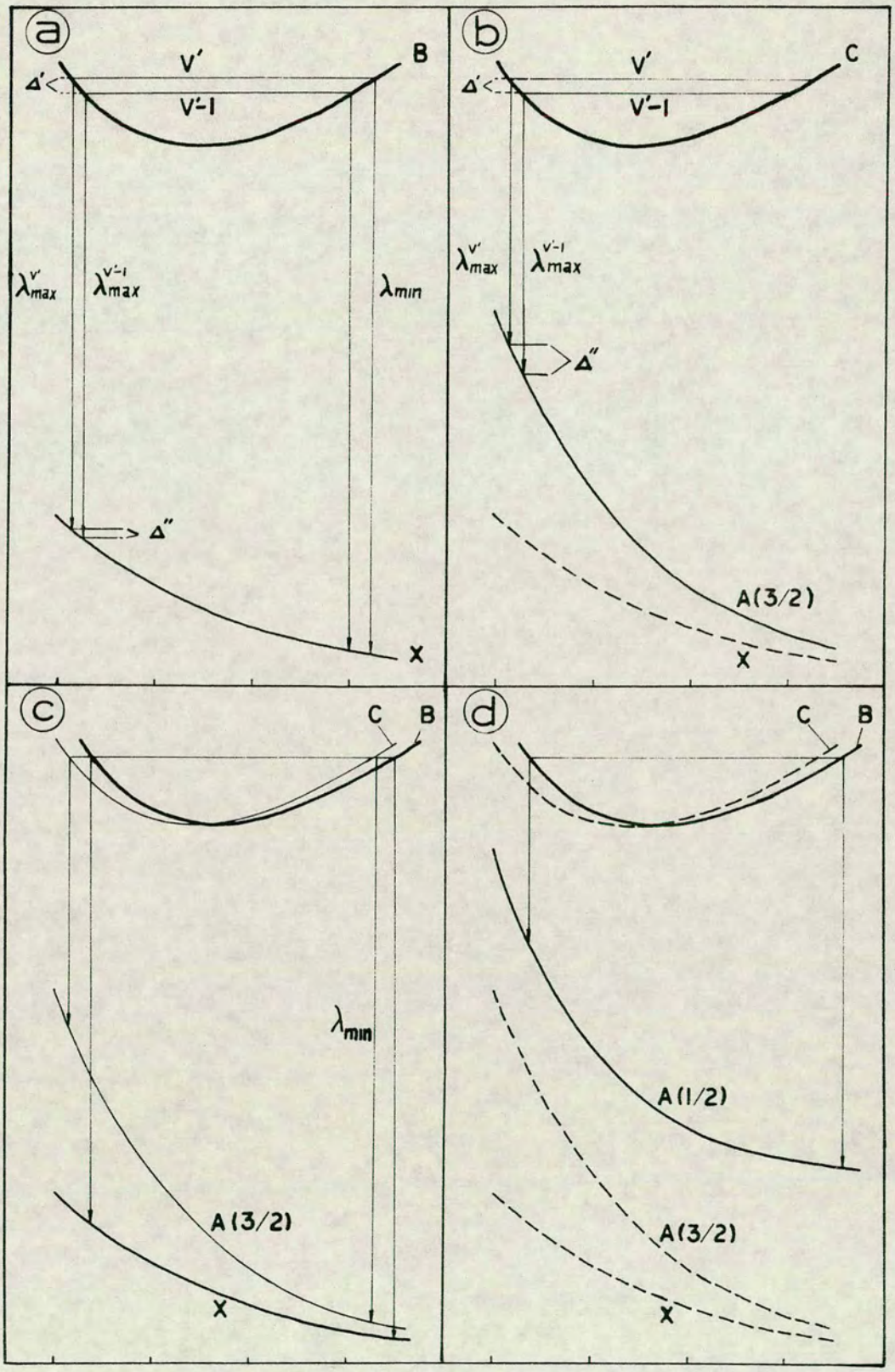

Fig. 3.16 Schematic potential curves and transitions from inner- and outer- turning points from vibrational levels in bound upper states: λ_{max} and λ_{min} respectively.

the total range of the vibrational contributions is determined by the slope of the repulsive lower state potential.

If the slopes of the two potentials are comparable in the region of the inner turning points, the peaks associated with the transitions from the various turning points are found at a similar wavelength. This can be seen from the schematic figure 3.16 a. Comparable slopes of potentials means that

$$\Delta' \sim \Delta'' \quad \text{and} \quad \lambda_{max}^{v'} \sim \lambda_{max}^{v'-1}$$

If however the slope of the lower potential is greater than that of the upper potential in the same region, then

$$\Delta' < \Delta'' \quad \text{and} \quad \lambda_{max}^{v'} > \lambda_{max}^{v'-1}$$

(see figure 3.16 b). Another consequence of increasing the slope of the lower potential is to make the structure of the spectral contributions broader. This will be dealt with in more detail in chapter 5.

Since the three excited states (B-, C- and D-states) are all expected to be of similar shape, the characteristic difference in the structure and the pressure dependence behaviour of the MC and the SC for ArBr can be interpreted as being due to transitions to different lower potentials with different slopes. The much broader structure in the

SC than in the MC suggests that the lower state potential for the "SC transition" is steeper than the lower state potential for the "MC transition". The shift of the SC intensity to shorter wavelength with pressure suggests that the lower potential is steeper than the upper potential so that the contributions from the inner turning point transitions for higher vibrational levels occur at longer wavelength than those from lower vibrational levels (figure 3.16 b).

Further comparison of the SC and the MC from the various reactions suggests that these two different transitions involve two different upper states as well as different lower states. The following findings suggest this.

a. The structure in the SC differs greatly for the different reactions while the structure in the MC does not. This is best seen by comparing the spectra for $CH_2Br_2+Ar^*$ and Br_2+Ar^* (figures 3.8 and 3.10 b).

b. The intensities of the SC differ relative to the intensities of the MC for different reactions as shown in figure 3.11. The ratio of the total integrated intensity of the SC (I_{SC}) over that for the MC (I_{MC}) (I_{SC}/I_{MC}) is about 1 for $CH_2Br_2+Ar^*$ but only about 0.35 for $HBr+Ar^*$ for the same pressure (0.6 torr (80 Nm^{-2})) (see figures 3.5 and 3.8).

c. The relative integrated intensity of the SC for $CH_2Br_2 + Ar^*$ decreases with pressure while the relative integrated intensity of the MC increases with pressure. I_{SC}/I_{MC} decreases from about 1 at 0.6 torr (80 Nm^{-2}) to about 0.8 at 2.66 torr (355 Nm^{-2}).

These findings cannot be explained easily except by assuming that there are two emitting states accounting for the two different transitions with different population distributions.

If the total SC- and the MC- intensities represent the total intensities corresponding to the two different electronic transitions one would expect the ratio I_{SC}/I_{MC} to be constant or independent of reagents as well as pressure if the upper states were the same for both transitions. It will be shown, however, that the SC and MC do not represent the two different radiative transitions properly, but that the spectra due to the two different transitions overlap in the MC- region. Thus if the ratio of the relative intensities of the spectra for both these transitions is constant (the same upper state) with pressure the "SC transition" in the MC region must show an increase in the intensity with pressure. However, that is inconsistent with predictions since the "SC transition" in that region will represent transitions near the outer turning point region of the same vibrational levels as are emitting in the SC (166.6 - 176.0 nm) and is

therefore expected to show a negative pressure dependence as well as the SC.

It should be clear from the above discussion that the total relative intensity due to the "SC transition" is expected to show a negative pressure dependence behaviour which suggest that the total relative intensity due to the "MC transition" shows a positive pressure dependence behaviour.

The MC and the SC have been assigned to radiative transitions from two different upper states for other noble gas halide systems, i.e. to the B-X and C-A (3/2) transitions respectively. Ab initio calculations predict that the A(3/2) state is greater in energy and steeper than the X-state at short internuclear distance, which suggests that the C-A(3/2) emission reaches to longer wavelength than the B-X emission, showing a broader structure in the C-A(3/2) spectrum than in the B-X spectrum.

If either of the two transitions in ArBr are to be assigned to a transition from the D-state, the D-X transition will have to be considered, since that will be expected to be the most favourable transition for the D-state judging from ab initio calculation results for other noble gas halide systems (see table 1.3). Due to the greater energy of the D-state than of the C- and the B- states (see figures 1.3 and 3.3) the D-X transition will occur to shorter

wavelength than the C-A(3/2) or the B-X transitions. Then the only alternative would be that the "MC transition" represents the D-X transition and the "SC transition" represents the C-A(3/2) transition. However, in other systems the D-X spectra have been observed as very low intensity continua compared to much stronger MC.[16] The potential surface which correlates with the D-state will cross the entrance channel at a shorter internuclear distance than the potential surfaces which correlate with the C- and the B- states, so the population of the D-state may be less favoured due to later curve crossing, which might explain the relatively low intensity of the D-X spectra. This must also be the case for ArBr, and the "MC transition" will be assigned to the B-X transition. Analogous to other noble gas halide spectra[16], the D-X band might then be found at shorter wavelength than the 165.4 nm peak at a separation approximately equal to the spin orbit splitting in the Ar^+ ion of 1432 cm^{-1} (17440 J $mole^{-1}$). Thus an estimated position of the D-X band will be at about 161.5 nm, but no new band structure was found in that region for any of the ArBr spectra, so the transition from the D-state must be negligible in any of these reactions. Possibly the D-state is completely predissociated.

b. TC

While the strongest SC peak in the $CH_2Br_2+Ar^*$ spectrum represents transitions from the inner turning point region of the C-state, the upper wavelength limit of the C-A(3/2) spectrum corresponds to the long wavelength edge of the SC peak ($\sim$ 176 nm). The spectrum in the region to longer wavelength, therefore, represents some different electronic transition.

Having assigned the spectra in the 158 - 176 nm region (MC+SC) to the B-X and C-A(3/2) transitions and found any transitions from the D-state to be negligible, it is an easy task to assign an electronic transition to the long wavelength spectrum (176 - 186 nm). It must be due to a transition from either the C- or the B- state to a lower state of greater energy than the A(3/2)-or the X-states, i.e. the A(1/2) state. The characteristic positive pressure dependence behaviour of this spectrum (see figure 5 in appendix 1) is in agreement with that observed for the B-X spectrum, but in contrast with the negative pressure dependence behaviour of the C-A(3/2) spectrum, suggesting that the upper state is the B-state. The long wavelength spectrum is therefore assigned to the B-A(1/2) transition (see figure 3.16 d). This transition is discussed further in reference 10 (see appendix 1) for ArBr as well as for

other noble gas halide systems. The pressure dependence behaviour of this spectrum is found to be comparable to that of the 165.4 nm MC peak for the various reactions. This is shown in figure 3.17, where ratios of intensities relative to the intensity at the 165.4 nm MC peak for two pressures, p_1 and p_2

$$\left[\frac{I_\lambda}{I_{165.4}}\right]_{p_1} \Big/ \left[\frac{I_\lambda}{I_{165.4}}\right]_{p_2}$$

are plotted vs wavelength for $p_1 > p_2$.

c. Overlap of spectra.

Because the A(3/2)- and the X-states have the same asymptotic energy value (zero energy) it would not be surprising if the short wavelength emission due to the C-A(3/2) transition would overlap with the B-X emission. In case both the lower states are close in energy in the region of the outer turning points of the highest emitting vibrational levels, as shown in figure 3.16 c, the low wavelength limits (λ_{min}) for the two transitions will be very similar.

The fact that an overlap of the C-A(3/2) and B-X emissions in the MC occurs in the ArBr spectra could be verified firstly by comparing the pressure dependence behaviour of the 165.4 nm MC peak and the B-A(1/2) spectrum, secondly by comparing short wavelength MC emission (160.5 nm) for CH_2Br+Ar^* and $HBr+Ar^*$ and thirdly by comparing the

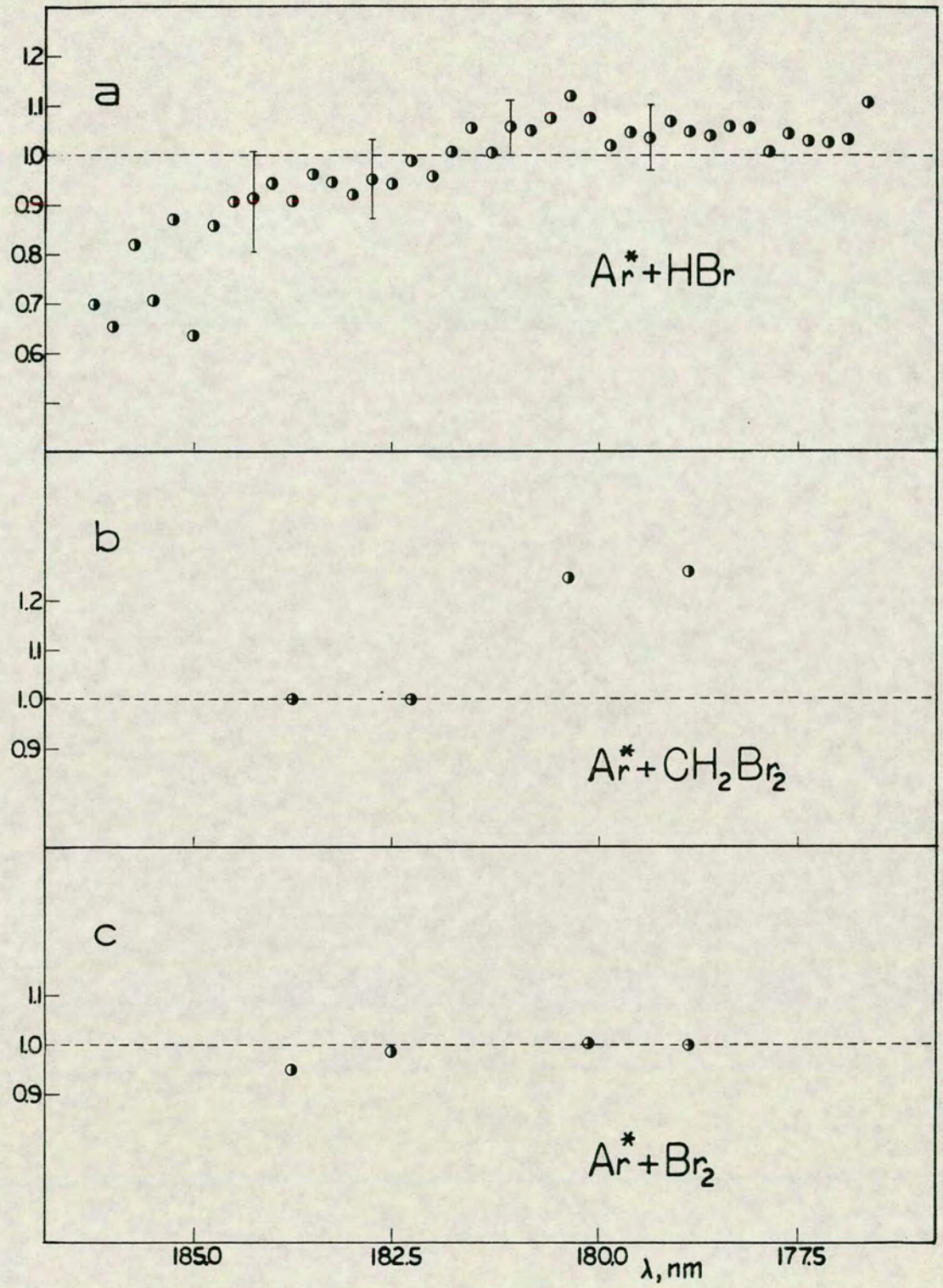

Fig. 3.17 Ratios of intensities relative to the intensity at 165.4 nm MC peak for two pressures, p_1 and p_2, $(I_\lambda/I_{165.4})_{p_1} / (I_\lambda/I_{165.4})_{p_2}$ vs wavelength for a. Ar^*+HBr, b. $Ar^*+CH_2Br_2$, c. Ar^*+Br_2. p_1=1.56 torr (208 Nm^{-2}), p_2 = 0.6 torr (80 Nm^{-2}).

structure in the MC for $CH_2Br_2+Ar^*$ and $HBr+Ar^*$.

The greatest increase in the relative intensity of the MC for $CH_2Br_2+Ar^*$ was found to occur at the 165.4 nm peak. This is shown in figure 3.18, where the relative intensities at the various wavelengths are plotted against pressure where the relative intensities have been normalized to a value of 1 for 0.6 torr (80 Nm^{-2}). Since it has been shown that the increase of the intensity of the whole resolved B-A(1/2) continuum for $CH_2Br_2+Ar^*$ with pressure is comparable to or greater than the intensity of the 165.4 nm peak of the MC, it is clear that the total increase in the B-A(1/2) spectrum is greater than that of the whole MC. That is an impossible result if both these spectra represent radiative transitions from the B-state alone. It is, however, consistent with a contribution of C-A(3/2) emission with characteristic negative pressure dependence in the MC region.

The second argument concerns the pressure dependence behaviour at 160.5 nm for $CH_2Br_2+Ar^*$ and $HBr+Ar^*$. $CH_2Br_2+Ar^*$ shows slightly greater negative pressure dependence than $HBr+Ar^*$ at 160.5 nm. According to the results in tables 3.5 and 3.7, this difference is small but definite. When the correction is made for the scattered light associated with the bromine atomic lines, this difference becomes still larger. This is shown in figure 3.19. This

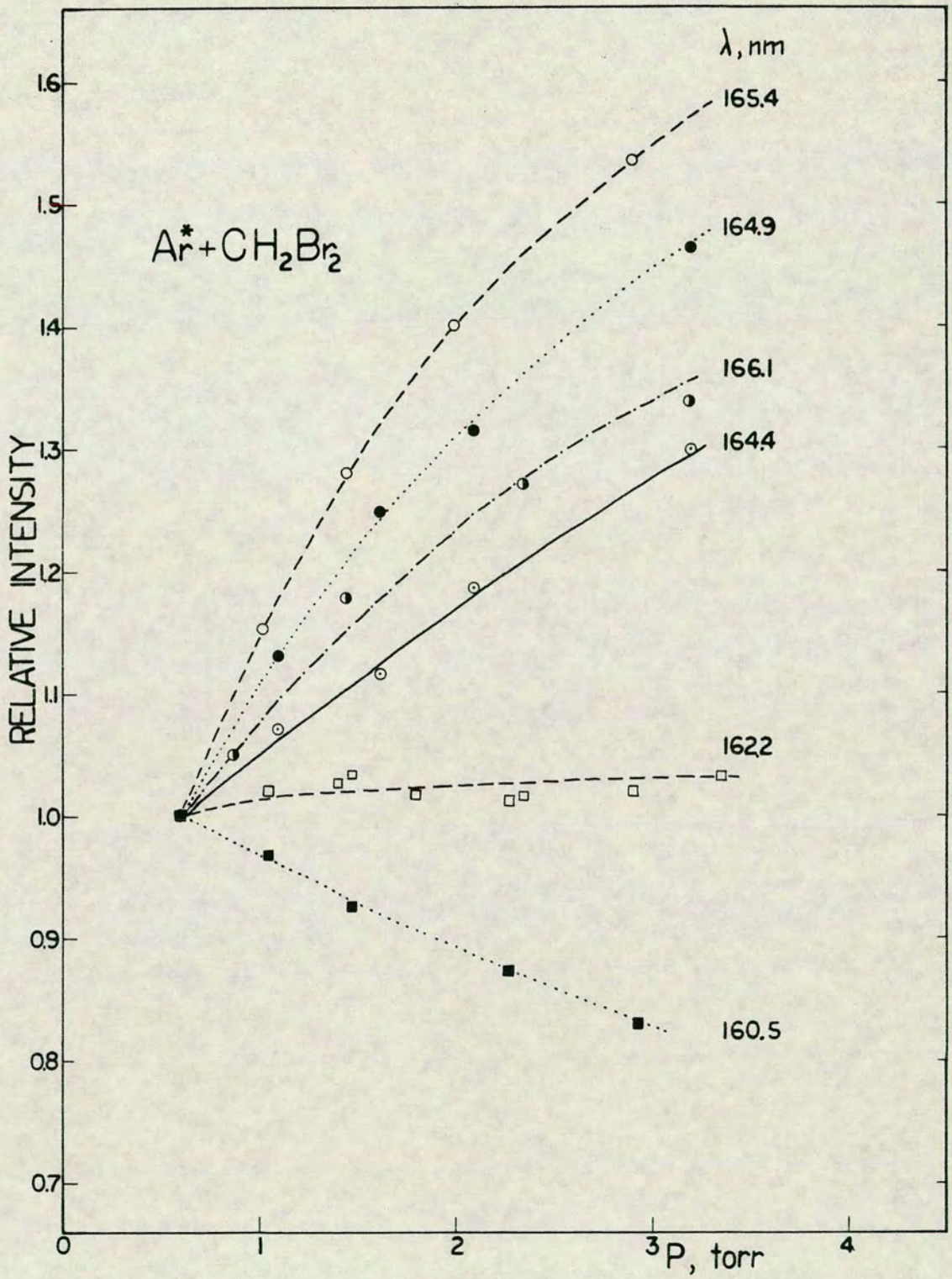

Fig. 3.18 $Ar^* + CH_2Br_2$. Relative intensities at the wavelengths shown in the figure (I_λ / I_{Br}) for various pressures. The relative intensities are normalized such that the relative intensities at 0.6 torr are 1. The curves are smoothed fits to the points.
1 torr = 133.322 Nm^{-2}.

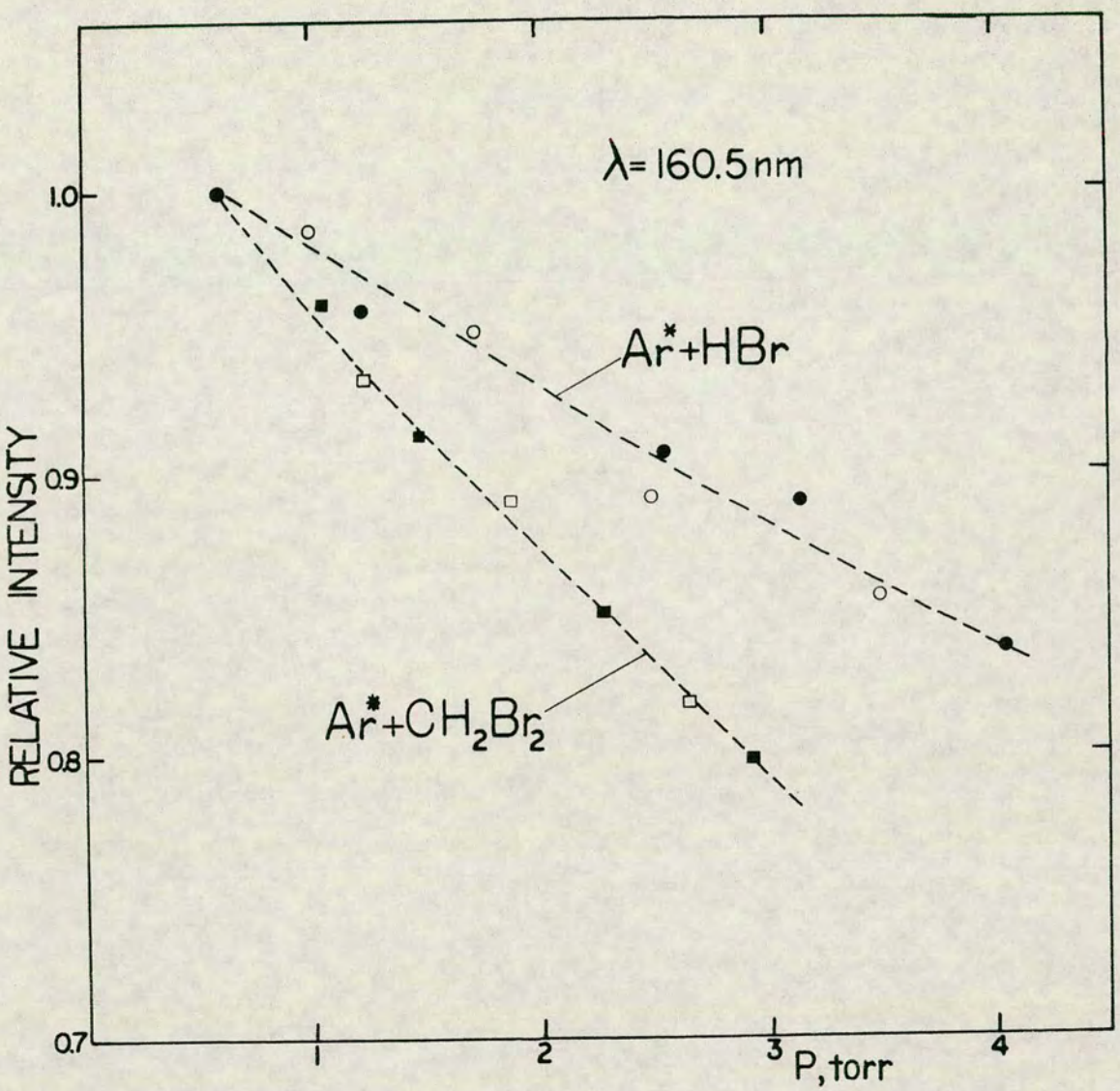

Fig. 3.19 Relative intensities at the wavelength 160.5 nm (I_λ/I_{Br}) for various pressures for Ar^* + HBr (circles) and Ar^* + CH_2Br_2 (square dots). Different types of dots represent values obtained from independent experiments. The relative intensities are normalized such that the relative intensities at 0.6 torr are 1. The dashed curves are smoothed fits to the points. 1 torr = 133.322 Nm^{-2}.

result is consistent with a relatively greater contribution of C-A(3/2) emission at 160.5 nm for $CH_2Br_2+Ar^*$ than $HBr+Ar^*$ with the C-A(3/2) contribution showing a greater negative pressure dependence than the B-X contribution. Judging from the difference in the relative total intensity of the SC for $CH_2Br_2+Ar^*$ and $HBr+Ar^*$ (see figure 3.11) one might in fact expect a greater contribution of the C-A(3/2) emission in the MC for $CH_2Br_2+Ar^*$ than for $HBr+Ar^*$.

Finally the greater irregularity in the structure in the MC for $CH_2Br_2+Ar^*$ than in the MC for $HBr+Ar^*$ (see figures 3.8, 3.5 and 3.6) can be explained as being due to a greater distortion of the structure in the B-X spectrum by a relatively greater C-A(3/2) contribution of a broader structure in that region for $CH_2Br_2+Ar^*$ than for $HBr+Ar^*$.

It is difficult to estimate the relative magnitude or detailed structure of the overlapping contributions of the B-X and C-A(3/2) systems to the MC spectra. From simulation calculations presented in chapter 5, an estimate of the ratios of the relative total intensities of the spectral contributions due to the two electronic transitions $(I_{B-X}/I_{C-A(3/2)})$ were made for $CH_2Br_2+Ar^*$ and $HBr+Ar^*$. The magnitude of the intensity due to the B-A(1/2) transition in the SC region was estimated and subtracted from the SC intensity from $HBr+Ar^*$, while

its contribution to the SC from $CH_2Br_2+Ar^*$ was ignored. Values of about 0.6 and 2.3 were obtained for this ratio for $CH_2Br_2+Ar^*$ and $HBr+Ar^*$ respectively from spectra at 0.6 torr (80 Nm^{-2}). If collision deactivation processes are assumed to be of minor importance at 0.6 torr (80 Nm^{-2}), the $I_{B-X}/I_{C-A(3/2)}$ values are approximately equal to the ratio of the rate of formation of B-state molecules $(ArBr^*(B))(R_B)$ over the rate of formation of C-state molecules $(ArBr^*(C))(R_C)$, i.e.

$$I_{B-X}/I_{C-A(3/2)} \sim R_B/R_C \qquad (3.13)$$

The emission due to the B-A(1/2) transition will extend to shorter wavelength and overlap with emission due to other transitions. The low wavelength limit of the B-A(1/2) spectrum will be determined by the asymptotic energy value of the A(1/2)-state (see figure 3.16 d), which is the same as the energy of the $Br(^2P_{1/2})$ state (3685cm^{-1}(44080 J $mole^{-1}$)).[85] The assumption was made that the low wavelength limits of the B-X and the B-A(1/2) spectra correspond to transitions from the outer turning points of the highest emitting levels in the B-state to energy levels which differ by 3685 cm^{-1} (44080 J $mole^{-1}$) in energy. Thus the short wavelength limit of the B-A(1/2) spectrum was estimated from the short wavelength limit of the B-X spectrum

(about 158.0 nm) to be about 167.8 nm. According to this an overlap of the B-X and B-A(1/2) emissions in the MC is not important, while an overlap of the C-A(3/2) and the B-A(1/2) emissions will appear in the SC.

3.124 Collision induced crossing.

It has been shown from the pressure dependence behaviour of the CH_2Br_2+Ar* spectrum that the total relative intensity due to the C-A(3/2) transition decreases while the total relative intensity due to the B-X and the B-A(1/2) transitions increases. This was also found in other ArBr spectra while the effect is not nearly as great as observed in the CH_2Br_2+Ar* spectrum. The increase in the relative intensity due to the transitions from the B-state balances the decrease in the relative intensity due to the C-A(3/2) transition so that the total intensity relative to the bromine intensity is constant. This indicates that the quenching of the C-state occurs by a collision induced crossing to the B-state.

While the collision induced crossing is experimentally found to be from the C- to the B-state, such processes are normally considered to be reversible. Cases of reversible collision induced crossing are known from the literature for small molecules like methylene[95] and CO.[94]

From the following processes, representing formation and collisional- and radiative- decay of $ArBr^*$ molecules in the C- and B- states which do not undergo predissociation:

$$Ar^* + RBr \longrightarrow ArBr^*(B) + R \qquad (8)$$

$$Ar^* + RBr \longrightarrow ArBr^*(C) + R \qquad (9)$$

$$ArBr^*(B) \xrightarrow{k_r^B} Ar + Br + h\nu \qquad (10)$$

$$ArBr^*(C) \xrightarrow{k_r^C} Ar + Br + h\nu \qquad (11)$$

$$ArBr^*(C) + Ar \underset{k_c^B}{\overset{k_c^C}{\rightleftharpoons}} ArBr^*(B) + Ar \qquad (12)$$

and from reaction (1), complicated expressions for the relative intensities of the C- and B- emissions (I_C/I_{Br} and I_B/I_{Br}) can be derived. I_C/I_{Br} is expressed as

$$I_C/I_{Br} = A/B \qquad (3.14)$$

where

$$A = R_C \left[1 + \frac{(k_c^B/k_r^B)\,[Ar]}{(1+(k_c^B/k_r^B)\,[Ar])}\, c' \right] \qquad (3.14\ a)$$

$$B = R_{Br} \left[1 + \frac{k_c^C}{k_r^C}[Ar] \left[1 - \frac{(k_c^B/k_r^B)\,[Ar]}{(1+(k_c^B/k_r^B)\,[Ar])} \right] \right] \qquad (3.14\ b)$$

where c' is defined as $c' = R_B/R_C$ (see section 3.123).

The fact that the dominant collision induced

crossing is found to be from the C- to the B- state either means that the reverse process (B→C) is slower, $k_c^B < k_c^C$, or that other loss processes which are competing with collision induced crossing occur faster for the B-state than for the C-state. Since the radiative transition is the only other major loss process, the latter case would mean that the radiative decay is a faster process for the B-state than for the C-state. That is in agreement with ab initio calculations for other noble gas halides[52-56] which show the transition probabilities for the strongest transitions B-X and C-A(3/2) to differ by an order of magnitude (see table 1.3).

The case where the rate of decay of the B-state due to radiative transitions is much greater than the rate of collision induced crossing and

$$k_r^B \gg k_c^B[Ar]; \quad (k_c^B/k_r^B)[Ar] \ll 1 \qquad (3.15)$$

is of special interest. The expression for I_C/I_{Br} (eq. 3.14) can then be simplified while the denominator reduces to

$$R_{Br}\left(1+\frac{k_c^C}{k_r^C}[Ar]\right)$$

For comparable magnitudes of the rate of formation for the two states ($c' \sim 1$) (see estimated values for $CH_2Br_2+Ar^*$ and $HBr+Ar^*$ in section 3.123) the numerator in equation 3.14 reduces to R_C and

$$I_C/I_{Br} \sim R_C/R_{Br}\left(1 + \frac{k_c^C}{k_r^C}[Ar]\right) \qquad (3.16)$$

From I_C/I_{Br}, I_{Br}/I_C can be obtained as

$$I_{Br}/I_C \simeq \alpha[Ar] + \beta \qquad (3.17)$$

for

$$\alpha = \beta(k_c^C/k_r^C) \qquad (3.18)$$

and

$$\beta = (R_{Br}/R_C) \qquad (3.19)$$

It should be noted that the expression for I_{Br}/I_C is analogous to the expression for $I_{Br}/I^{\lambda}_{ArBr}$ (eq. 3.9), which was derived from the relative ArBr intensity at the wavelength λ by ignoring any possible secondary formation reactions for the emitting species. According to the expression for I_{Br}/I_C (eq. 3.17), the reciprocal value of the relative integrated intensity of the C-A(1/2) spectrum is expected to change linearly with pressure (increasing [Ar]). The ratio of the slope over intercept of the corresponding straight line will give an estimate of the ratio k_c^C/k_r^C.

Since the total relative integrated intensity of the C-A(3/2) spectrum can not be directly evaluated from an experimental ArBr spectrum due to the overlap of other spectral contributions, estimates of I_{Br}/I_C values were obtained by

evaluating I_{Br}/I_{SC} at various pressures from the SC spectra for $CH_2Br_2+Ar^*$ shown in figure 3.9. These values are plotted in figure 3.20. A value of $k_c^C/k_r^C = 6.8\ 10^{-18}\ cm^{+3}$ was obtained from the ratio of the slope over intersect of the straight line, fitted to these points, which is shown in figure 3.20.

The simulation calculations for the SC for $CH_2Br_2+Ar^*$ at two different pressures, which will be discussed in chapter 5, gave an estimate of the total relative integrated intensity of the C-A(3/2) spectrum at these two pressures, from which an approximate value of $k_c^C/k_r^C \sim 6.9\ 10^{-18}\ cm^{+3}$ could be obtained. Similarly, an estimated value of $k_c^C/k_r^C = 6.3\ 10^{-18}\ cm^{+3}$ was obtained from the simulation calculations for the SC for $HBr+Ar^*$ at two pressures.

The good agreement between the values obtained for the two different reactions is striking and indicates that the rate of the total collision induced crossing does not depend greatly on different population distribution in the C-state..

3.125 Vibrational relaxation.

It has already been mentioned that the observed shift of the SC intensity for $CH_2Br_2+Ar^*$ to short wavelength (see figures 3.8, 3.9 and 3.15) and the shift of the MC intensity to long wavelength (see figures 3.6 and 3.8) with pressure is consistent

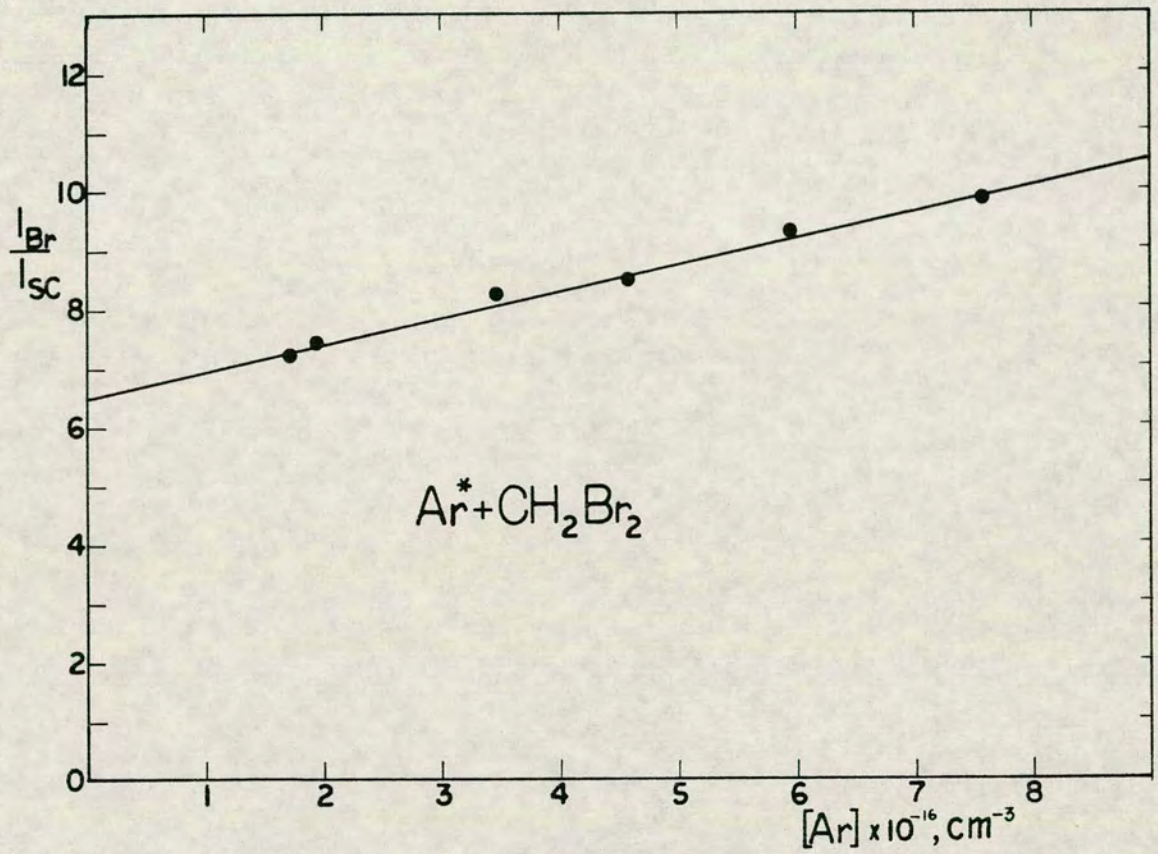

Fig. 3.20 The ratio of the bromine atomic intensity to the integrated SC intensity (I_{Br}/I_{SC}) for various Ar concentration values (dots) obtained for $Ar^* + CH_2Br_2$. The straight line is the least square fit to the data points.

with the occurrence of a vibrational relaxation in the emitting states (the C- and B- states) (see section 3.123). Further evidence of vibrational relaxation in the emitting states derived from the pressure dependence results are discussed in this section.

The intensity at a particular wavelength in the SC (I^{λ}_{SC}) is a sum of contributions from the B-A(1/2) spectrum (I^{λ}_{B}) and from the C-A(3/2) spectrum (I^{λ}_{C})

$$I^{\lambda}_{SC} = I^{\lambda}_{B} + I^{\lambda}_{C} \qquad (3.20)$$

By considering the intensity in the SC relative to the TC or relative to the strongest MC peak ($I'^{\lambda}_{SC} = I^{\lambda}_{SC}/I^{165.4}_{MC}$) (which shows similar pressure dependence behaviour to the TC) the corresponding relative B-A(1/2) intensity in the SC ($I'^{\lambda}_{B} = I^{\lambda}_{B}/I^{165.4}_{MC}$) was assumed to be unchanged with pressure. If the assumption is made that the decrease in the relative I^{λ}_{C} with pressure is due to collision induced crossing only with a rate independent of vibrational levels (see section 3.124), I'^{λ}_{C} ($I'^{\lambda}_{C} = I^{\lambda}_{C}/I^{165.4}_{MC}$) will decrease by a factor independent of wavelength

$$I'^{\lambda}_{C}(\text{high P}) = f \cdot I'^{\lambda}_{C}(\text{low P}) \qquad (3.21)$$

where $f < 1$. The total relative intensities at two different pressures (high = h and low = l) at λ are

expressed as

$$I'^{\lambda}_{SC}(h) = I'^{\lambda}_{B} + f\ I'^{\lambda}_{C}(1) \qquad (3.22)$$

$$I'^{\lambda}_{SC}(1) = I'^{\lambda}_{B} + I'^{\lambda}_{C}(1) \qquad (3.23)$$

from which I'^{λ}_{B} can be evaluated as

$$I'^{\lambda}_{B} = I'^{\lambda}_{SC}(h) \cdot \frac{(1 - f \cdot I'^{\lambda}_{SC}(1)/I'^{\lambda}_{SC}(h)}{(1 - f)} \qquad (3.24)$$

If the factor f was known I'^{λ}_{B} could be constructed from two spectra at different pressures normalized so that the intensity at the MC peak is constant.

Such spectra are shown in figure 3.21 for HBr+Ar*, where the intensity of the strongest MC peak is 1 for both spectra. The ratio of the intensities for these spectra ($I'^{\lambda}_{SC}(1)/I'^{\lambda}_{SC}(h)$) is shown at the top of this figure. I'^{λ}_{B} was constructed from these values and from the various f values. I'^{λ}_{B} values obtained for f =0.75 are plotted at the bottom of figure 3.21, showing a slight increase to short wavelength. Similar results were obtained for other spectra (Br_2+Ar* and CH_2Br_2+Ar*).

Such a shape of an underlying B-A(1/2) spectrum in the SC is not realistic. The B-A(1/2) spectrum is expected to decrease in intensity in that region to a short wavelength limit near 168 nm, as mentioned earlier (see section 3.123). This suggests that the model used to derive I'^{λ}_{B} is not valid. Thus, other quenching processes than collision induced crossing

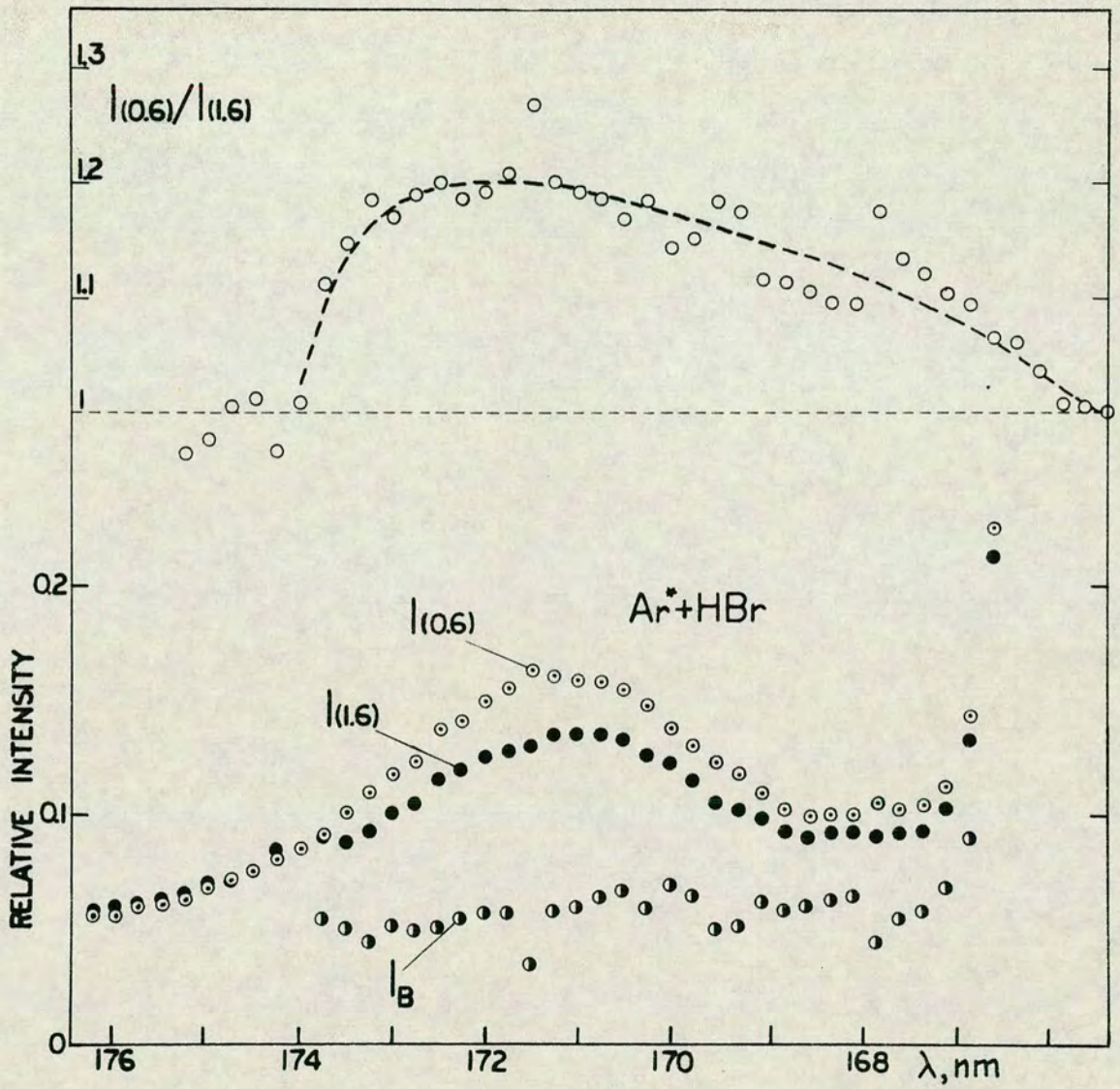

Fig. 3.21 Relative intensities (I_λ/I_{Br}) in the SC from Ar^*+HBr for two different pressures : ⊙, 0.6 torr (80 Nm^{-2}) (I(0.6)), ●, 1.6 torr (213 Nm^{-2}) (I(1.6)) and calculated relative intensities due to the B - A(1/2) transition (I_B) (bottom of figure). The relative intensities are normalized such that the relative intensity at 165.4nm is 1 for both pressures. The ratio of the relative intensities are plotted at the top of the figure. The dashed curve is a smoothed curve to fit the points.

are also occurring and can account for the change in the shape of the spectrum with pressure, namely vibrational relaxation.

A different interpretation of the pressure dependence results for the SC for $CH_2Br_2+Ar^*$ leads to the same conclusion. The assumption was made that I_{Br}/I_C^λ could be expressed as a linear function of concentration, [Ar], which holds, according to equation 3.9 (see also section 3.124), if the assumption is made that vibrational relaxation in the C-state is negligible and that collision induced crossing is independent of vibrational levels in the C-state. As a first approximation, I_C^λ was replaced by I_{SC}^λ by assuming that the B-A(1/2) contribution is negligible in the SC. $\alpha_\lambda/\beta_\lambda (= k_c^\lambda/k_r^\lambda)$ values were then constructed from the pressure dependence data for $CH_2Br_2+Ar^*$ for various wavelengths from plots of I_{Br}/I_{SC}^λ values vs [Ar] (see figure 3.22) in a way analogous to that described in the previous section. These values which are tabulated in table 3.11 vary a lot with wavelength. According to the basic assumptions, however, these values ($= k_c^\lambda/k_r^\lambda$) are expected to be constant. If this discrepancy in the $\alpha_\lambda/\beta_\lambda$ values is to be corrected for by taking account of a B-A(1/2) spectral contribution with a positive pressure dependence, new lines have to be constructed and the values of α_λ and β_λ to be replaced by new

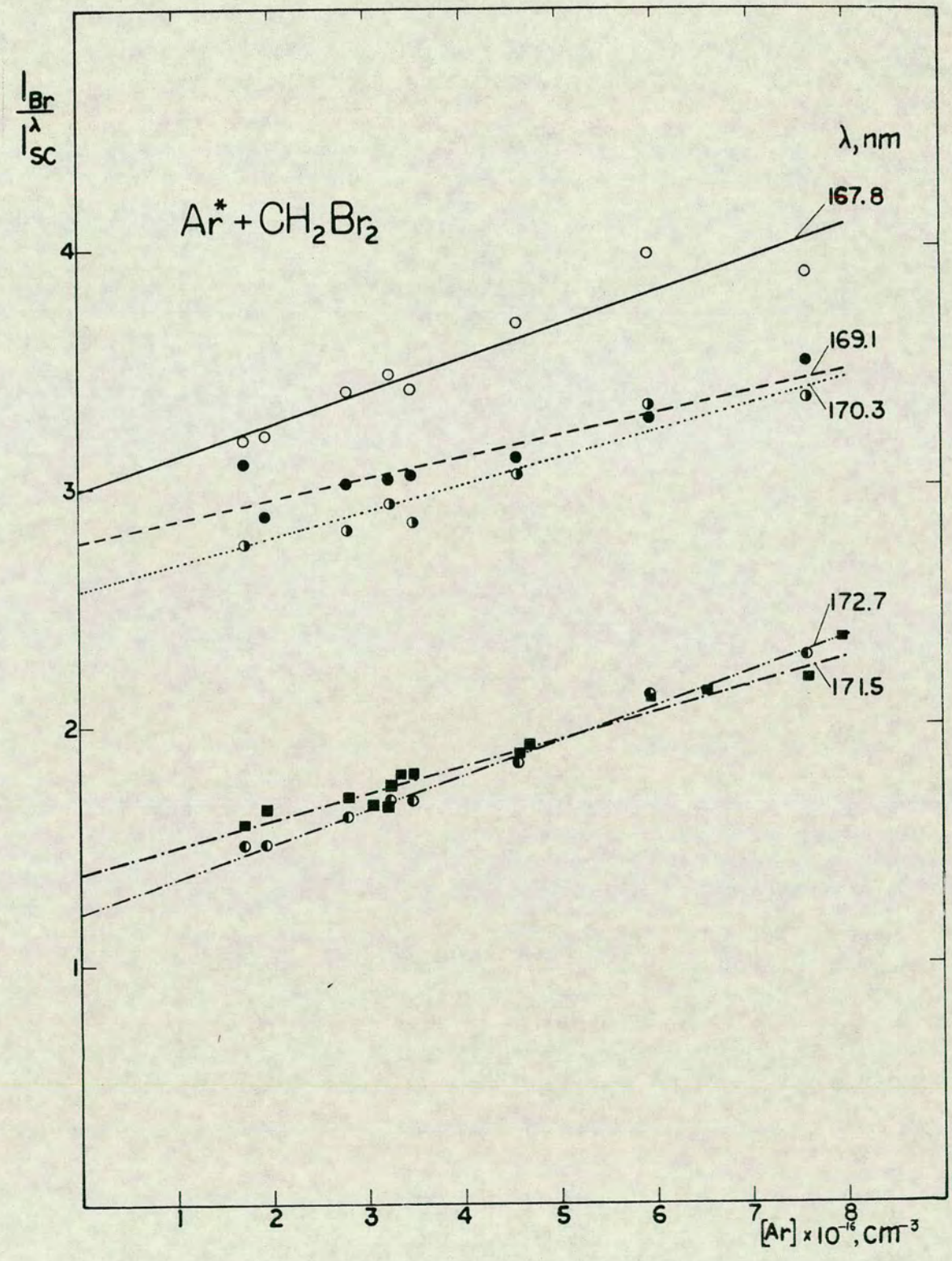

Fig. 3.22 The ratio of the bromine atomic intensity to the intensity at the wavelengths shown in the figure for various Ar concentration values obtained for $Ar^* + CH_2Br_2$. The straight lines are the least square fits to the data points.

Table 3.11

Slope over intercept $(\alpha_\lambda/\beta_\lambda)$ obtained from fitting straight lines through plots of I_{Br}/I_{SC}^{λ} vs [Ar] for various wavelengths (λ) in the SC for $CH_2Br_2+Ar^*$ and 500 μm slit width.	
λ(nm)	$(\alpha_\lambda/\beta_\lambda)\cdot 10^{18}$ (cm^3)
175.2	5.4
172.7	12.0
171.5	8.1
170.3	4.3
169.1	3.2
167.8	4.6
166.6	1.2

values, α'_λ and β'_λ to obtain

$$I_{Br}/I_C^{\lambda} = \alpha'_\lambda[Ar] + \beta'_\lambda \qquad (3.25)$$

Since $I_{SC}^{\lambda} > I_C^{\lambda}$ the I_{Br}/I_C^{λ} values are greater than I_{Br}/I_{SC}^{λ} for any [Ar]. Therefore, both $\beta'_\lambda > \beta_\lambda$ and $\alpha'_\lambda/\beta'_\lambda > \alpha_\lambda/\beta_\lambda$ must be satisfied. From table 3.11 it is found that $\alpha'_\lambda/\beta'_\lambda \geq 1.2\ 10^{-17}$ also must hold, which corresponds to the greatest value obtained for the ratio of the slope over intersect. For each chosen value of $\alpha'_\lambda/\beta'_\lambda$, I_C^{λ} values were constructed from equation 3.25 and I_B^{λ} found from $I_B^{\lambda} = I_{SC}^{\lambda} - I_C^{\lambda}$. Thus I_B^{λ} values were obtained as a function of pressure. β'_λ and α'_λ values which made I_B^{λ} values to increase with pressure in a comparable way to that of the strongest MC peak were selected specially. Only α'_λ and β'_λ

values within a limited range could satisfy the necessary requirements. Thus certain limitations for the range of calculated I_B^λ values for a particular spectrum at a particular pressure were obtained. The low and the high limit values obtained for I_B^λ at 0.6 torr (80 Nm^{-2}) are shown in figure 3.23, as well as the total relative intensities obtained at several wavelengths. Such structure of an underlying B-A(1/2) spectrum is not believed to be realistic. A decrease in the intensity to lower wavelength is not observed as would be expected. Instead, an overall increase in the intensity is observed (see figure 3.23). This suggests that the basic assumptions which were made are not valid and that vibrational relaxation is occuring in the C-state.

The pressure dependence behaviour of the intensity in the MC for HBr + Ar^* showed a slight shift of the strongest peak at 165.4 nm to shorter wavelength which was only obvious from a careful investigation of the pressure dependence behaviour at various wavelengths across the peak. Thus an increasing positive pressure dependence behaviour was observed across the peak to shorter wavelength from 165.9 nm to about 164.7 nm, as shown in figure 3.24. Further to short wavelength a decreasing positive pressure dependence behaviour was observed

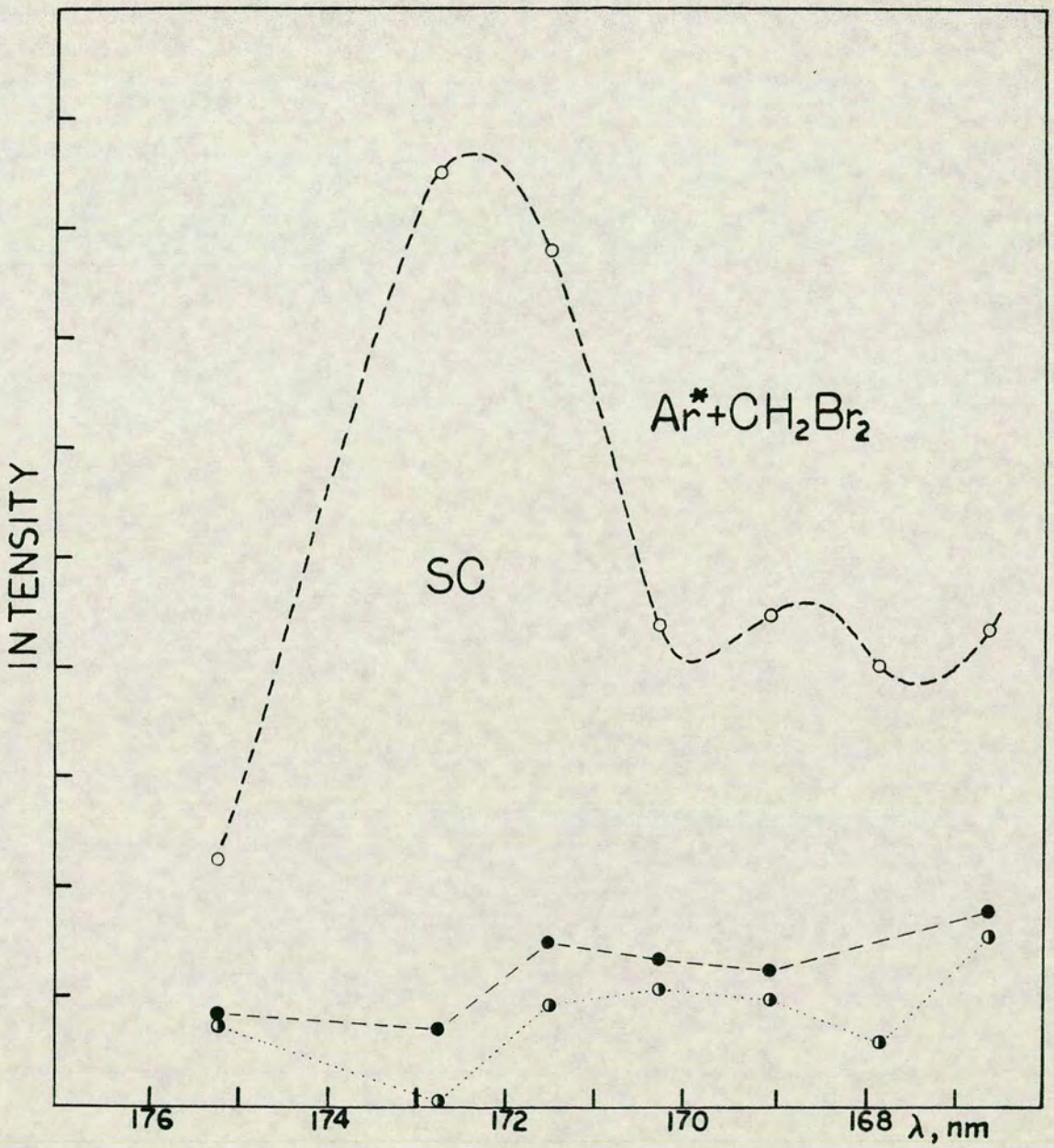

Fig. 3.23 ArBr , SC spectrum generated by $Ar^{*}+CH_2Br_2$ (---O---) at 0.6 torr (80 Nm^{-2}) total pressure and for 500 μm slit width and calculated maximum (●) and minimum (◑) intensity contributions due to the B - A(1/2) transition, by assuming that vibrational relaxation is of no importance in the C - state.

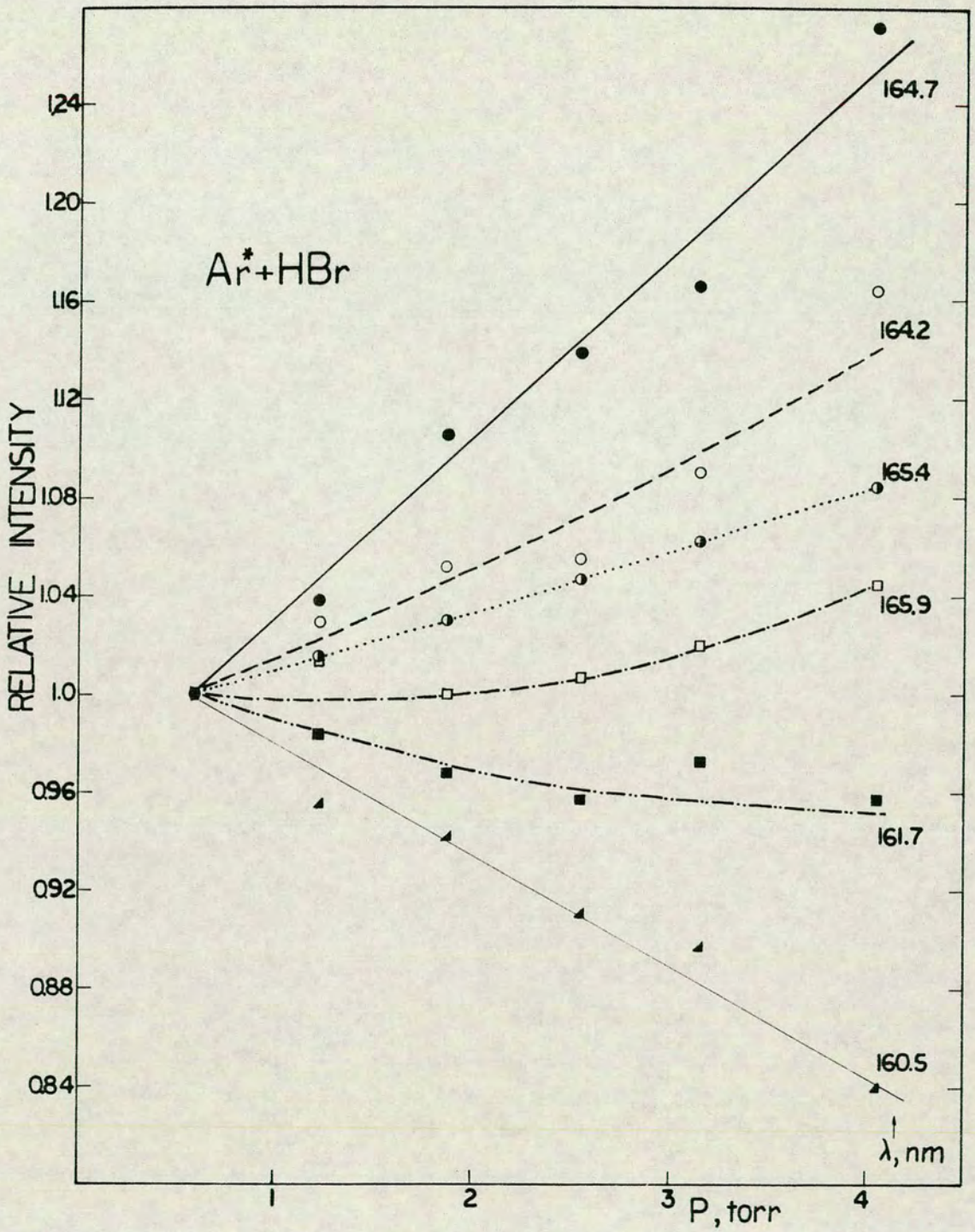

Fig. 3.24 $Ar^* + HBr$. Relative intensities at the wavelengths shown in the figure (I_λ / I_{Br}) for various pressures. The relative intensities are normalized such that the relative intensities at 0.6 torr are 1. The curves are smoothed fits to the points.
1 torr = 133.322 Nm^{-2}.

and beyond about 162 nm a negative pressure dependence was found. The shift of the strongest MC peak is analogous to that observed for the strongest SC peak for $CH_2Br_2+Ar^*$ and is due to a decrease in the high v′ contributions relative to the low v′ contributions, due to a vibrational relaxation.

3.126 Temperature dependence.

The intensities at various wavelengths in the MC and the SC and of the bromine atomic line ($^4P_{5/2} \rightarrow {}^2P_{3/2}$) at 157.7 nm in $HBr+Ar^*$ were measured at two different temperatures - room temperature and a temperature obtained by cooling the inlet tubings and the reaction vessel with dry ice (196 °K).

All the intensities were found to decrease with cooling relative to the strongest MC peak at 165.4 nm, as shown in table 3.12. The relative intensity of the bromine atomic line dropped the most (44%). The % decrease in the relative intensities was found to increase to shorter wavelength in the MC, and the SC showed a % decrease in the relative intensity similar to the greatest effect observed in the MC ($\sim$ 20%).

The great change in the relative intensity of the bromine atomic line is consistent with the fact that the formation of $Br^*(^4P_{5/2})$ from $Ar^*(^3P_2)+HBr$ is endothermic, as mentioned previously (section 3.11).

Table 3.12

% decrease in the relative intensity at various wavelengths of the spectrum for $HBr+Ar^*$ with cooling of the reaction vessel and the inlet tubings.		
Spectrum	λ(nm)	% decrease
Br	157.7	44
	159.1	19
	159.8	12.3
	160.4	6.4
MC	161.1	4.9
	162.0	4.2
	162.9	4.0
	164.0	1.4
	165.4	0
SC	170.8	18

The greatest % decrease in the relative intensity observed in the ArBr spectrum (~20%) was assumed to represent the change in the population in the highest emitting rovibrational levels in the endothermic region. The energy difference between these levels (ΔE) and the threshold level determined by equation 3.1 could be estimated if the temperature inside the reaction vessel (T) was known. The intensity is proportional to the population, whose dependence on temperature is determined by the Boltzmann factor and

$$I_T = c \exp(-\Delta E/kT) \qquad (3.26)$$

where c is a constant and I_T is the intensity at the

temperature T. From this expression the % decrease in the intensity with lowering of the temperature from T_0 to T_1 can be obtained as

$$\% \text{ decrease} = 10^2(1 - \exp(\frac{\Delta E}{k}(\frac{1}{T_0} - \frac{1}{T_1}))) \qquad (3.27)$$

The temperature inside the reaction vessel which corresponds to the cooling by dry ice (T_1) is uncertain. Measurements of the temperature near the inlet to the reaction vessel which were made by Dr M.F. Golde in Pittsburgh in a different experiment showed T_1 to be approximately 240 °K. An estimate of T_1 = 265 °K was made as a reasonable upper limit value for the experiment from which the results in table 3.12 were obtained. ΔE for 20% decrease was then found from equation 3.27 to be about 380 cm^{-1} (4550 J $mole^{-1}$).

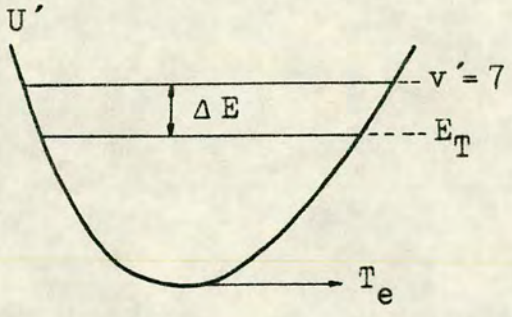

It has already been suggested that at least 8 vibrational levels (v′ = 0-7) are emitting in the B-state for HBr+Ar*. By assuming that the highest emitting level is v′ = 7 and that the thermoneutral limit is determined by the threshold energy for HBr+Ar* ($^3P_2$), E_T (see table 3.3), the position of the minimum of the B-state potential (T_e) can be estimated if the vibrational frequency or the spacing between the

vibrational levels is known.

For the simulation calculations for the ArBr spectra (chapter 5) an upper potential (U'_{b1}) was constructed to represent the B- and the C- state potentials (table 5.1). The energy of the $v'=7$ level above the minimum of the potential ($G'(7)$) is 1421 cm^{-1} (17000 J $mole^{-1}$) (see table 5.2). T_e is therefore found to be approximately

$$T_e \sim E_T + \Delta E - G'(7) \qquad (3.28)$$
$$\sim 62891 + 380 - 1421 = 61850 \text{ cm}^{-1} (739910 \text{ J mole}^{-1})$$

and the bond strength of the B-state approximately 38126 cm^{-1} (456100 J $mole^{-1}$), which is slightly less than for the ground state of KBr (table 1.2). Comparison of this difference in bond strength with that found for other noble gas halides and corresponding alkalihalides suggests that a greater bond strength (lower T_e) is hardly reasonable. If T_1 is chosen of lower value (<265 °K), ΔE is smaller, or the maximum emitting energy level is of greater energy than $v'=7$. T_e, calculated in the same way, will be less. Possible formation of $ArBr^*$ molecules with higher energy than the threshold energy for $HBr+Ar^*(^3P_2)$, such as molecules formed from the reaction $HBr+Ar^*(^3P_0)$, can alter the estimated value of T_e to obtain slightly greater value (less bond strength).

3.2 RCl+Ar*

Vacuum UV spectra from reactions of the chlorine containing reagents Cl_2, CCl_4, HCl, DCl and CNCl with Ar^* were recorded. All these spectra showed ArCl spectra with the strongest MC peak near 175 nm in agreement with what others have found.[8,15] Chlorine atomic lines were observed on the short wavelength side of the ArCl spectrum from $Ar^* + Cl_2$ only. The spectra for HCl and DCl also showed banded structure extending over a wide wavelength range which was assigned to HCl- and DCl- spectra respectively. The main features of these spectra as well as the pressure dependence behaviour of the ArCl MC spectra for Cl_2+Ar^* and CCl_4+Ar^* will be presented in this section. The various ArCl MC spectra are compared. Band progressions which were identified in the HCl and DCl spectra are shown.

3.21 Cl lines and ArCl spectra.

A schematic potential curve diagram for ArCl is shown in figure 3.25 as well as the threshold energies for reactions of the various chlorine containing reagents with $Ar^*(^3P_2)$ (shown by arrows). Threshold energies and bond energies are listed in table 3.13.

Only the reaction of Cl_2 with $Ar^*(^3P_2)$ has a greater threshold energy than the lowest excited

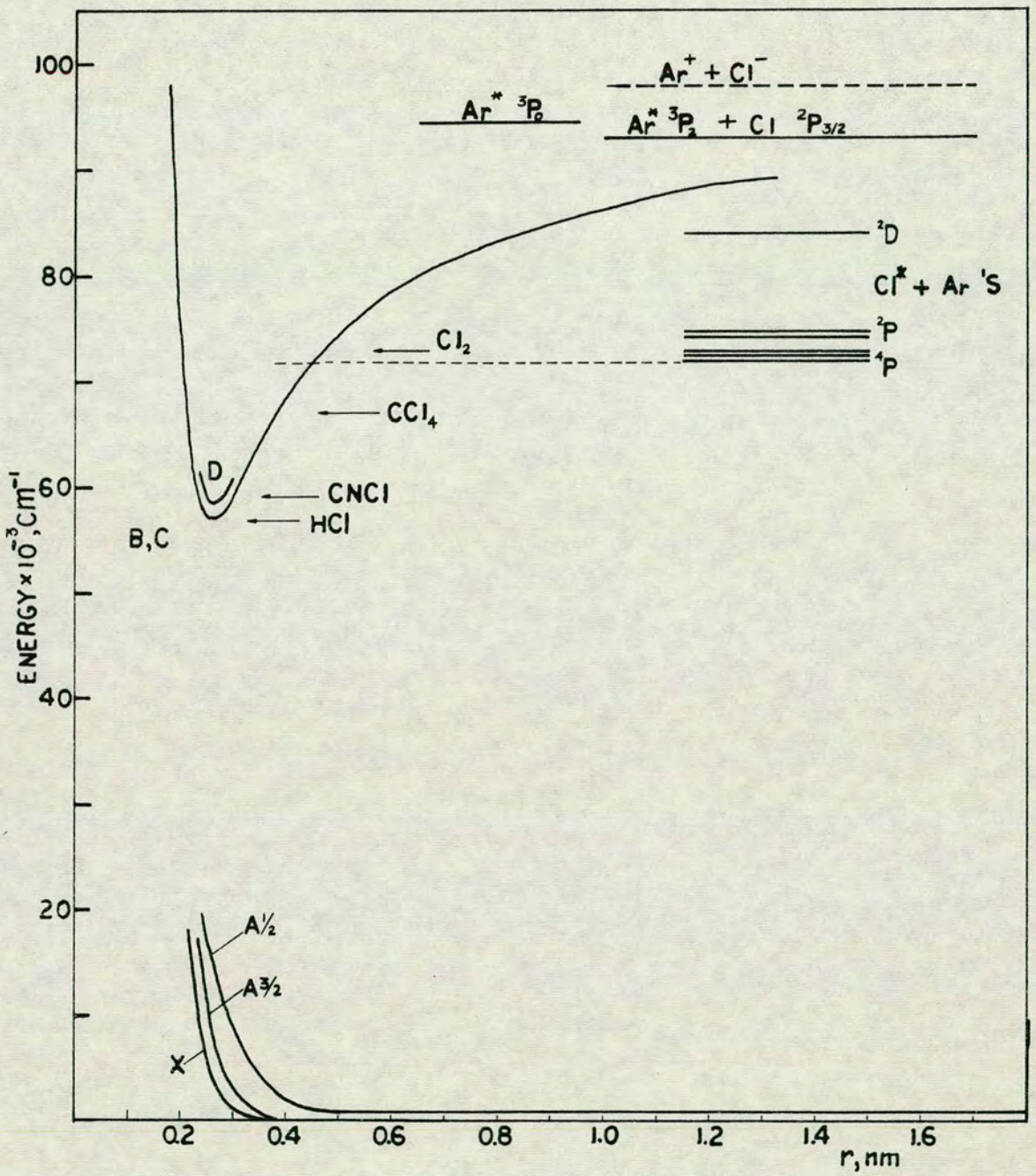

Fig. 3.25 Schematic potential curves for the ArCl - states correlating diabatically with $Ar(^1S) + Cl\ (^2P_{3/2,1/2})$ and $Ar^+(^2P_{3/2,1/2}) + Cl^-(^1S)$ and asymptotic energies for Rydberg states which correlate with $Cl^*(4s) + Ar(^1S)$. Threshold energies for the various chlorine containing reagents are indicated by arrows. $1 cm^{-1} = 11.963\ J\ mole^{-1}$.

Table 3.13

Bond strengths for the various chlorine containing compounds (R-Cl) and threshold energies (E_T) for $Ar^*(^3P_2)$+RCl.

RCl	Bond energies $x10^{-4}(cm^{-1})$	$E_T x10^{-4}$ (cm^{-1})	reference numbers for bond energies
DCl	3.618	5.696	99
HCl	3.606	5.708	89,98
CNCl	3.4	5.9	89,97
CCl_4	2.6	6.7	89,96
Cl_2	2.0308	7.2836	89,90
KCl	3.543		89,93

$1cm^{-1} = 11.963\ J\ mole^{-1}$.

states of chlorine which explains why chlorine atomic lines are only observed for that reaction. The chlorine atomic lines are shown in figure 3.26. Since the $3p^5 4s\ ^2P$-states are of higher energy than the threshold energy, the fact that an emission due to transitions from these states is observed suggests that these may also be populated by reactions of $Ar^*(^3P_0)$ with Cl_2.

The ArCl spectra differ in structure and total spectral range for the different reagents. ArCl MC spectra are shown in figures 3.27 and 3.28 for Cl_2+Ar^* and CCl_4+Ar^* respectively for different pressures. Also a MC spectrum for Cl_2+Ar^* is shown in chapter 2, figure 2.4, uncorrected for spectral response. The structure and the pressure dependence

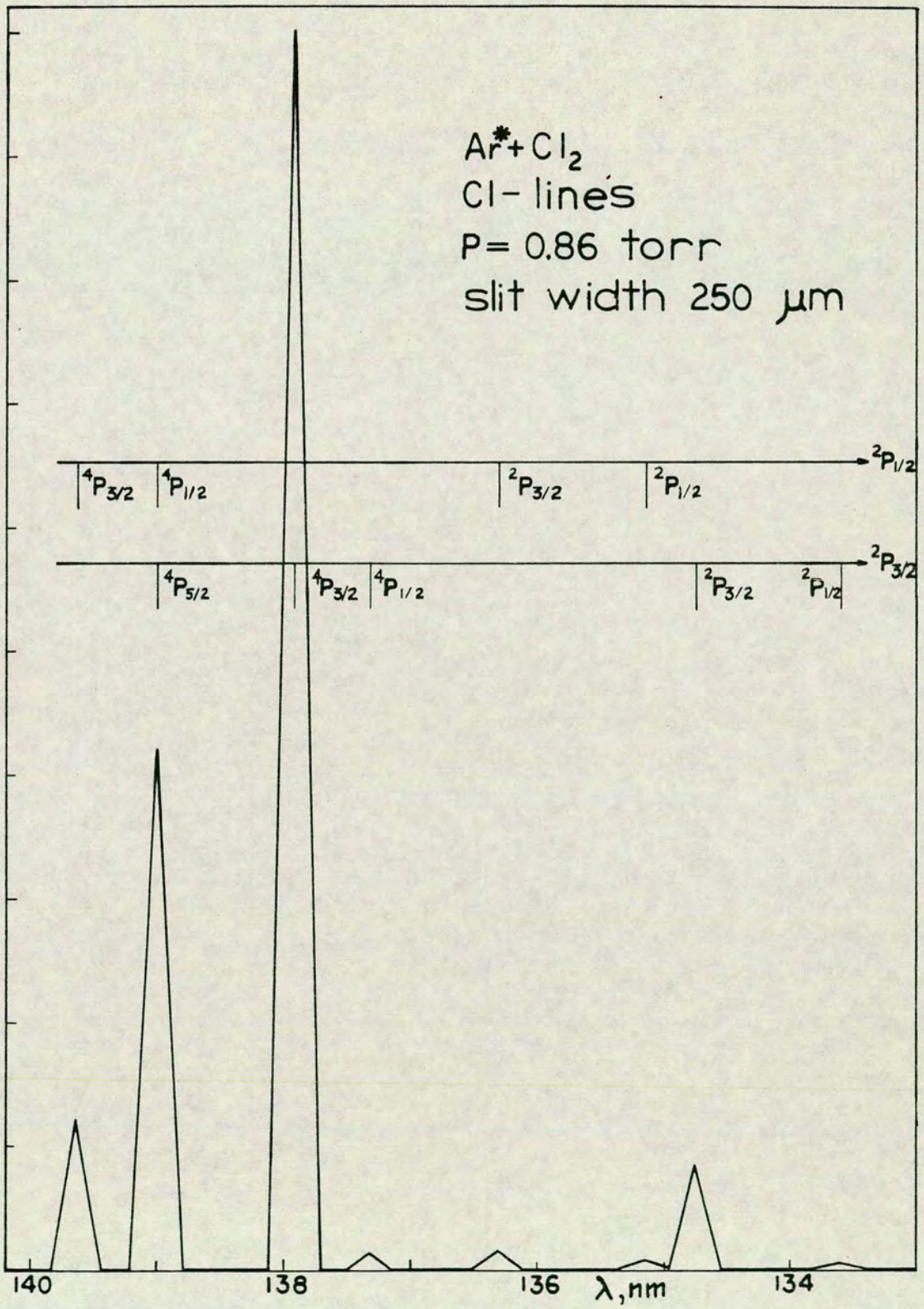

Fig. 3.26 Chlorine atomic lines generated by $Ar^* + Cl_2$. The chlorine lines are assigned to transitions from $Cl^*(4s)$ atoms as indicated. 1 torr = 133.322 Nm^{-2}.

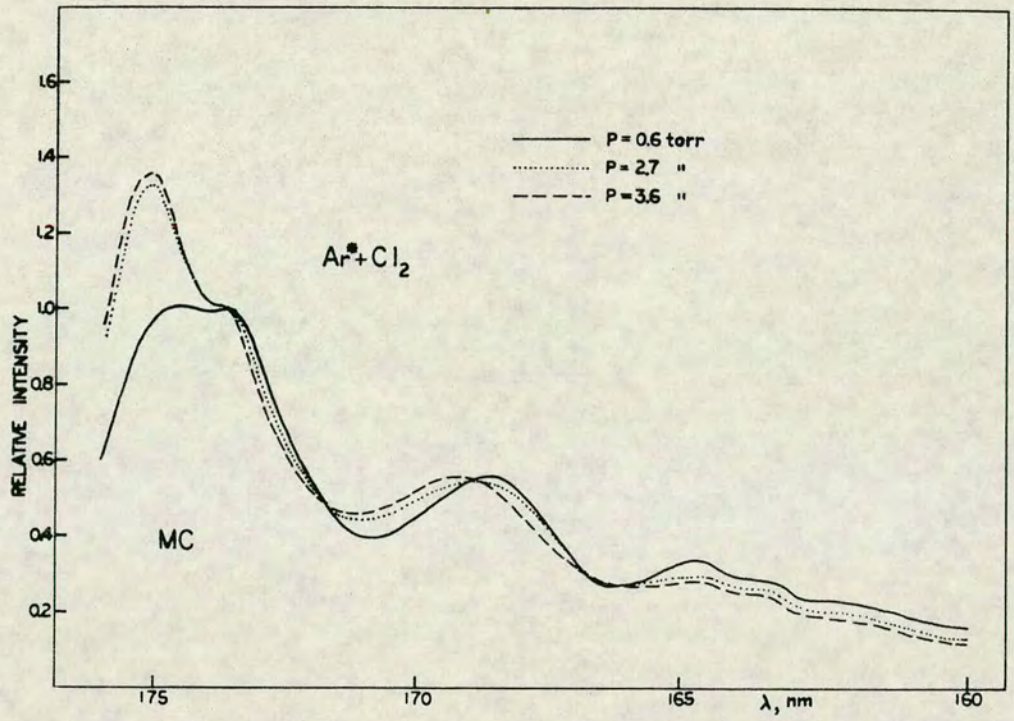

Fig. 3.27 ArCl, MC spectra generated by $Ar^* + Cl_2$ at three different total pressures, for 500 μm slit width. Relative intensities are normalized such that the relative intensity at 173.6 nm is 1.
1 torr = 133.322 Nm^{-2}.

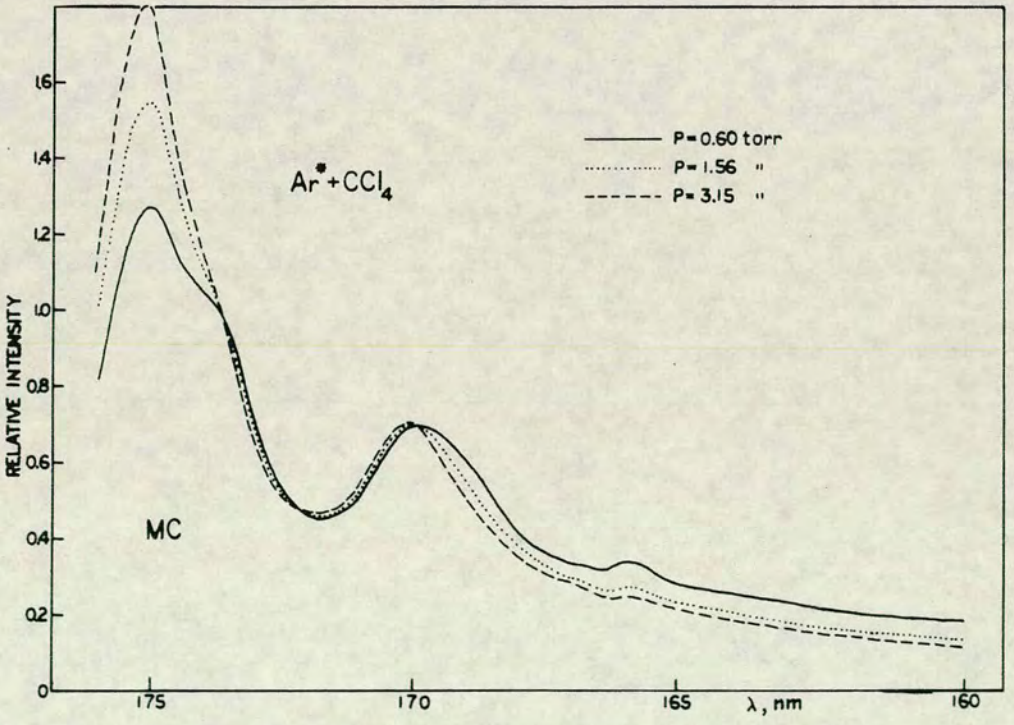

Fig. 3.28 ArCl, MC spectra generated by $Ar^* + CCl_4$ at three different total pressures for 500 μm slit width. Relative intensities are normalized such that the relative intensity at 173.6 nm is 1.
1 torr = 133.322 Nm^{-2}.

behaviour of these spectra agree with what others have found.[8,9,15]

The spectra for the reactions of CNCl, HCl and DCl all showed very weak ArCl spectra and of much narrower spectral range than for the other reactions. The ArCl spectrum for HCl+Ar* is shown in figure 3.29. It has also been identified by Setser et al.[15]

Judging from the difference in the bond strength of HCl, DCl and KCl (which is approximately the same as the bond strength of ArCl) the formation of ArCl by the reactions of HCl and DCl with $Ar^*(^3P_2)$ is endothermic by about 630 and 750 cm^{-1} (7540-8970 J $mole^{-1}$) respectively. This suggests that the ArCl* molecules are also formed by reactions of $Ar^*(^3P_0)$. These spectra correspond to transitions from the lowest v′ levels.

The position of the narrow ArCl peaks found in the spectra like the one for HCl+Ar* (figure 3.29) corresponds to the position where the greatest increase in the relative intensity is observed in the spectra for Cl_2+Ar* and CCl_4+Ar* (see figures 3.27 and 3.28). This suggests, therefore, that this characteristic increase in the relative intensity is due to an increase in the low v′ contributions relative to the high ones.

The oscillatory structure of the MC spectra for Cl_2+Ar* and CCl_4+Ar* has been interpreted in terms of

transitions from high vibrational levels of a strongly bound upper state of ArCl to a much flatter region of a lower state by use of a very simple model.[9] More detailed calculations which are presented in chapter 5 have been carried out in order to interpret the structure and the pressure dependence behaviour of the spectra. These calculations showed the lowest v´ levels also to contribute significantly to the spectra. The results of these calculations also suggest strongly that the MC can not be ascribed to one electronic transition only (B-X),but that a C-A(1/2) contribution is also of significant importance in that region.

The SC spectra were not studied in detail because the measured intensity in that region was very low due to the low sensitivity of the detection system. No indication of a D-X spectrum in the MC region was found.

3.22 HCl- and DCl spectra.

The HCl- and DCl- spectra observed from the reactions of Ar^* with HCl and DCl respectively were found in the region between 110 nm and 186 nm. Others have found the HCl spectrum to extend even further to long wavelength.[15] These spectra, showed banded structure in this region as shown in figure 3.29 for $HCl+Ar^*$ for 500 μm slit width. The hydrogen

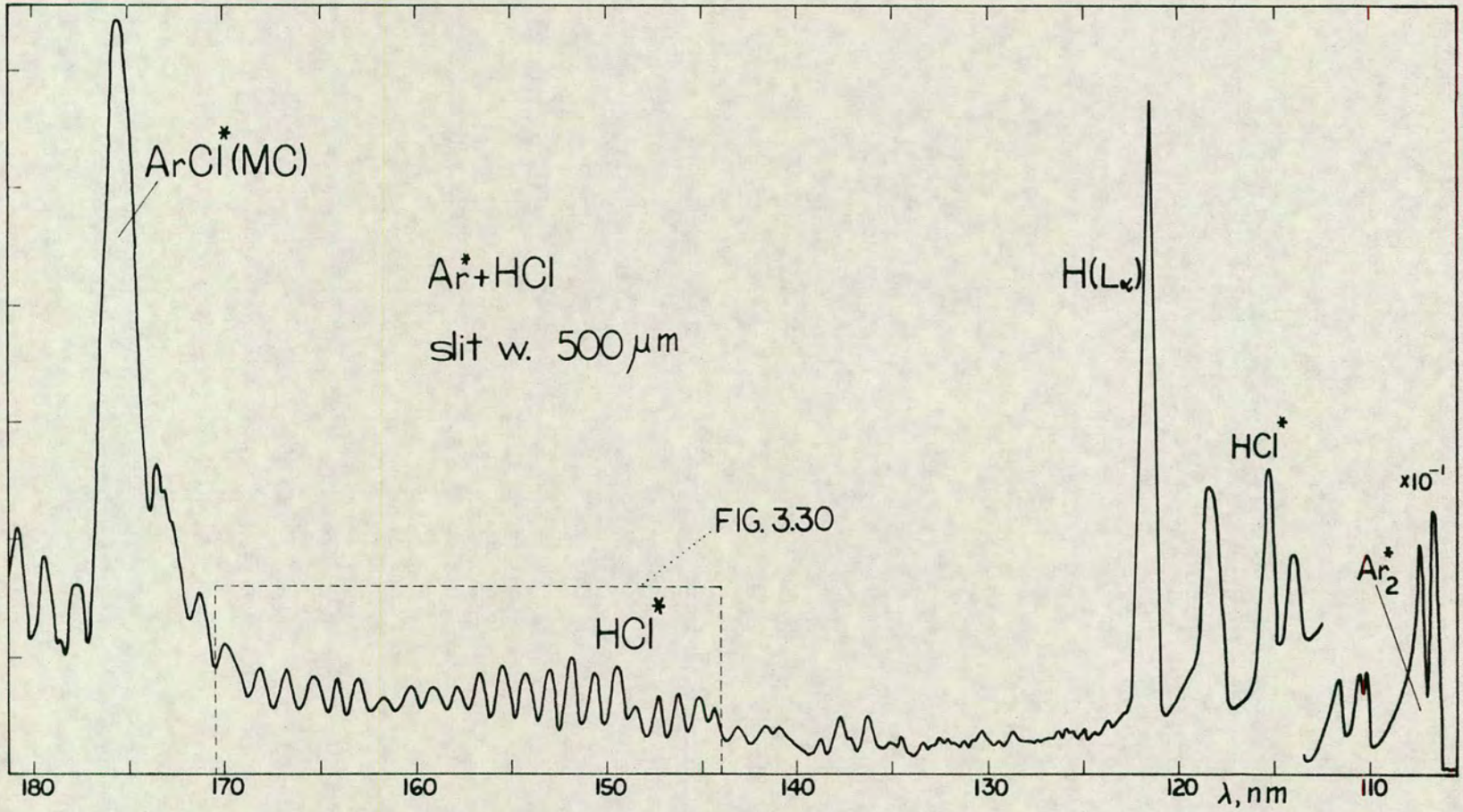

Fig. 3.29 Spectrum generated by Ar^* + HCl showing ArCl , MC (peaking at 175.6nm), HCl spectrum (110 - 180nm), the Lyman α atomic hydrogen line at 121.56nm and Ar_2^* spectrum, which extends from peaks at 106.6nm and 107.5nm to longer wavelength.

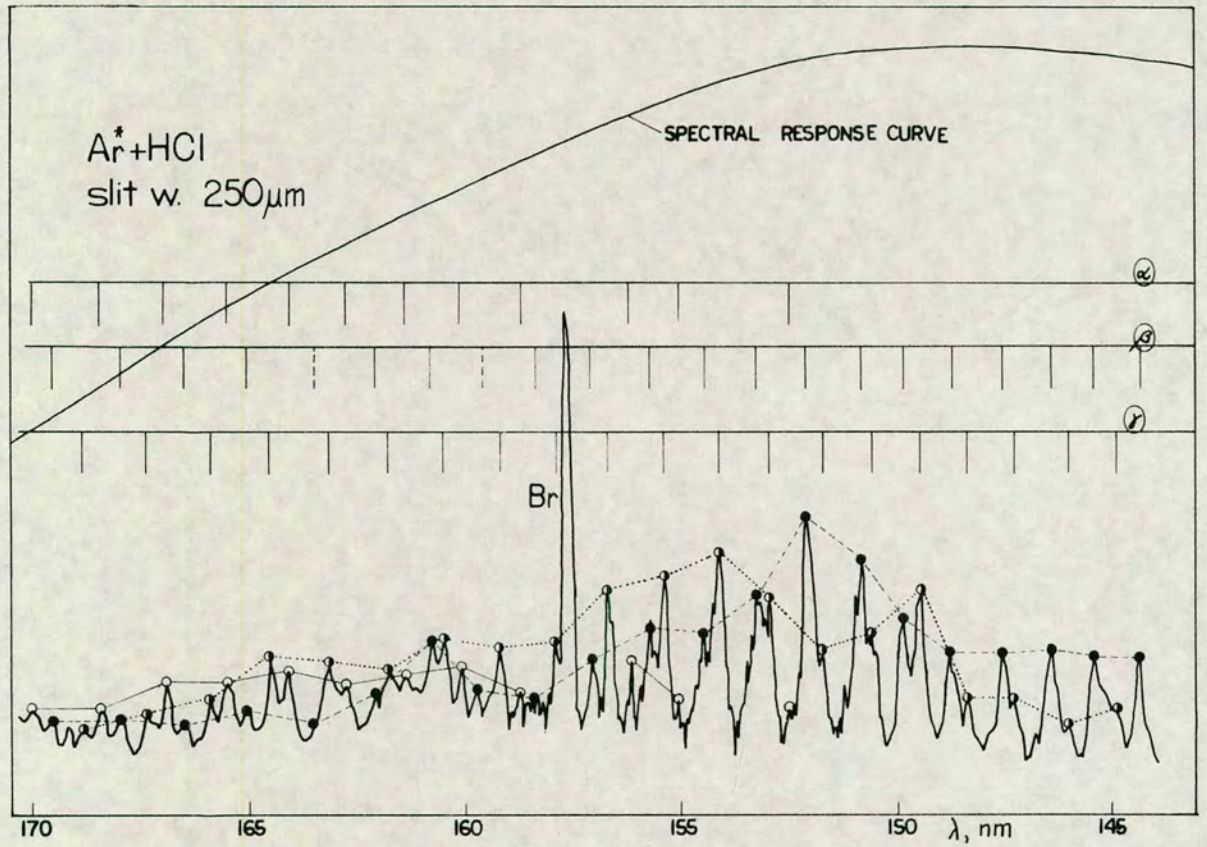

Fig. 3.30 HCl spectrum generated by Ar^* + HCl, showing three band progressions, α(o), β(●) and γ(◑). The bromine atomic line at 157.7nm is due to HBr impurities on the vacuum line. The spectrum has not been corrected for spectral response but the change in spectral response with wavelength is shown in the figure.

($L\alpha$) atomic line (121.56 nm) and the Ar_2 spectrum were also observed in these spectra.

The spacing between the bands in the region 145 - 170 nm was found to vary only slightly over the total range, as shown in table 3.14. An average value of 509 cm^{-1} (6090 J $mole^{-1}$) was found for this spacing for HCl and 358 cm^{-1} (4280 J $mole^{-1}$) for DCl. Higher resolution spectra obtained for $HCl+Ar^*$ for 250 μm slit width showed more structure in this region (see figure 3.30), and three band progressions, which I have chosen to call α, β and γ, were identified (see table 3.15). The spacing between the bands in each of these progressions was also found to vary only slightly over the total range. The average spacing between the bands in these progressions was found to be 518, 512 and 515 cm^{-1} (6200, 6130 and 6160 J $mole^{-1}$) for α, β and γ respectively.

The ratio of the average spacing between the bands for DCl and HCl (358/509 = 0.703) is close to that of a ratio of vibrational frequencies (ν) for two harmonic potentials with the same force constants (k), determined by the difference in the reduced masses (m) of DCl and HCl

$$\nu = (1/2\pi) \cdot (k/m)^{1/2} \qquad (3.29)$$

$$\nu_{DCl}/\nu_{HCl} = (m(HCl)/m(DCl))^{1/2} = 0.717 \qquad (3.30)$$

This suggests that the band structure is due to a

Table 3.14

Positions of bands (E(cm^{-1})) and spacing between bands (ΔE(cm^{-1})) observed in the HCl and DCl spectra for HCl+Ar^* and DCl+Ar^* respectively for 500 μm slit width.

HCl+Ar^*		DCl+Ar^*	
E	ΔE	E	ΔE
59810	523	63724	371
60333	480	64095	339
60813	510	64434	384
61323	493	64818	338
61816	512	65156	370
62328	473	65526	347
62801	520	65873	402
63321	504	66275	329
63825	510	66604	
64335	550		
64885	485		
65410	525		
65935	520		
66455			

$1 cm^{-1} = 11.963$ J $mole^{-1}$.

progression in states with vibrational frequencies of about 515 cm^{-1} ($1.55 \cdot 10^{13}$ s^{-1}) for HCl and 360 cm^{-1} ($1.08 \cdot 10^{13}$ s^{-1}) for DCl. Such progressions must occur in some upper states, while the lower potentials are the ground states, which have much higher vibrational frequencies (ω_e) (see table 3.16 for HCl).

Very limited information is available on excited states of HCl and DCl. Barrow[101] has observed

Table 3.15

Positions of bands (cm^{-1}) in the HCl spectrum for HCl+Ar* for the three progressions, α, β and γ obtained for 250 μm slit width.

α	β	γ
58806	58974	59214
59360	59524	59734
59882	60049	60263
60415	60569	60777
60931		61278
61425	61687	61797
61948	62193	62290
62441	62643	62806
62996	63135	63323
	63662	63828
63996	64222	64338
64514	64735	64889
	65253	65374
65576	65761	65900
	66295	66421
	66737	66912
	67245	67399
	67758	67893
	68304	68488
	68764	69004
	69264	

$1 cm^{-1} = 11.963$ J $mole^{-1}$

a vacuum UV emission spectrum from HCl, excited in a discharge, and assigned bands observed in this region to the transition $V^1\Sigma^+ \rightarrow X^1\Sigma^+$ where $V^1\Sigma^+$ is an ionic state with a vibrational frequency, ω_e, of 880 cm^{-1} ($2.64 \cdot 10^{13}$ s^{-1}). Several excited states

Table 3.16

Spectroscopic constants for various electronic states for HCl obtained from references 99, 101, and 102.

	$X^1\Sigma^+$	$B^1\Pi$	$C^1\Pi$	$V^1\Sigma^+$
$T_e(cm^{-1})$	0	75133	77540	77250
$\omega_e(cm^{-1})$	2990.9463	2993	2873	880
$r_e(nm)$	0.12745			0.243
$D_o^o(cm^{-1})$	35740			38370

$1cm^{-1} = 11.963\ J\ mole^{-1}$.

have been identified from absorption spectra[104,105,102] in gas phase and matrices at low temperature,[103] the best characterized ones being the $B^1\Pi$ and $C^1\Pi$ states (table 3.16) which, however, have much greater vibrational frequencies (ω_e).

The small change in the spacing between the bands in the spectra for $HCl+Ar^*$ and $DCl+Ar^*$ over a wide range could not be explained as being due to a progression in any of these states. To be able to to characterize the emitting states,a rotational analysis of the spectra would have to be made,which was not possible for the spectra obtained in our apparatus.

3.3 RI+Ar*

Spectra from reactions of the iodine containing reagents, CF_3I and C_3F_7I, with Ar^* were recorded. Only iodine atomic lines were observed in the vacuum-UV region (see figure 3.31). No ArI spectrum was observed. Estimated position of ArI MC peak obtained by using the ground state potential for KI, adjusted to the asymptotic limit for $Ar^+ + I^-$ (see figure 3.32) is about 152 nm. The fact that no ArI emission is observed must be due to a complete predissociation of levels in the ArI^* states, by relatively low lying molecular states, which correlate with $I^* + Ar(^1S)$. The asymptotic energies of the lowest of these Rydberg states are shown in figure 3.32 to lie below the minimum of the ArI^* states.

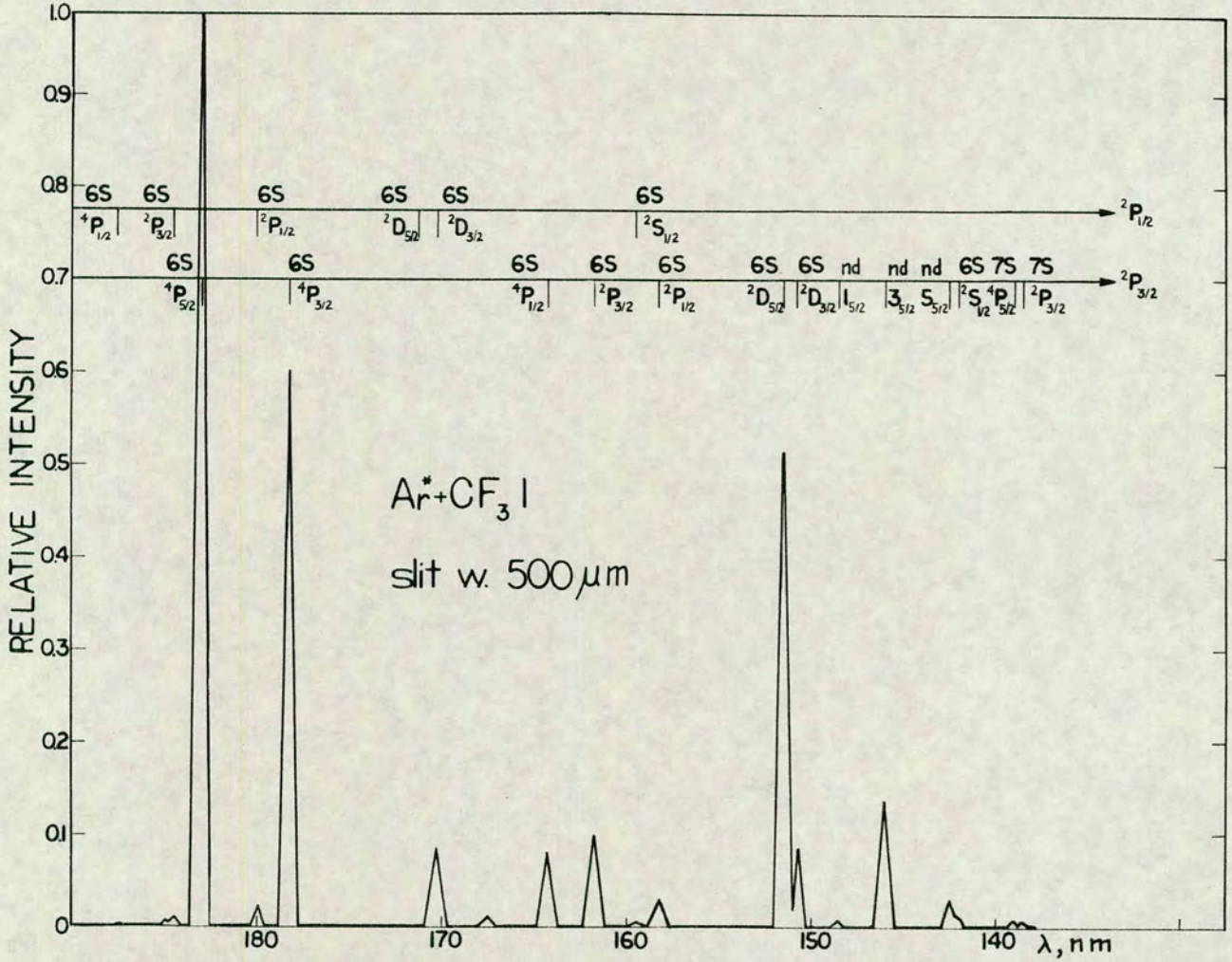

Fig. 3.31 Spectrum for $Ar^{*}+CF_3I$ showing iodine atomic lines. The various iodine atomic transitions are indicated.

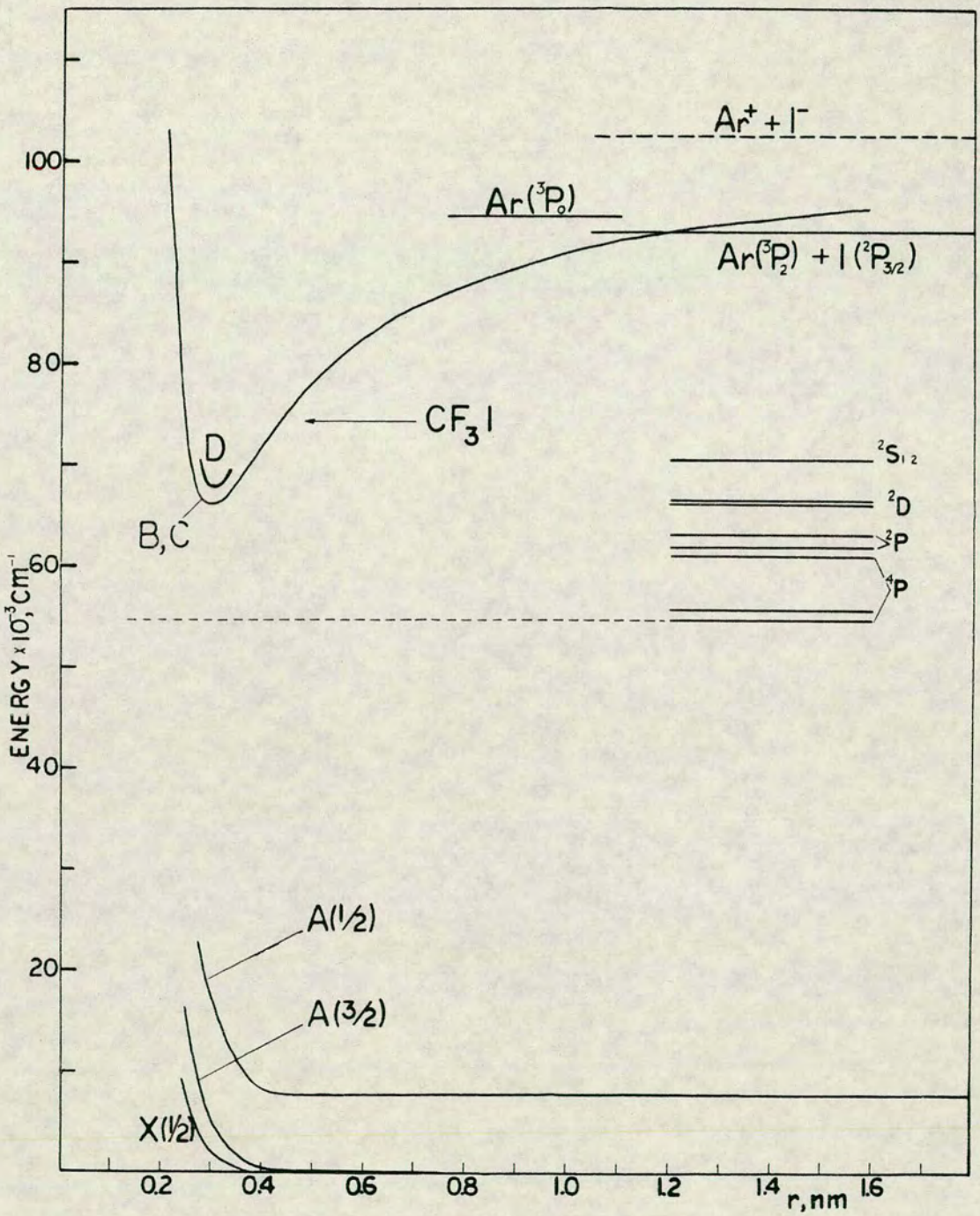

Fig. 3.32 Schematic potential curves for the ArI- states correlating diabatically with $Ar(^1S)+I\ (^2P_{3/2,1/2})$ and $Ar^+(^2P_{3/2,1/2})+I^-(^1S)$, and asymptotic energies for Rydberg states which correlate with $I^*(6s)+Ar(^1S)$. The threshold energy for CF_3I is indicated by an arrow. $1cm^{-1} = 11.963\ J\ mole^{-1}$.

4. THEORY OF CALCULATIONS.

The method used in the simulation calculations for the ArBr- and the ArCl- spectra (chapter 5) will be discussed in this chapter.

4.1 Basic theory.

The intensity of a spectral line in emission is proportional to the Einstein coefficient, A_{nm} [106] A_{nm} was first invented by Einstein in 1916 [109,110] as a measure on a transition probability of a spontaneous emission due to a transition between two states, n and m. By applying the perturbation theory [111] to the interaction of a molecule with the electric field associated with an electromagnetic wave, the probability coefficient can be expressed as

$$A_{nm} = C \cdot \nu_{nm}^3 \left(\int \Psi_n^{\circ} \, \bar{M} \, \Psi_m^{\circ} \, d\tau \right)^2 \qquad (4.1)$$

where C is a constant

$$C = 64\pi^4/3hc^3 \qquad (4.2)$$

ν_{nm} is the frequency of the electromagnetic wave,

Ψ_n^0 and Ψ_m^0 are the wavefunctions for the two states and $\bar{M}$ is the dipole moment vector

$$\bar{M} = \sum_i q_i \bar{r}_i \qquad (4.3)$$

where $\bar{r}_i$ is the co-ordinate of the charge q_i.

The greatest difficulty in calculating A_{nm} is to evaluate the wavefunctions. Those are solutions of the time - independent wave equation, which can not be solved analytically except for the simplest forms of the Hamiltonian . The wave equation has the form

$$H^0 \Psi^0 = E \Psi^0 \qquad (4.4)$$

where H^0 is the Hamiltonian operator and E is the total energy. The Born - Oppenheimer approximation[112] is normally applied in order to calculate the integral in equation 4.1. The wavefunctions are expressed as products of electronic-(Ψ_e) and nuclear- wavefunctions (Ψ_n)

$$\Psi^0 = \Psi_e \cdot \Psi_n \qquad (4.5)$$

and substituted in that form into the wave equation. The resulting expression can then be simplified greatly and Ψ_n becomes a solution of the radial wave equation

$$\left[\frac{d^2}{dr^2} + \frac{p^2(r)}{\hbar^2}\right] \Psi(r) = 0 \qquad (4.6)$$

where

$$p(r) = (2m \cdot (E - U_{eff}))^{1/2} \qquad (4.7)$$

m is the reduced mass. U_{eff} equals the sum of the electronic potential energy (U(r)) and the rotational energy

$$U_{eff} = U(r) + J(J+1) \cdot \hbar^2/2m \cdot r^2 \qquad (4.8)$$

By neglecting the rotational energy the wavefunction solution of equation 4.6 equals the vibrational wavefunction Ψ_v, for a linear anharmonic oscillator.

By substituting the wavefunctions as

$$\Psi^0 = \Psi_e \cdot \Psi_v \qquad (4.9)$$

and the dipole moment as a sum of two terms including the positive and the negative charges respectively

$$\bar{M} = \bar{M}_e + \bar{M}_n \qquad (4.10)$$

into equation 4.1 A_{nm} becomes[106,111]

$$A_{nm} = C \cdot \nu_{nm}^3 \left(\int \Psi_v' \cdot \mu \, \Psi_v'' \, dr\right)^2 \qquad (4.11)$$

where

$$\mu = \int \Psi_e' \cdot \bar{M}_e \cdot \Psi_e'' \, d\tau_e \qquad (4.12)$$

is the transition moment. Ψ' and Ψ'' are wavefunctions for the two states n and m respectively.

The vibrational wavefunctions in equation 4.11 can be derived analytically for the simplest analytical forms of potential curves only. Solutions can be

derived for bound potentials like harmonic oscillators[116,111,106] and Morse potentials[115] for instance. Analytical solutions are obtainable for repulsive potentials of the form $a/(r-b)^2$ where a and b are constants.[113] To solve the radial wave equation for more complicated analytical expressions for potentials or for RKR potentials several methods have been developed. The most widely used methods are the numerical methods.[118-121] Those, however, require much computer time and are very expensive.[21] The WKB method is a semiclassical method which allows the vibrational wavefunctions to be evaluated for any analytical forms of potentials in a relatively simple way.

The WKB method was first invented in 1926 by Wentzel, Kramers and Brillouin[122-124] and is named after them. Their method, however, has the disadvantage of being very inaccurate in the regions of the classical turning points where the WKB wavefunctions become infinite. Several attempts have been made to modify the wavefunctions and make them continuous in the regions of the turning points.[125,126] The uniformized (uniform) WKB solutions, first presented by Miller and Good,[127] satisfy this and have been shown by comparison with numerical solutions to be very accurate.[128]

4.2 Vibrational wavefunctions.

The two different WKB methods, the normal- (n-) WKB and the uniform- (u-) WKB methods, were used to derive vibrational wavefunctions for upper and lower potentials in the simulation calculations for the ArBr- and the ArCl- spectra. FORTRAN computer programs, such as the one shown in appendix 2 were made to calculate spectra and these include calculations of the vibrational wavefunctions.

4.21 Normal - (n-) WKB wavefunctions.

The method of evaluating n - WKB wavefunctions is described at various places in the literature.[129-132] The method is based on expressing the wavefunction as an exponential function

$$\Psi_v = \exp(\tfrac{i}{\hbar} S(r)) \qquad (4.13)$$

and substituting it in that form into the radial wave equation (4.6). S is some function of internuclear distance. The basis of the approximation is that of expanding S(r) in powers of $\hbar$:

$$S = S_0 + \tfrac{\hbar}{i} S_1 + (\tfrac{\hbar}{i})^2 S_2 + \cdots \qquad (4.14)$$

and neglecting terms of order equal to or greater than $\hbar^2$.

The following general expression for vibrational wavefunctions is obtained from this procedure

$$\Psi_v = c_1 p^{-1/2} \exp(+(\tfrac{i}{\hbar}) \int p dr) + c_2 p^{-1/2} \exp(-(\tfrac{i}{\hbar}) \int p dr) \quad (4.15)$$

where

$$p = (2m(E-U(r)))^{1/2} \quad (4.16)$$

and c_1 and c_2 are constants.

If U(r) is a potential well (two turning points r_1 and r_2) the semiclassical eigenvalues (E) are quantized and can be determined approximately by the Bohr - Sommerfeld quantum condition[128,147]

$$\hbar^{-1} \int_{r_1}^{r_2} p(r')dr' = (v + 1/2)\pi \quad (4.17)$$

where v is the vibrational quantum number.

In the case that p is an imaginary quantity, which is the case in the nonclassical region (E-U < 0), the wavefunction becomes a sum of real exponential terms. One of these terms has the asymptotic limit zero, while the other one increases indefinitely. In order to satisfy the necessary requirement that the wavefunction decreases with increasing distance from the classical turning point, the constant c_2 in the increasing exponential term has to be equal to zero. Thus the wavefunction in the nonclassical region is

$$\Psi_v^{E<U} = c_1 p^{-1/2} \exp(+(\tfrac{i}{\hbar}) \int p dr) \quad (4.18)$$

In the classical region real terms will have to be selected from imaginary terms after having

expressed the exponential terms as sums of trigonometric functions, which gives

$$\psi_v^{E>U} = \frac{c_3}{\sqrt{p}} \sin\left(\frac{1}{\hbar}\int_{r_1}^{r} p\,dr' + \frac{\pi}{4}\right) \qquad (4.19)$$

where c_3 is a constant. The terms in the sine expression can be expressed as $2\cdot\pi\cdot\varphi(r)$ where $\varphi(r)$ is the phase integral

$$\varphi(r) = \int_{r_1}^{r} \lambda(r')^{-1} dr' + \varphi(r_1) \qquad (4.20)$$

and $\lambda(r)$ is the wavelength of the wavefunction at any point

$$\lambda(r) = h/p \qquad (4.21)$$

which is the de Broglie expression.

At turning points (E-U = 0) the amplitude factor $p^{-1/2}$ in equations 4.18 and 4.19 becomes infinite. Various methods have been used to connect the wavefunctions in the classical and the nonclassical regions to obtain continuous functions across the turning points.[122,123]

4.22 Uniform - (u-) WKB wavefunctions.

The method of evaluating u - WKB wavefunctions for anharmonic oscillators has been described in the literature by a number of authors.[128,127] This

method will be described in this section. A similar method was developed for evaluating wavefunctions for repulsive potentials and will also be described here.

In the u - WKB method the wavefunction is written as

$$\Psi_v = T(r) \cdot \phi(S(r)) \tag{4.22}$$

S(r) is expanded in the same way as in the n - WKB method (eq. 4.14). $\phi(S)$ is chosen to be a solution of an equation related to the radial wave equation 4.6 by replacing r by S(r) and p(r) by a function P(S)

$$\left[\frac{d^2}{dS^2} + \frac{P^2(S)}{\hbar^2}\right] \phi(S) = 0 \tag{4.23}$$

Substitution of the product $T \cdot \phi$ into the wave equation leads to a relatively simple differential equation in S

$$\hbar^2 T''/T - S'^2 P^2 + p^2 = 0 \tag{4.24}$$

if

$$T(r) = S'^{-1/2} \tag{4.25}$$

By neglecting terms of order equal to or greater than $\hbar^2$, as is done in the n - WKB method, one obtains

$$dS_o P = dr\, p \tag{4.26}$$

and

$$\int_{S_1}^{S} P dS' = \int_{r_1}^{r} p(r')dr' \qquad (4.27)$$

From equation 4.27, S can be evaluated as a function of r. By choosing r_1 a classical turning point ($p(r_1) = 0$) S_1 has to satisfy $p(S_1) = 0$.

The procedure for calculating the value of a wavefunction at a particular internuclear distance (r) for a particular total energy and potential energy is the following. a. First a suitable P - function is chosen. P is chosen of some simple form such that equation 4.23 can be solved analytically. P is chosen as a continuous differentiable function with the same number of zero points as the p - function. b. S(r) is evaluated from equation 4.27. c. $\phi(S)$, derived from equation 4.23, is evaluated at r. d. T(r) is calculated from equation 4.25. e. $\Psi_v(r) = T(r) \cdot \phi(S(r))$ is calculated and a normalized value is obtained by multiplication by a normalization factor N_v where

$$N_v = 1/(\int \psi_v^2 dr)^{1/2} \qquad (4.28)$$

To obtain vibrational wavefunctions for anharmonic oscillators, equation 4.23 can be chosen on the form analogous to the radial wave equation for harmonic oscillators. Thus the P - function can be chosen as

$$P = (2m(C^2 - S^2))^{1/2} \qquad (4.29)$$

where C is a constant. The corresponding wave equation can be solved[116,106] and $\phi(S)$ derived for a particular quantum number v as

$$\phi_v(S) = \exp(-1/2\ \lambda\ S^2) H_v(\sqrt{\lambda} \cdot S) \qquad (4.30)$$

where $\lambda^2 = 2m/\hbar^2$. H_v is a Hermite polynomial of order v. P is a continuous and differentiable function on the entire real axis with two zero points for any nonzero value of C. A special care has to be taken in chosing C properly and thus to specify the P - function. For a particular vibrational level, C has to be chosen such that the integrals in equation 4.27 over the interval between the zero points equal one another. Solving the integral on the left hand side of equation 4.27 gives

$$C^2 = ((\frac{2}{m})^{1/2} / \pi) \int_{r_1}^{r_2} P(r')dr' \qquad (4.31)$$

where r_1 and r_2 are the zero points for p(r). The zero points for P, S_1 and S_2, are found to be -C and +C respectively.

Relating the S- and the r- scales is now readily achieved. The integral on the right hand side of equation 4.27 can be solved numerically. In the simulation calculations it was solved by a Gaussian quadrature[134] while the integral on the left hand side

was solved analytically.[89] S(r) was then evaluated numerically as a zero point (root) of a function by the binomial bisection method.[133] (see appendix 2).

$\phi(S)$ is obtained by substituting the S - value directly into equation 4.30. The Hermite polynomial was calculated by a recurrence relation.[133,134]

T(r) expressed by equation 4.25 is found directly from equation 4.26 to be

$$T(r) = (p(r)/P(S))^{-1/2} \qquad (4.32)$$

Finally $\Psi_v = T \cdot \phi$ is multiplied by the normalization factor N_v (eq. 4.28).

The eigenvalues can be determined by equation 4.17.

To obtain wavefunctions for repulsive potentials, similar calculations are carried out.

A wave equation for

$$P = (2m(C_1 - C_2/S^2))^{1/2} \qquad (4.33)$$

can be solved analytically for suitable choices of values for the constants C_1 and C_2. P has one zero point for any positive value of C_1 and is continuous and differentiable on the real positive axis. By chosing

$$C_2 = (n^2 - 1/4)\hbar^2/2m \qquad (4.34)$$

where n is a positive integer, equation 4.23 can be

solved to yield[113]

$$\phi(S)=\left[\frac{\pi \kappa C_1^{1/2}}{R}\right]^{1/2} S^{1/2}\, J_n(\kappa C_1^{1/2} S) \qquad (4.35)$$

where

$$\kappa = (2m)^{1/2}/\hbar \qquad (4.36)$$

R is a constant and J_n is a Bessel function of order n. By using a first order Bessel function, C_2 is determined from equation 4.34 for n = 1 and C_1 can be chosen to be any positive number. C_1 was chosen to be equal to one. The zero point for P was then found to be

$$S_1 = (C_2)^{1/2} \qquad (4.37)$$

The procedure for evaluating S(r), $\phi(S)$ and T(r) to obtain Ψ_v is then analogous to that described for a bound state.

The eigenvalues for nonbound potentials are nonquantized. The wavefunctions are normalized if the amplitudes at long internuclear distance ($r\to\infty$) are proportional to $1/(E)^{1/4}$. The factor $1/(E)^{1/4}$ results from taking account of density of states as described by Wiesenfeld et al.[114] The wavefunctions $\Psi_v = T\cdot\phi$ calculated by the procedure, which has just been described, were found to obey this requirement. Any wavefunctions $\Psi_E = c\cdot\Psi_v$ where c is a positive constant independent of E are therefore normalized wavefunctions.

4.23 Calculated wavefunctions.

Figures 4.1, 4.2 and 4.3 show some calculated WKB wavefunctions for bound and repulsive potentials.

The wavefunction shown at the top of figure 4.1 is a normalized vibrational wavefunction for $v' = 7$ for the bound state U'_{b2} (see table 5.1), calculated according to the u - WKB method. The various contributions to the wavefunction, the Hermite polynomial, the exponential function and $S'^{-1/2}$, whose product gives the nonnormalized wavefunction (Ψ_v) (see eqs. 4.22, 4.25 and 4.30) are also shown in figure 4.1. The normalization factor is $N_7 = 7.35\ 10^{-3}$. These functions are plotted vs internuclear distance, r and S(r). While the r - scale is undistorted in figure 4.1 the S(r) - scale is slightly distorted - spacing between integer values of S increases with increasing S. Thus the wavefunction, the exponential term and H_v differ from that for a simple harmonic oscillator in being nonsymmetric (these are symmetric for undistorted S(r) - scale). The $S'^{-1/2}$ function increases slightly with internuclear distance. This factor causes the amplitude to increase slightly with internuclear distance relative to that for a harmonic oscillator.

Small spikes were observed at the classical outer turning points, r_2, for $(S')^{-1/2}$ (see figure 4.1). These are due to inaccurate evaluations of

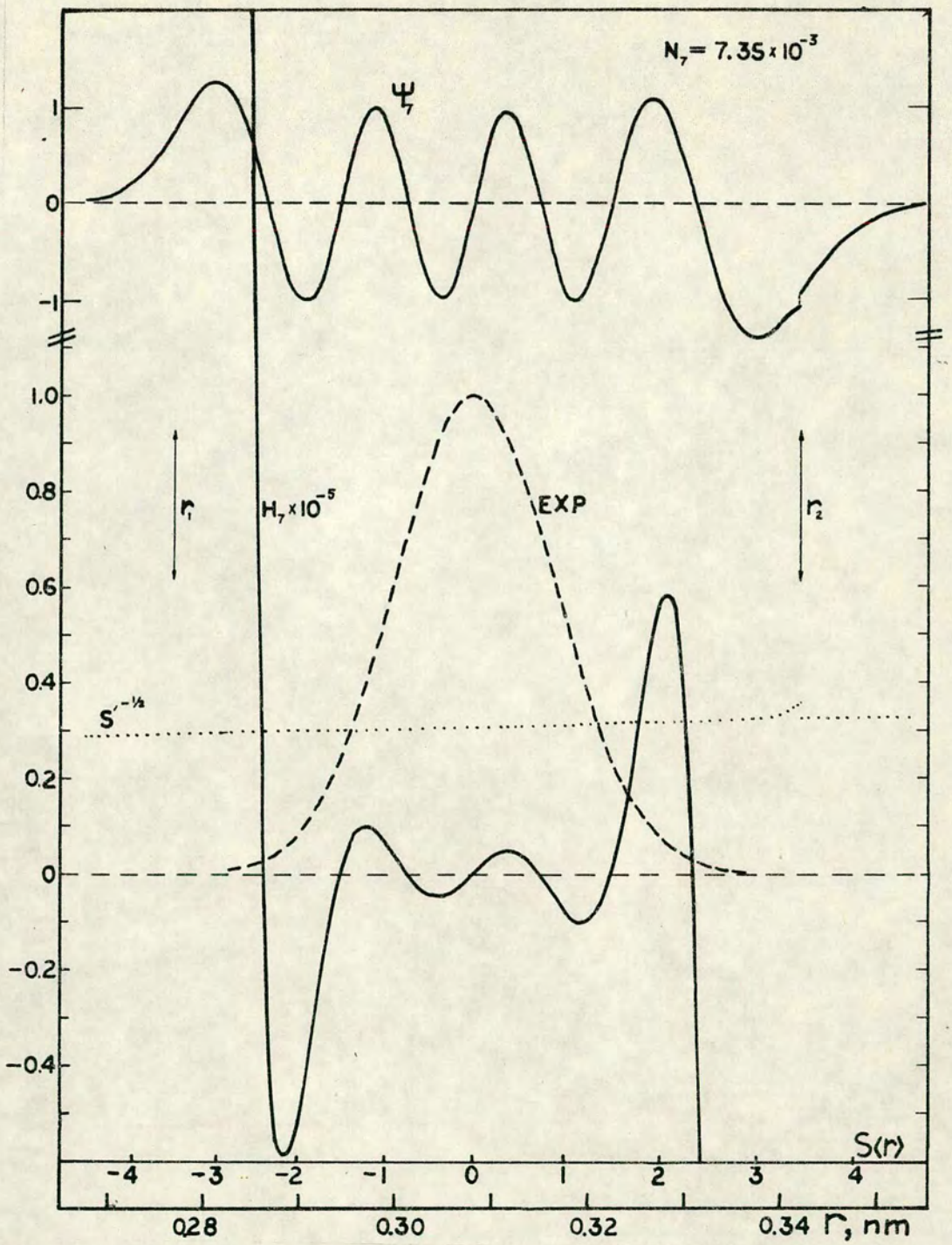

Fig. 4.1 Vibrational wavefunction (Ψ_7, top of figure) for $v' = 7$ and the bound potential U_{b2}' calculated by the uniform WKB method:

$$\Psi_7 = S'(r)^{1/2} \; N_7 \exp(-1/2 \; \lambda \; S^2(r)) \; H_7(\sqrt{\lambda}\, S(r))$$

The various components of the expression for Ψ_7 are also shown. The classical turning points (r_1 and r_2) are indicated. Both r-and S(r) - scales are shown..

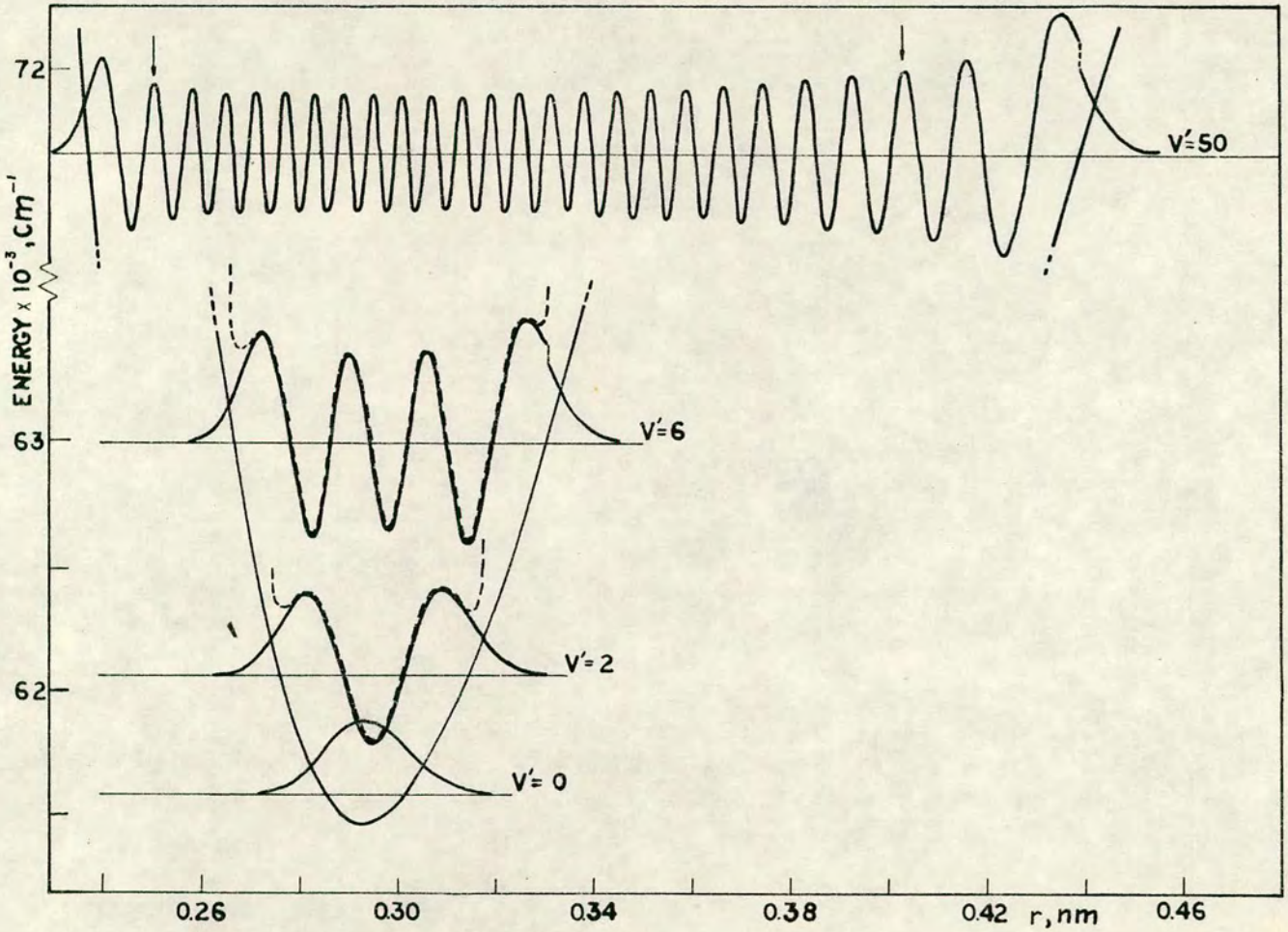

Fig.4.2 Vibrational wavefunctions for $v' = 0,2,6$ and 50 for the bound potential U'_{gl} calculated by the normal WKB method (dashed curves) and the uniform WKB method (solid curves). $1 cm^{-1} = 11.963$ J mole^{-1}.

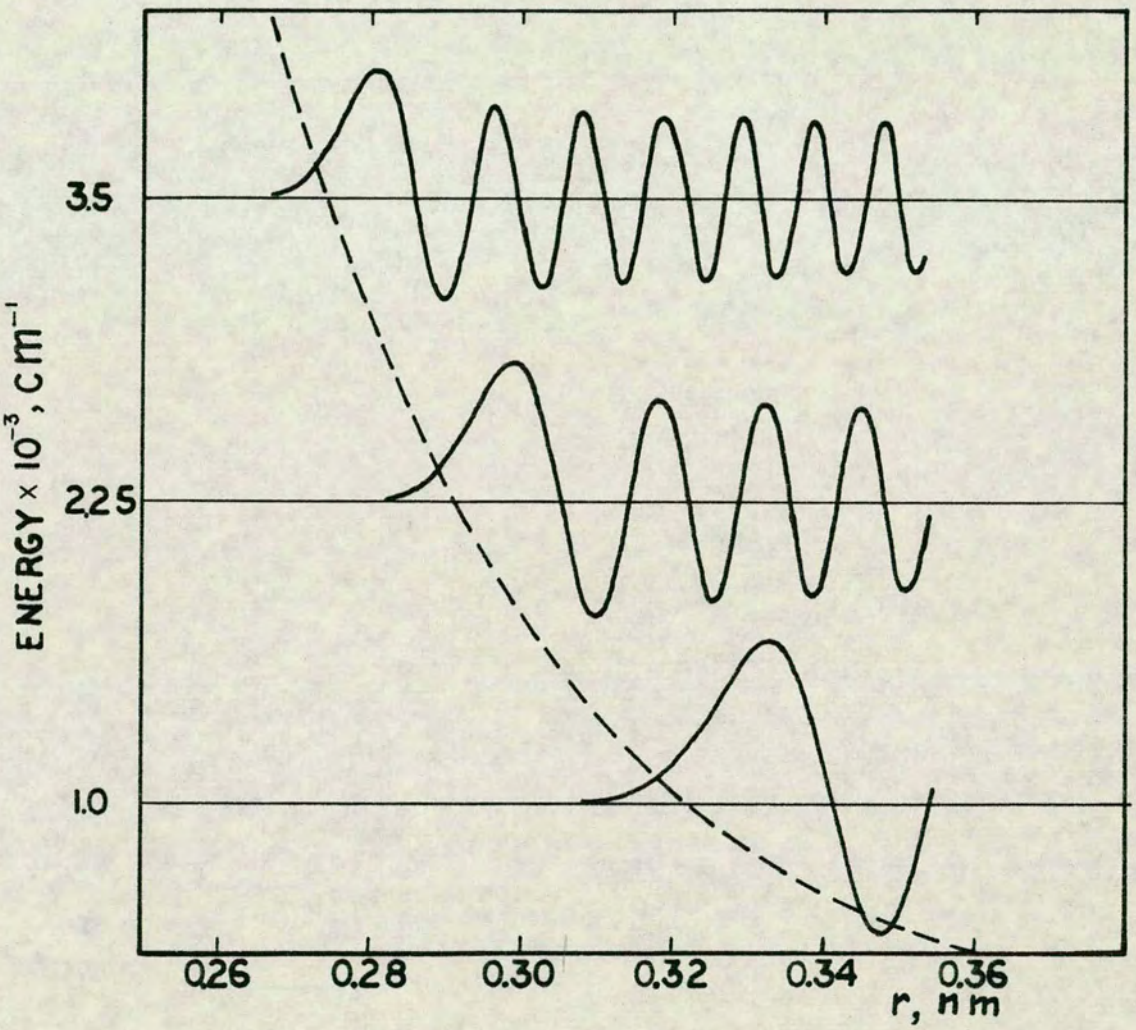

Fig. 4.3 Vibrational wavefunctions for three energy levels, 1000, 2250 and 3500 cm^{-1} above the asymptotic energy for the unbound potential U''_{b7}. $1cm^{-1} = 11.963$ J $mole^{-1}$.

the integral $\int_{r_1}^{r} p(r')dr$ for r slightly less than or equal to r_2 by applying the fourth order Gaussian quadrature. This method only makes possible evaluations of approximate values of S. S enters the expression for S′

$$S' = (E-U)^{1/2}/(C^2 - S^2)^{1/2} \qquad (4.38)$$

Therefore, evaluations of $S'^{-1/2}$ can also be inaccurate, especially near turning points where both the denominators and the nominators are close to zero. The evaluations of S become less accurate as the intervals over which the integrals are evaluated become bigger. Thus only very small spikes were observed near r_1 (not shown in figures). A way of decreasing the spikes near r_2 would be to evaluate S always from the closest turning points and thus to evaluate $\int_{r}^{r_2} p(r')dr'$ near r_2. This was done for the evaluation of S(r) for $r > r_2$ where no such spikes were observed. These spikes were found to be negligible for wavefunctions for the lowest vibrational levels but to increase with increasing vibrational quantum number (see figure 4.2).

The wavefunctions drawn as solid curves in figure 4.2 were obtained for the potential U'_{cl} (table 5.14) for various vibrational levels (v′) by use of the u - WKB method. The dashed curves for v′ = 2 and 6 are wavefunctions calculated by the

n - WKB method in the classical region (eq. 4.19). In general, wavefunctions calculated by the two different WKB methods were found to fit closely except in the closest region of the turning points where the n - WKB wavefunctions increase indefinitely

While the computing of the u - WKB wavefunctions requires much more computer time than the computing of the n- WKB wavefunctions the two different methods were combined in calculations of wavefunctions for high vibrational levels (> 7) to save computer time. n - WKB wavefunctions were used in the classical region between the third peak of the wavefunctions from r_1 and the fifth peak from r_2 (see arrows in figure 4.2 for $v'=50$). u - WKB wavefunctions were used in the closest region of the turning points and for lowest vibrational levels ($v'=0-7$). Instead of evaluating the eigenvalues for each vibrational level from equation 4.17 these were only evaluated for few levels and an expansion formula of the form

$$G'(v') = \sum_i a_i (v'+1/2)^i \qquad (4.39)$$

were constructed. These represent the energies of the vibrational levels above the potential minima ($G'(v')$). a_i are constants.

Some u - WKB wavefunctions for the repulsive potential U''_{b7} (see table 5.3) for several energy

levels are shown in figure 4.3. These are normalized. The amplitudes of these wavefunctions decrease and approach some asymptotic values for increasing internuclear distance. The asymptotic values change as $1/(E'')^{1/4}$ where E'' represents the energy of the levels above the zero asymptotic energy for the potential U''_{b7}. Figure 4.3 shows clearly how the wavelength increases for a fixed internuclear distance and decreasing E'' in agreement with de Broglie equation (4.21), which states that the wavelength increases with decreasing kinetic energy (or momentum).

4.3 Franck - Condon (FC) factors.

To calculate an emission spectrum the transition probabilities for the various radiative transitions involved have to be evaluated and the population distribution in the emitting state will have to be accounted for. The structure of a spectrum is largely determined by the variations in the transition probabilities due to the variations in the overlap integrals (eq. 4.11) basically due to the rapid oscillations of the wavefunctions. This effect can be considered by evaluating FC factors as functions of frequency for particular transitions. The FC factor is the square of the overlap integral for $\mu(r) = \text{constant}$. For bound - free transitions it can be written as

$$\text{FC - factor} = \left(\int \Psi'_v \cdot \Psi''_{E''} dr \right)^2 \qquad (4.40)$$

Figure 4.4 (left) shows the variation in FC factors calculated for transitions from $v' = 0$, 1 and 2 respectively for a particular bound state, U'_{bl} (see table 5.1), to ranges of energy levels in the repulsive state

$$U''(cm^{-1}) = 20.67/(r(nm) - 0.1836)^2 \; * \qquad (4.41)$$

These are plotted so that the FC factors which

* $1 cm^{-1} = 11.963$ J mole^{-1}.

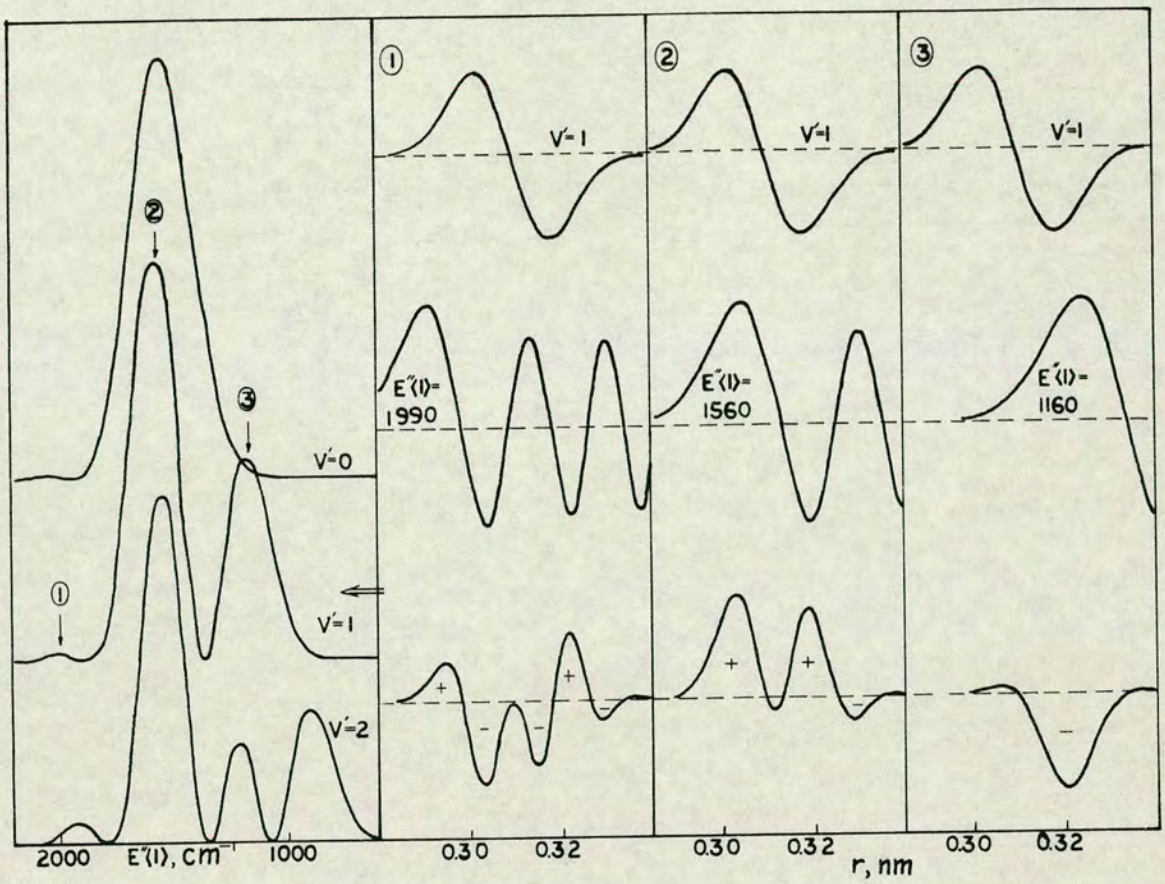

Fig. 4.4 Variation in FC factors (left) for transitions from $v' = 0, 1$ and 2 in the bound state potential, U'_{b1} to energy levels in the repulsive state $U''(cm^{-1}) = 2067/(r(nm) - 0.1836)^2$. On right: (figures ①, ② and ③) vibrational wavefunctions for $v' = 1$, U'_{b1} (top) and for three different energy levels for the lower state, 1990, 1560 and 1160 cm^{-1} above the zero energy. The corresponding overlap functions ($\Psi'_1 \cdot \Psi''_{E''}$) are shown at the bottom of these figures. $1 cm^{-1} = 11.963$ J mole^{-1}.

correspond to transitions of same frequency are at the same $E''(1)$ value. The abscisse axis ($E''(1)$) corresponds to E'' levels for transitions from $v'=1$. The scale is assigned as $E''(1)$. Generally a scale is assigned as $E''(v')$ corresponding to transitions from v' to E'' levels. $E''(v')$ is related to the absolute frequency $\bar{\nu}(cm^{-1})$ by

$$E''(v') = \bar{\nu} - T_e - G'(v') \qquad (4.42)$$

where T_e is the energy of the minimum of the bound potential. The relationship between two scales, $E''(v_1')$ and $E''(v_2')$, is

$$E''(v_1') = E''(v_2') + G(v_1') - G(v_2') \qquad (4.43)$$

Figures 4.4 ①, ② and ③ show how the FC factors at $E''(1) = 1990$ 1560 and $1160 cm^{-1}$ (23810, 18660, 13880 J $mole^{-1}$) were obtained for the transitions from $v'=1$. Each of these FC factors correspond to values of the maxima in the FC plot for $v'=1$. The figures show the wavefunctions Ψ_1' (top) and $\Psi_{E''}''$ (middle) and the overlap functions $\Psi_1 \cdot \Psi_{E''}''$ (bottom) vs r.

The FC factor at $E''(1) = 1990 cm^{-1}$ (23810 J $mole^{-1}$) for $v'=1$ is shown in figure 4.4 ① to be due to an overlap of the $v'=1$ wavefunction and a wavefunction with more rapid oscillations (higher frequency) in the repulsive state. The overlap

function reflects this difference in wavefunctions in showing also rapid oscillatory structure. By integrating $\Psi_1' \cdot \Psi_{E''}''$ over this range the positive and the negative contributions almost cancel each other. The integral is negative due to slightly greater negative contributions.

As one moves to lower E'' levels the lower state wavefunctions show broader oscillatory structure and the turning points move to longer internuclear distance (see also figure 4.3).

At $E''(1) = 1560\ cm^{-1}$ (18660 J $mole^{-1}$) the two humps of the repulsive state wavefunction closest to the turning point (the outermost ones) match closely the two humps of the $v' = 1$ wavefunctions. Therefore a great excess positive contribution to the overlap integral is obtained.

At $E''(1) = 1160\ cm^{-1}$ (13880 J $mole^{-1}$) the outermost hump of the repulsive state wavefunction matches the hump closest to the outer turning point of the $v' = 1$ wavefunction. Therefore an excess negative contribution to the overlap integral is obtained.

For E'' levels on both sides of these three E'' levels the absolute values of the overlap integrals decrease. For certain intermediate E'' levels the negative and the positive contributions cancel completely to give zero overlap integrals (corresponding

to the minima in the FC plots in figure 4.4). For the closest E″ levels on both sides of these the overlap integrals have opposite signs.

In a similar way as the two strongest peaks in the plots of the FC factors for v′=1 in figure 4.4 (at E″(1) = 1560 and 1160 cm^{-1}) represent favourable overlaps of the humps closest to the turning points of the v′=1 wavefunction with humps of repulsive state wavefunctions closest to the turning points there are always corresponding peaks to be found for transitions from other v′ levels. For higher vibrational levels more structure was found in the plots of the FC factors. Thus for v′=2 (figure 4.4) the fourth peak appears at E″(1) = 1210 cm^{-1} (14480 J $mole^{-1}$) between two peaks which are associated with favourable overlaps of the humps closest to the turning points. This peak is associated with favourable overlap of the third hump in the v′=2 wavefunction.

For transitions from very high vibrational levels the FC factor plots show a fine oscillatory structure over a wide frequency range, as shown in figures 4.5 b and 4.6 a. This reflects the great number of nodes (and humps) for the wavefunctions for high v′ levels.

Bound-free transitions for high vibrational levels have been treated theoretically by Mulliken in a discussion of the I_2 McLennan bands.[107,108] Mulliken introduces a special "difference potential ",

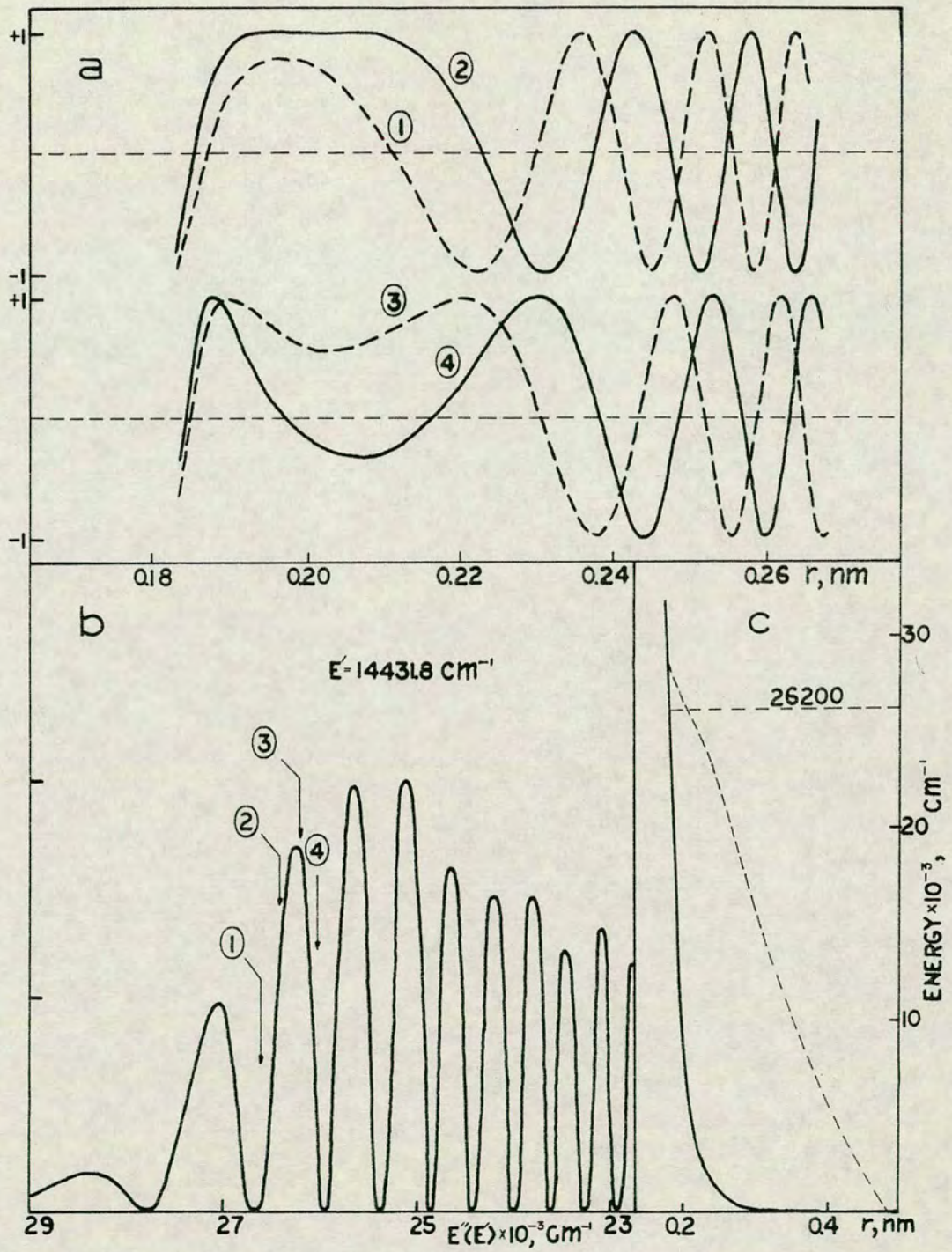

Fig. 4.5 a. Overlap functions for bound-free transitions for a fixed energy level (G′) in a bound state (see text) and four different energy levels in a lower state (see text), ① : 26609 cm^{-1}, ② : 26406 cm^{-1}, ③ : 26204 cm^{-1} and ④ : 26004 cm^{-1} calculated by the normal WKB method. b. FC - factors. c. The repulsive lower state (solid curve) and the "difference potential" (dashed curve).
$1 cm^{-1} = 11.963$ J $mole^{-1}$.

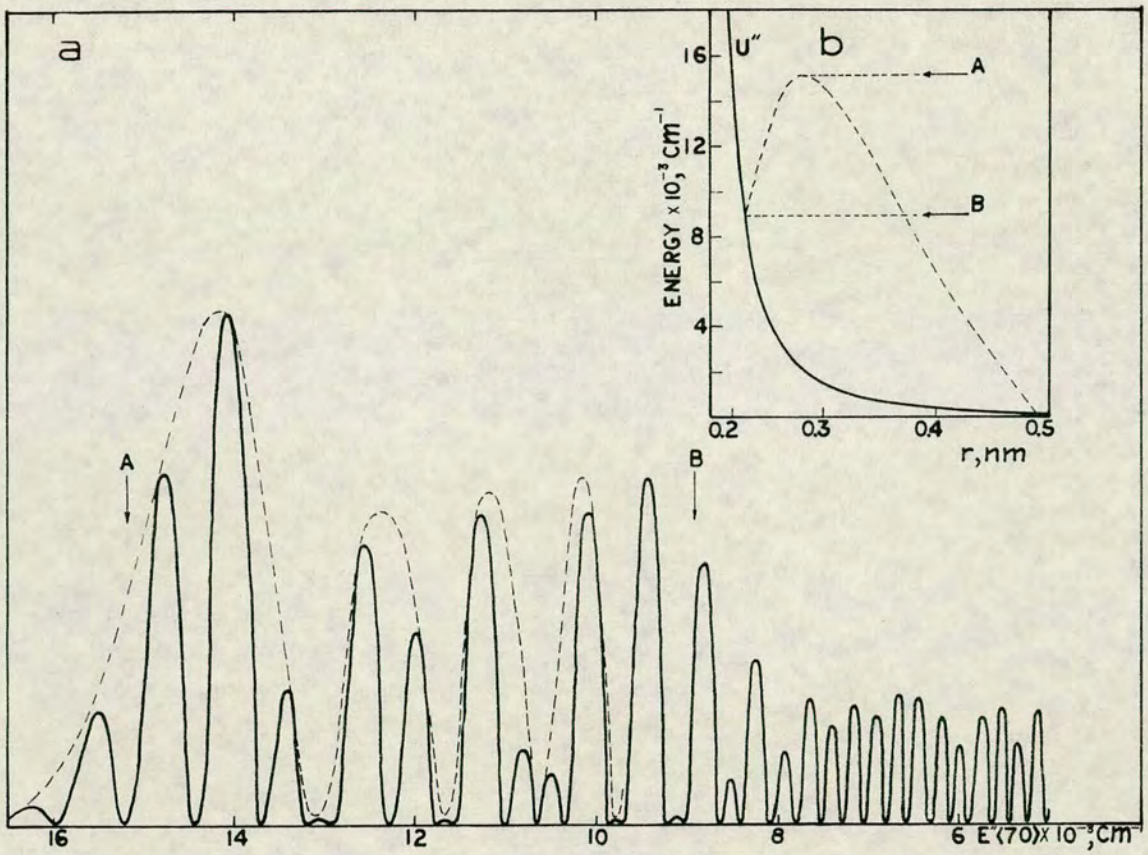

Fig. 4.6 a. Variation in FC - factors for transition from $v'=70$ in the bound potential U'_{cl} to energy levels in the repulsive state U''_{cl}. The dashed line shows the broad oscillatory structure which determines the variation in the relative intensity of the diffuse bands (see text) b. The U''_{cl} potential (solid curve) and the "difference potential" (dashed curve). The arrows labeled A and B indicate the positions which correspond to the classical transitions to the maximum of the "difference potential" and from the inner turning point in U'_{cl} respectively. $1 cm^{-1} = 11.963$ J mole^{-1}.

$U_m(r)$

$$U_m(r) = (E'_{v'} - U'(r)) + U''(r) \qquad (4.44)$$

which is the locus of points which conserve nuclear position and momentum (and therefore also kinetic energy) in the transition from the v′ level of energy $E_{v'}$ for U′(r) to the U″(r) potential.

"Difference potentials" are obtained by "reflecting" the upper potential curves (below $E_{v'}$) on the lower potential curves. Some "difference potentials" are shown in figures 4.5 c and 4.6 b (dashed curves) and also in figure 5.36 for particular potentials and v′ levels. At any point on a particular "difference potential" the wavelength of the wavefunction for the repulsive potential is the same as for the v′ wavefunction in the upper state at the same internuclear distance. This is in agreement with the de Broglie expression for the relationship between kinetic energy and wavelength (eq. 4.21), which states that the wavelengths are the same for the same kinetic energy. At any other points the wavelengths will differ. For a particular transition between two levels contributions to the overlap integral from internuclear distances far away from points on the corresponding "difference potential" will therefore be negligible. Close to points on the "difference potentials" the contributions to the overlap integral can be significant depending

on the phase difference for the two wavefunctions. This is illustrated in figure 4.5.

The curves shown in figure 4.5 a are overlap functions obtained for n - WKB wavefunctions for transitions from one upper level to different lower levels. The bound state wavefunction was obtained for a particular level of energy $G' = 14431.8\ cm^{-1}$ ($172648\ J\ mole^{-1}$) above the minimum of the bound state

$$U'(cm^{-1})^{*} = 1.87 \cdot 10^{7} \exp(-r/0.0315) - 1.16 \cdot 10^{4}/r - 22/r^{4} + 99975.7 \quad (4.45)$$

for r in nm. The lower state wavefunctions were obtained for four different energy levels (E''), ① : 26609 cm^{-1}, ② : 26406 cm^{-1}, ③ : 26204 cm^{-1} and ④: 26004 cm^{-1} for the potential*

$$U''(cm^{-1})^{*} = 1.8 \cdot 10^{8} \exp(-r/0.0206) \quad (4.46)$$

For simplicity the amplitude factor for the wavefunctions (eq. 4.19) was replaced by a constant. Figure 4.5 b shows the variation in the FC factors. The overlap functions (figure 4.5 a) were obtained in the region of the crossing of the E'' levels with the "difference potential" shown in figure 4.5 c (dashed curve). Moving from ① to ② to ③ shows an increase in the FC factors due to increasing positive

* $1 cm^{-1} = 11.963\ J\ mole^{-1}$.

overlap integrals mainly due to contributions in the region 0.185 - 0.23nm (figure 4.4 a). The maximum value was obtained for $E'' = 26204$ cm^{-1} ($3.1348\ 10^5$ J $mole^{-1}$) (③). Moving to a slightly lower E'' level (④) the overlap integral decreases. This explains the peak in figure 4.5 b at about 26200 cm^{-1} ($3.1343\ 10^5$ J $mole^{-1}$).

If the "difference potential" has a maximum like the one in figure 4.6 b, which is obtained for U'_{c1}, U''_{c1} (see section 5.21) and $v' = 70$ there are two crossing points for any one E'' level in the region between A and B (see figure 4.6 b). This means that there are two regions (of r) which may contribute significantly to the overlap integral. These contributions may add constructively or destructively. This causes the diffuse bands to vary in a broad oscillatory pattern as shown in figure 4.6 a. This is a well known characteristic of bound-free transitions.[9,21,37,36,148].

4.4 Simulation calculations.

In the simulation calculations the transition probabilities were evaluated by equation 4.11. Light intensity of a particular frequency (ν) due to transitions from all the emitting vibration levels for particular electronic states is expressed as

$$I(\nu) = c\ \nu^5 \sum_{v} N(v')\left(\int \psi'_v \cdot \mu_i^{eff}\, \psi''_{E''(v')} dr\right)^2 \qquad (4.47)$$

where c is a constant and $N(v')$ is the population in the v' level. $E''(v')$ is an energy level in the lower state depending on v' such that the transition from v' to E'' occurs at ν. μ_i^{eff} is the effective transition moment. The wavefunctions are normalized. The ν^5 term is appropriate for experimental detection of quanta per unit wavelength interval.

When repulsive potentials of the type $a/(r-b)^2$ were used, the wavefunctions were obtained analytically and used unnormalized with the amplitude for $r \to \infty$ of constant value for all E'', instead of varying as $1/(E'')^{1/4}$ as mentioned earlier. This, however, could be accounted for by adjusting the transition moment function slightly.

For simplicity the ν^5 factor was ignored throughout the simulation calculations but its effect could be accounted for by adjusting the transition moment function slightly.

Generally a light intensity was therefore

calculated from

$$I(\nu) = c \sum_{v'} N(v')\left(\int \Psi'_{v'} \cdot \mu_i \Psi''_{E''(v')} dr\right)^2 \qquad (4.48)$$

where μ_i represents an unadjusted transition moment function and $\Psi''_{E''(v')}$ is a nonnormalized wavefunction, if $U'' = a/(r-b)^2$ was used, but a normalized wavefunction if it is evaluated by the u - WKB method.

No attempt was made to calculate the transition moments (eq. 4.12), but some simple functions of internuclear distance were used for μ_i in order to obtain proper fits of calculated and experimental spectra. μ_i^{eff} (eq. 4.47) could then be estimated from comparison of equations 4.47 and 4.48.

Spectra which were calculated from equation 4.48 were compared with experimental spectra which had been corrected for spectral response.

Estimates of population distributions in emitting states were obtained by use of calculated vibrational level contributions by nonlinear least square analyses of some spectra. The least square calculations were made by use of a computer program based on a program given by P.R.Bevington:[138] a polynomial function of intensity at each experimental wavelength as a function of the populations in each vibrational level was generated. The populations were then varied by a nonlinear least square routine until the "best fit" of populations was found. The

least square method involves expanding the least square expression (CHI-square) in Taylor series as a function of the parameters (populations).

5. SIMULATION CALCULATIONS

Simulation calculations for various ArBr-and ArCl-spectra are discussed in this chapter. These simulation calculations were carried out in order to see whether more detailed information on the noble gas halide systems could be obtained from these spectra than what has already been obtained from the experimental results, discussed in chapter 3.

The theoretical expression for the radiative intensity, due to electronic transitions (eq. 4.47) includes vibrational population values, transition moment, and indirectly the potential curves (the wavefunctions depend on the shape of the potential curves according to the Schrödinger equation). These are therefore the factors which one might especially hope to obtain information on from simulation calculations. Apart from rough estimates of the vibrational frequency and the bond strength for the B - state ArCl,[9] no detailed

information was available on these factors. It was therefore necessary to carry out quite comprehensive simulation calculations, where the effect of the various factors on calculated spectra was studied to search for what could be achieved from the simulation calculations. The large number of uncertain factors made it necessary to make various assumptions in order to obtain further information on individual factors. These assumptions are partly based on the characteristic similarity between the alkali halide- and the noble gas halide- systems[2] and partly on theoretical calculations for other noble gas halide systems.[52-56] Thus the relatively complicated continous spectra were shown to contain additional information on these systems, which could not be derived from the experimental analyses described in chapter 3. This is especially true for the ArBr system, whose spectra are less complicated than the ArCl spectra. The additional information, however, is limited by the number of assumptions, that were made.

5.1 ArBr.

5.11 Introduction; Upper state potentials.

Simulation calculations for some ArBr spectra will be presented in this section. The MC spectra, generated by HBr + Ar^* and DBr + Ar^*, were taken to represent the B-X transitions, by simply ignoring any possible C-A(3/2) contributions in that region. The SC spectrum, generated by CH_2Br_2 + Ar^*, was taken to be the long wavelength part of the C-A(3/2) spectrum, by disregarding any B-A(1/2) contribution in that region. An estimate of the B-A(1/2) contributions in the SC spectra for HBr + Ar^* and DBr + Ar^* was made to obtain the shape of the C-A(3/2) spectra for these reactions. Simulation calculations were carried out for these experimental spectra. These simulation calculations gave information on population distributions in the vibrational levels of the emitting states and also, but to a less extent, information on the shape of potential curves and transition moment functions.

A fixed bound upper potential was used in the simulation calculations for the B- and the C- states. This potential (U'_{b1}) was chosen as a Rittner potential[117] of the same type as has been derived for the B-state for KrF:[59]

$$U'_b = a_1\exp(-r/b_1) + a_2\exp(-r/b_2) - c_1/r - c_3/r^3 - c_4/r^4 + d \qquad (5.1)$$

where a_1, a_2, b_1, b_2, c_1, c_3, c_4 and d are constants and r is the internuclear distance. d is the asymptotic energy for the potential (for $r \to \infty$).

Other terms in the Rittner potential expression for other systems[59,177,139] represent different types of interactions between the two atoms. Thus the c_n/r^n terms represent Coulombic interaction for n = 1, ion-quadrupole interaction for n = 3 and ion-induced dipole interaction for n = 4. The two exponential terms in the Rittner potential for KrF express repulsion due to overlap of orbitals and configuration interaction between ionic and covalent configurations respectively.

To obtain the U'_{b1} potential, the value for the constant c_1 could be easily determined from the ion charges. c_4 is a function of the polarizability of the ions and could be determined approximately by assuming that the polarizability of Ar^+ is the same as for K^+.[2] Values for the constants in the other terms were estimated from comparison with terms in the Rittner potential expressions for the ground states for the alkalihalides[140] (U_X^{MX}):

$$U_X^{MX} = a \cdot \exp(-r/b) - c_1/r - c_4/r^4 - c_6/r^6 - c_7/r^7 \qquad (5.2)$$

and the expression for the B-state for KrF. Values for the c_n constants for U_X^{MX} (c_n^{MX}) show regular changes with changes in alkali atoms and halogen

atoms, almost independent of n. The assumption was made that the same was true for the c_3 constants for the noble gas halides (c_3^{NgX}). c_n^{ArBr} was derived from the expression :

$$c_3^{ArBr} = c_3^{KrF} \left(c_n^{KBr}/c_n^{RbF}\right) \qquad (5.3)$$

Values for the constants in the exponential terms were obtained in an analogous way, from the values of the corresponding constants for KrF and the values of the a- and b- constants for KBr and RbF. The values of the constants in the expression for U'_{b1} (equation 5.1) are tabulated in table 5.1, as well as the corresponding values for another potential, U'_{b2}. U'_{b2} was chosen by substituting the two exponential terms in U'_{b1} by one different exponential term.

Table 5.1

Values of constants in the Rittner potential expressions for U'_{b1} and U'_{b2} (equation 5.2) for r expressed in nm.

Const.	$U'_{b1}(cm^{-1})$	$U'_{b2}(cm^{-1})$
a_1	$1.144\ 10^7$	$9\ 10^6$
b_1	0.03747	0.045
a_2	$5.944\ 10^6$	0
b_2	0.04514	0
c_1	$1.161\ 10^4$	$1.161\ 10^4$
c_3	$1.563\ 10^2$	$1.563\ 10^2$
c_4	32.79	32.79
d	99975.7	99975.9

$1 cm^{-1} = 11.963\ J\ mole^{-1}$.

The U'_{b1} potential fulfils the requirements that it has a slightly a. larger bond distance, b. smaller dissociation energy and c. lower fundamental frequency than the ground state of KBr[53] (see arguments in chapter 1 and table 1.2). The U'_{b1} potential, partly derived from the calculated B - state Rittner potential for KrF, is thus an approximate expression for the B - state for ArBr. By assuming that the B- and the C- states do not differ greatly, U'_{b1} can also be used as an approximate expression for the C - state. While the determination of most of the terms in the expression for U'_{b1} is based on approximations or guess-work, the shape and the energy of the B- and the C- state potentials are of great uncertainty. Comparison of the U'_{b1} potential and the results from the temperature dependence experiments, discussed earlier (section 3.126), suggests that the potential minimum for U'_{b1} (T_e) is higher than what there might be expected for the B - state potential. This will be discussed in more detail later (see section 5.132).

U'_{b2} has a similar bond strength as U'_{b1}, but a different vibrational frequency. U'_{b2} was tried in the simulation calculations for the B-X spectrum (MC - spectrum) for HBr + Ar^* only, and the calculation results were compared with those obtained by using U'_{b1}, mainly to see the effect of making slight changes in the shape (vibrational frequency) of the upper

state potential. Spectroscopic constants for the two potentials and for the ground state of KBr are shown in table 5.2

Table 5.2

Spectroscopic constants for the U'_{bi} (i = 1,2) potentials and for the ground state of KBr (X(KBr)).[140]

a. r_e, D_e, ω_e

	r_e(nm)	D_e(cm^{-1})	ω_e(cm^{-1})
U'_{b1}	0.3092	37131.6	193.8
U'_{b2}	0.3048	37099.0	186.2
X(KBr)	0.2821	39730.5	219.2

b. a_i in equation 4.39

i =	1	2	3
U'_{b1}	193.82	-0.5600	-0.0020
U'_{b2}	186.2	-0.4856	-0.0031

$1cm^{-1} = 11.963\ J\ mole^{-1}$.

Calculated spectra were obtained for various lower state potentials, different μ_i functions and various population distributions in order to see the effect of changes in these parameters on calculated spectra and to see how to obtain spectra of shape similar to experimental spectra. Studies were made of the effect of making some changes in the shape of potentials and μ_i functions on the population distributions which gave best fits of calculated

spectra and experimental spectra. Various linear functions of internuclear distance were used for μ_i functions. Analytical functions on the forms $a/(r-b)^2$ and $c \cdot \exp(-r/d)$ were tried for lower potentials.

To properly evaluate the full expression of equation 4.48, and thus calculate a spectrum due to a particular transition, one needs to know the number of emitting vibrational levels as well as the population distribution. It has already been suggested that a total of 8 vibrational levels ($v' = 0\text{-}7$) in the B-state are emitting in the spectra for $HBr+Ar^*$ and $DBr+Ar^*$. The number of emitting vibrational levels in the C-A(3/2) spectra is not known with certainty. Therefore, the effect of varying the total number of emitting vibrational levels in the C-state was also considered.

5.12 Results of simulation calculations.

5.121 MC for HBr+Ar* and DBr+Ar*.

Simulation calculations for various ArBr, MC spectra, generated by HBr+Ar* and DBr+Ar* will now be discussed.

a. Effect of changing the lower state potential.

The effect of using different repulsive lower state potentials on the shape of calculated spectra, for a fixed bound potential (U'_{bl}), fixed μ_i function and even population distribution will now be considered.

The uncertainty in the position of the upper state potential (the B - state) causes equally great uncertainty in the position of the lower state potential (the X - state). Since it has been suggested that the minimum energy of U'_{bl} is higher than the energy of the B - state potential, repulsive potentials which gave calculated spectra at lower frequency than the ArBr, MC spectra, similarly, were expected to be higher in energy than the X - state potential. Only repulsive potential curves which gave spectra at the same frequency or greater (potentials of lower energy) than the experimental spectra were therefore tried.

The asymptotic value for the energy of the X - state is zero. This state is repulsive at short internuclear distances and has possibly a slight

Van der Waals minimum at long internuclear distance like in other noble gas halide systems. For comparison it can be mentioned that the Van der Waals minimum for the X - state for ArCl has been estimated to be at about 0.49nm internuclear distance,[141] while the equilibrium internuclear distance (r_e) for the B - state is estimated to be at about 0.29nm (see section 5.2). The assumption was made that the ArBr, X - state is repulsive in the FC - region of interest, and purely repulsive model potentials (U''_{bi}) were used in the simulation calculations.

The potentials U''_{bi} (i = 1,2,3,4) (see table 5.3) all have different slopes in the region of r_e for U'_{b1}, as shown in figure 5.1. Calculated spectra for these potentials were obtained for U'_{b1}, μ_i=constant (μ_0, transition moment μ_0^{eff}), a total of seven vibrational levels in the upper state (v'= 0-6) and even population distribution in these levels. The spectra vary with the slope of the lower potential, as shown in figure 5.2. All these spectra show qualitatively the same structure as the MC for HBr+Ar* and DBr+Ar* - a strong peak at the high E'' end and finer oscillatory structure on the low E'' side of the peak.

The v' contributions for the spectra for U''_{b1} and U''_{b3} are shown in figure 5.3 (solid curves), as well as the total spectra (dashed curves). These figures show that the strongest peak in the spectra is made of contributions from many vibrational

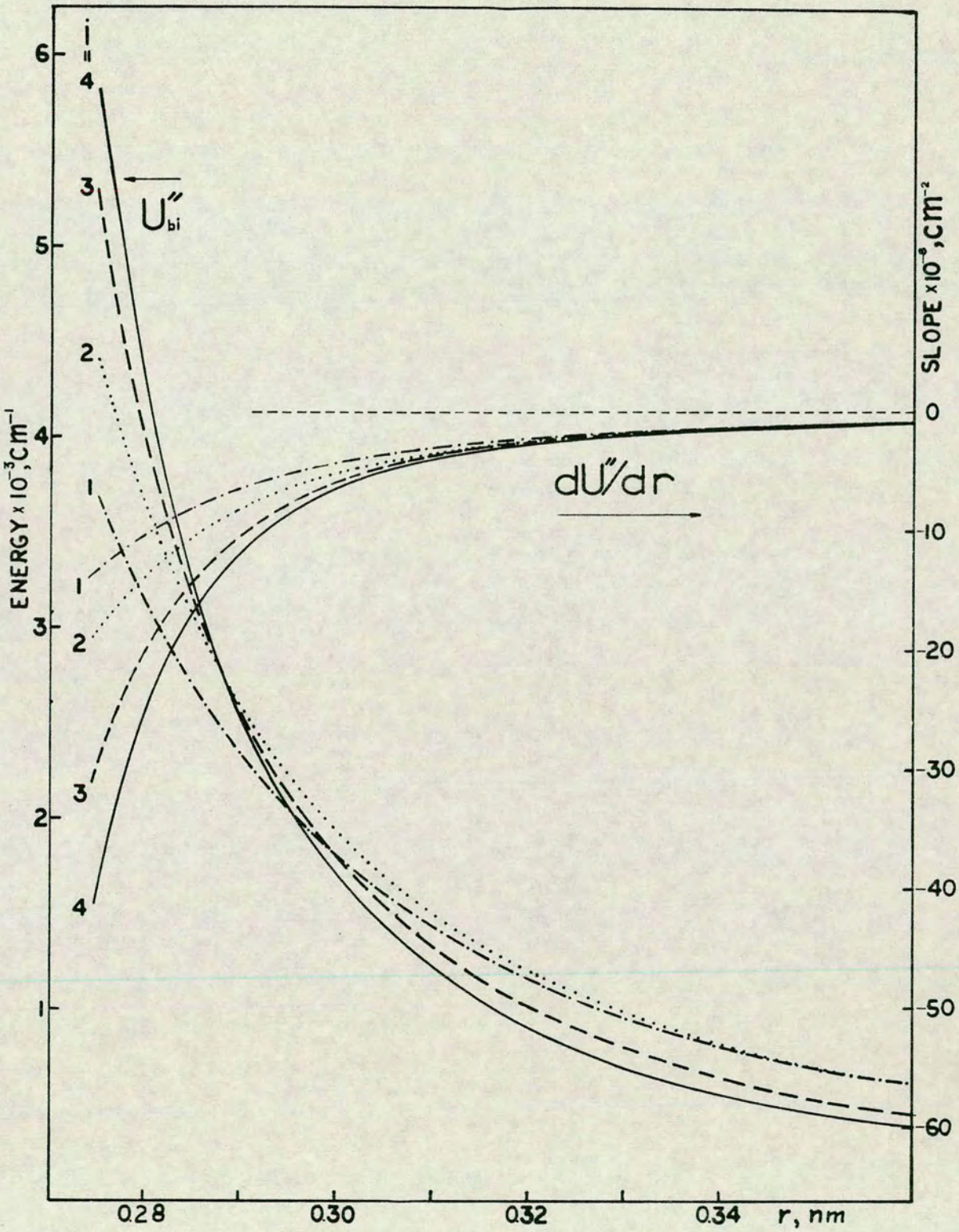

Fig. 5.1 Repulsive potential curves, U''_{bi} (i = 1,2,3,4), and the slopes of these, dU''_{bi}/dr. $1 cm^{-1} = 11.963$ J mole^{-1}.

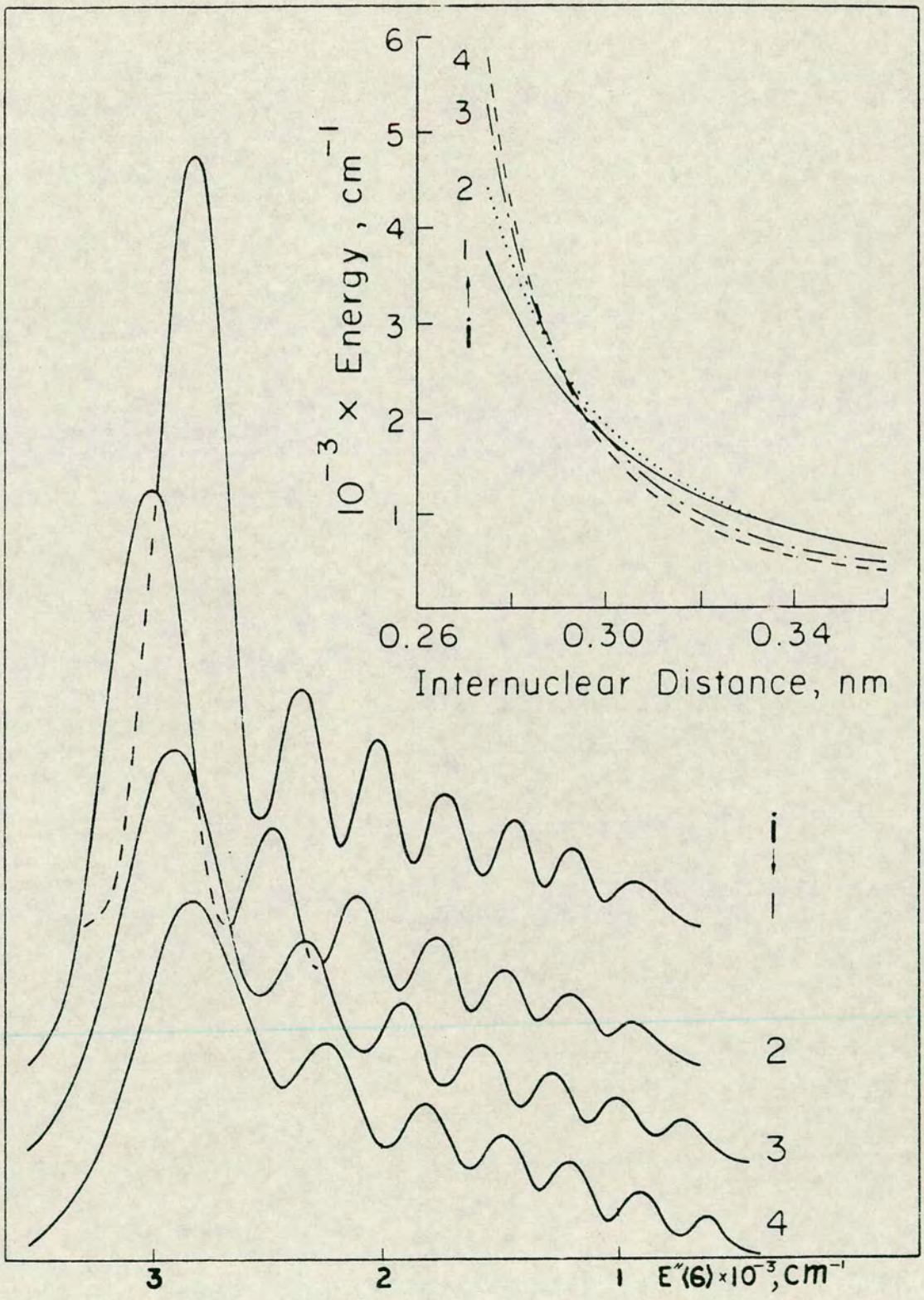

Fig. 5.2 Calculated spectra for transitions from U'_{b1}, $v' = 0 - 6$ to U''_{bi} for $i = 1,2,3,4$, μ_i = constant (μ_0) and even vibrational population distribution. The U''_{bi} potentials are shown at the top of the figure (see also figure 5.1). $1 cm^{-1} = 11.963$ J mole^{-1}.

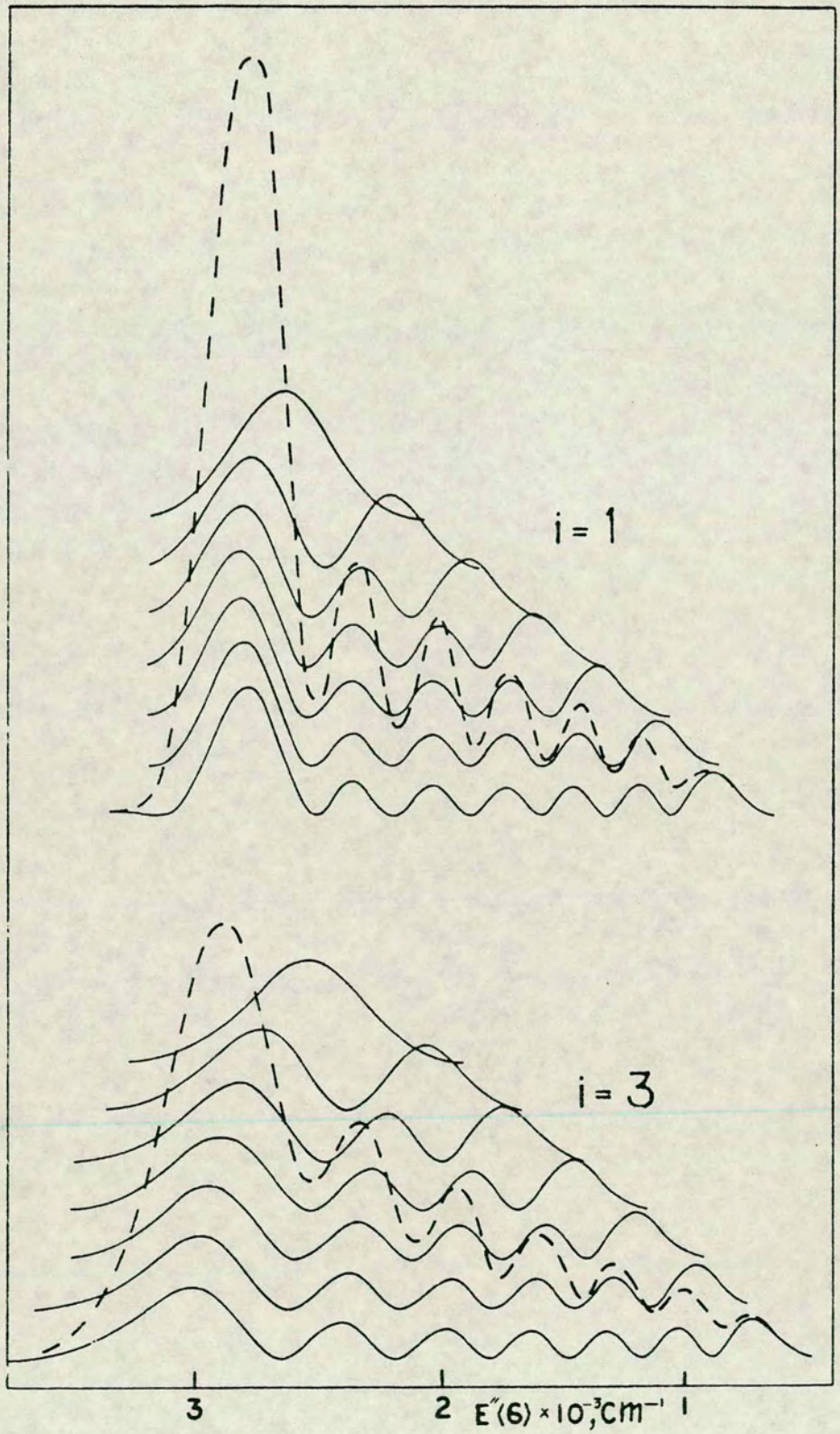

Fig. 5.3 Calculated vibrational contributions (solid curves) for two of the calculated spectra (dashed curves) shown in figure 5.2 for U''_{bi}, i = 1 and 3. $1cm^{-1} = 11.963\ J\ mole^{-1}$.

levels. The peaks in the v′ contributions which add up in that region correspond to transitions near the classical inner turning points. The oscillatory structure of the spectra depends on the characteristic oscillatory structure of the v′ contributions, which roughly mirrors the radial probability distribution for the v′levels. For a spectrum like the one for U''_{b1}, the peaks for many v′ contributions are at similar positions and add up to give relatively strong peaks. As the lower potential gets steeper,the oscillatory structure of the v′contributions broadens and the peaks are displaced as in the spectral contributions for U'_{b3}. This causes a broadening in the structure for the total spectrum.

Table 5.3

Repulsive lower state potential curves, U''_{bi} (cm^{-1}) used in simulation calculations for ArBr, MC spectra. r is expressed in nm.

			Type of potential
i	a	b	U''_{bi}
1	12.25	0.2176	$a/(r-b)^2$
2	10.64	0.2260	"
3	6.480	0.2399	"
4	4.961	0.2458	"
5	19.85	0.2100	"
6	$7.197\ 10^6$	0.03673	$a\ \exp(-r/b)$
7	$5.055\ 10^6$	0.03775	"

$1 cm^{-1} = 11.963\ J\ mole^{-1}$.

By changing the slope of the lower potential the total range of calculated spectra can be changed as

well as the spacing between peaks. The range of the spectra in figure 5.2 is determined by the range of the v′ contribution for the highest vibrational level which is emitting (v′=6) (see figure 5.3). This spectral range is approximately determined by the difference in the potential energy for U''_{bi} at the turning points r_1 and r_2 for (v′=6) (according to the FC - principle)

$$U''_{bi}(r_1) - U''_{bi}(r_2) = E''_{max} - E''_{min} \qquad (5.4)$$

(see figure i). $U''_{bi}(r_1) - U''_{bi}(r_2)$ and the total range of the spectra in figure 5.2 increases with increasing slope of U''_{bi}, as shown in table 5.4. The spacing between the peaks in the spectra increases with increase in the slope of the U''_{bi} potentials.

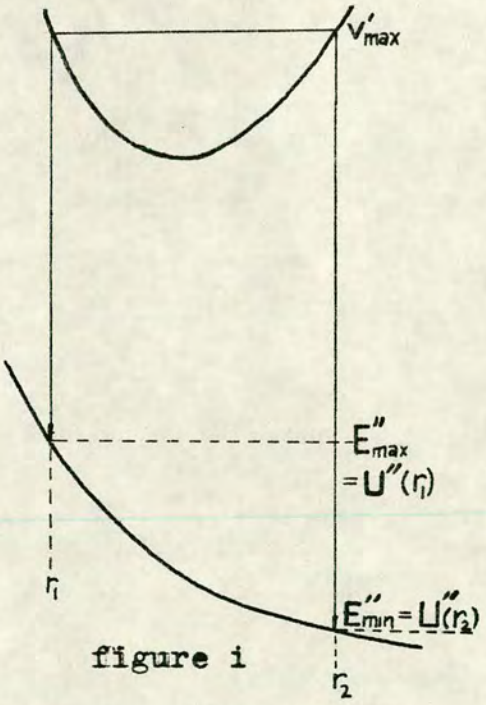

figure i

The potentials U''_{b5} and U''_{b6} (table 5.3) both satisfy the conditions:

$$U''_{bi}(r_1) - U''_{bi}(r_2) = 2698\,cm^{-1}\ (32280\ J\ mole^{-1}) \qquad (5.5)$$

where r_1 and r_2 are the classical turning points for v′=7 and U'_{b1}. These gave spectra with the same total range and the same number of peaks (8) as observed for

Table 5.4

$U''_{bi}(r_1) - U''_{bi}(r_2)$ and the total range of the calculated spectra for U''_{bi}(i 1,2,3,4). r_1 and r_2 are the classical turning points for v′ 6, U'_{b1}.

i	$U''_{bi}(r_1) - U''_{bi}(r_2)$ (cm^{-1})	Total spectral ranges (cm^{-1})
1	1987	2500
2	2369	2800
3	2700	3000
4	2852	3050

$1 cm^{-1} = 11.963$ J $mole^{-1}$

the MC spectrum for HBr+Ar*, if a total of 8 vibrational levels were used (v′=0-7). Calculated spectra and vibrational contributions for U''_{b5} and U''_{b6} are shown in figures 5.4 and 5.5, as well as a low pressure (0.6 torr, 80 Nm^{-2}) MC spectrum for HBr+Ar*. The slopes of the two repulsive potentials differ slightly, as shown in figure 5.6, the U''_{b5} potential being significantly steeper than U''_{b6} at short internuclear distances. This causes a slight difference in the positions of the peaks in these two spectra. The relative positions of the peaks in the spectrum for U''_{b6} is fairly consistent with that observed in the experimental spectrum (figure 5.5), while the position of some of the peaks in the spectrum for U''_{b5} are slightly displaced (figure 5.4). The U''_{b5} potential is of the type $a/(r-b)^2$. The calculated spectrum for U''_{b5} is at approximately the same absolute frequency as the experimental spectrum. Thus U''_{b5} is in the

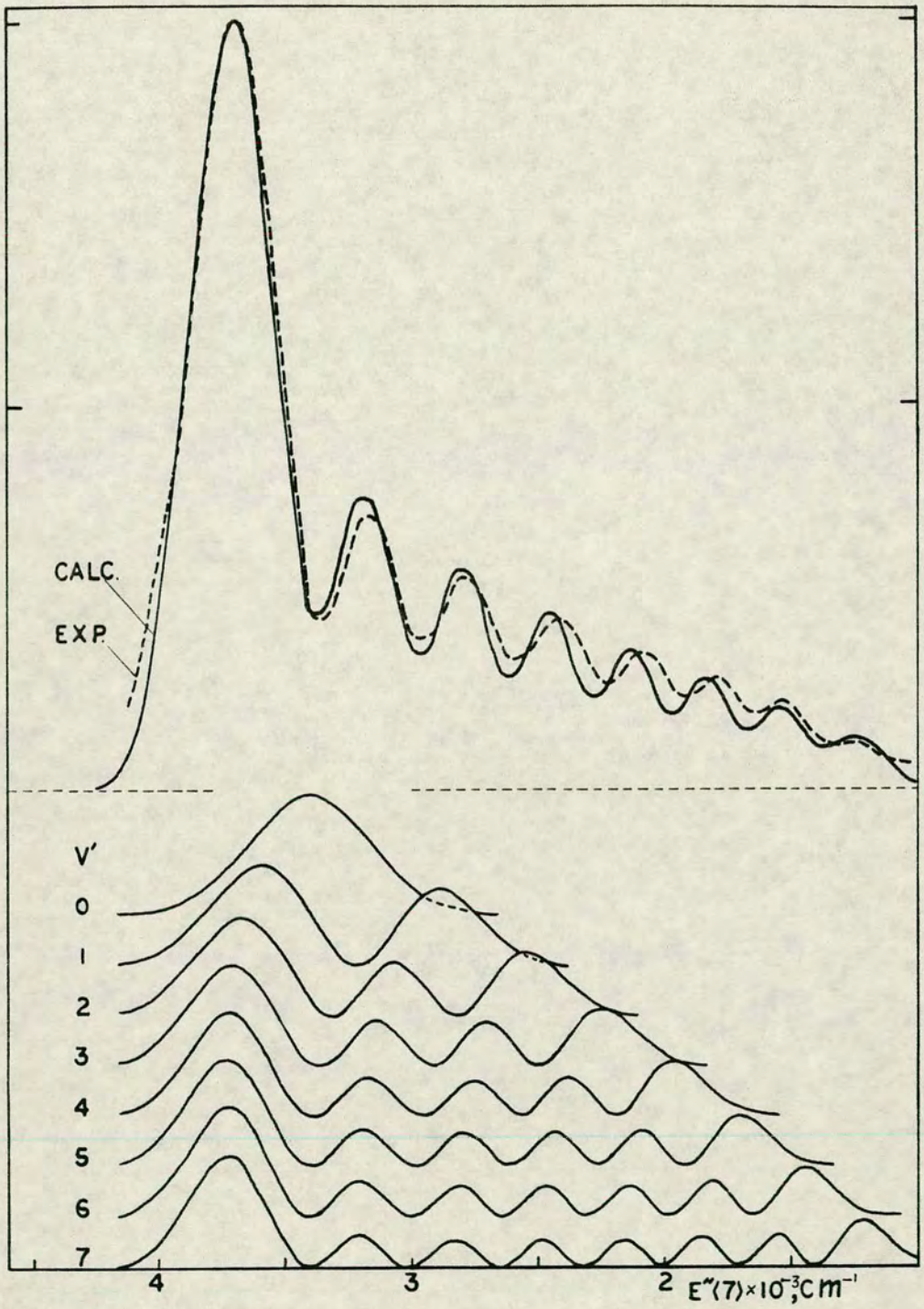

Fig. 5.4 Calculated spectrum (top) and vibrational contributions (bottom) for transitions from U'_{b1}, $v' = 0\text{-}7$ to U''_{b5} for μ_i=constant (μ_0) and even vibrational population distribution (solid curves). The dashed curve (top) is experimental ArBr , MC spectrum generated by $Ar^* + HBr$ at 0.6 torr (80 Nm^{-2}) total pressure and for 250 μm slit width. $1cm^{-1} = 11.963$ J $mole^{-1}$.

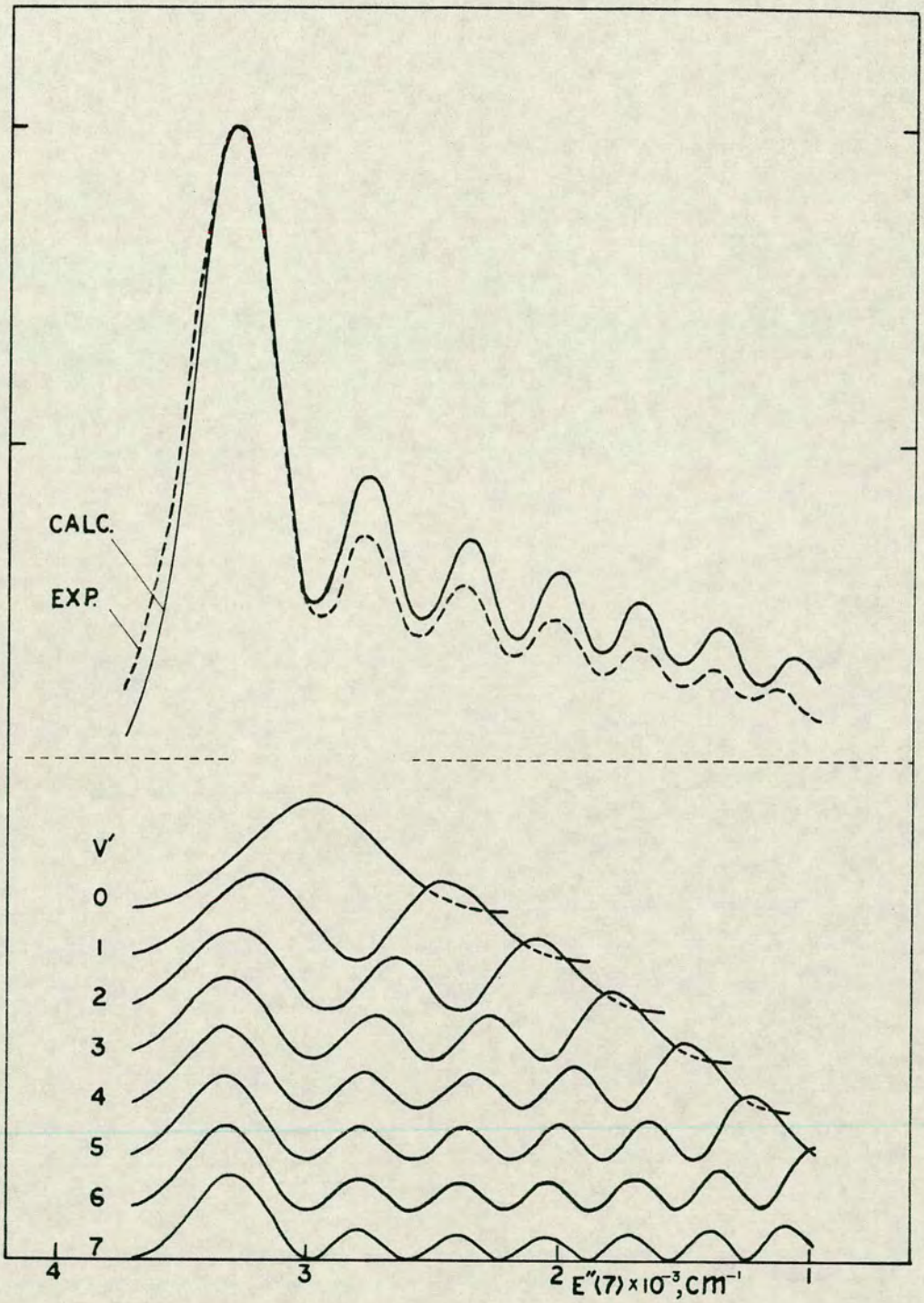

Fig. 5.5 Calculated spectrum (top) and vibrational contributions (bottom) for transitions from U'_{b1}, $v' = 0\text{-}7$ to U''_{b6} for μ_i = constant (μ_0) and even vibrational population distribution (solid curves). The dashed curve (top) is experimental ArBr , MC spectrum generated by $Ar^* + HBr$ at 0.6 torr (80 Nm^{-2}) total pressure and for 250 μm slit width. $1cm^{-1} = 11.963$ J $mole^{-1}$.

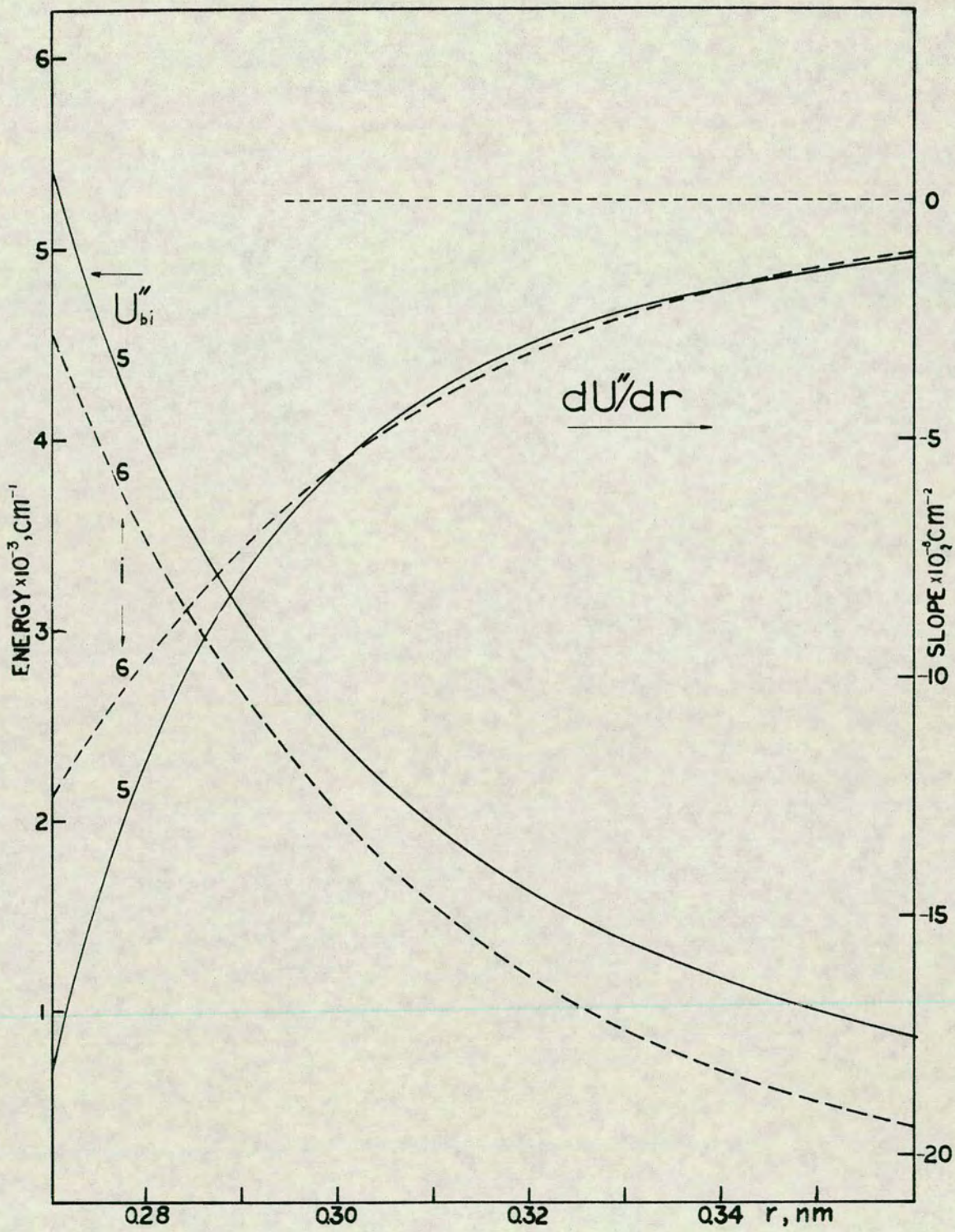

Fig. 5.6 Repulsive potential curves, U''_{bi} (i = 5,6) and the slopes of these, dU''_{bi}/dr. $1 cm^{-1} = 11.963$ J mole^{-1}.

upper limits of the potential energy range which is considered to be realistic for the X-state potential (see earlier). Any potential curves of the same type $(a/(r-b)^2)$ which are lower in energy and satisfy equation 5.5 (to give a spectrum with same total spectral range as the experimental spectrum) can be shown to be even steeper than U''_{b5} at short internuclear distances. Thus any such potential curves are expected to give spectra with peaks which are even more displaced relative to those of the experimental spectrum than those in the spectrum for U''_{b5}.

The following important conclusions can be drawn from studying the effect of changing the shape of the lower state potential. By a proper choice of a potential one can obtain a calculated spectrum with the same total spectral range, the same number of peaks and the same spacing between the peaks as observed in the experimental ArBr, MC spectra for a fixed upper potential, μ_i = constant (μ_0, transition moment μ_0^{eff}) even population distribution and by using the same number of v´ levels (lowest levels) as the number of peaks.

The effect of using different μ_i functions (or different transition moments) and different population distributions now has to be looked at.

b. Effect of changing the transition moment.

The effect of changing the transition moment on the shape of calculated spectra for U'_{b1} and even population distribution will now be considered. It is known for other noble gas halide systems that the transition moments for the B-X transitions vary a great deal with internuclear distances[53-56] and can by no means be ignored in simulation calculations.[21]

The variation in the transition moments with internuclear distance for other systems has been discussed earlier (section 1.2) and is shown in figures 1.5 and 1.6. A decrease in the transition moments with internuclear distance in the closest region of the equilibrium internuclear distance (r_e) for the B - state potentials is characteristic for the noble gas fluorides and the xenon halides.

The effect of the transition moment term on calculated spectra were shown by including various μ_i functions, which decrease linearly with internuclear distance, inside the FC integral in equation 4.48. The corresponding transition moment functions (μ_i^{eff}) are defined by equation 4.47 as mentioned earlier (section 4.4).

The μ_i functions which are tabulated in table 5.5 were included in calculations of spectra for the lower potentials U''_{b5} and U''_{b6} (table 5.3). The calculated spectra are shown in figures 5.7 and 5.8.

The overall decrease in the μ_i functions over

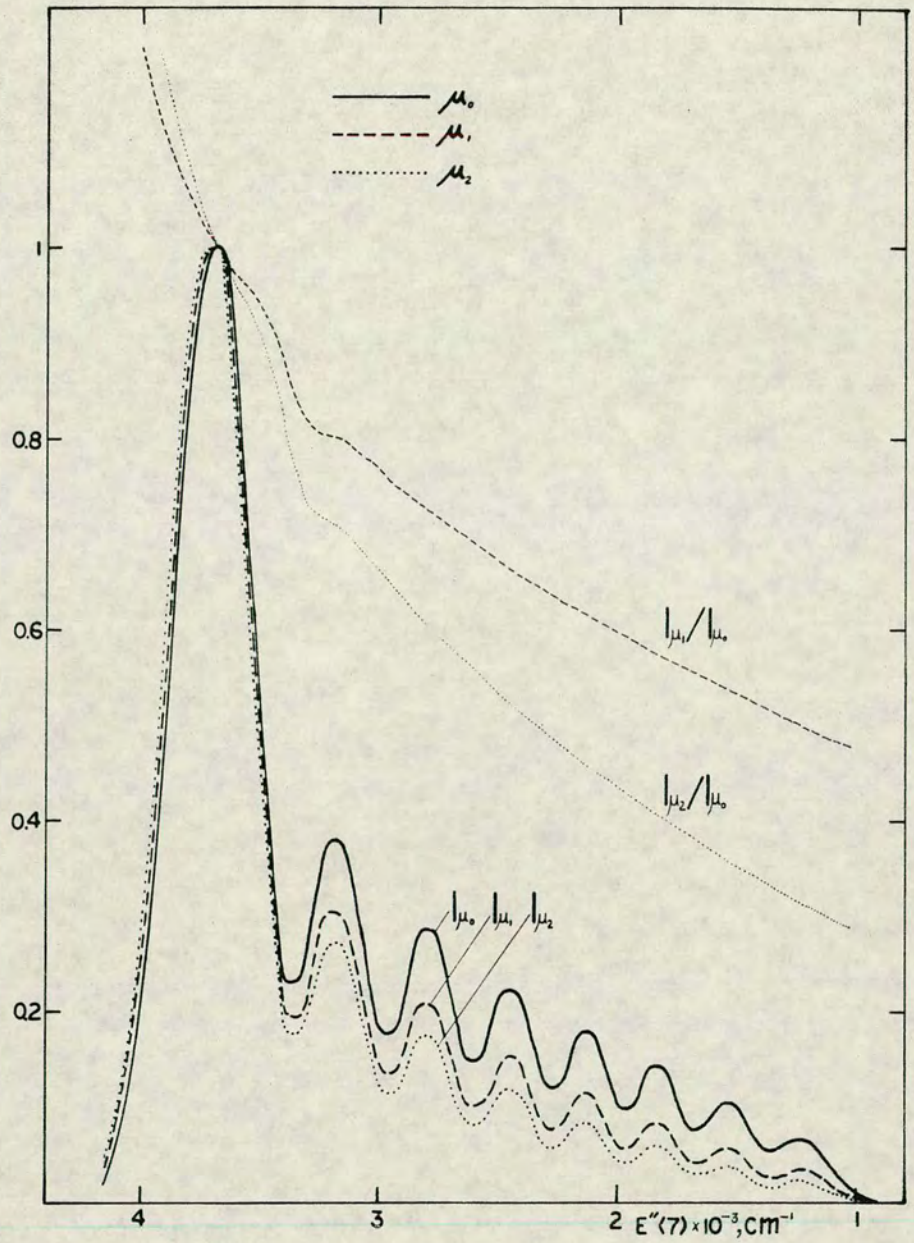

Fig. 5.7 Calculated spectra for transitions from U'_{b1}, $v' = 0$-7 to U''_{b5} for even vibrational population distribution and three different μ_t- functions, μ_0, μ_1 and μ_2. The calculated spectra are normalized such that the height of the strongest peak is the same for all of them. The fine dashed and dotted curves represent the ratios for the calculated intensities of the spectra obtained by using μ_1 ($I\mu_1$) and μ_2 ($I\mu_2$) respectively over the calculated intensity for the spectrum obtained by using μ_0 ($I\mu_0$): $I\mu_1 / I\mu_0$ and $I\mu_2 / I\mu_0$. $1 cm^{-1} = 11.963$ J mole^{-1}.

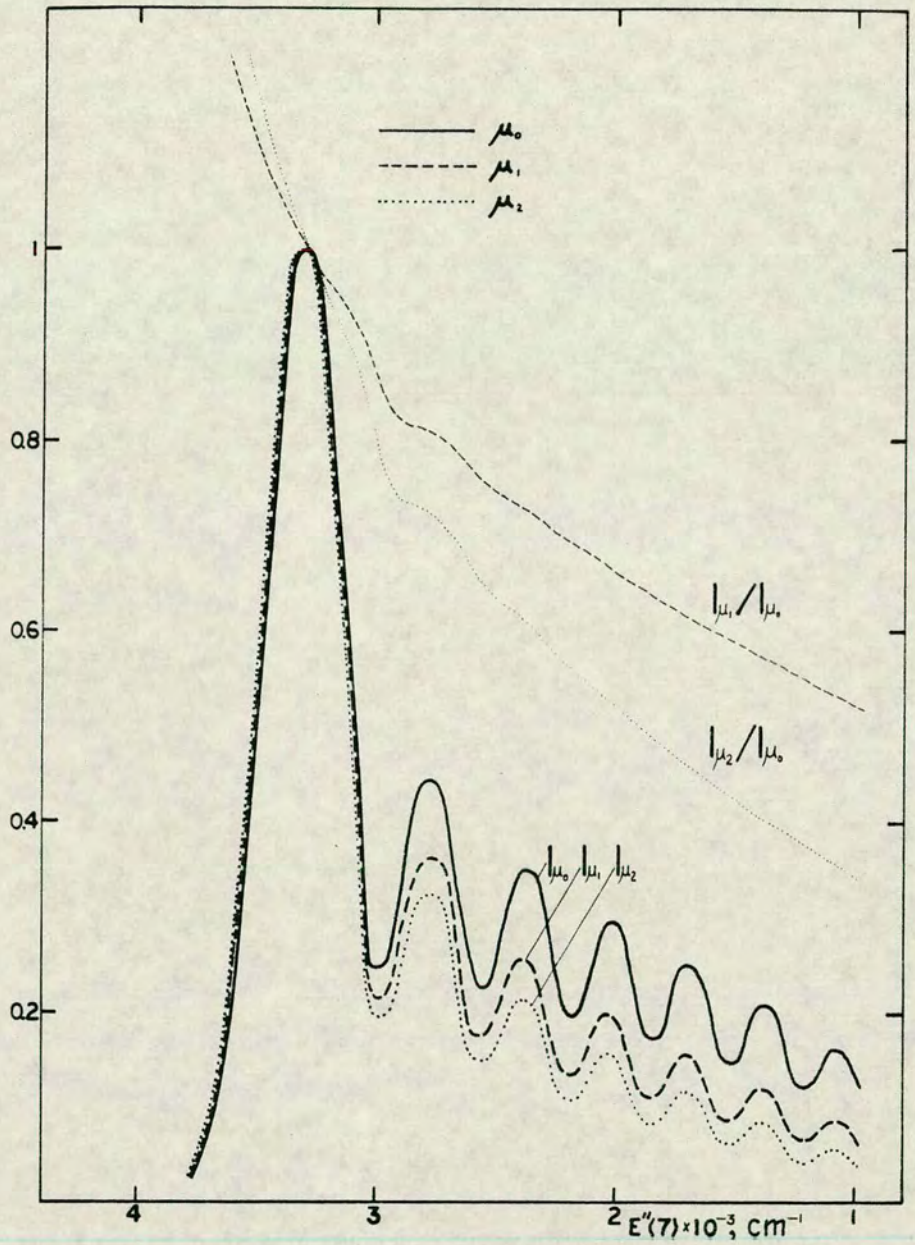

Fig. 5.8 Calculated spectra for transition from U_{b1}', $v' = 0\text{-}7$ to U_{b6}'' for even vibrational population distribution and three different μ_i-functions μ_0, μ_1 and μ_2. The calculated spectra are normalized such that the height of the strongest peak is the same for all of them. The fine dashed and dotted curves represent the ratios for the calculated intensities of the spectra obtained by using μ_1 (I_{μ_1}) and μ_2 (I_{μ_2}) respectively over the calculated intensity for the spectrum obtained by using μ_0 (I_{μ_0}): I_{μ_1}/I_{μ_0} and I_{μ_2}/I_{μ_0}.
$1 cm^{-1} = 11.963$ J $mole^{-1}$.

the FC region of interest increases as $\mu_0 < \mu_1 < \mu_2$. The percent decrease in μ_i over the internuclear distance range determined by the classical turning points for the maximum vibrational level ($v' = 7$) for U'_{b1} is tabulated in table 5.5. The corresponding transition moments (μ_i^{eff} functions) were estimated for both these calculations and are shown in figures 5.9 a and b as well as the μ_i functions. The μ_i^{eff} functions vary almost linearly with internuclear distance .

Table 5.5

μ_i functions : $\mu_i = ar + b$ (cm^{-1}), $i = 0,1,2$ and percent decrease in μ_i over an interval $[r_1, r_2]$ where r_1 and r_2 are the classical turning points for $v' = 7$, U'_{b1}. r is expressed in nm.

i	a	b	% decrease
0	0	1	0
1	-5.9	2.67	37.6
2	-8.4	3.37	53.6

$1 cm^{-1} = 11.963$ J $mole^{-1}$.

The spectra in figures 5.7 and 5.8 are normalized so that the strongest peak has the same height for all of them. The effect of using μ_i functions, which decrease with the internuclear distance (μ_1, μ_2) instead of μ_i=constant (μ_0), on the shape of such normalized spectra is that of causing a steady decrease in the intensity on the low E'' side of the strongest peak with decreasing E'' but a steady increase in the intensity on the high E'' side of it with increasing E''. The greater the percent decrease of the

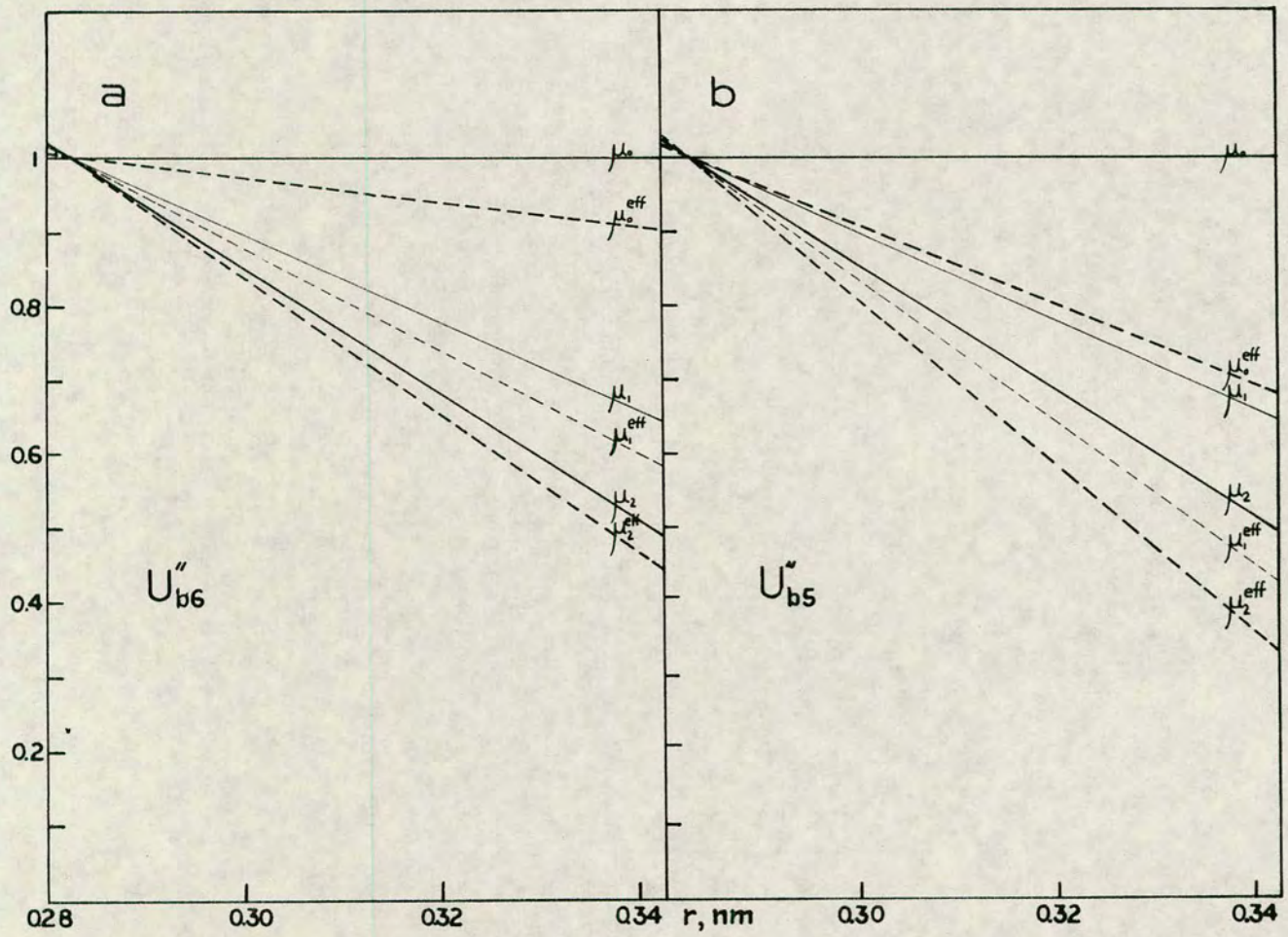

Fig. 5.9 μ_i - functions and corresponging μ_i^{eff} - functions for i = 0,1 and 2 for a. the potentials U'_{b1} and U''_{b6} and b. the potentials U'_{b1} and U''_{b5}.

μ_i function, the greater this effect. This is shown in figures 5.7 and 5.8 where the ratios for the calculated intensities of the spectra obtained by using μ_1 ($I\mu_1$) and μ_2 ($I\mu_2$) respectively over the calculated intensity for the spectra obtained by using μ_0 ($I\mu_0$) are plotted (I_{μ_i}/I_{μ_0}, i=1,2).

As shown in figure 5.4, a calculated spectrum for μ_0, U''_{b5} and even population distribution fits closely to a low pressure spectrum (0,6 torr,80 Nm^{-2}) for $HBr + Ar^*$. If μ_0 is replaced by a decreasing μ_i function, the calculated intensity on the low E″ side of the strongest peak decreases relative to the strongest peak and a poorer fit is obtained. The calculated spectrum for μ_0, U''_{b6} and even population distribution (figure 5.5),however,shows relatively too high intensity on the short E″ side of the strongest peak compared to the experimental spectrum. By replacing μ_0 with a decreasing μ_i function a better fit could be achieved. Thus the spectrum for μ_1 (U'_{b1}, U''_{b6} and even population distribution) in figure 5.8 fits better to the experimental spectrum than the corresponding spectrum for μ_0. It should be noted that the corresponding transition moment functions (μ_i^{eff}) for these two cases, μ_0^{eff} (for U''_{b5}) and μ_1^{eff} (for U''_{b6}) respectively are very similar (see figures 5.9 a and b) with a % decrease (defined as above) within the range 35-45%. Thus it is found that the fit of calculated and experimental spectra can be improved by a proper

choice of transition moment functions so as to obtain a closer fit of the overall intensity. A general feature of importance is that by varying the overall decrease in the transition moment in the FC region by use of simple functions (linear or approximately linear ones) the relative intensity in the overall calculated spectra can be controlled without affecting the positions of peaks or the total range of the spectra greatly.

c. Effect of changing the population distribution.

As mentioned previously the vibrational population distribution in the emitting states is not likely to be thermal. Judging from comparison with what there has been estimated for other noble gas halide systems the radiative lifetime of the ArBr B - state is expected to be in the order of 10-50 nsec. The lowest pressure results (0.6 torr, 80 Nm^{-2}) for the transition B-X should therefore be almost free of collisional relaxation and the corresponding spectra should approximately reflect radiative transitions from initial population distributions in the B-state. In fact it has already been mentioned that an even population distribution can provide a fairly good fit of a calculated spectrum to a low pressure MC spectrum for $HBr+Ar^*$ by a proper choice of a repulsive potential and a transition moment. More detailed studies of the effect of changing the vibrational population distribution on the shape of calculated spectra were carried out and will now be considered.

Figures 5.10, 5.11 and 5.12 show calculated spectra for the potentials U'_{b1}, U''_{b5}, μ_i-constant (μ_0) and various vibrational population distributions. The population distribution for a particular spectrum is shown on the same figure and is plotted as N(v′) vs v′ where N(v′) has been chosen such that the total sum equals 8 for all the spectra:

$$\sum_{v'=0}^{7} N(v') = 8 \qquad (5.6)$$

For a thermal distribution (T = 298°K), only the very lowest vibrational levels are populated as is shown in figure 5.10 (dashed curve). The corresponding spectrum (dashed curve) exhibits only one broad peak centered at E″(7) = 3500cm^{-1}*. As the population values in the higher vibrational levels increase relative to those in the lower vibrational levels, more structural variations appear and the spectra extend further to low E″. First there appear shoulders close to the strongest peak, which then gradually turn into clearly resolved peaks as in the case of an even population distribution. By increasing the population in the higher vibrational levels even more relative to that in the lower ones to obtain an inverse population distribution (figure 5.11), peaks are even more resolved; the ratio of a peak intensity to a nearest trough intensity increases. By a proper selection of population distributions the resolution or the peak to trough ratio could somewhat be controlled.

* 1cm^{-1} = 11.963 J mole^{-1}.

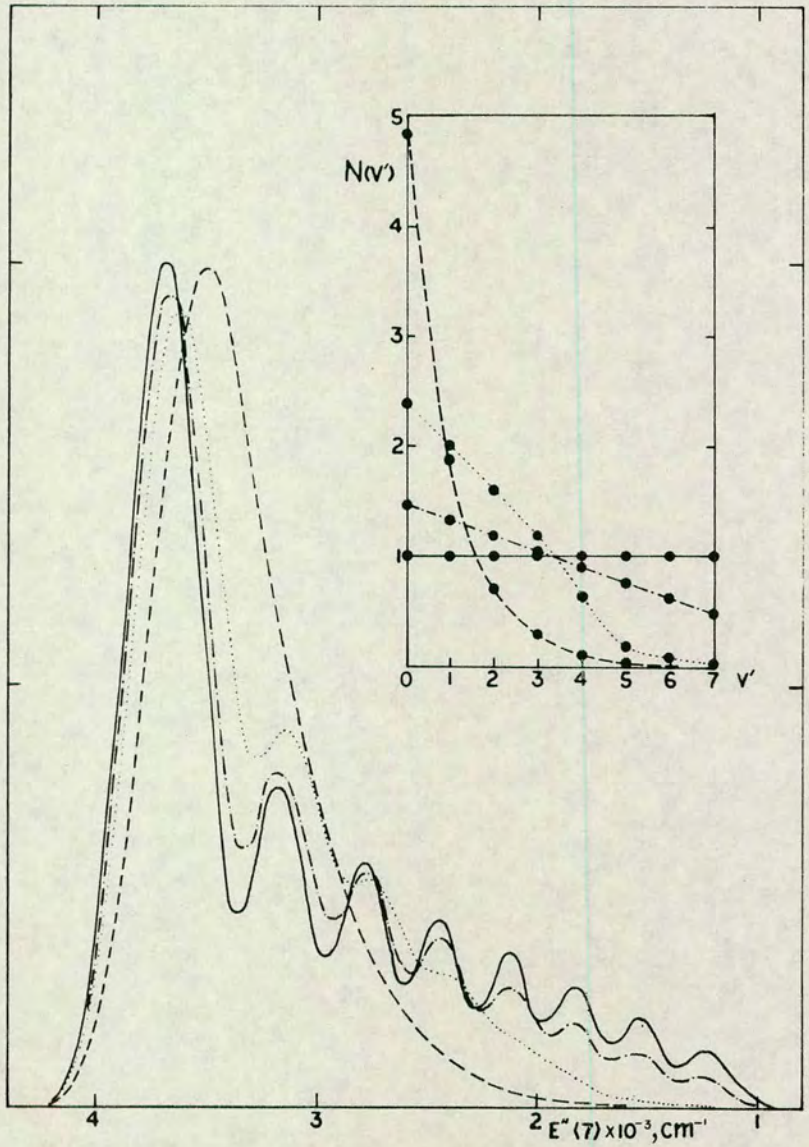

Fig. 5.10

See text on next page

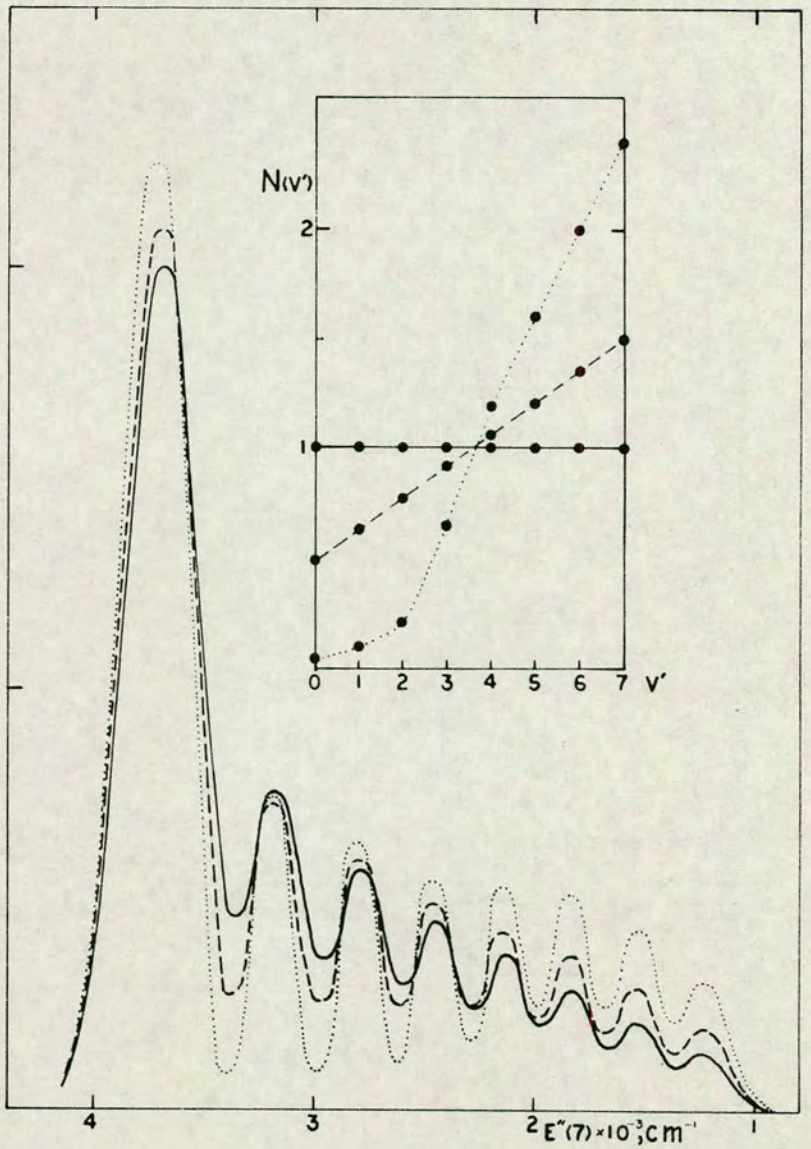

Fig. 5.11

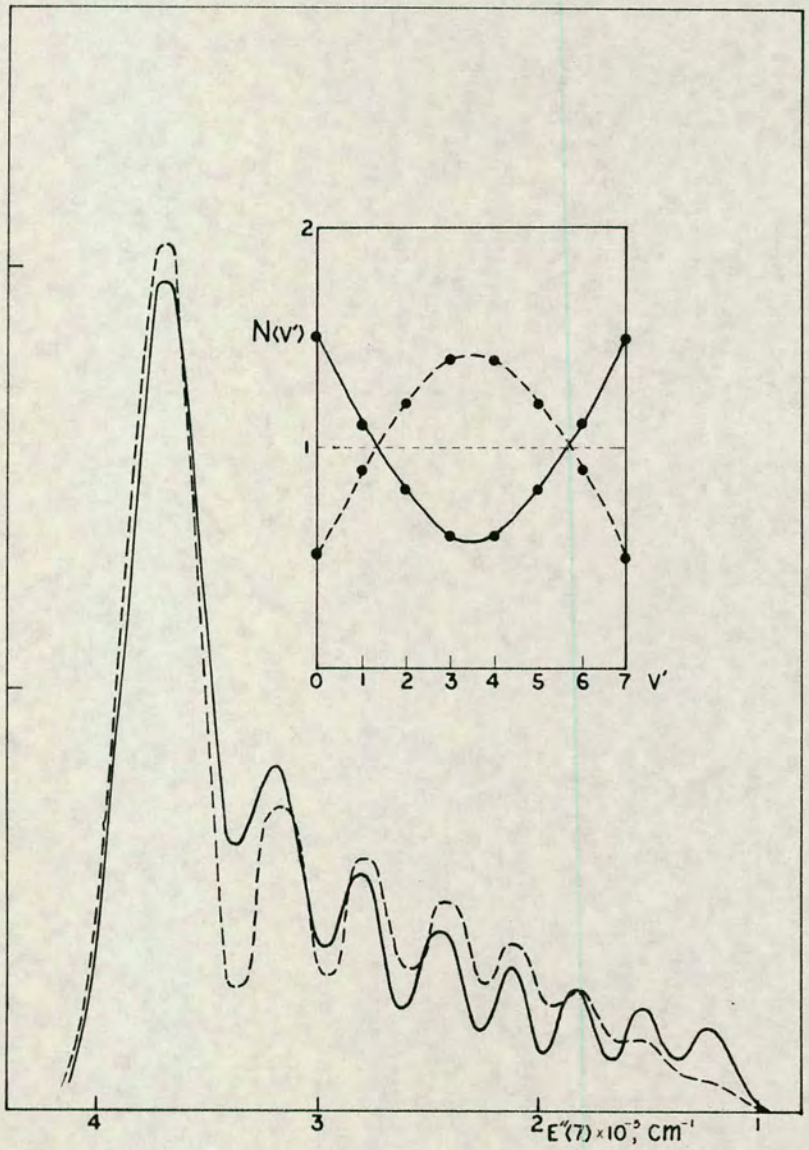

Fig. 5.12

Figures 5.10, 5.11, 5.12 Calculated spectra for transitions from U'_{b1}, $v' = 0\text{-}7$ to U''_{b5} for μ_i = constant (μ_0) and various vibrational population distributions (plotted as $N(v')$ vs v'). A particular calculated spectrum is drawn by a particular type of curve and is obtained for the vibrational distribution shown by dots through which a same type of curve is drawn. $1 cm^{-1} = 11.963$ J mole^{-1}.

An increase in the peak to trough ratio at high E'', where both v' contributions for higher and lower v' levels are of importance (see figure 5.4), is associated with a decrease in the population values for lower v' levels as well as an increase in the population values for the higher vibrational levels. An increase in this ratio at low E'', however, is mainly associated with a relative increase in the population values for the high v' levels. Thus by lowering the population values for the lowest and highest vibrational levels relative to those for the intermediate levels higher peak to trough ratios were achieved at high E'' than at low E''. The opposite effect was found in the case of a population distribution with a minimum for intermediate v' levels (figure 5.12).

It is of interest to compare the peak to trough ratios in experimental and calculated spectra. The calculated spectra which have been shown to fit the low pressure MC spectrum for HBr+Ar* reasonably well (the spectrum for U''_{b5}, μ_0 and N(v') = 1 for v' = 0-7 in figure 5.4 and spectrum for U''_{b6}, μ_1, N(v') = 1, v' = 0-7 in figure 5.8 mentioned in previous section) exhibit almost linear decrease in the ratio of a peak intensity to a nearest trough intensity with increasing distance from the strongest peak. This is shown in

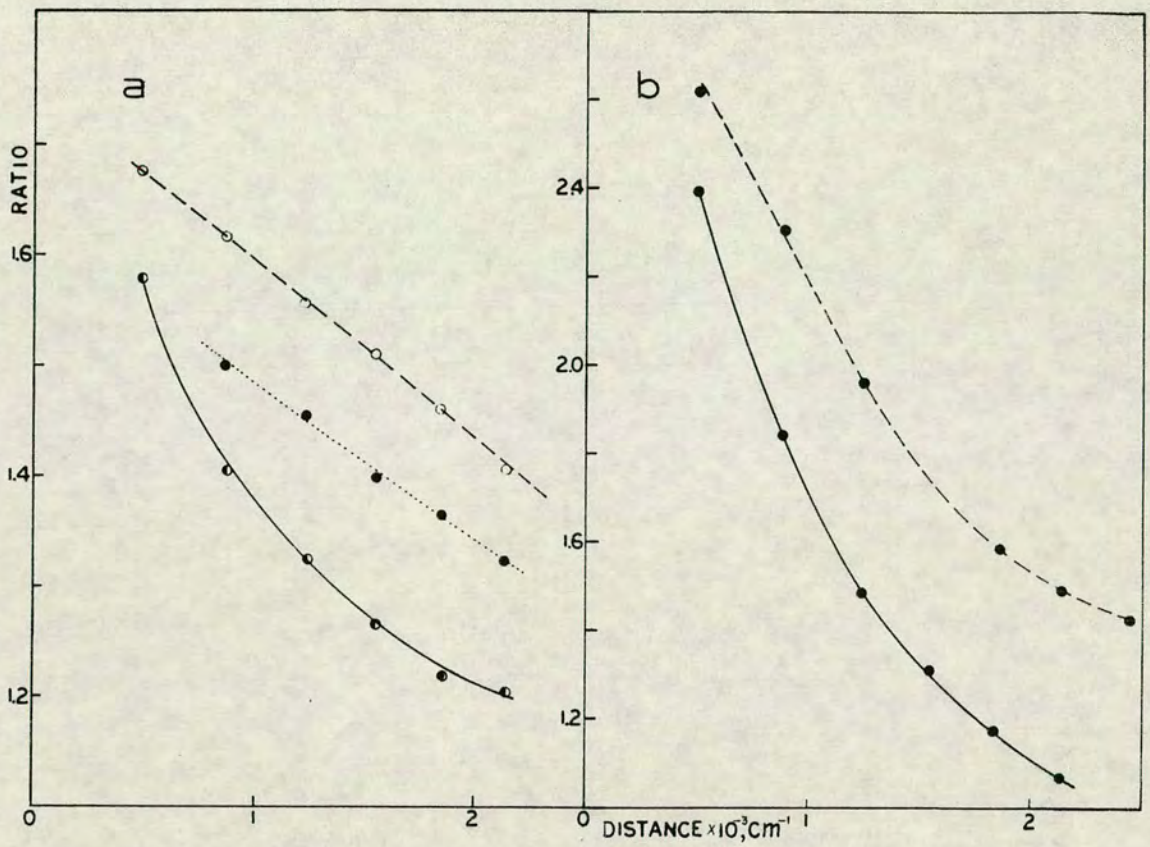

Fig. 5.13 Ratios of the intensity of a peak over the intensity of the nearest trough on the long wavelength (high E˝) side of the peak vs distance of peaks from the strongest (MC-) peak in calculated spectra and experimental ArBr, MC spectra. a. (- - 0 - -) for the calculated spectrum shown in figure 5.4 (for U'_{b1}, U'_{b5}, N(v′) = constant for v′= 0-7); (·····●·····) for the calculated spectrum shown in figure 5.5 (for U'_{b1}, U'_{b6}, N(v′)= constant for v′= 0-7); (——●——) for experimental ArBr, MC spectrum generated by Ar^*+HBr, 0.6 torr (80 Nm^{-2}). b. (- - ● - -) for the calculated spectrum shown in figure 5.11 (dashed curve); (——●——) for the calculated spectrum shown in figure 5.12 (dashed curve). $1cm^{-1} = 11.963\ J\ mole^{-1}$.

figure 5.13 a (broken and dotted curves). The experimental spectrum exhibits only a slight deviation from such linearity which suggests that the population distribution does not deviate greatly from being even (figure 5.13 a solid curve). However, the plot exhibits a slight positive curvature which is consistent with that observed for calculated spectra with higher vibrational levels more populated than lower levels. Peak to trough ratios for two such calculated spectra are shown in figure 5.13 b. Notice the difference in the ratio - scales for the two figures.

The characteristic effect of changing the vibrational population distribution and the above mentioned comparison of calculated and experimental spectra suggests that information on the population distribution in the emitting state (B - state) can be obtained from the finer details of the structure in the experimental spectra.

d. Vibrational population distributions in the B - state found from MC spectra for HBr + Ar^* and DBr + Ar^* by least square analyses.

The vibrational population distribution in the B - state has been calculated from various MC spectra for HBr + Ar^* and DBr + Ar^* from nonlinear least square analyses as described in chapter 4. Spectra for HBr + Ar^* obtained at 0.6 torr (80 Nm^{-2}) (250 μm slit width) and 4 torr (533 Nm^{-2}) (350 μm slit width and

500 μm slit width) were analysed as well as one spectrum for DBr + Ar^* (0.6 torr (80 Nm^{-2}), 500 μm slit width). The effects of using the two different potentials (U''_{b5}, U''_{b6}) and different linear μ_i functions (μ_0, μ_1) were considered. Some calculated population distributons are shown in figures 5.14 to 5.16.

Calculated population distributions obtained from the low pressure spectrum (0.6 torr, 80 Nm^{-2}) for HBr + Ar^* (shown in figure 5.14) show only a slight deviation from an even population distribution. All these calculated results show slightly smaller populations in the lower vibrational levels than in the higher levels while the populations in the very highest levels are relatively small.

The population distributons obtained from least square fit of the v´ contributions calculated for U'_{b1}, U''_{b5} where the linear μ_i moment functions, μ_1 and μ_0, were used are shown in figure 5.14 a and b respectively. Greater error limits were obtained for the population values for the individual vibrational levels where μ_1 was used. That is due to a poorer fit of the calculated and the experimental spectrum versus that which was obtained by using μ_0. Within error limits, the population distributions obtained from these two calculations differ insignificantly, however.

The calculated population values shown in figure 5.14 c obtained from a least square fit of the v´

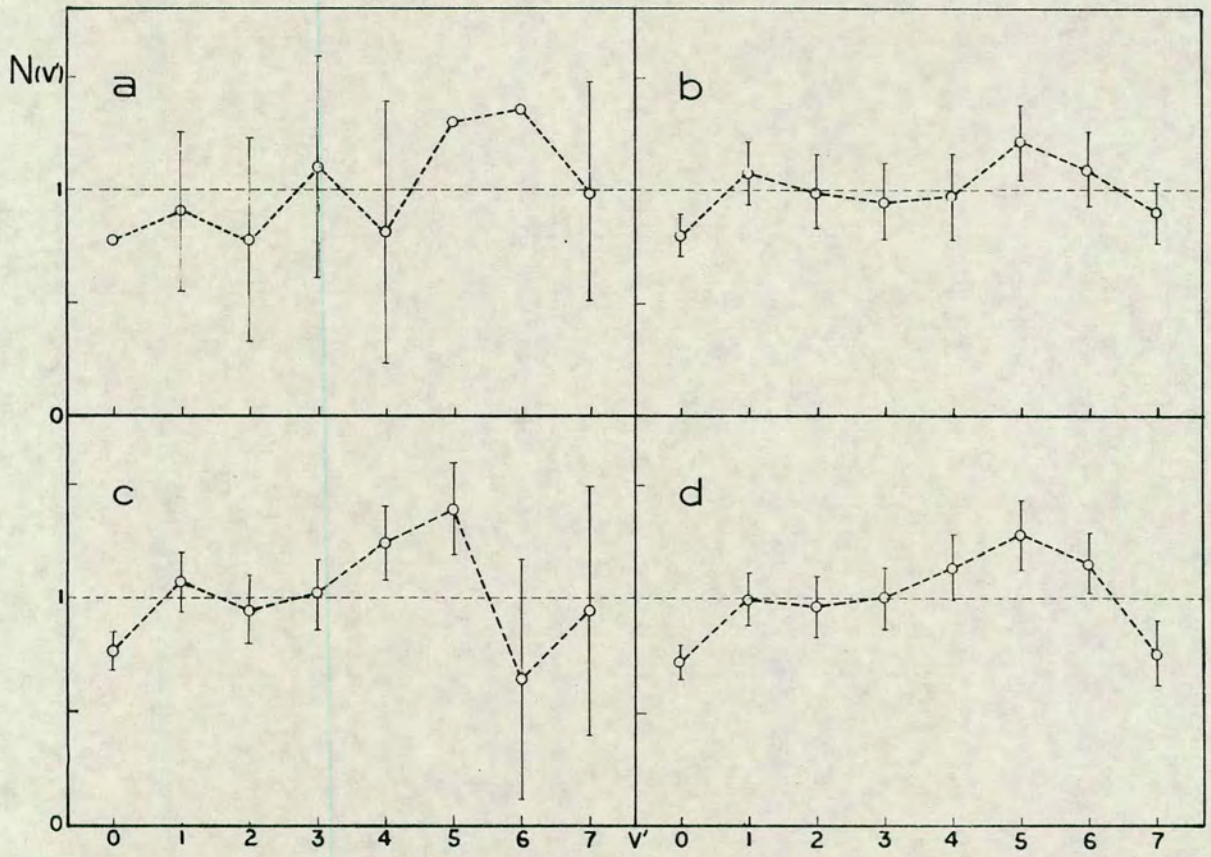

Fig. 5.14 Estimated vibrational population distributions in the B - state obtained from a ArBr , MC spectrum generated by $Ar^* + HBr$, 0.6 torr (80 Nm^{-2}), 250 μm slit width, from least square analysis by using vibrational contributions calculated for : a. U'_{b1}, U''_{b5}, μ_1, b. U'_{b1}, U''_{b5}, μ_0, c. U'_{b1}, U''_{b6}, μ_1 and d. U'_{b2}, U''_{b7}, μ_1. The population values satisfy: $\sum_{v'=0}^{7} N(v') = 8$.

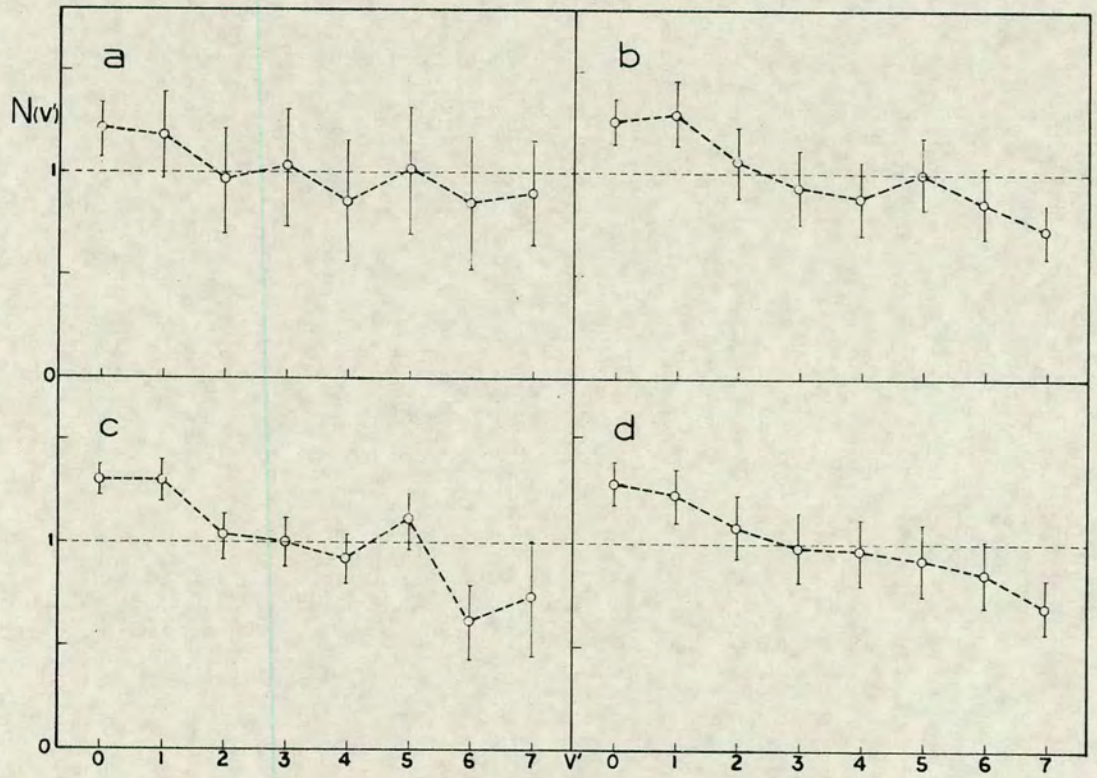

Fig. 5.15 Estimated vibrational population distributions in the B - state obtained from ArBr , MC spectra generated by $Ar^* + HBr$, 4.0 torr (533 Nm^{-2}), 500 μm slit width (a, b, c,) and 350 μm slit width (d), from least square analysis by using vibrational contributions calculated for : a. U'_{b1}, U''_{b5}, μ_1, b. U'_{b1}, U''_{b5}, μ_0, c. U'_{b1}, U''_{b6}, μ_1, d. U_{b1}', U''_{b5}, μ_0. The population values satisfy: $\sum_{v'=0}^{7} N(v') = 8$.

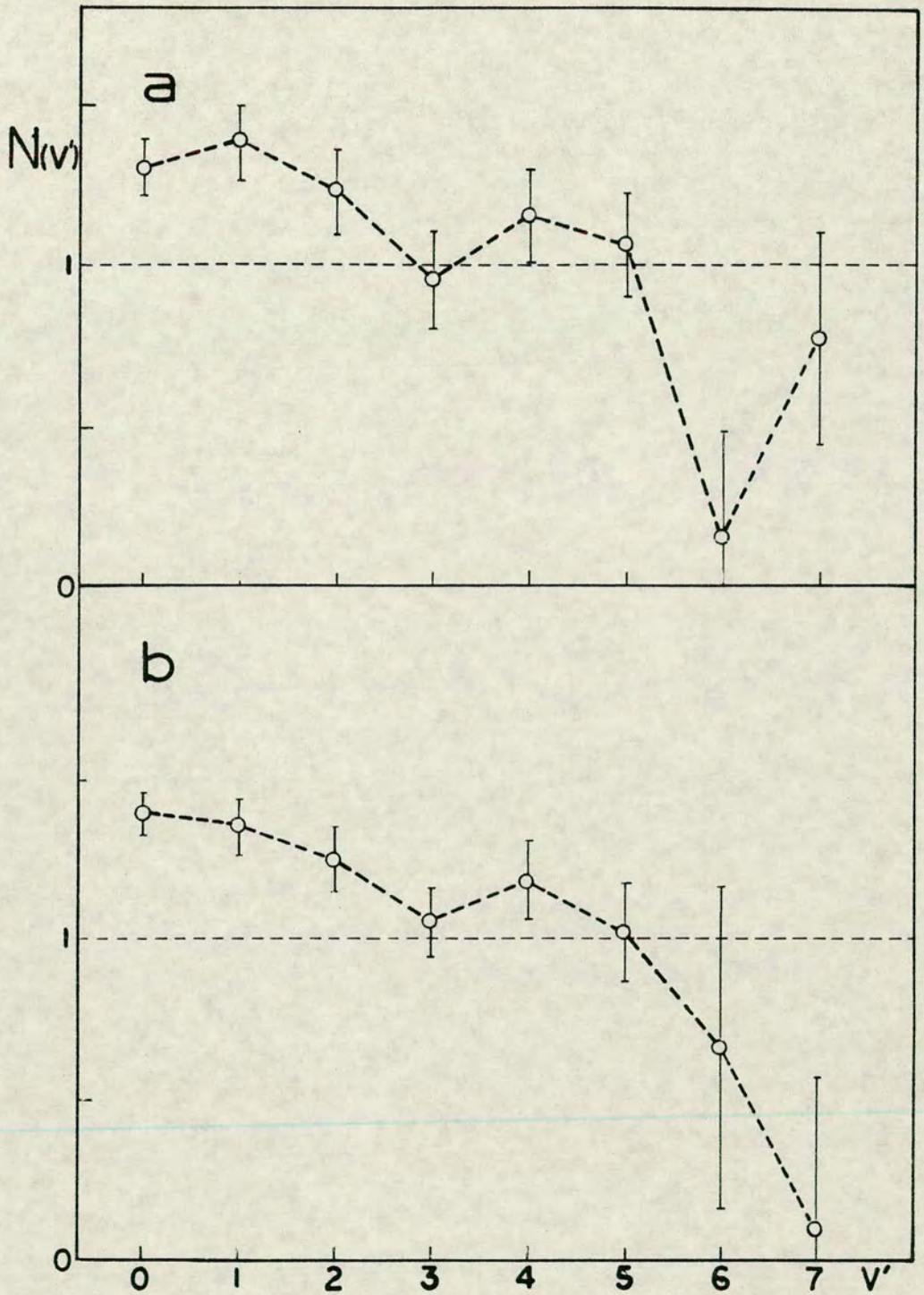

Fig. 5.16 Estimated vibrational population distributions in the B - state obtained from a ArBr, MC spectrum generated by Ar^{*}+DBr, 0.6 torr (80 Nm^{-2}), 500 μm slit width from least square analysis by using vibrational contributions calculated for : a. U'_{b1}, U''_{b5}, μ_0, b. U'_{b1}, U''_{b6}, μ_1. The population values satisfy : $\sum_{v'=0}^{7} N(v')=8$.

contributions for U'_{b1}, U''_{b6}, μ_1 are close to those obtained for U'_{b1}, U''_{b5}, μ_0 (figure 5.14 b) for the vibrational levels $v' = 0 - 5$. The population values for $v' = 6$ and $v' = 7$ are of great uncertainty, as the calculation of the vibrational contributions was not carried sufficiently far to low E'' (see figure 5.5).

The calculated population values shown in figure 5.14 d were obtained from least square fit of the v' contributions for U'_{b2}, U''_{b7} and μ_1. U'_{b2} has a lower frequency ($\omega_e = 185 cm^{-1}$) than U'_{b1} ($\omega_e = 194 cm^{-1}$)*. U''_{b7} (see table 5.1) is an exponential potential selected to give an equivalent spacing between peaks and the same total spectral range as the experimental spectrum by use of eight vibrational levels ($v' = 0-7$). The calculated population distribution is very similar to that found for U'_{b1}, U''_{b5}, μ_0 (figure 5.14 b) and for $v' = 0-5$ for U'_{b1}, U''_{b6}, μ_1 (figure 5.14 c). The error limits for these results are less than for any of the other results and the population distribution is chosen to represent the best estimate of the initial vibrational population distribution in the ArBr B - state for $HBr + Ar^*$. It is tabulated in table 5.6.

The calculated population distributions obtained from the MC spectrum for $HBr+Ar^*$ at higher pressures (4 torr, 533 Nm^{-2}) show an overall decrease in population from lower to higher vibrational levels (figure 5.15). The change in the population distribution from that observed at a lower pressure

* $1 cm^{-1} = 3\ 10^{10}\ s^{-1}$.

(figure 5.14) is consistent with the occurence of a vibrational relaxation in the B - state. The calculated population distributions shown in figure 5.15 differ only slightly for the different calculations, mentioned in the text of the figure. The population distribution shown in figure 5.15 d and listed in table 5.6 was obtained from analysis of a spectrum which was recorded in Pittsburgh by Dr M.F. Golde while the other results were obtained from a spectrum recorded in Edinburgh. The less irregular population distribution obtained from this simulation is thought to be in part due to the absence of ghost lines associated with bromine atomic lines which were observed in the spectra from Edinburgh.

Table 5.6

Selected best estimates for relative vibrational population values (N(v′)) in the ArBr, B - state for HBr + Ar^* (0.6 torr and 4.0 torr) and DBr + Ar^* (0.6 torr). The N(v′) - values satisfy:

$$\sum_{v'=0}^{7} N(v') = 8$$

	HBr + Ar^*				DBr + Ar^*	
	0.6 torr		4.0 torr		0.6 torr	
v′	N(v′)	σ(v′)	N(v′)	σ(v′)	N(v′)	σ(v′)
0	0.717	0.075	1.287	0.103	1.390	0.065
1	0.995	0.112	1.228	0.132	1.353	0.093
2	0.960	0.131	1.076	0.152	1.247	0.104
3	1.002	0.133	0.982	0.167	1.055	0.110
4	1.134	0.143	0.960	0.162	1.176	0.119
5	1.283	0.148	0.919	0.172	1.018	0.148
6	1.150	0.129	0.854	0.160	0.667	0.500
7	0.759	0.135	0.695	0.127	0.094	0.474

1 torr = 133.322 Nm^{-2}.

Calculated population distributions obtained from a low pressure (0.6 torr, 80 Nm^{-2}) spectrum of the MC for DBr + Ar^* from least square analyses of the v′ contributions for U'_{b1}, U''_{b5}, μ_0 and U'_{b1}, U''_{b6}, μ_1 are shown in figures 5.16 a and b respectively. The population decreases with an increase in vibrational quantum number. The relative population in the very highest vibrational levels (v′=6 and 7) is especially low. These calculation results are fairly consistent with one another. The less irregular distribution in figure 5.16 b is tabulated in table 5.6.

As mentioned previously, a change in the population distribution is associated with a change in the structure of the spectra, such as a change in the relative peak to trough ratios (see figures 5.10-5.13). The relatively small effect of making slight changes to the potentials and the μ_i functions on the calculated population distributions is therefore of great interest. It suggests that the effects of these changes on those features in the structure which clearly are affected by the population distribution are relatively unimportant. This agrees with what has already been shown for changes in U''_{bi} and μ_i (figure 5.13 a).

The effect of the underlying C-A(3/2) emission in the MC on the calculated population distribution has to be considered. This underlying contribution is expected to decrease to shorter wavelength with a broad oscillatory structure (this will be delt with in more detail later

in this chapter). This underlying continuum is not expected to have a great effect on the structure of the B-X spectrum. Thus the change in the peak to trough ratios will not be affected greatly, nor will the calculated population distribution.

5.122 SC for $CH_2Br_2 + Ar^*$, HBr + Ar^* and DBr + Ar^*

Due to the overlap of the C-A(3/2) - and the B-X - spectra in the MC region, the simulation calculations for the C-A(3/2) spectra were basically limited to the SC region - the long wavelength end of the C-A(3/2) spectra. This fact and the lack of structure in the SC made the simulation calculations for the C-A(3/2) spectra more difficult than the calculations for the B-X spectra. One basic problem was that the number of the emitting vibrational levels could not be determined directly from the experimental spectra.

The spectra for $CH_2Br_2 + Ar^*$ show the relatively strong SC spectra with two distinct peaks. A low pressure (0.6 torr, 80 Nm^{-2}) SC spectrum for $CH_2Br_2 + Ar^*$ was selected as a basis for performing detailed simulation calculations where the effects of the

various parameters were considered. Selected parameters from these calculations ("best" parameters) were then used in simulation calculations for a higher pressure spectrum for $CH_2Br_2 + Ar^*$- as well as for HBr+Ar*- and DBr + Ar* spectra.

a. Effect of changing the lower state potential.

As mentioned previously U'_{b1} was also used to represent the C - state potential. The uncertainty in the position of the C - state causes equally great uncertainty in the position of the A(3/2) - state. To be consistent with the results of the simulation calculations for the MC spectra, only repulsive model potentials which gave calculated spectra at higher E'' than the calculated MC spectra were tried in the simulation calculations for the SC for CH_2Br_2+ Ar*. In the experimental spectrum (0.6 torr, 80 Nm^{-2}) the energy difference between the positions of the strongest SC peak and the strongest MC peak is about 2472 cm^{-1} (29570 J $mole^{-1}$). Compared to the calculated MC spectra where the lower potentials U''_{b5} and U''_{b6} were used, this would correspond to positions of the strongest SC - peak on the E''(7) - scale of about E''(7) = 6152 cm^{-1} (73600 J $mole^{-1}$) and E''(7) = 5772 cm^{-1} (69050 J $mole^{-1}$) respectively. It is therefore reasonable to restrict the choice of the model potentials to those which make the strongest peak (or the outermost peak on the high E'' end) of the

calculated spectra not lie much outside this range (5772 - 6152 cm^{-1}; 73600 - 69050 J $mole^{-1}$). Various calculated spectra were obtained by use of repulsive potentials of greater energy and slope than the repulsive potentials used in the MC - simulation. Several such potentials are tabulated in table 5.7, some of which are shown in figure 5.17. The potentials shown in figure 5.17 cross at about 0.308 nm internuclear distance and have different slopes. As a first approximation it was decided to use the same number of emitting vibrational levels as in the B - state ($v' = 0-7$). The corresponding calculated spectra for even population distribution and μ_i=constant (μ_0) are shown in figure 5.18. In agreement with earlier observations, the structure gets broader and the spacing between peaks increases as the slope of the lower potential increases. Also for these particular potentials the spectra extend further to high E'' as the slope increases.

In order to obtain the same spacing between the two outermost peaks, as observed in the SC spectrum for $CH_2Br_2 + Ar^*$, the slope of the lower potential has to be increased over that for the repulsive potentials used in the simulation calculations for the MC (U''_{b5} and U''_{b6}). Thus the spectrum in figure 5.18 for U''_{b12} (see table 5.7) exhibits approximately the same spacing between peaks as in the experimental spectrum - 1240 cm^{-1} (14830 J $mole^{-1}$). However, this spectrum

Table 5.7

Repulsive lower state potential curves, U''_{bi} (cm^{-1}) used in simulation calculations for ArBr, SC spectra. r is expressed in nm.

i	a	b	Type of potential U''_{bi}
8	69.78	0.1835	$a/(r-b)^2$
9	39.50	0.2138	"
10	34.66	0.2195	"
11	32.81	0.2222	"
12	30.13	0.2256	"
13	26.74	0.2301	"
14	$8.925\ 10^7$	0.02991	$a \exp(-r/b)$
15	$3.292\ 10^7$	0.03383	"
16	$7.530\ 10^7$	0.03052	"

$1 cm^{-1} = 11.963\ J\ mole^{-1}$.

extends too far to high E″, which suggests that the U''_{b12} potential is too high in energy. It will be shown later however that the position of the peaks varies with the number of emitting vibrational levels as well as energy of the lower potential.

The overall shape of the spectra in figure 5.18 is far from that observed in the SC spectrum for $CH_2Br_2+Ar^*$ (see figures 3.8 and 3.9). The ratio of the two peaks (the intensity of the outermost peak over the intensity of the second outermost peak) is much too low. This may be corrected by using a μ_i function which decreases with internuclear distance or by changing the population distribution.

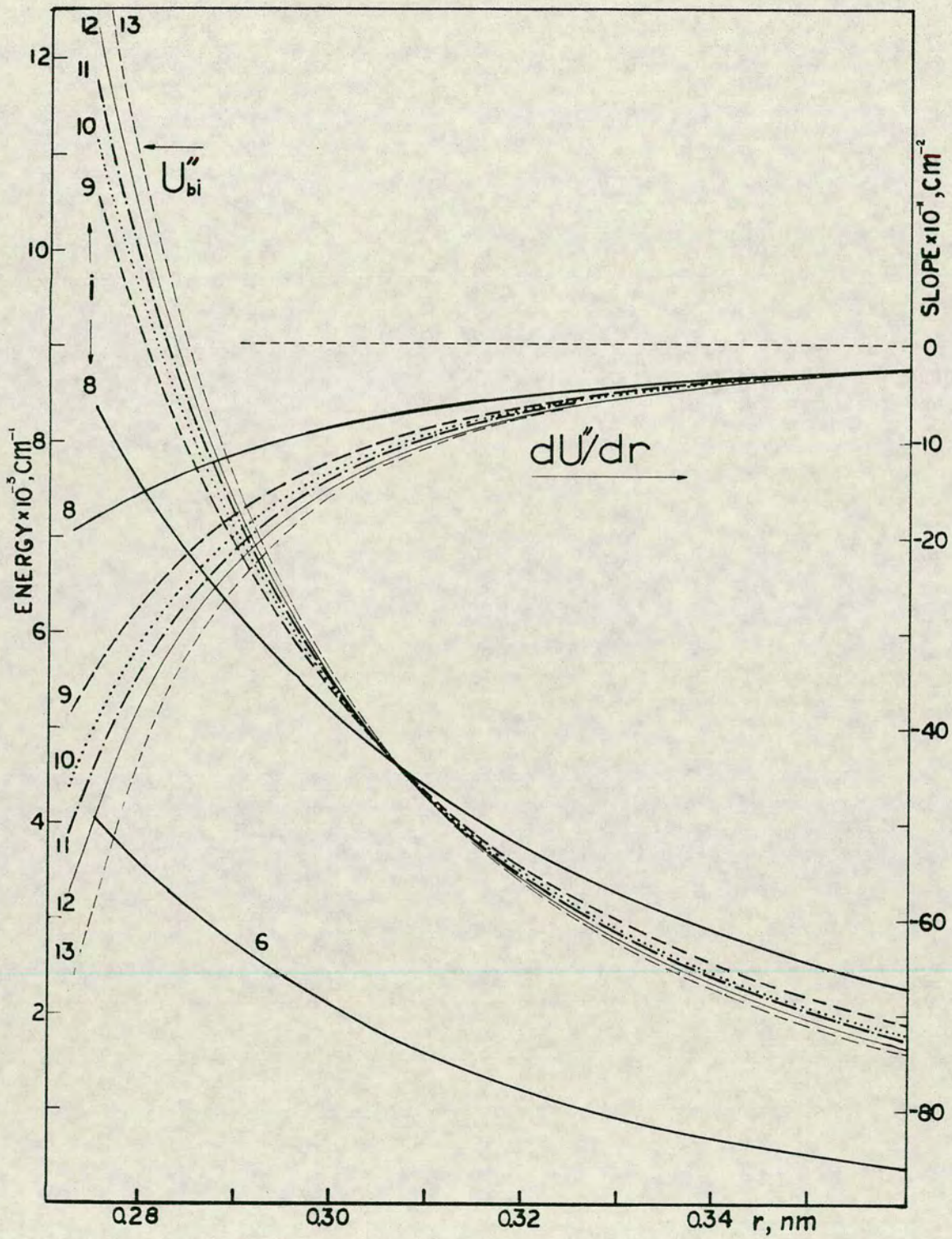

Fig. 5.17 Repulsive potential curves, U''_{bi} (i=7-12), and the slopes of these, dU''_{bi}/dr. $1cm^{-1} = 11.963\ J\ mole^{-1}$.

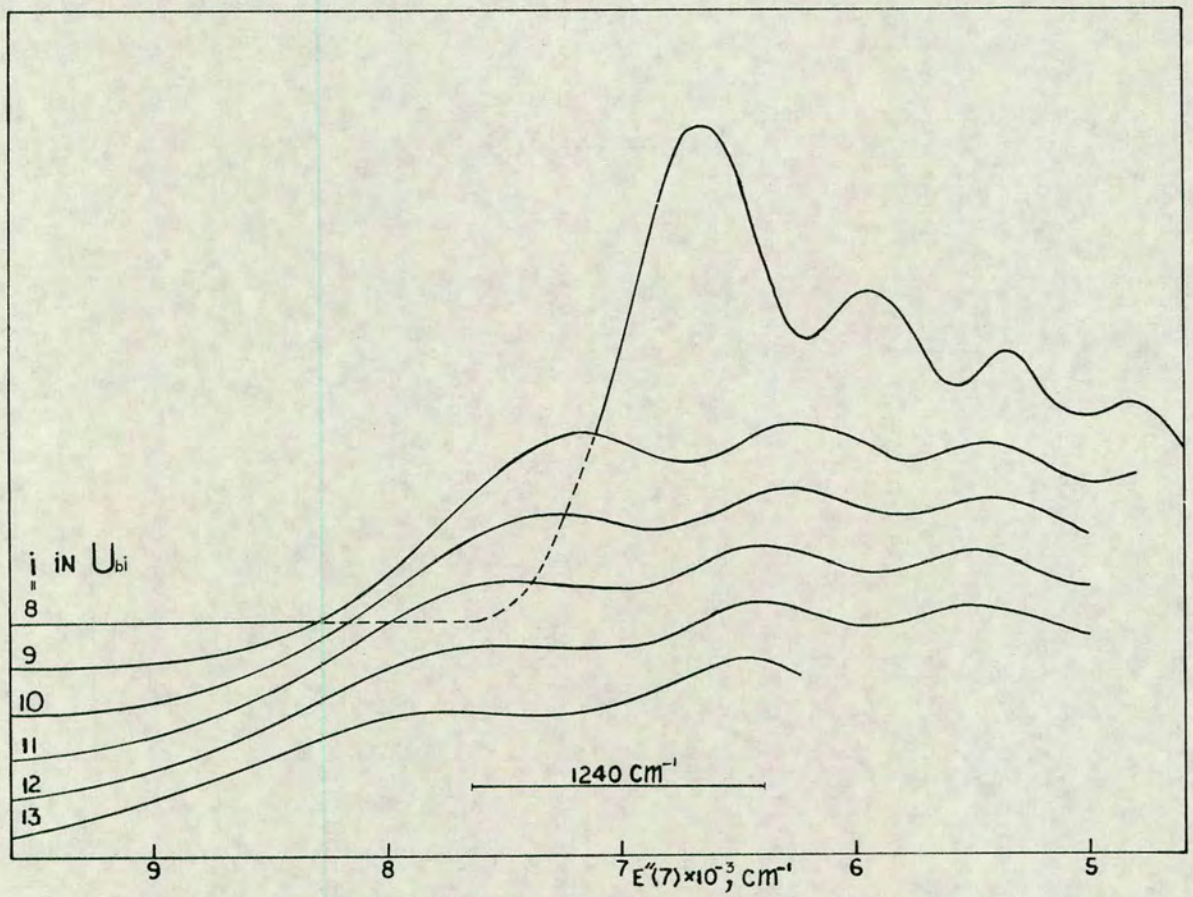

Fig. 5.18 Calculated spectra for transitions from U'_{b1}, $v'=0$-7 to U''_{bi} for $i = 7$-12, μ_i=constant (μ_0) and even vibrational population distribution. 1240cm^{-1} is the approximate energy difference between peaks in the ArBr, SC spectrum generated by $Ar^* + C\ H_2Br_2$. 1cm^{-1} = 11.963 J mole^{-1}.

b. Effect of changing the transition moment.

Ab initio calculations show the transition moments for the C-A(3/2) transitions for other noble gas halide systems to be significantly lower than for the B-X transitions in the region of r_e.[53-56] The overall % decrease in the transition moments with increasing internuclear distance in the region of r_e is found to be greater for the C-A(3/2) transitions than for the B-X transitions (see figure 1.5 and 1.6)

From plots of the various calculated transition moments[53-56] vs internuclear distances, values for % decrease over intervals in the region of r_e corresponding to the separation of the classical turning points for $v'=7$ for U'_{b1} from r_e of U'_{b1} were obtained (table 5.8). The low and the high limits of the intervals (r_l and r_h respectively) were determined from

$$\begin{aligned} r_l &= r_e - 0.027 \text{ (nm)} \\ r_h &= r_e + 0.039 \text{ (nm)} \end{aligned} \qquad (5.7)$$

It is of interest to compare the % decrease in the transition moments for the B-X transitions in other systems with the similarly defined % decrease for the transition moment functions (μ_i^{eff}) and the corresponding μ_i functions which were used in the MC simulations. The μ_I function which was used in the simulation calculations for U''_{b6} (exponential potential) has a comparable % decrease (table 5.5) to that of the transition moments for the xenon halides and KrF.

Table 5.8

Percent decrease in transition moment functions over intervals defined as described in the text for B-X and C-A(3/2) transitions for various noble gas halide systems, obtained from ab initio calculations.[53-56]

Noble gas halides	% decrease B-X	C-A(3/2)
ArF	21	70
KrF	40	73
XeF	35	71
XeCl	45	63
XeBr	48	61

The same is true for the corresponding transition moment function (μ_1^{eff}) since it is only slightly different from μ_1 (figure 5.9). To be consistent with this, linear μ_i functions with values for % decrease of similar magnitudes as those for the transition moments for the C-A(3/2) transitions for other systems were tried in the simulation calculations for the C-A(3/2) spectra, and exponential lower potentials were used (U''_{bi}, i = 14-16). Three such μ_i functions are tabulated in table 5.9.

The effect of including these μ_i functions on calculated spectra is shown in figure 5.19. These spectra were obtained for U'_{b1}, even population distribution for v' = 0-7 and U''_{b14} (table 5.7) and are normalized in such a way that they have the same height at E''(7) = 6750 cm^{-1} (80750 J $mole^{-1}$). The effect of including these μ_i functions in the calculations is

Table 5.9

μ_i functions : $\mu_i = a \cdot r + b$ (cm^{-1}), i = 3,4,5 and percent decrease in μ_i over an interval $[r_1, r_2]$, where r_1 and r_2 are the classical turning points for v′ = 7, U'_{b1}. r is expressed in nm.

i	a	b	% decrease
3	-16.3	6.36	61.2
4	-20.1	7.43	75.3
5	-23.9	8.49	89.5

$1 cm^{-1} = 11.693$ J $mole^{-1}$.

analogous to the effect noticed in the MC simulations (figures 5.7 and 5.8). It causes a steady decrease in the intensity with decreasing E″ and the greater the % decrease of the μ_i function, the greater this effect. Due to the great lowering in the relative intensities by use of these μ_i functions, a shift of peaks to high E″ also occurs.

The v′- contributions of the spectra for μ_0 and μ_4 are shown in figures 5.20 and 5.21 respectively as well as the total spectra. Comparison of these figures shows how the effect of including decreasing μ_i functions (μ_4) on the change in shape of calculated spectra reflects an analogous change in shape of the vibrational contributions.

A lowering of the second outermost peak relative to the outermost peak at the high E″ end of these spectra is a consequence of increasing the % decrease of the μ_i function. However, the ratio of these peaks

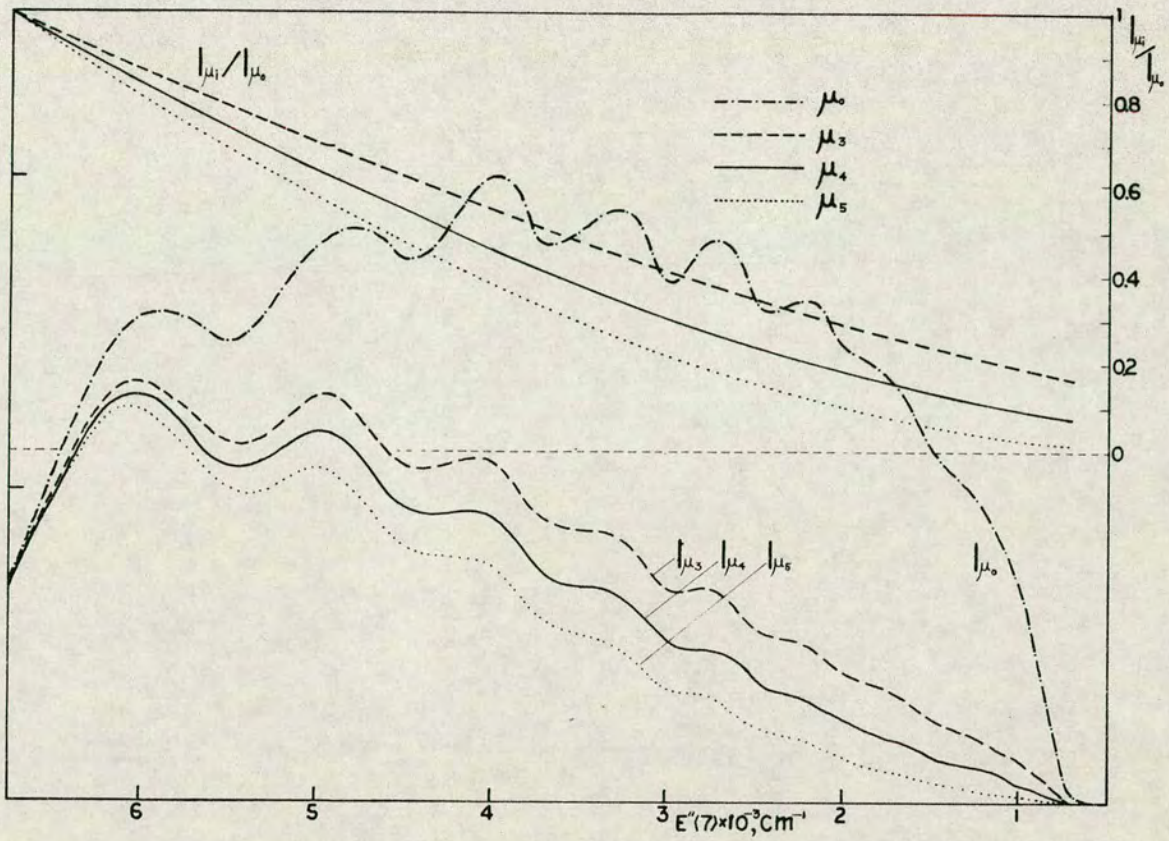

Fig. 5.19 Calculated spectra for transitions from U'_{b1}, $v' = 0$-7 to U''_{b14} for even vibrational population distribution and four different μ_i- functions, μ_0, μ_3, μ_4, μ_5. The calculated spectra are normalized such that they have the same intensity at $E''(7) = 6750 cm^{-1}$. The top curves (I_{μ_i}/I_{0}) represent the ratios for the calculated intensities of the spectra obtained by using $\mu_i(I_{\mu_i})$, $i = 3,4,5$, over the calculated intensity for the spectrum obtained by using $\mu_0(I_{\mu_0})$. $1 cm^{-1} = 11.963$ J mole^{-1}.

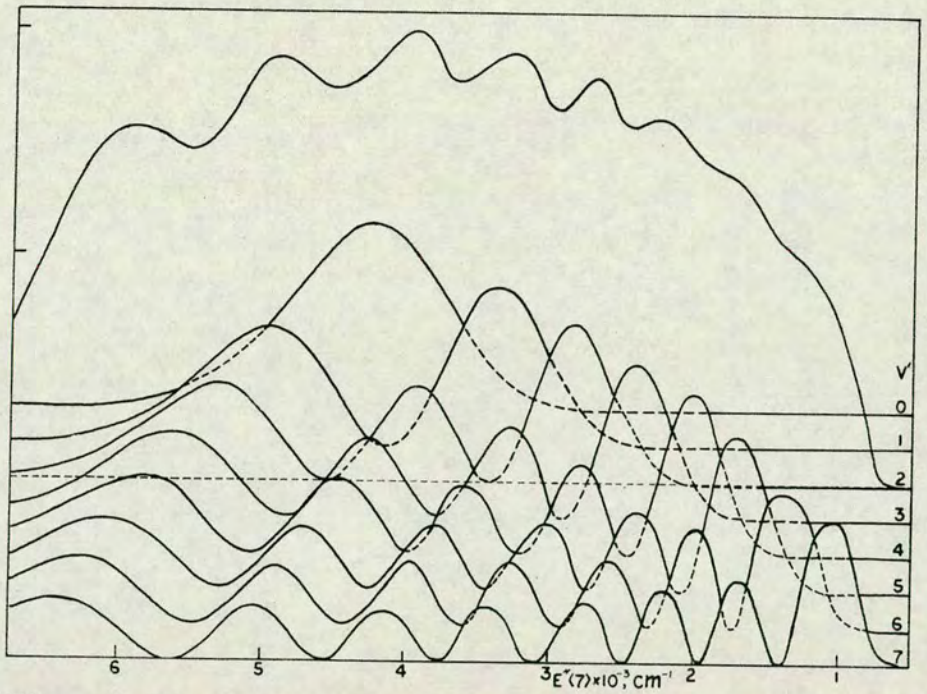

Fig. 5.20 Calculated spectrum and vibrational contributions for transitions from U'_{b1}, $v' = 0\text{-}7$, to U''_{b14} for even vibrational population distribution and μ_i=constant (μ_0).

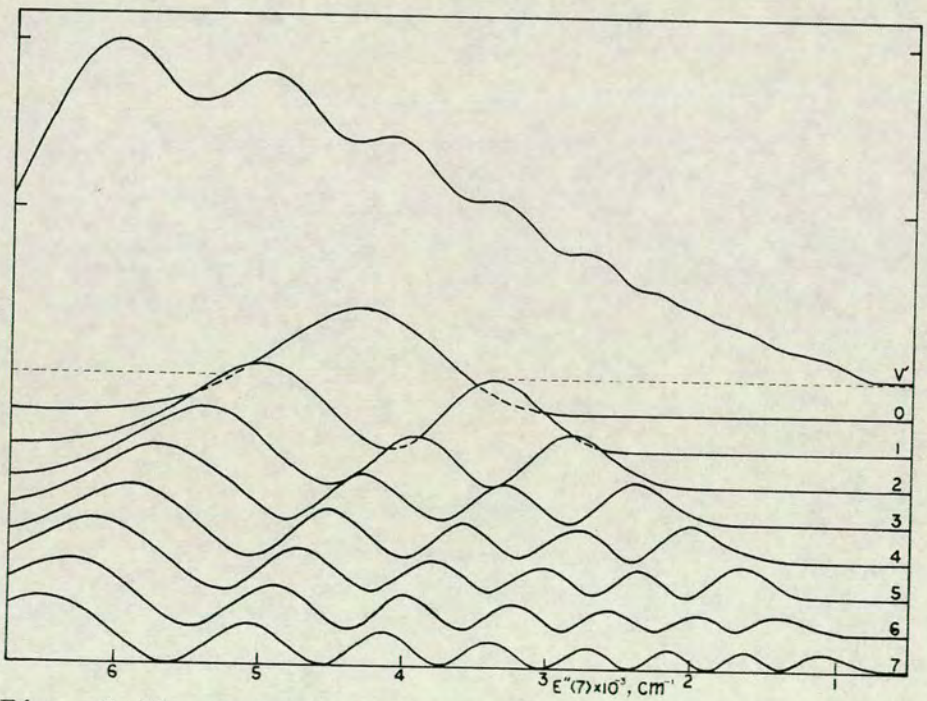

Fig. 5.21 Calculated spectrum and vibrational contributions for transitions from U'_{b1}, $v' = 0\text{-}7$, to U''_{b14} for even vibrational population distribution and the μ_4-function.
$1 cm^{-1} = 11.963$ J mole^{-1}.

(the intensity of the outermost peak over the intensity of the second outermost peak) is far from that observed in the low pressure spectrum from $CH_2Br + Ar^*$ (0.6 torr, 80 Nm^{-2}) (figures 3.8 and 3.9) for any of the calculated spectra in figure 5.19.

c. Effect of changing the population distribution.

The effect of changes in the population distribution in eight vibrational levels ($v' = 0-7$) on the shape of calculated spectra for U'_{b1}, U''_{b14} and μ_4 is shown in figure 5.22. The population values which are also shown in the same figure satisfy equation 5.6. The spectra change from showing only one broad peak when contributions from the lowest vibrational levels are dominating (spectrum ① in figure 5.22) to showing an oscillatory structure with eight peaks (level ④) when contributions from the highest vibrational levels are dominating. The intensity of the intermediate region of the spectra lowers as the population in the higher v' levels increases relative to the population in the lower v' levels, while the intensity in the outer regions increases. This is consistent with the fact that the main contributions from the lowest vibrational levels are in the intermediate region while the contributions from the higher vibrational levels also extend to the outer regions, as shown in figure 5.21. This causes an increase in the ratio of the intensity of the strongest outermost peak over the

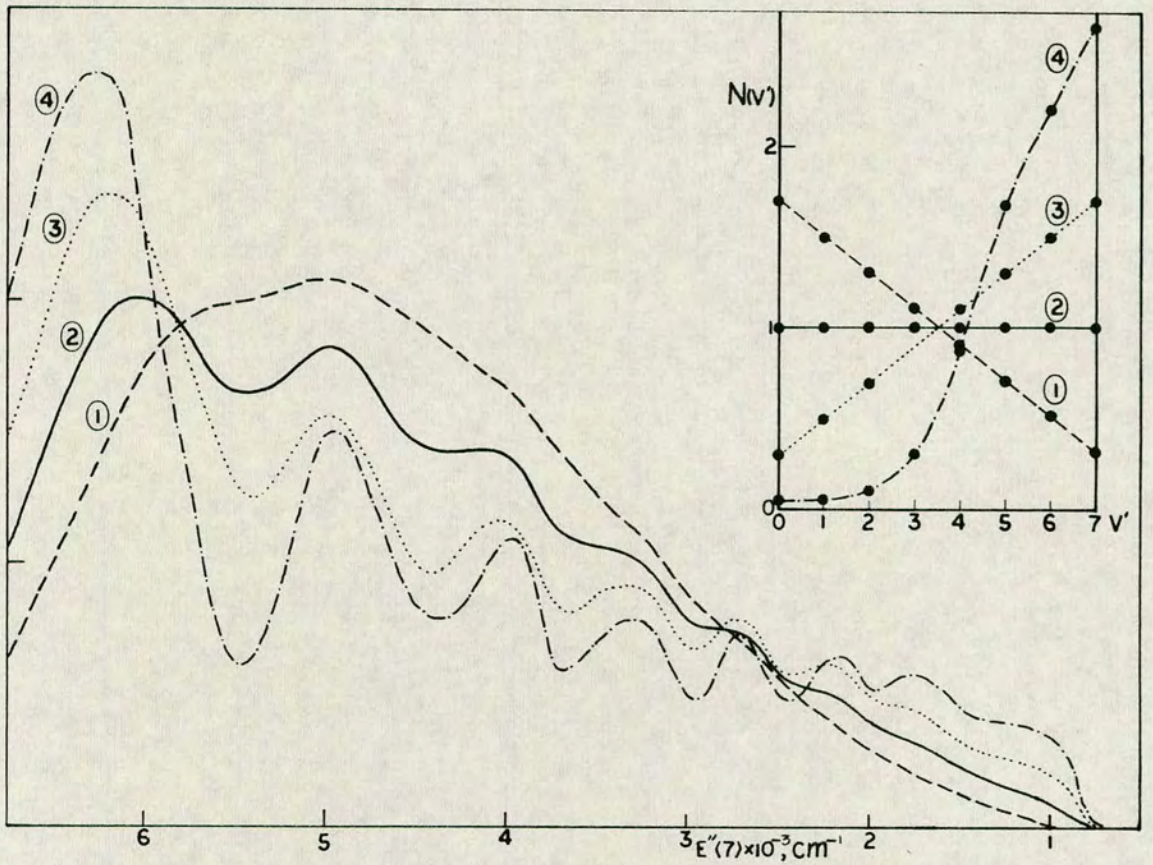

Fig. 5.22 Calculated spectra for transitions from U'_{b1}, v′=0-7 to U''_{b14} for the μ_4 - function and various vibrational population distributions (plotted as N(v′) vs v′). A particular calculated spectrum is drawn by a particular type of curve and is obtained for the vibrational distribution shown by dots through which a same type of curve is drawn. $1 cm^{-1} = 11.963$ J mole^{-1}.

intensity of the second outermost peak. Also the strongest outermost peak shifts further to high E″. This is due to the great displacement of the outermost peaks of the v′ contributions to higher E″ as the vibrational quantum number increases (figure 5.21). For the particular choice of population distributions shown in figure 5.22, other peaks than the outermost peak at the long E″ end of the total spectra show an insignificant shift. Due to this fact the spacing between the two outermost peaks increases as the population in the higher v′ levels increases relative to the population in the lower v′levels.

The characteristic changes in the peak to trough ratios with changes in the population distributions which were found to occur in the MC simulation calculations were also found in these calculations. By varying the population distribution the ratio of the intensities of the two outermost peaks and the ratios of these over the intensity of the trough between these could be changed so as to fit the low pressure SC spectrum for $CH_2Br_2 + Ar^*$. Only an inverse population distribution could account for that structure. This will be shown later in this chapter.

Hitherto the assumption has been made that the number of the emitting vibrational levels is the same as in the B-state - a total of eight levels. The effect of changing the total number of the emitting levels on the calculated spectra was also considered.

Due to the similar energies of the C- and the B- states, a great difference in the number of the emitting v′ levels for these two states is not expected. In the calculations, the assumption was made that a total of 8 v′ levels or fewer are contributing to the total C-A(3/2) spectra - v′ = 0-v'_{max}, where v'_{max} is the maximum vibrational level (v'_{max} = 7).

Spectra for different v'_{max} are shown in figure 5.23. These are for U'_{b1}, U''_{b14}, μ_4 and even population distribution where the population values (N(v′)) were chosen such that

$$\sum_{v'=0}^{v'_{max}} N(v') = 8 \text{ for } v'_{max} = 1\text{-}7 \qquad (5.7)$$

The spectrum for v'_{max} = 0 is identical to the v′ = 0 contribution which is shown at the bottom of the figure. The spectrum for v'_{max} = 7 is the same as shown earlier (figures 5.19, 5.21 and 5.22).

One effect of using $v'_{max} < 7$ on the spectra is that of shortening the total spectral range (figure 5.23). The total range is determined by the range of the v'_{max} - contribution which gets shorter with lowering of v'_{max} (see figure 5.21). Another consequence of using $v'_{max} < 7$ is that the ratio of the outermost peak to the second outermost peak near the high E″ end increases with lowering of v'_{max}. The spacing between the two outermost peaks however does not differ appreciably.

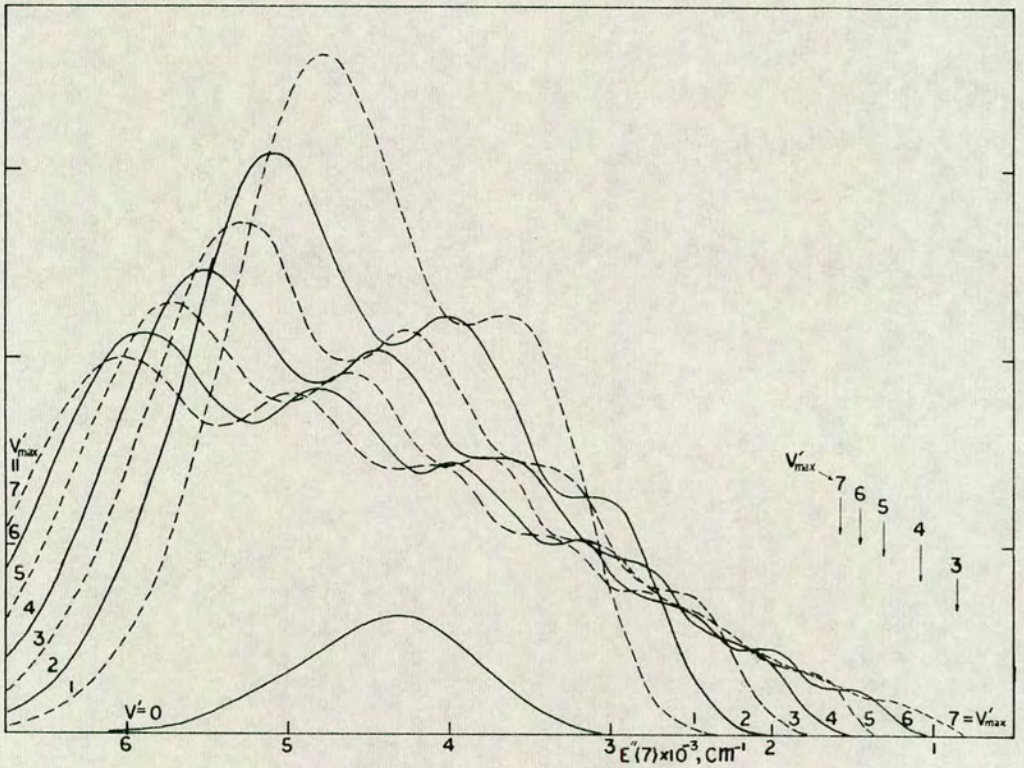

Fig. 5.23 Calculated spectra for transitions from U'_{b1} to U''_{b14} for the μ_4 - function and even vibrational population distributions in the vibrational levels $v'=0-v'_{max}$, where $v'_{max}= 1-7$. The $v'=0$ contribution is also shown. The arrows represent positions at $4500cm^{-1}$ distance from the strongest peaks in the various calculated spectra (characterized by the v'_{max} values) and correspond to an estimated short wavelength limit for the C-A(3/2) spectrum in $Ar^{*}+CH_2Br_2$. $1cm^{-1} = 11.963$ J mole^{-1}.

Judging from the pressure dependence of the MC spectrum for $CH_2Br_2 + Ar^*$, there appears to be a C-A(3/2) spectral contribution at about 160.2nm as discussed earlier (section 3.122). The rapid fall off in the intensity of the spectrum on the short wavelength side of the peak at 159.7nm (see figure 3.8) suggests that the outermost peak near the short wavelength end of the C-A(3/2) spectrum is placed near there (see figure 3.8). This corresponds to a distance of about 4500 cm^{-1} (53830 J $mole^{-1}$) from the strongest peak in the SC at low pressure (0.6 torr, 80 Nm^{-2}). The arrows in figure 5.23 represent the positions corresponding to this distance from the strongest peaks in the calculated spectra (characterized by the v'_{max} values). This shows that the spectra for the lower v'_{max} (v'_{max}= 1,2,3,4) do not extend far enough to low E''. Spectra for the higher v'_{max} (v'_{max}= 5,6,7),however, extend approximately over the total range expected. Thus the outermost peak near the low E'' end of the spectrum for v'_{max}= 6 is approximately at 4500 cm^{-1} (53830 J $mole^{-1}$) distance from the strongest peak of that spectrum.

The intensity at the low E'' end of a particular spectrum as shown in figure 5.23 is due to transitions near the classical outer turning point for v'_{max}. The low E'' limit of a spectrum is determined by the energy of the lower state in that region for a fixed upper state. The low E'' limits of spectra can be

changed without changing the position of the peaks near the high E″ end significantly by changing the energy of the lower potential in the region of the outer turning points without altering the shape of the potential at shorter internuclear distance significantly. Thus the low E″ limits of spectra for v'_{max}= 6 can be made to extend further to low E″ to obtain calculated spectra with comparable spectral range to that expected for the experimental C-A(3/2) spectrum by lowering the energy of the lower potential in the region of the outer turning points for v'_{max}. The magnitude of the lowering, for a particular v'_{max}, is approximately determined by the difference between the outermost peak at the low E″ end of the spectra shown in figure 5.23 and the position noted by the corresponding arrow (figure 5.23). This energy difference is tabulated in table 5.10 for the various v'_{max}. Similarly the lower potential will have to be increased in energy in the region of the outer turning points to move the low E″ limit of the spectrum for v'_{max}= 7 to higher E″ (see table 5.10)

The great lowering in energy which will have to be made for the very lowest v'_{max} ($v'_{max} < 5$) is not realistic since it means that a great change in the shape of the lower potential from the shape of an exponential potential will have to be made (see figure 5.24). v'_{max} is therefore most probably in the range 5 to 7.

Table 5.10

Difference between positions of the outermost peaks at the low E″ end of the calculated spectra shown in figure 5.23 for the various v'_{max} and the positions corresponding to a distance of 4500 cm^{-1} from the strongest peaks in each spectrum (ΔE)	
v'_{max}	ΔE (cm^{-1})
3	-1650
4	-1025
5	-375
6	0
7	+375
$1 cm^{-1} = 11.963$ J $mole^{-1}$.	

d. Vibrational population distributions in the C - state found from SC spectra for CH_2Br_2 + Ar^*, HBr+Ar^* and DBr+Ar^* by least square analyses.

Least square analyses of the low pressure SC spectrum for $CH_2Br_2 + Ar^*$ were made to estimate the corresponding vibrational population distribution in the C - state. Due to the uncertainty in the number of the emitting vibrational levels these calculations were carried out for the various v'_{max} values (v'_{max}= 2-7). The positions of the strongest peaks in the spectra shown in figure 5.23 obtained for the lowest v'_{max} are far outside the range E″= 5772 - 6152 cm^{-1} (69050 - 73600 J $mole^{-1}$) (see section 5.122). A potential of a higher energy than U''_{b14} is needed to shift spectra for low v'_{max} inside this range. By use of the potential

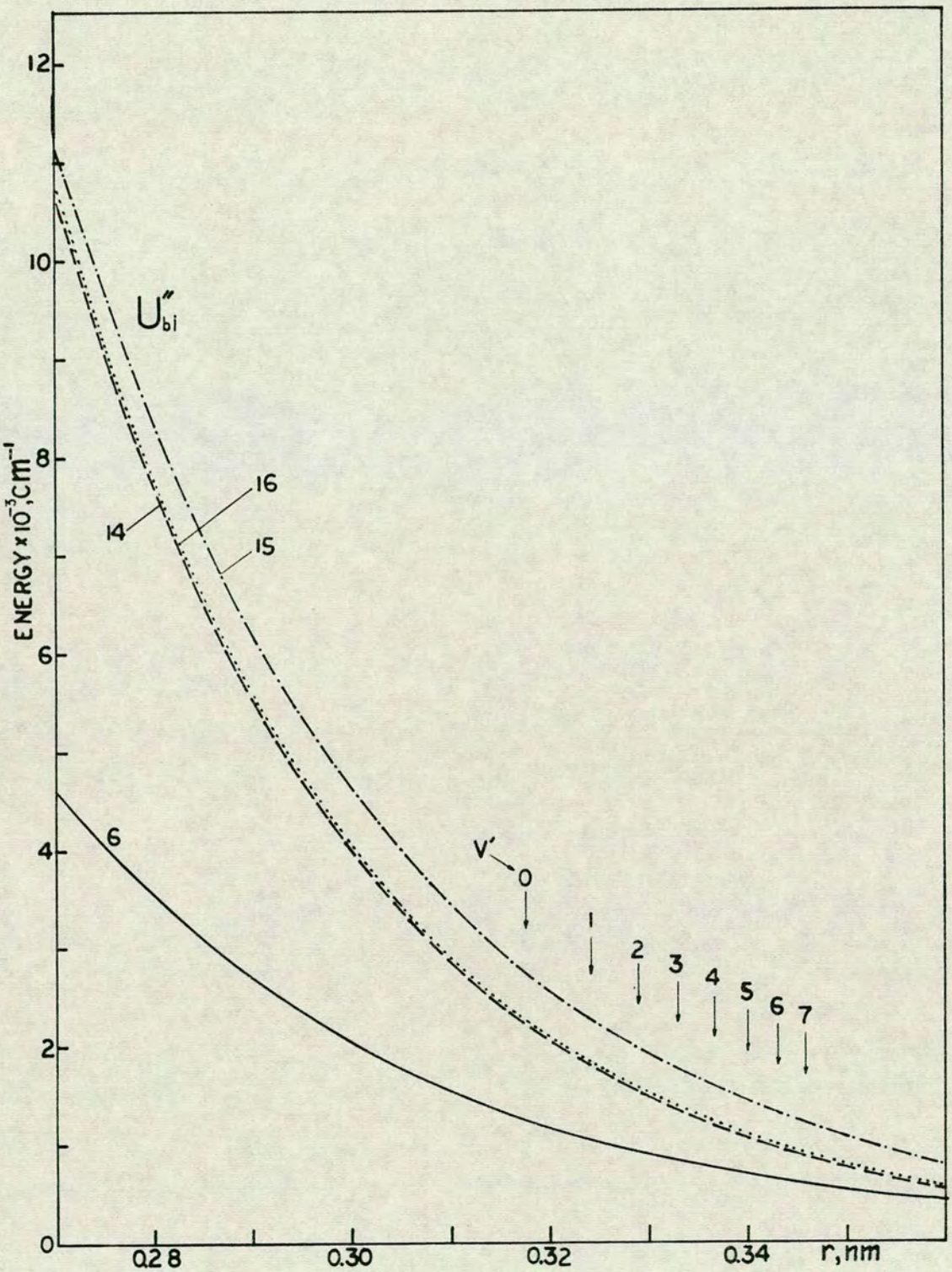

Fig. 5.24 Repulsive potential curves, U''_{bi} (i = 6,14,15,16). The arrows represent the internuclear distances for the classical outer turning points for the various vibrational levels (v′ = 0-7) in the U'_{b1} potential. $1 cm^{-1} = 11.963\ J\ mole^{-1}$.

U''_{b15} (see figure 5.24 and table 5.7) almost identical v′ contributions for the lowest vibrational levels were obtained as for the U''_{b14} potential when other parameters were kept the same. U''_{b15} was used in the least square analysis for $v'_{max} < 5$. The U''_{b16} potential (see figure 5.24 and table 5.7) is very close in energy to the U''_{b14} potential. It was used in the least square analysis for $5 \leq v'_{max} \leq 7$.

Reasonably good fits could be obtained for a range of relative positions of the calculated v′ contributions and the experimental spectrum. Therefore, the relative positions and the corresponding calculated population distributions for which the lowest CHI square (best fit) was obtained (see section 4.4) were searched for especially. Since the use of $v'_{max} < 5$ is not considered to be a realistic choice for the simulation calculations for the low pressure SC spectrum from $CH_2Br_2+Ar^*$ its use is only considered here to illustrate the effect of shifting the experimental spectrum relative to the position of the v′ contributions and to show the effect of using different μ_i functions on the calculated population distributions.

The effect of changing the position of the experimental spectrum relative to the positions of the v′ contributions for $v'_{max} = 3$ is illustrated in figure 5.25. The experimental spectrum is shifted to low E″ by 100 cm^{-1} (1200 J $mole^{-1}$) in each figure in going from figure a to b to c to d. In figure 5.25 a the main contribution to the strongest peak in the

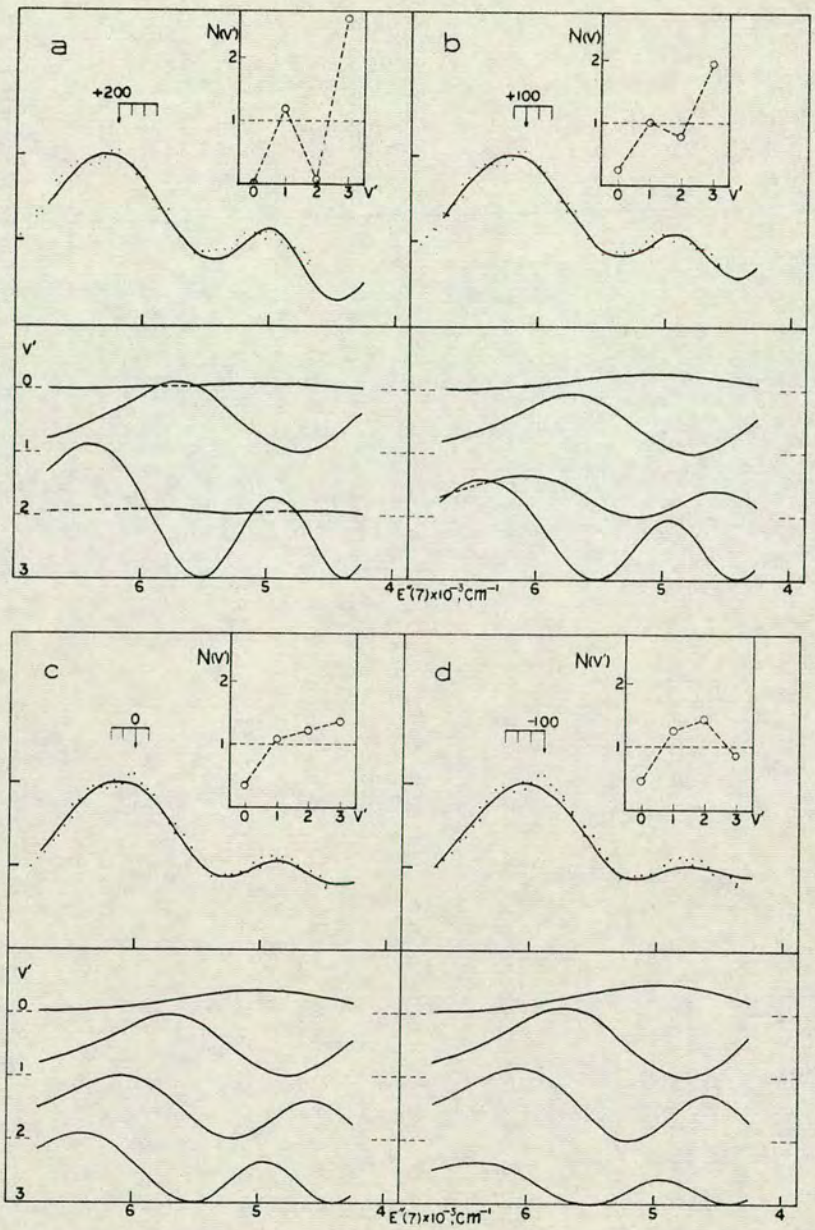

Fig. 5.25 Effect of shifting an ArBr, SC spectrum ($Ar^* + CH_2Br_2$) (small dots) reltive to fixed positions of calculated vibrational contributions on calculated vibrational population distributions. The vibrational contributions obtained for transitions from U'_{b1}, $v' = 0\text{-}3$ to U''_{b15} weighed by the population factors, $N(v')$, (shown in the top right corner of each figure) are shown in bottom of each figure. The solid curves above represent the sum of the vibrational contributions (calculated spectra). A shift of $100cm^{-1}$ to lower $E''(7)$ is carried out in each step (each figure) from "position" +200(a) to +100(b) to 0(c) to -100(d). $1cm^{-1} = 11.965\ J\ mole^{-1}$.

calculated spectrum is the outermost peak of the v'_{max} (= 3) contribution and partly the $v'=1$ contribution, while the contributions from $v'_{max}-1$ (=2) and $v'=0$ are negligible. The main contribution to the other peak in the calculated spectrum is the second outermost peak of the v'_{max} contribution. As the experimental spectrum is shifted to lower E'' the contribution from v'_{max} decreases while the contribution from $v'_{max}-1$ (= 2) increases. Thus by shifting the spectrum far enough to low E'' (beyond that shown in figure 5.25 d) one ends up eventually with a negligible $v'_{max}= 3$ contribution but a dominating $v'_{max}-1 = 2$ contribution or, effectively, only significant contributions from the three lowest vibrational levels where $v'_{max}= 2$. The $v'=0$ contribution grows with shift to low E'' and makes the second outermost peak in the total spectrum broader. The characteristic change in the contributions for v'_{max} and $v'_{max}-1$ with shift of the spectrum was found to be general for the various v'_{max} values.

The CHI - square values obtained for the fits shown in figure 5.25 are tabulated in table 5.11. These show that the best fits (lowest CHI square values) are obtained for positions in the range 0 to +100 while the fits get worse for slight shifts in either direction beyond this range. It should be noted, however that a further shift to lower E'' (negative shift) leads to a new minimum in the CHI - square corresponding to the best fit for the remaining spectral contributions

Table 5.11

CHI square values for the least square fits of the spectra shown in figure 5.25 for the various relative positions of the experimental spectrum and the calculated v′ contributions (see figure 5.25).		
figure 5.25	positions (cm^{-1})	CHI square
a	+200	8.844
b	+100	3.225
c	0	3.166
d	-100	6.408
$1 cm^{-1}$ = 11.963 J $mole^{-1}$.		

when the contribution for the originally chosen v'_{max} equals zero. A further positive shift, however, leads to a worse fit except if a contribution for a higher levels than v'_{max} are considered.

The population distributions shown in figures 5.26 and 5.27 represent selected population distributions which gave the best fit (lowest CHI - square) of spectra for particular v'_{max} and μ_i functions.

The calculated population distributions shown in figure 5.26 were obtained from least square fits of the v′ contributions obtained for U'_{b1}, U''_{b15} and v'_{max} = 2, 3 and 4 and μ_0, μ_4, μ_5. Those shown in figure 5.27 were obtained for U'_{b1}, U''_{b16}, v'_{max} = 5, 6 and 7 and μ_4. The population distributions obtained for a particular v'_{max} shown in figure 5.26 were found for the same position of the experimental spectrum for the different μ_i - functions. All these distributions show an

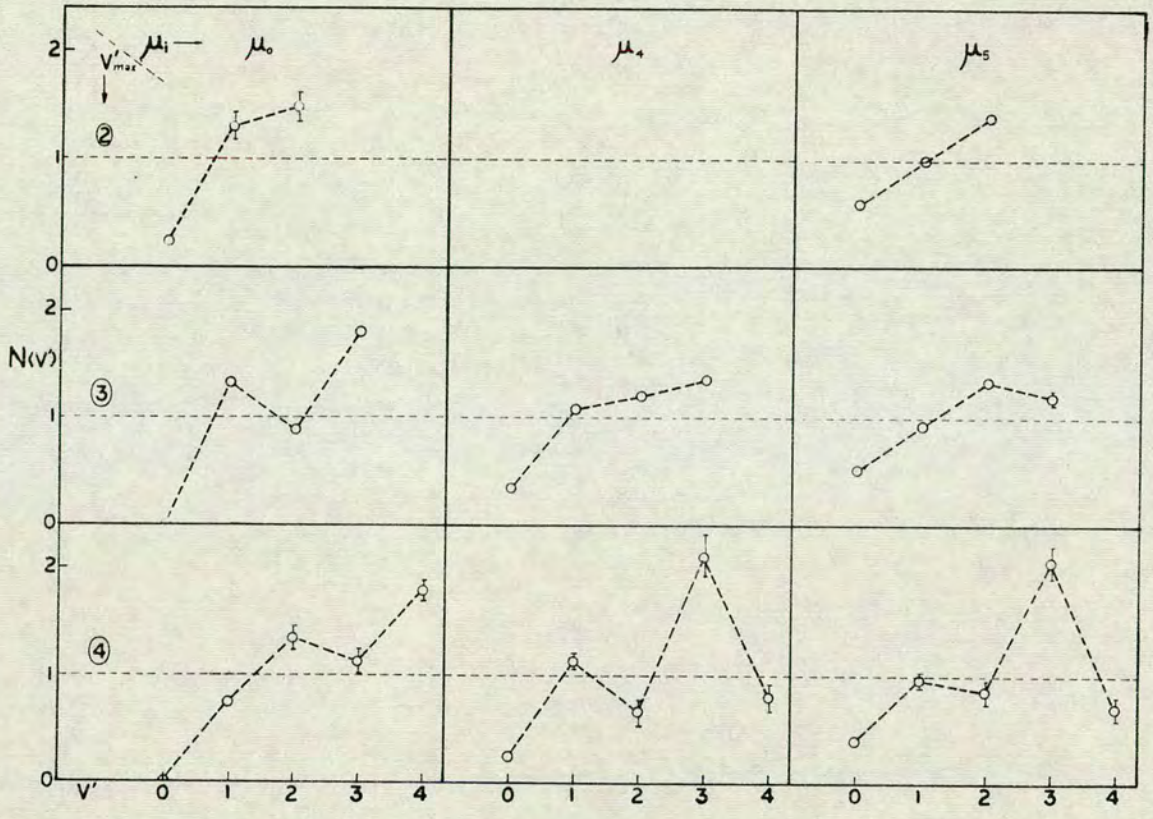

Fig. 5.26 Estimated vibrational population distributions in the C-state, obtained from a ArBr, SC spectrum generated by $Ar^* + CH_2Br_2$, 0.6 torr (80 Nm^{-2}), 500 μm slit width from least square analysis by using vibrational contributions calculated for the potentials U'_{b1} and U''_{b15} and the μ_i- functions, μ_0, μ_4 and μ_5 (columns 1, 2 and 3 from left respectively) and the vibrational levels $v' = 0\text{-}v'_{max}$ for $v'_{max} = 2$, 3 and 4 (rows 1, 2 and 3 from top respectively). The population values satisfy: $\sum_{v'=0}^{v'_{max}} N(v') = v'_{max} + 1$. The population distributions were found for the relative positions of the vibrational contributions and experimental spectrum which gave the lowest CHI-square.

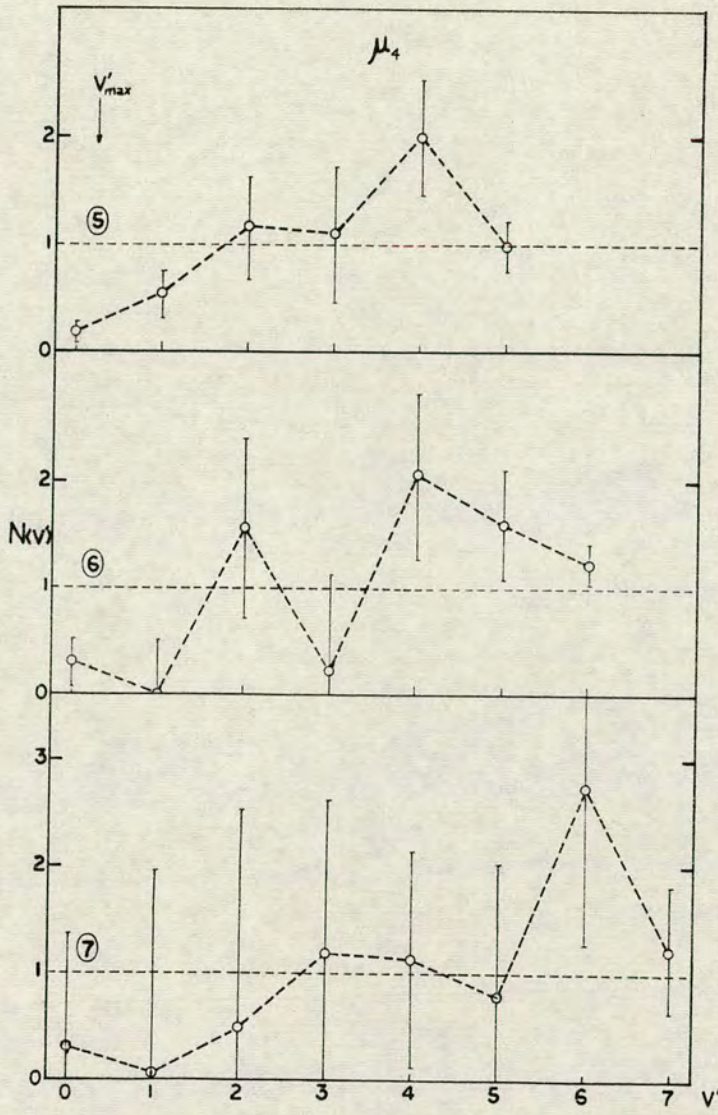

Fig. 5.27 Estimated vibrational population distributions in the C - state obtained from a ArBr, SC spectrum generated by $Ar^* + CH_2Br_2$, 0.6 torr (80 Nm^{-2}), 500 μm slit width from least square analysis by using vibrational contributions calculated for the potentials U'_{b1} and U''_{b16} and the μ_4 - function and the vibrational levels $v' = 0 - v'_{max}$ for $v'_{max} = 5$ (top), 6 (middle) and 7 (bottom). The population values satisfy : $\sum_{v'=0}^{v'_{max}} N(v') = v'_{max}+1$. The population distributions were found for the relative positions of the vibrational contributions and experimental spectrum which gave the lowest CHI - square. The corresponding calculated spectra are shown in figure 5.28.

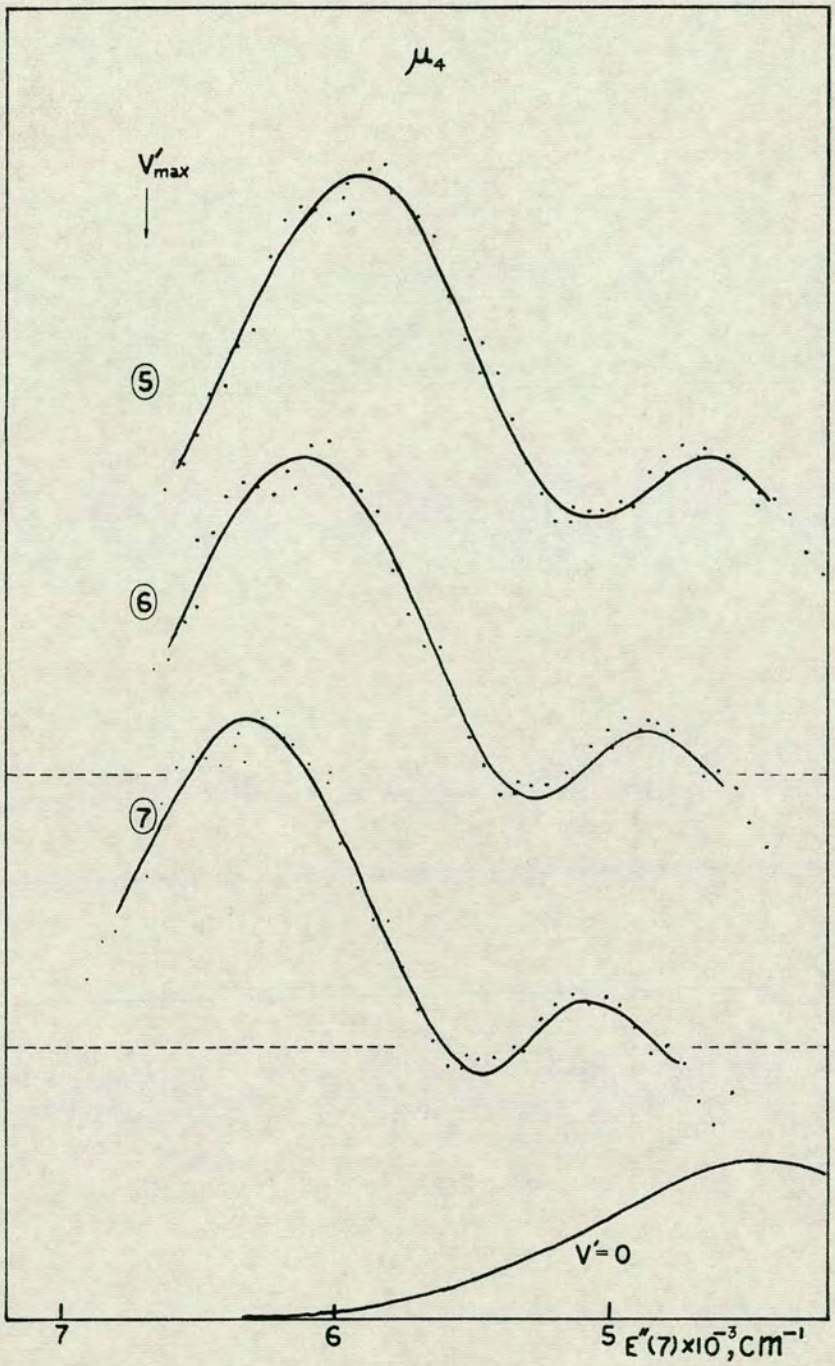

Fig. 5.28 Calculated spectra (solid curves) and experimental ArBr, SC spectrum generated by $Ar^* + CH_2Br_2$, 0.6 torr (80 Nm^{-2}), 500 μm slit width (dots). The calculated spectra were obtained for transitions from U'_{b1} to U''_{b16} for the μ_4 - function and the vibrational levels $v' = 0 - v'_{max}$ for $v'_{max} = 5$ (top), 6 (middle) and 7 (bottom) and the corresponding population distributions shown in figure 5.27. The $v' = 0$ contribution is shown at the bottom at the figure. $1 cm^{-1} = 11.963$ J $mole^{-1}$.

overall increase in the population with an increase in the vibrational quantum number - an inverse population distribution. This is consistent with the conclusion drawn from studying the effect of changing the population distribution on calculated spectra for $v'_{max} = 7$. (section 5.122 c).

A slight difference in the population distributions was observed, depending on whether μ_0 was used or μ_4 and μ_5 as shown in figure 5.26. The relative contribution from v'_{max} lowers as the % decrease in the μ_i function increases. This is consistent with the observed shift of the outermost peaks near the high E'' end as the % decrease in the transition moment increases for an unchanged population distribution (see section 5.122 c and figure 5.19). Thus to keep the outermost peaks in unchanged positions as the % decrease in the μ_i - functions is increased the contribution from v'_{max} which extends furthest to high E'' has to be decreased. The relative contribution from the very lowest vibrational levels such as $v' = 0$ increases with increasing % decrease in the μ_i function. The overall change in the population distribution is consistent with earlier findings where a better fit of spectra was obtainable both by increasing the % decrease in μ_i (figure 5.19) and by increasing the population of the higher v' - levels relative to the lower levels (figure 5.22). Thus by increasing the % decrease in the μ_i functions less inverse population distributions were found to give

satisfactory fits.

Only a slight difference in the calculated population distributions was found, depending on whether μ_4 or μ_5 was used (see figure 5.26). This suggests that the effect of varying the % decrease in linear μ_i functions within the realistic range (see section 5.122 b) on the final calculated population distribution is insignificant. One of these functions (μ_4) was selected and used in the simulation calculations described below.

As the total number of the vibrational levels used in the simulation calculations increases the number of different population distributions which can give reasonably good fits of spectra increases. This is reflected in the increasing uncertainty limits for the populations in individual vibrational levels as v'_{max} increases (see figures 5.26 and 5.27). The uncertainty limits for the intermediate vibrational levels were normally found to be greater than for $v' = 0$ and v'_{max}. This reflects the importance of the $v' = 0$ and v'_{max} contributions in determining the shape of the total spectrum. Thus the v'_{max} contributions largely determine the shape of the calculated spectra near the high E'' limits and the extension of the spectra to high E''. The $v' = 0$ contribution is important in determining the relative intensities of the two peaks in the spectra. A great change in the relative magnitudes of these contributions will have a great effect on the calculated

spectra which cannot be corrected by changing the relative magnitudes of other v′ contributions. The importance of the v′= 0 contribution in determining the shape of the calculated spectra in this region, however, becomes less important for the spectra obtained by use of the very highest v'_{max}, in which case its maximum contribution is outside the region of interest. This is shown in figure 5.28 where the calculated spectra for v'_{max}= 5, 6 and 7 for the population distributions shown in figure 5.27 and the v′= 0 contribution are shown. The dots represent the experimental values. The observed increase in the uncertainty limits for the relative population in v′= 0 with increasing v'_{max}, as shown in figure 5.27, is consistent with this.

The fact that the relative populations in the vibrational levels can be changed within the uncertainty limits without affecting the shape of the calculated spectra significantly is illustrated in figure 5.29. The population distribution shown at top of that figure (no ①) is the same as obtained earlier for v'_{max}= 5 (figure 5.27). The corresponding spectrum (no ①) was obtained for this population distribution for U'_{b1}, U''_{b14} and μ_4. The kinky shape of this population distribution was replaced by a smoother one (no ②) obtained by lowering the relative population in v′=4 and increasing the populations in v′= 3 and 5. The shape of the corresponding spectrum (no ②) only deviates slightly from that of the spectrum no ① in the region of interest,

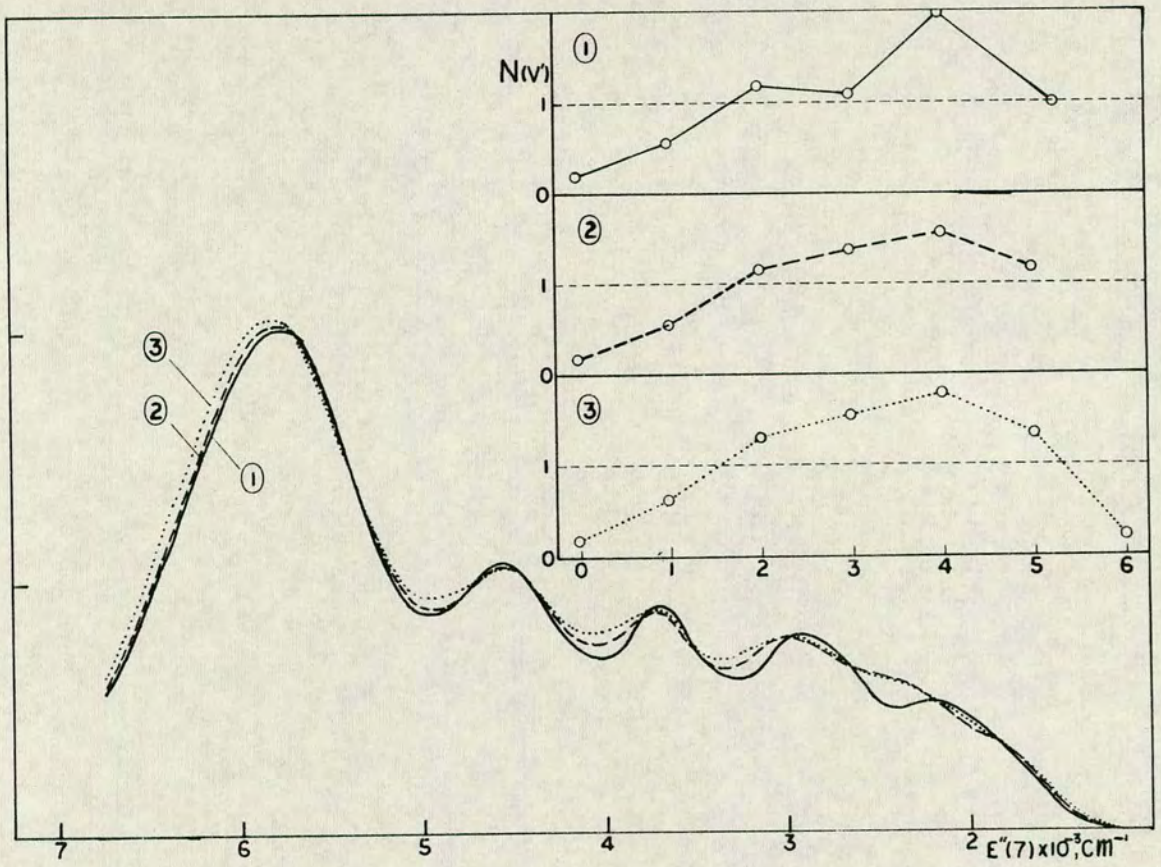

Fig. 5.29 Effect of slight change in the vibrational population distribution on the shape of calculated spectra. Population distributions are shown in the top right corner (①, ② and ③). The corresponding calculated spectra are obtained for transitions from U'_{b1} to U''_{b14} for the μ_4 function. The population distribution, ①, is a calculated one (see fig. 5.27) for $v'_{max} = 5$.

between E″= 4000 and 6750 cm^{-1} (47850-80750 J $mole^{-1}$). The main difference appears in the lower E″ region, corresponding to the MC region. The effect of taking account of a slight contribution from v′=6 does not cause great changes to the spectrum either. The main effect is in agreement with what might be expected. The strongest peak shifts slightly to higher E″. The intensity near E″ (7)= 5000 cm^{-1} (59820 J $mole^{-1}$) increases due to the contribution from the second outermost peak of the v′=6 contribution which peaks near there (see figure 5.21).

Analogous simulation calculations to those for the low pressure SC spectrum for CH_2Br_2+Ar^* were made for a higher pressure SC spectrum for CH_2Br_2+Ar^* (2.1 torr, 280 Nm^{-2}). Population distributions for the various v'_{max} were calculated for the experimental spectrum in the same positions on the absolute frequency scale as those for which the best fits (lowest CHI - square) were obtained for the lower pressure spectrum. These calculated population distributions showed a clear increase in the populations of the lower vibrational levels relative to the higher levels compared to that obtained from the calculations for the low pressure spectrum, which indicates that vibrational relaxation is occurring in the C - state at these pressures. The total populations decrease from the population obtained from the low pressure spectrum in agreement with the observed decrease in the relative intensity of the C-A(3/2) spectrum with pressure due to collision induced crossing.

The calculated population distributions for $v'_{max} = 5$ for the two different pressures are shown in figure 5.30 as well as the corresponding calculated spectra for U'_{b1}, U''_{b14} and μ_4. The low pressure experimental spectrum (0.6 torr, 80 Nm^{-2}) shown in figure 3.8 is also shown in figure 5.30 where the height of the strongest SC peak has been adjusted to the same height and position as the strongest peak in the calculated low pressure spectrum. While these calculated spectra do not extend far enough to low E'' to represent C-A(3/2) spectra properly (see also discussion in section 5.122 c) the observed lowering in the intensity in the MC region is definite. The percent lowering in the intensity increases to lower E'' in the MC region, as the effect of the relatively greatest lowering of the populations in the very highest emitting v' levels becomes increasingly important.

The total integrated intensities for the two calculated (C-A(3/2)) spectra obtained for $v'_{max} = 5$, shown in figure 5.30, were used to obtain an estimate of the ratio for the rate constant for the total collision induced crossing (k_c^C) over the rate constant for the radiative transition (k_r^C) according to the method described in chapter 3 (section 3.124). A value of $k_c^C/k_r^C = 6.9\ 10^{-18} cm^3$ was obtained.

The method for evaluating this ratio is based on the approximation that the intensities are assumed to be linearly proportional to the number of the excited

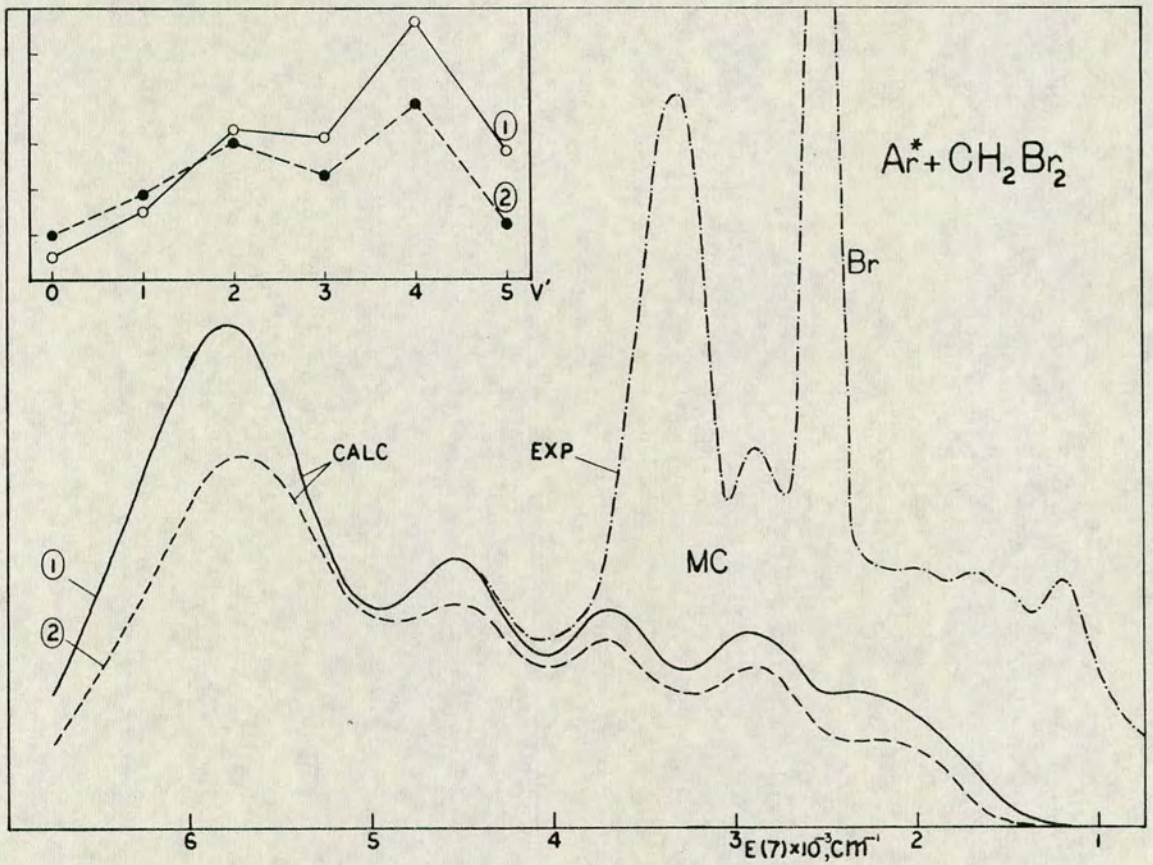

Fig. 5.30 Calculated ArBr, C-A(3/2) spectra for two different total pressures, 0.6 torr (80 Nm^{-2}) (solid curve) and 2.1 torr (280 Nm^{-2}) (dashed curve) for $Ar^{*}+CH_2Br_2$ and experimental ArBr, MC spectrum, 0.6 torr (80 Nm^{-2}), 500 μm slit width (dotted broken curve). The calculated spectra were obtained for transitions from U'_{b1}, $v'=0-5$ to U'_{b14} for the μ_4 - function and the calculated population distributions shown in the top left corner.

state species in the observation vessel. Thus the total integrated intensity of the C-A(3/2) spectrum (I_C) was assumed to be proportional to the total number of excited $ArBr^*$ molecules in the C-state in the observation vessel

$$I_C = k \; N_{ArBr^*(C)} \tag{5.8}$$

where k is a constant. The total intensity (I_T) is proportional to the sum of the vibrational contributions, expressed as

$$I_T = c' \sum_{v'=0}^{v'_{max}} N(v') \int_{-\infty}^{+\infty} \nu^3 \left(\int \Psi'_v \cdot \mu_i^{eff} \Psi''_{E''(v')} dr \right)^2 d\nu \tag{5.9}$$

where c′ is a constant. From this expression one can see that equation 5.8 is valid if the integral in equation 5.9 is constant and of same value for all of the emitting v′ levels

$$\int_{-\infty}^{+\infty} \nu^3 \left(\int \Psi'_v \cdot \mu^{eff} \Psi''_{E''(v')} dr \right)^2 = \text{constant} \tag{5.10}$$

so that I_T can be express as

$$I_T = c'' \sum_{v'=0}^{v'_{max}} N(v') = c''' \; N_{ArBr^*(C)} \tag{5.11}$$

since

$$\sum_{v'=0}^{v'_{max}} N(v') \propto N_{ArBr^*(C)} \tag{5.12}$$

c″ and c‴ are constants. This was found to be a relatively good approximation for the calculations for U'_{b1}, U''_{b14}, μ_4. Thus by replacing I_C in equation 3.17

by $\sum_{v'=0}^{v'_{max}} N(v')$ one could obtain values for k_c^C/k_r^C in an analogous way as before. Thus the values $7.2 \cdot 10^{-18} cm^3$ and $7.5 \cdot 10^{-18} cm^3$ were obtained for $v'_{max} = 5$ and $v'_{max} = 4$ respectively.

The results from the simulation calculations for the SC spectra for $CH_2Br + Ar^*$ were used in order to estimate the ratio for the rate constant for the vibrational relaxation over the rate constant for the radiative transition. The ratio for the rate constant for the total collisional deactivation of the species in v'_{max} ($k_c^{v'_{max}}$) over the rate constant for the radiative transition ($k_r^{v'_{max}}$) was evaluated from the values for $N(v'_{max})$ obtained at the two pressures. The method of evaluating $k_c^{v'_{max}}/k_r^{v'_{max}}$ is analogous to the method used to evaluate k_c^C/k_r^C from $\sum_{v'=0}^{v'_{max}} N(v')$. The assumption was made that the rate contants for the collision induced crossing are the same for all the emitting v' levels and equal to k_c. Also the rate constants for the radiative transitions were assumed to be the same for all the emitting v' levels

$$k_r^{v'_{max}} = k_r^C \qquad (5.13)$$

Thus the ratio for the rate constant for the vibrational relaxation ($k_v^{v'_{max}}$) over the rate constant for the radiative transition was obtained from a simple subtraction

$$\frac{k_v^{v'_{max}}}{k_r^C} = \frac{k_c^{v'_{max}}}{k_r^{v'_{max}}} - \frac{k_c^C}{k_r^C} \qquad (5.14)$$

Such ratios are tabulated in table 5.12 for $v'_{max} = 5$ and 4. Only slight shifts of the experimental spectra were found to make significant changes to this ratio as shown in table 5.12

Table 5.12

Ratios of $k_v^{v'_{max}}/k_r^C$ for $v'_{max} = 4$ and 5 for relative positions of the experimental spectra and the calculated v′ contributions for which the best fits were obtained for the lower pressure spectrum (positions 0) and for the positions +10 and -10 (for $v'_{max} = 5$) which correspond to shifts of the calculated spectra by 10 cm^{-1} in both directions from position 0.

$k_v^{v'_{max}}/k_r^C$ (cm^3)	v'_{max}	positions (cm^{-1})
$6.7\ 10^{-17}$	5	+10
$9.2\ 10^{-17}$	5	0
$9.8\ 10^{-17}$	5	-10
$6.7\ 10^{-17}$	4	0

$1 cm^{-1} = 11.963$ J $mole^{-1}$.

From comparison with the estimated reciprocal values of the transition probabilities for transitions for other noble gas halide systems (table 1.3) an estimate

for a value for k_r^C of about $2 \cdot 10^7$ s^{-1} was made. From the ratio values in table 5.12 $k_v^{v'max}$ was then found to be in the range $(1.3 - 2) \cdot 10^{-9}$ cm^3 s^{-1}, which corresponds to a cross-section of about 2.7 - 4.1 nm^2. This corresponds to a very rapid rate of vibrational relaxation. Thus the cross-section is much greater than is generally found for vibrational relaxation in rare gas media.[100]

A kinetic model was tried, which included vibrational relaxation of molecules in a particular v′ level to the next level below (v′- 1) as well as formation reactions, electronic quenching and radiative decays. Vibrational excitation, however, was not included. By using the ratios for the rate constants and the calculated population distribution for $v'_{max} = 5$ for 0.6 torr (80 Nm^{-2}) total pressure the population distribution for the total pressure 2.1 torr (280 Nm^{-2}) was predicted by use of the model. The derived distribution did not agree with that calculated by the simulation procedure. An overestimation of the rate of vibrational relaxation or of the ratio $k_v^{v'max}/k_r^C$ could explain the discrepancy. That would then most likely be due to an overestimation of the value for the ratio $k_c^{v'max}/k_r^{v'max}$ (eq. 5.14) rather than an underestimation of k_c^C/k_r^C since the former ratio is much more uncertain. That suggests then that the calculated pressure dependence of the population in

v'_{max} is relatively too great.

The calculated population distributions for the C-state are possibly being affected by the small contribution from the underlying B-A(1/2) spectrum in the SC region which was not considered. Because the population distribution is greatly determined by the peak to trough ratios in the spectra the effect of the underlying B-A(1/2) spectrum on these ratios will have to be considered. As mentioned earlier, the B-A(1/2) spectrum is expected to decrease in intensity to shorter wavelength. That means that the ratio of the second outermost peak in the C-A(3/2) spectrum to the trough on the long wavelength side of it in the C-A(3/2) spectrum (when the B-A(1/2) contribution has been subtracted) is greater than the corresponding ratio for the SC. While the increase in this ratio is associated with a greater inverse population distribution this suggests that the populations in the lowest levels should be even lower relative to the higher levels than has been calculated. At higher pressures the relative contribution of the underlying B-A(1/2) spectrum increases while the C-A(3/2) emission decreases, and this effect might be even greater.

Simulation calculations for SC spectra for $HBr+Ar^*$ were carried out for U'_{b1}, U''_{b15}, μ_4 and various v'_{max}. The experimental spectra were kept in the same position on the absolute frequency scale as the experimental

low pressure spectrum (0.6 torr, 80 Nm^{-2}) for $CH_2Br_2+Ar^*$ for which the best fit (lowest CHI square) for $v'_{max}= 5$ was obtained. In an attempt to allow for a B-A(1/2) contribution in the SC, the B-A(1/2) spectrum was assumed to decrease linearly from an intensity equal to that observed in the $HBr+Ar^*$ spectrum at 174.5 nm for low pressure (0.6 torr, 80 Nm^{-2}) to zero intensity at 167nm. Such a contribution was subtracted from the SC spectra for $HBr+Ar^*$ to give estimated C-A(3/2) spectra, which were used in the simulation calculations.

Population distributions obtained for $v'_{max}= 2-5$ from least square analysis of a low pressure (0.6 torr, 80 Nm^{-2}) C-A(3/2) spectrum are shown in figure 5.31 as well as a population distribution obtained for $v'_{max}= 3$ for a higher pressure spectrum (2.4 torr, 320 Nm^{-2}). The calculated spectra for $v'_{max}= 3$ and the experimental data points for these two spectra are also shown in figure 5.31. Only the calculations for $v'_{max}= 3$ show a realistic type of population distribution.

These population distribution results for $v'_{max}= 3$ could be replaced by linear fits as shown in figure 5.32 a and c without altering the goodness of the fits significantly. Thus the linear population distribution for the lower pressure spectrum is slightly inverse while the linear distribution for

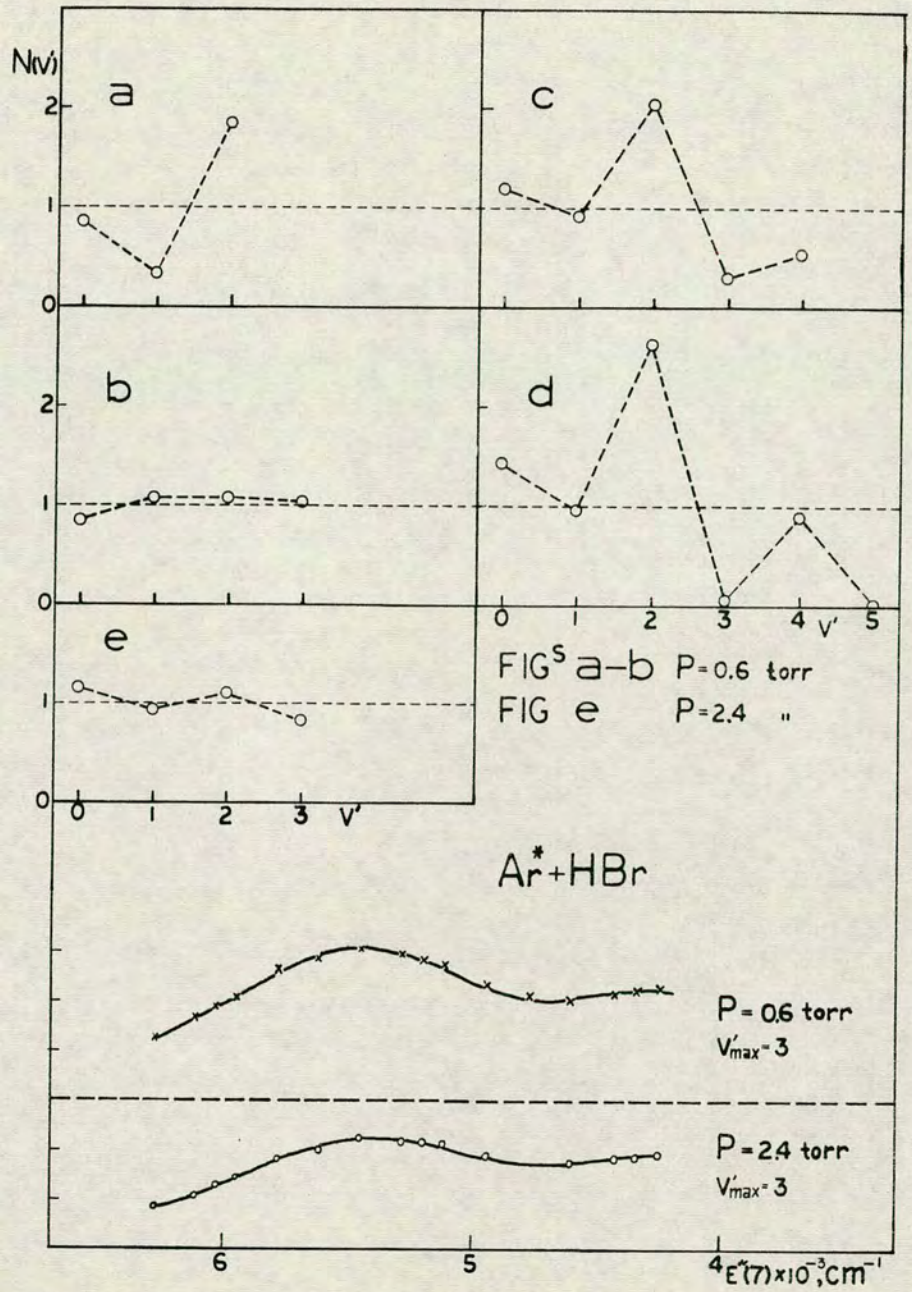

Fig. 5.31 Figures a - e show estimated vibrational population distributions in the C - state obtained from ArBr, SC spectra generated by Ar^*+HBr, 0.6 torr (a - d) and 2.4 torr (e), 500 μm slit width from least square analysis by using vibrational contributions calculated for transitions from U'_{b1} to U''_{b16} and the μ_4 - function and vibrational levels $v' = 0\text{-}v'_{max}$ for $v'_{max} = 2\text{-}5$. Calculated spectra for the estimated population distribution for $v'_{max} = 3$ and the two different pressures are shown below (solid curves) as well as experimental dots. $1 cm^{-1} = 11.963$ J mole^{-1}. 1 torr = 133.322 Nm^{-2}

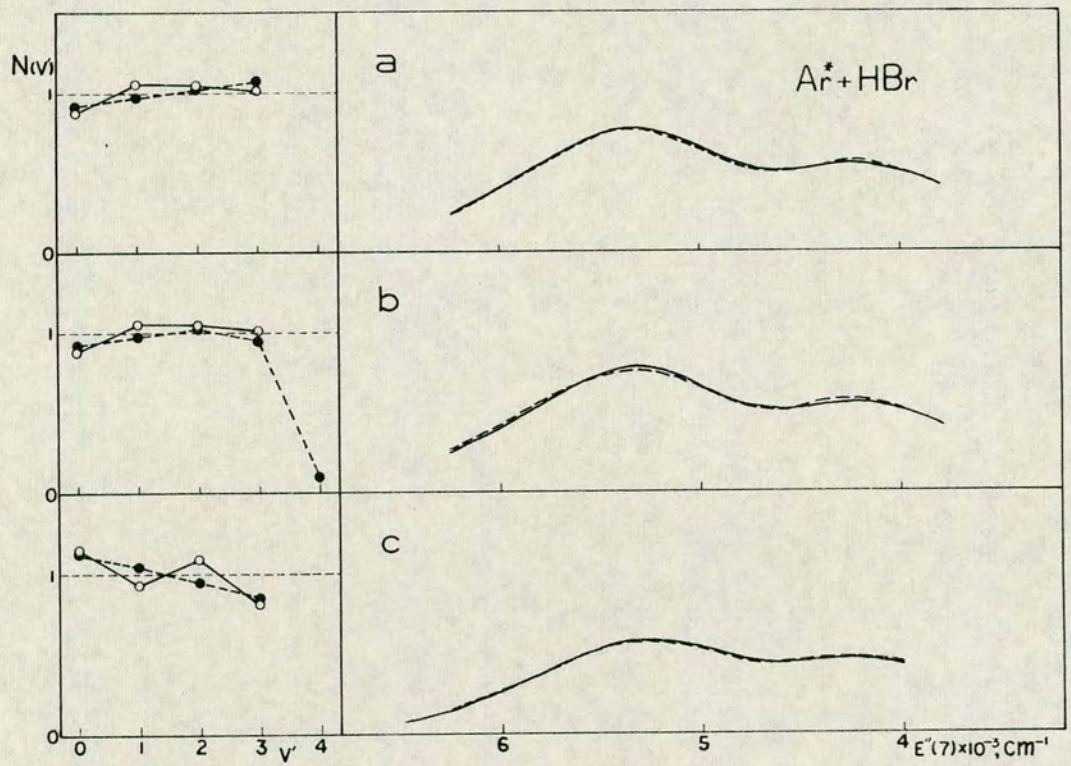

Fig. 5.32 Effect of slight change in vibrational population distribution on the shape of calculated spectra, (Ar^*+HBr). The vibrational populations represented by circles connected by solid lines are calculated ones (see figure 5.31) and the solid curves are the corresponding calculated spectra. Dashed curves are calculated spectra for population distributions represented by black dots connected by dashed lines. $1 cm^{-1} = 11.963$ J $mole^{-1}$.

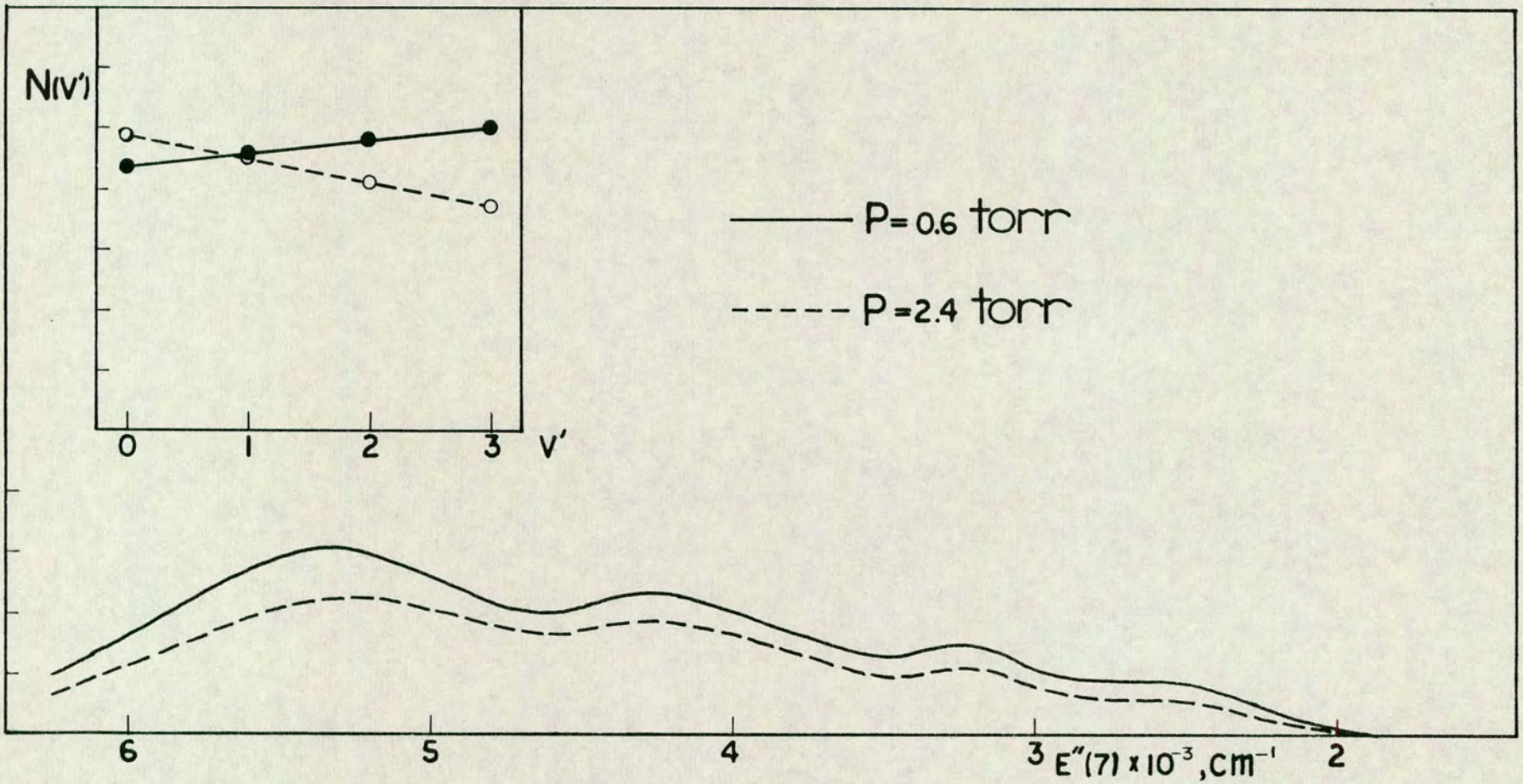

Fig. 5.33 Calculated ArBr, C-A(3/2) spectra for two different total pressures, 0.6 torr (80 Nm^{-2}) and 2.4 torr (320 Nm^{-2}) for Ar^{*} + HBr. The calculated spectra were obtained for transitions from U'_{b1}, v'= 0-3 to U'_{b14} for the μ_4 - function and the population distributions shown in the top left corner.

the higher pressure spectrum shows a slight decrease with increasing v′ quantum number. A slight contribution from v′=4 also does not alter the goodness of the fit significantly as shown in figure 5.32 b. In an analogous way to that observed from the analysis of the SC for CH_2Br_2+Ar* the total population as well as the total intensity was found to decrease with pressure. This is shown in figure 5.33. These calculated spectra were used to obtain the ratio k_c^C/k_r^C in a similar way as from the CH_2Br_2+Ar* spectra. $k_v^{v'max}/k_r^C$ ratios were also obtained in an analogous way to that described for CH_2Br_2+Ar*. These results were discussed in chapter 3 (see section 3.124).

The SC for DBr+Ar* was treated in a similar way as the SC for HBr+Ar* and an estimated B-A(1/2) contribution subtracted from the total intensity. For the same relative position of the v′ contributions and the experimental spectrum for 0.6 torr (80 Nm^{-2}) as for HBr+Ar* a total of 4 v′ levels (v'_{max}= 3) was found to give the most realistic type of population distribution from least square analysis. This population distribution differed from that obtained for HBr+Ar* in showing relatively less population in the higher v′ levels than the lower levels or a decreasing population distribution with increasing v′.

5.123 Other spectra.

A low pressure spectrum for $CH_2Br_2+Ar^*$ obtained by Dr M.F. Golde in Pittsburgh for small slit width showed a clearly resolved oscillatory structure in the MC. The change in the peak to trough ratio with wavelength is close to that observed for the MC for $HBr+Ar^*$ at low pressure (figure 5.13). This indicates that the initial population distribution in the B-state for the reaction $CH_2Br_2+Ar^*$ is similar to that obtained for $HBr+Ar^*$ - almost even population distribution.

The structure of the low pressure SC spectrum obtained for Br_2+Ar^* differ slightly from that of the low pressure SC spectrum for $HBr+Ar^*$ and $DBr+Ar^*$ (figure 3.11). It shows relatively greater intensity in the region 169 - 167nm than the others. The $DBr+Ar^*$, SC spectrum which shows relatively greater intensity in this region than the $HBr+Ar^*$ was shown to represent transitions from a population distribution with lower levels more populated than higher ones while the $HBr+Ar^*$ SC spectrum was analysed to represent transitions from almost even population distribution (section 5.122). As the SC of Br_2+Ar^* resembles more that for $DBr+Ar^*$ than for $HBr+Ar^*$ the conclusion is reached that the initial population distribution in the C-state is such that lower levels are relatively more populated than higher ones. Also more levels in the C-state are expected to be populated for the Br_2+Ar^* system than for the two

others or the same number of levels as in $CH_2Br_2+Ar^*$ (6-8). The fact that negative pressure dependence was observed to longer wavelength in the SC region for Br_2+Ar^* than for $HBr+Ar^*$ verifies this.

The SC in CF_3Br+Ar^* resembles that for $CH_2Br_2+Ar^*$, suggesting that the initial population distribution in the C-state for CF_3Br+Ar^* is somewhat similar to that in $CH_2Br_2+Ar^*$ - an inverse population distribution.

5.13 Discussion.

5.131 Population distribution.

Estimated vibrational population distribtuions in the ArBr B- and C- states have been obtained from the various ArBr spectra. The population distribution has been estimated from simulation calculations for the B-state from the MC spectra for HBr+Ar^* and DBr+Ar^* (section 5.121) and for the C-state from the SC spectra for CH_2Br_2+Ar^*, HBr+Ar^* and DBr+Ar^* (section 5.122) for different pressures. From comparison of these results and the spectra with other ArBr spectra rough estimates of population distributions in the emitting states have been made for the B-state from the CH_2Br_2+Ar^* MC spectra and for the C-state from the Br_2+Ar^*- and CF_3Br+Ar^* spectra (section 5.123).

All the estimated population distributions are nonthermal (unrelaxed) distributions and change significantly with slight changes in pressure, which indicates that a rapid vibrational relaxation and a collision induced crossing is occuring. The population distribution obtained for the lowest pressure results (0.6 torr, 80 Nm^{-2}) therefore may deviate slightly from the initial population distribution for the reactions.

The analyses of the HBr+Ar^* and DBr+Ar^* spectra suggest that fewer v´ levels are populated in the C-state than in the B-state. This suggests that the B- and the C- states are not degenerate but differ

slightly in energy.

This is consistent with that the C-state is greater in energy than the B-state and that the number of emitting levels is determined by the number of v´ levels which are lower in energy than the threshold energy (E_T) (figure i).

Another alternative would be that the equilibrium internuclear distance of the C-state is greater than for the B-state (figure ii) in which case lower levels are being predissociated in the C-state than in the B-state by the lowest repulsive molecular state which correlates with $Br^*+Ar(^1S)$ (the crossing point of this state with the C-state (a in figure ii) is lower in energy than the corresponding crossing point with the B-state (b in figure ii))

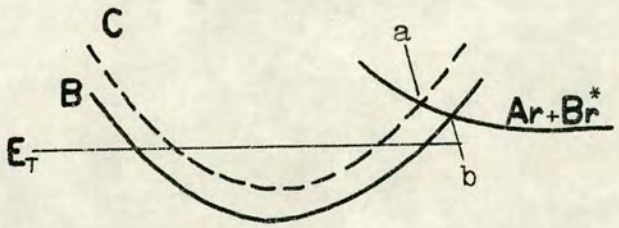

figure i

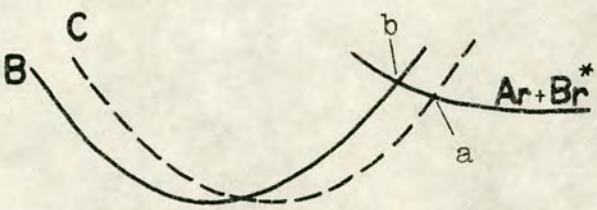

figure ii

While the number of identified peaks in the MC spectra suggests that the same number of v´ levels (8) are emitting in the B-state for $CH_2Br_2+Ar^*$, HBr+Ar* and DBr+Ar*, fewer v´ levels are found to emit in the C-state for HBr+Ar* and DBr+Ar* than for $CH_2Br_2+Ar^*$. This suggests that v´=7 is the next vibrational level below the crossing point for the B-state and the

lowest Rydberg state (b in figures i and ii) and that higher levels are predissociated. The relative position of the electronic states shown in figure ii cannot explain the different number of emitting levels in the C-state for HBr+Ar^*, DBr+Ar^* and CH_2Br_2+Ar^*. This difference must be due to the difference in the threshold energies. The threshold energy for HBr+$Ar^*(^3P_2)$ and DBr+$Ar^*(^3P_2)$ lies below the asymptotic limit for the lowest lying molecular states while that for CH_2Br_2+Ar^* is much higher. All the v′ levels in the C-state below the crossing point a (figures) are therefore expected to be populated for CH_2Br_2+Ar^* but not for HBr+Ar^* and DBr+Ar^* and the relative position of the B- and C- states to be as mentioned earlier and shown in figure i. Such relative position of the excited states agrees with what theoretical calculations have predicted.[52-56]

The calculated population distribution in the C-state (inverse population distribution) and the estimated population distribution in the B-state (flat distribution) for CH_2Br_2+Ar^* (0.6 torr, 80 Nm^{-2}) suggest that the initial population distribution in these two states differ. This difference in population distributions in these two states is in agreement with what Setser et al found for KrF^* from various reactions of Kr^* with fluorine containing reagents[21] as mentioned earlier in chapter 1 (see section 1.2)

Velocity analyses of product molecules KBr from the reaction K+HBr in molecular beam studies[142] show the molecules to have almost evenly distributed translational energy with perhaps a slight excess number of molecules with lower translational energy than higher. This corresponds to a slightly inversed population distribution among internal energy modes (vibrational- and rotational energy). This is in a qualitative agreement with what is found for the population distribution in the excited states (C and B) for $ArBr^*$ from the analogous reaction Ar^*+HBr.

Throughout the simulation calculations the effect of possible rotational excitation has been ignored. Only the lowest rotational level with the zero rotational quantum number ($J = 0$) has been assumed to be populated and each radiative transition assumed to occur to a $J = 0$ level in the lower state. A more complete analysis of a spectrum would require to take account of transitions from all populated rotational levels and the population distribution in these and sum over all the spectral contributions to obtain the total calculated spectrum. This would require much more calculations.

Usually in spectroscopic simulation calculations where the purpose is not to simulate rotational structure either $J = 0$ is used or a single rotational level corresponding to the average rotational energy. To apply the latter approximation, information on rotational population distribution is needed. Unfortunately they

are not available for the noble gas halide systems.

Tellinghuisen et al have analysed high pressure B-X spectra for other noble gas halide systems by calculating transitions from such average rotational levels (J_{av}) which were found by assuming that the molecules thermalize before they radiate. They studied the effect of substituting a range of rotational levels by J_{av} levels and came to the conclusion that it is a good approximation. They find that the spacing between peaks only changes slightly by varying the rotational levels and the peak to trough ratios do not seem to change much either (figure 7 in reference 40).

The change in the spectra due to taking account of transitions from a particular $J > 0$ level instead of the $J = 0$ level is due to the effect of the centrifugal term in the expression for the effective potential (see eq. 4.8). Thus, the slope of the effective lower state potential increases as well as the inner wall of the effective upper state. The slope of the outer wall decreases, however. Such changes in the effective potentials might be expected to cause some distortion of the position of peaks in the spectra, which could be adjusted by making slight changes in either or both of the two potentials. A similar procedure was carried out earlier by changing both potential curves for the B-X simulation calculation to see the effect of change in vibrational frequency on the calculated population distribution. This showed very little effect on the

calculated population distribution. It is therefore believed that taking account of rotational excitation (to some extend) will not alter the calculated population distribution significantly.

5.132 Potential curves.

In the simulation calculations which have been presented a particular bound potential U'_{b1} was used to represent the shape of the B- and the C- states near the equilibrium internuclear distance (see section 5.11 and table 5.1). After comparing calculated spectra for U'_{b1} and various repulsive potential curves (U''_{bi}) with experimental spectra, U''_{bi} potentials which gave best fits of spectra were selected. These represent the X- and the A(3/2)- states for the MC and SC simulations respectively. Thus, U''_{b6} was selected to represent the X-state (table 5.3) and U''_{b14} or U''_{b16} to represent the A(3/2) state (table 5.7) of the repulsive potentials which were tried.

The simulation calculations for ArBr showed that for a particular bound upper state, only lower potentials within a very limited energy range and shape could be used in order to obtain proper fit. The main problem in determining exact lower potentials lies in the uncertainty in the shape and energy of the upper potentials.

The calculated B-X spectrum for U'_{b1} and U''_{b6} is placed at too high frequency on the absolute frequency

scale by about 400 cm^{-1} (4790 J $mole^{-1}$) compared with the experimental MC spectra. The minimum of the bound potential therefore needs to be shifted down in energy by about 400 cm^{-1}. The adjustable parameters in the expression for U'_{bi} (see discussion in section 5.11), the exponential factors and c_3/r^3, can easily be varied to obtain a new potential with virtually the same shape near the minimum as U'_{b1} but slightly lower in energy Thus, a potential curve with T_e,400 cm^{-1} (4790 J $mole^{-1}$) lower than for U'_{b1} could be easily derived without altering the shape of the potential or the vibrational frequency significantly. The various parameters in the Rittner potential expression for such a potential and the spectroscopic constants are tabulted in table 5.13.

It has already been suggested that the minimum of the U'_{b1} potential (T_e = 62844 cm^{-1}, 751800 J $mole^{-1}$) is too high to represent the B-state properly compared with the estimated value of T_e = 61850 cm^{-1} (739900 J $mole^{-1}$) (see eq. 3.28) from temperature dependence experiments ($\Delta E \sim 1000$ cm^{-1} (11900 J $mole^{-1}$)). For further shift of the bound potential to lower energy the repulsive potential also needs to be shifted down, without altering the shape of the potential. The maximum possible further shift will thus be determined by the energy of the U''_{b6} potential in the region of the outer turning point for the maximum v′ level which is emitting (v′=7), which is about 600 cm^{-1} (7180 J $mole^{-1}$) (see figure 5.34). Thus, the maximum total shift which can be made without

Table 5.13

a. Values of constants in the Rittner potential expression for U'_{b3} (eq. 5.2) for r in nm.
b. Spectroscopic constants for the U'_{b3} potential.

a.

constants	$U'_{b3}(cm^{-1})$	constants	$U'_{b3}(cm^{-1})$
a_1	$7.602 \cdot 10^6$	c_1	$1.161 \cdot 10^4$
b_1	0.03747	c_3	$1.795 \cdot 10^2$
a_2	$7.711 \cdot 10^6$	c_4	37.66
b_2	0.04514	d	99975.7

b.

	U'_{b3}
r_e(nm)	0.309
$D_e(cm^{-1})$	37532
$\omega_e(cm^{-1})$	194
$T_e(cm^{-1})$	62444

$1 cm^{-1} = 11.963$ J mole^{-1}.

altering the shape of the potentials, is about 1000 cm^{-1} (=400÷600) (11900 J mole^{-1}) (the same as predicted from the temperature dependence experiments), in which case the energy of the lower state potential in the region of the outer turning point for $v'=7$ is zero.

Ab initio calculations show the ground state for other noble gas halide systems to have slight Van der Waals minima at long internuclear distance. These calculations show the ground state potentials to approach zero energy more rapidly than can be predicted

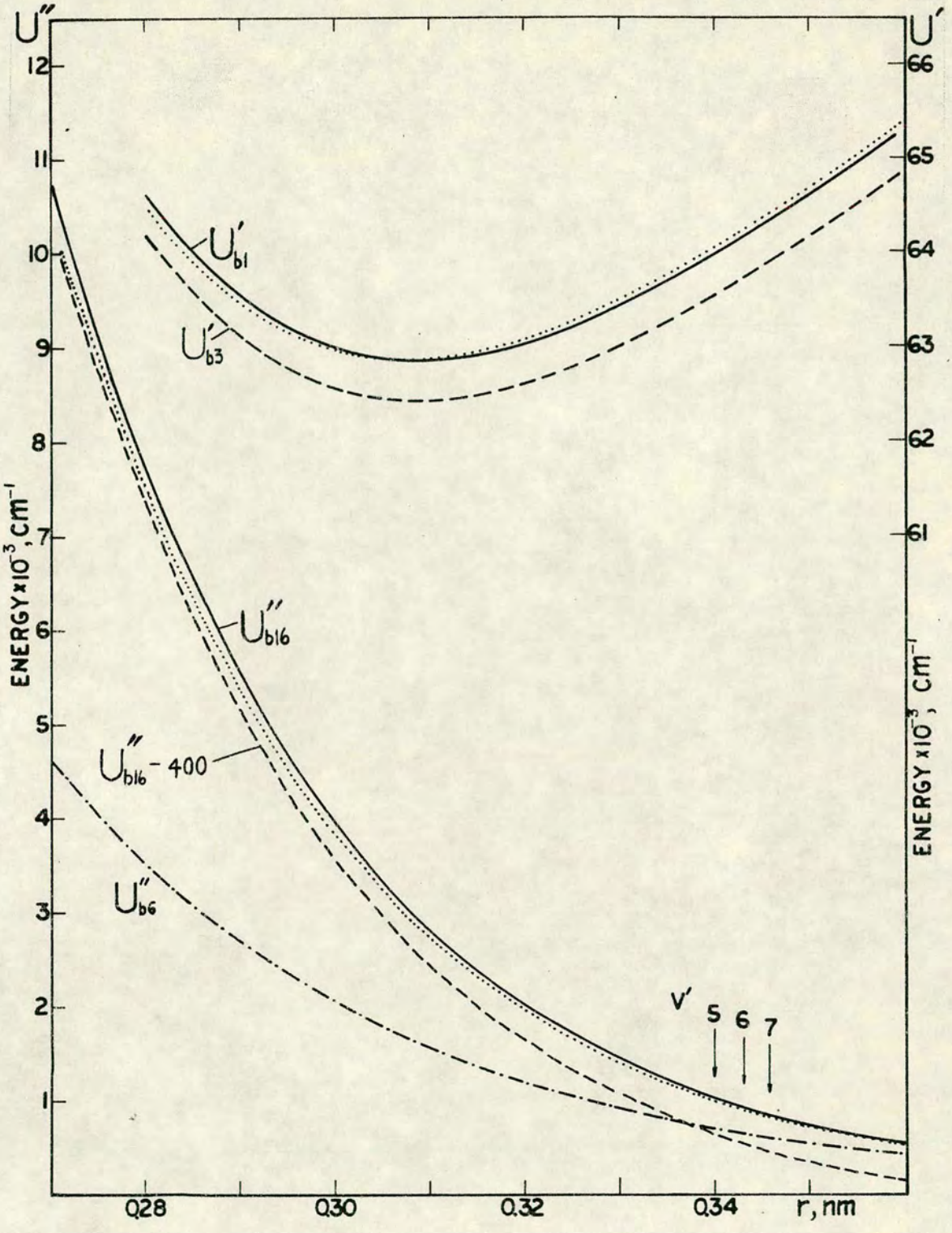

Fig. 5.34 Effect of change in position of the bound upper state (C - state) on the position of the repulsive lower state (A(3/2) - state). The arrows represent the internuclear distances for the classical outer turning points for the vibrational levels, $v' = 5$, 6 and 7 in the U'_{b1} - potential. $1 cm^{-1} = 11.963$ J mole^{-1}.

by simple exponential potentials or $a/(r-b)^2$ type potentials as shown for ArCl in section 5.2 (see figure 5.43). This may suggest that the ground state potential for ArBr is in fact lower in energy than U''_{b6} and that both potentials will need to be shifted further down.

The uncertainty in the energy and shape of the C- and the A(3/2)- potentials is even greater than for the B- and the X- states, partly due to the uncertainty in the energy difference between the B- and the C- states (see section 1.2) and partly due to the uncertainty in the number of emitting levels in the C- state (see section 5.122).

It has already been shown (section 5.123) that the observed difference in the population distribution in the C- and the B- state from HBr+Ar* and DBr+Ar* spectra is consistent with the C-state lying above the B-state.

If similar adjustment was made for the C-state as for the B-state and its representitive potential curve (U'_{b1}) lowered by 400 cm^{-1} (4790 J $mole^{-1}$) the representative repulsive potentials for the A(3/2) state (U''_{b14} and U''_{b16}) will also have to be lowered. Due to the uncertainty in the number of emitting v′ levels (v'_{max}= 5,6,7) the lowering that is necessary varies from about 150 cm^{-1} (for v'_{max}= 5) to 350 cm^{-1} (v'_{max} = 6) to 550 cm^{-1} (v'_{max} = 7) (1790, 4190, 6580 J $mole^{-1}$) in order to obtain the position of the strongest calculated SC peak for CH_2Br_2+Ar* in a correct distance from the strongest

MC peak. In addition, the shape and the energy of the repulsive lower state potential will need to be changed to obtain the correct range of the calculated C-A(3/2) spectra, as mentioned previously (section 5.122). This corresponds to a lowering of the potential energy in the region of the outer turning points by about 500 cm^{-1} ($v'_{max} = 5$), 350 cm^{-1} ($v'_{max} = 6$) and 200 cm^{-1} ($v'_{max} = 7$) (5980, 4190, 2390 J $mole^{-1}$). The maximum possible lowering in that region, however, is determined by the energy difference between the U''_{b14} and U''_{b16} potentials and the U''_{b6} potential, which is about 250 - 350 cm^{-1} (2990 - 4190 J $mole^{-1}$) (see figure 5.34). Thus a lowering in the C-state below the B-state cannot be made except for $v'_{max} = 7$.

If the average internuclear distance of the C-state is smaller than for the B-state the possible shift is even less, as one will then also have to shift the repulsive potentials to shorter internuclear distance and the energy difference between these and the X potential decreases. This is illustrated in figure 5.34 for U''_{b14}.

Figure 5.35 shows the potentials U'_{b3}, U'_{b6} and U'_{b16} which have been selected to represent the B, X and A(3/2) states respectively. It should be clear from the above discussion, however, that these potentials are probably slightly too high in energy.

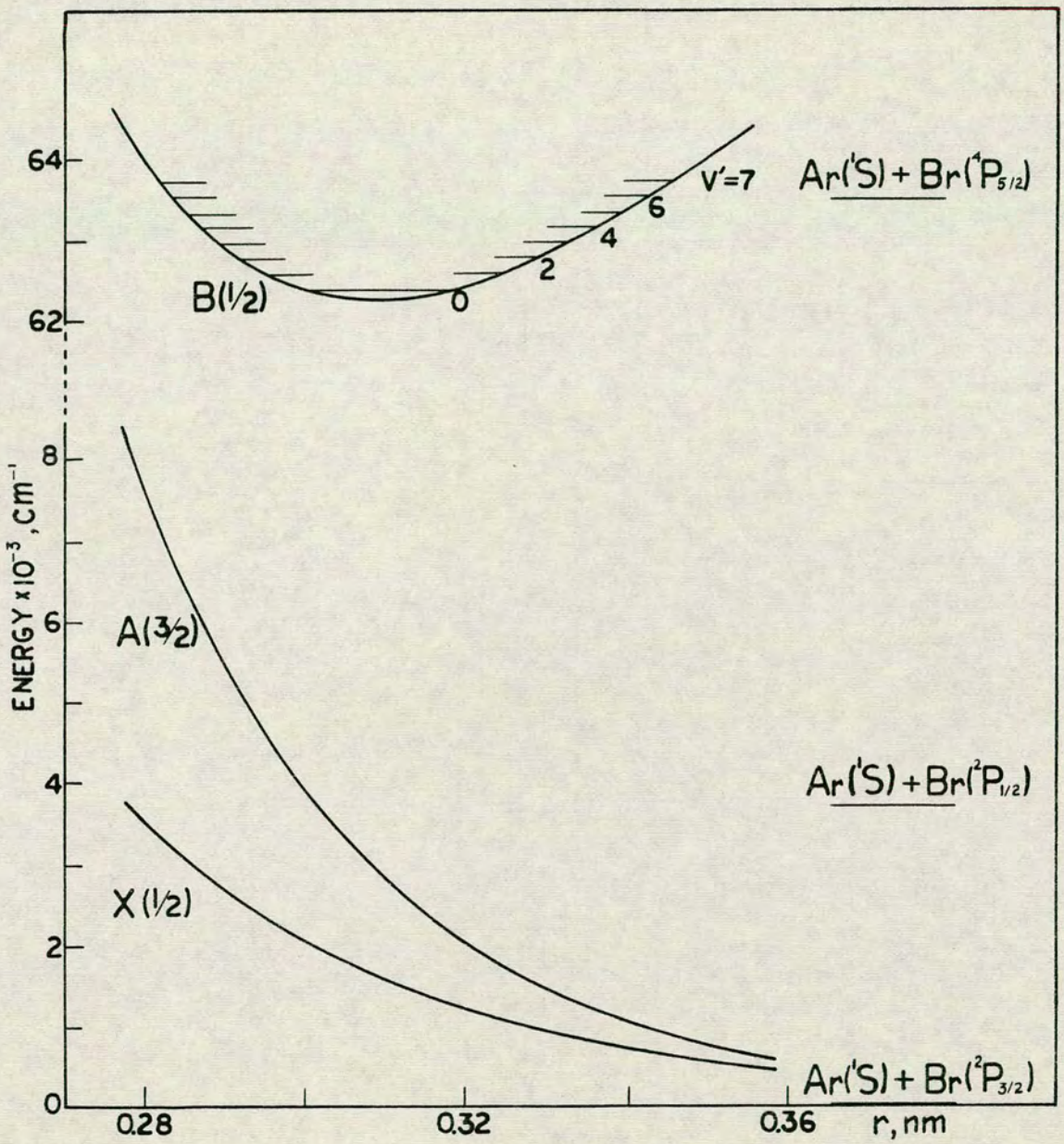

Fig. 5.35 Selected potential curves for the X-, A(3/2)- and B(1/2)- states for ArBr. $1 cm^{-1} = 11.963$ J mole^{-1}.

5.133 Transition moments.

Information on the detailed shape of the transition moments as functions of internuclear distance could not be obtained from the simulation calculations. However, it was found to be of importance to take account of a decreasing transition moment with internuclear distance in order to obtain a proper fit of calculated spectra with the MC spectra for HBr+Ar* and in order to obtain population distributions of realistic type from simulation calculations for the SC for CH_2Br_2+Ar*. Thus, it was found to be necessary to use a (linear) function with overall decrease in the FC region of about 35 - 45 % for the MC simulation calculations (see section 5.121), which is in a agreement with what theoretical calculations have predicted for other systems as mentioned before.

5.134 General conclusions.

Spectral continua due to bound-free transitions for ArBr spectra have been analysed by simulation calculations. Studies of the effect of changing the various parameters, the potential curves, the transition moments and the population distribution showed the main effects to differ for the different parameters. Thus, the change in the relative shape of the potentials mainly determines the relative positions of the peaks in the spectra, the magnitude of the change in the transition moment determines the overall relative intensity in the spectrum, while the population

distribution determines the relative intensity of peaks and troughs (the peak to trough ratio). Therefore the structure of these spectra was proved to contain important information on these parameters. This is an important general conclusion for spectra for bound-free transitions where a number of the lowest vibrational levels are emitting. While a number of such spectra have been observed, both in emission and absorption, not many detailed and systematic analyses of such spectra have been made.

It is of importance to be able to study the noble gas halide systems at low pressures or under collision free conditions in order to obtain information on the mechanism of the various reactions such as relaxation- and formation- reactions for the excited noble gas halides.

Most of the low pressure noble gas halide spectra which have been observed show a broad oscillatory structure and indicate that a great number of v′ levels are emitting.[9,21] These have been shown to contain rather limited information because of the extensive overlap of many different transitions from a great number of v′ levels and limited structure of the spectra.

The relative simplicity of the low pressure ArBr spectra and the fact that more information can be derived from these, based on the efficient predissociation of the high vibrational levels and the appearance of the bromine atomic lines makes these spectra ideal for the

purpose of studying the noble gas halide systems in general. It is expected that the fewer v′ levels are populated the more information can be derived from the simulation calculations of the spectra. This can be further verified by comparing simulation calculations for ArCl spectra for Cl_2+Ar^* and CCl_4+Ar^* discussed in the next section with the ArBr simulations. In order to obtain such spectra, systems where efficient predissociation of the highest v′ levels occurs (such as ArBr and KrI) or with threshold energy close to the minima of the excited states ($D(NgX^*)\sim D(RX)$), have to be chosen for study.

5.2 ArCl.

Simulation calculations for some ArCl spectra will now be presented. These calculations were carried out to interpret the structure and the pressure dependence behaviour of the ArCl MC spectra for Cl_2+Ar^*, CCl_4+Ar^* and $HCl+Ar^*$ and in the hope of being able to predict something about the shape (or the relative shape) of the B- and X- states and the population distribution in the B-state. The MC was assumed to represent the B-X transition.

5.21 Potential curves and calculated spectra.

Various bound state potentials with similar bond strengths and vibrational frequencies as the ground state of KCl were tried in calculations of spectra and spectral contributions. Spectral contributions due to transitions from levels corresponding to the threshold energy for Cl_2+Ar^* were calculated for these potentials and lower potentials chosen such that the corresponding Mulliken "difference potentials" had maxima and the diffuse bands of the spectral contributions varied in broad oscillatory patterns (see figures 4.6 a, 5.37 and 5.38). An upper potential which gave the spectral contribution with a spacing between the broad peaks close to that observed in the ArCl MC for Cl_2+Ar^* was especially searched for.[9] A potential curve for ArCl found in an analogous way to the potential for ArBr (see section 5.11) was found to satisfy this. This potential (U'_{Cl}) is expressed in the

same form as the calculated Rittner potential for KrF (see eq. 5.1). The values of the constants in that expression are tabulated in table 5.14.

Table 5.14

Values of constants in the Rittner potential expression for U'_{cl} (eq. 5.2) for r expressed in nm.

constants	$U'_{cl}(cm^{-1})$	constants	$U'_{cl}(cm^{-1})$
a_1	$1.110 \cdot 10^7$	c_1	$1.161 \cdot 10^4$
b_1	0.03580	c_3	$1.238 \cdot 10^2$
a_2	$5.766 \cdot 10^6$	c_4	26.29
b_2	0.04313	d	99975.7

$1 cm^{-1} = 11.963$ J mole^{-1}.

U'_{cl} fulfils the necessary requirements that it has a slightly, a. larger bond distance, b. smaller dissociation energy and c. lower fundamental frequency than the ground state of KCl[53] (see arguments in chapter 1 and table 1.2). This is shown in table 5.15 a.

Table 5.15

a. spectroscopic constants for the U'_{cl} potential and for the ground state of KCl (X(KCl)), b. a_i constants in the expression for $G'(v')$ (cm^{-1}) for U'_{cl} (see eq. 4.39). $1 cm^{-1} = 11.963$ J mole^{-1}.

a.

	U'_{cl}	X(KCl)[140]
r_e(nm)	0.294	0.267
$D_e(cm^{-1})$	38531.8	41269.32
$\omega_e(cm^{-1})$	244.4	279.8

b.

i	a_i
1	244.4
2	-0.9266
3	0.001827

U'_{Cl} was used to represent the B-state for ArCl. It is shown in figure 5.36 a. $v'=70$ is the closest vibrational level to the threshold energy for $Cl_2+Ar^*(^3P_2)$. The energy of the v' levels above the minimum of the potential ($G'(v')$) is determined by equation 4.39 for the values of the constants shown in table 5.15 b.

The relatively sharp cut off in the broad structure of the MC for Cl_2+Ar^* (see figure 2.4) at about 159 nm suggests that the broad oscillatory structure in the contributions from the highest emitting vibrational levels do not extend further to shorter wavelength. This was used to construct some lower potentials.

The potential U''_{Cl} was chosen such that the total energy range of the "difference potential" for $v'=70$

$$U_m = (G'(70)-U'_{Cl})+U''_{Cl} \qquad (5.15)$$

is approximately the same as the total range of the ArCl MC spectrum for Cl_2+Ar^* (~ 14900 cm^{-1}; 1.78×10^5 J mole^{-1}) (see figure i). This corresponds to the energy difference

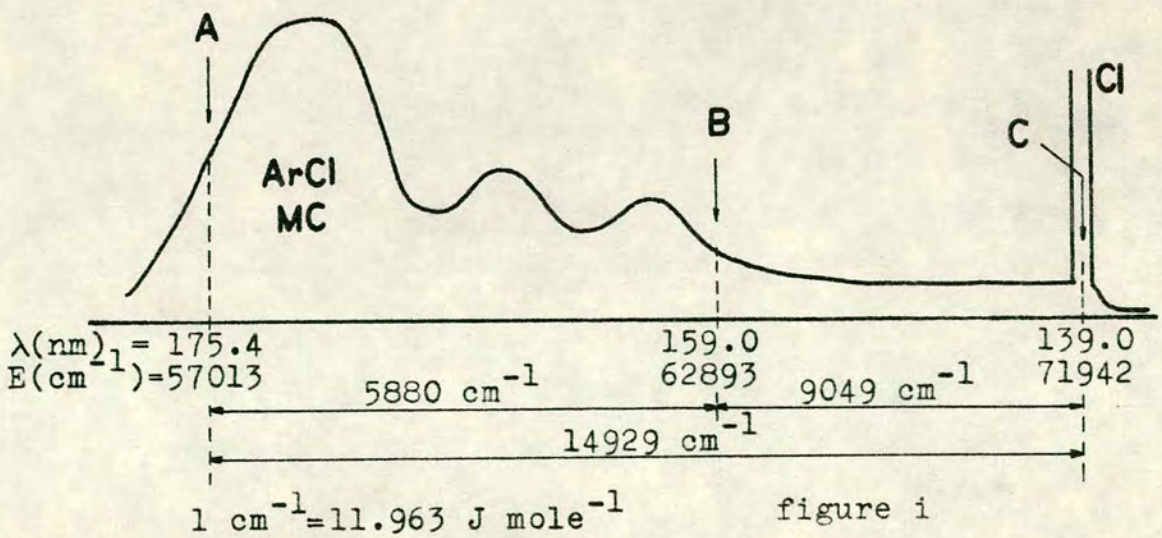

figure i

between A and C(ΔAC) shown in figure 5.36 a which is determined by the energy difference of the "difference potential" near r_e (the maximum) and the outer turning point of $v'=70$ ($r_2(70)$). In addition the value of U''_{c1} at the inner turning point of $v'=70$ ($r_1(70)$) was chosen such that the energy difference between A and B (ΔAB) (figure 5.36 a) is approximately the same as the range of the broad structure in the experimental spectrum (~ 6000 cm^{-1}, 71800 J mole^{-1}). The absolute value of U''_{c1} at r_e was then chosen to obtain the calculated spectrum at the correct absolute frequency, and U''_{c1} was expressed on the form $a/(r-b)^2$ (see table 5.16 and figure 5.36 a).

Table 5.16

Repulsive lower state potential curves U''_{ci} (cm^{-1}) $= a/(r-b)^2$ used in the simulation calculations for ArCl, MC spectra. r is expressed in nm.

i	a	b
1	20.68	0.1836
2	31.24	0.1761
3	28.14	0.1815
4	26.17	0.1851

The potentials U''_{c2}, U''_{c3} and U''_{c4} (see figure 5.36 b and table 5.15) were chosen in the following way: U''_{c2} was chosen to fulfil the same type of requirements for $v'=64$ as U''_{c1} for $v'=70$. $v'=64$ is the next vibrational level below the asymptotic energy value of the molecular

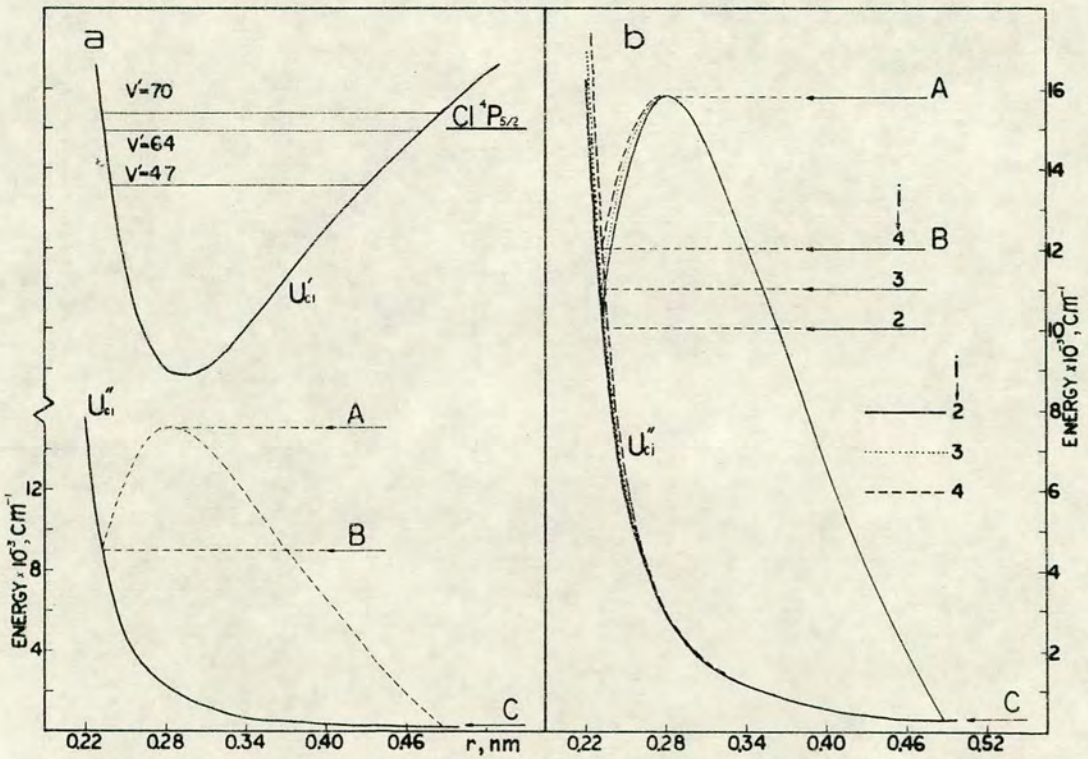

Fig. 5.36 Potential curves used in the simulation calculations for ArCl, MC spectra (U'_{Cl}, U''_{Cl} (a) and U''_{Ci} (i= 2,3,4) (b)) and "difference potentials" for v'=70 and U'_{Cl}. The arrows labeled A, B, and C indicate the positions which correspond to the classical transition to the maximum of the "difference potential" and the transitions from the inner and outer turning points for U'_{Cl} (v'=70) respectively. $1cm^{-1} = 11.963\ J\ mole^{-1}$.

states which correlate with $Cl^*(^4P_{5/2})+Ar(^1S)$, as shown in figure 5.36 a. This is a more realistic choice for a maximum emitting v′ level in Cl_2+Ar^*, as higher levels are probably predissociated. The potentials U''_{c3} and U''_{c4} differ in energy at short internuclear distance so that the A and C points do not differ significantly but the B points differ as shown in figure 5.36 b.

A spectrum and several v′ contributions, calculated by use of the two potentials U'_{c1} and U''_{c1} for even population distribution over the range v′= 0 to 70 and μ = constant, are shown in figures 5.37 and 5.38. The v′=70 contribution has been shown earlier, extended further to short E″ (figure 4.6). Analogous to what was obtained in the ArBr MC simulation the low v′ contributions mainly appear near the high E″ end of the spectrum while high v′ contributions extend further to low E″. The position of the broad peaks in the contour structure of the v′ contributions shift slightly to high E″ as v′ decreases. The broad structure in the calculated total spectrum reflects the broad structure in a number of v′ contributions.

The lowest vibrational levels mainly contribute to the strongest peak of the spectrum at the high E″ side of it, while the highest levels contribute to the low E″ side of it. This is consistent with what has been suggested earlier when the strongest MC peaks were compared for Cl_2+Ar^* (figure 3.27) and CCl_4+Ar^* (figure 3.28) and $HCl+Ar^*$ (figure 3.29) (see arguments in section 3.22).

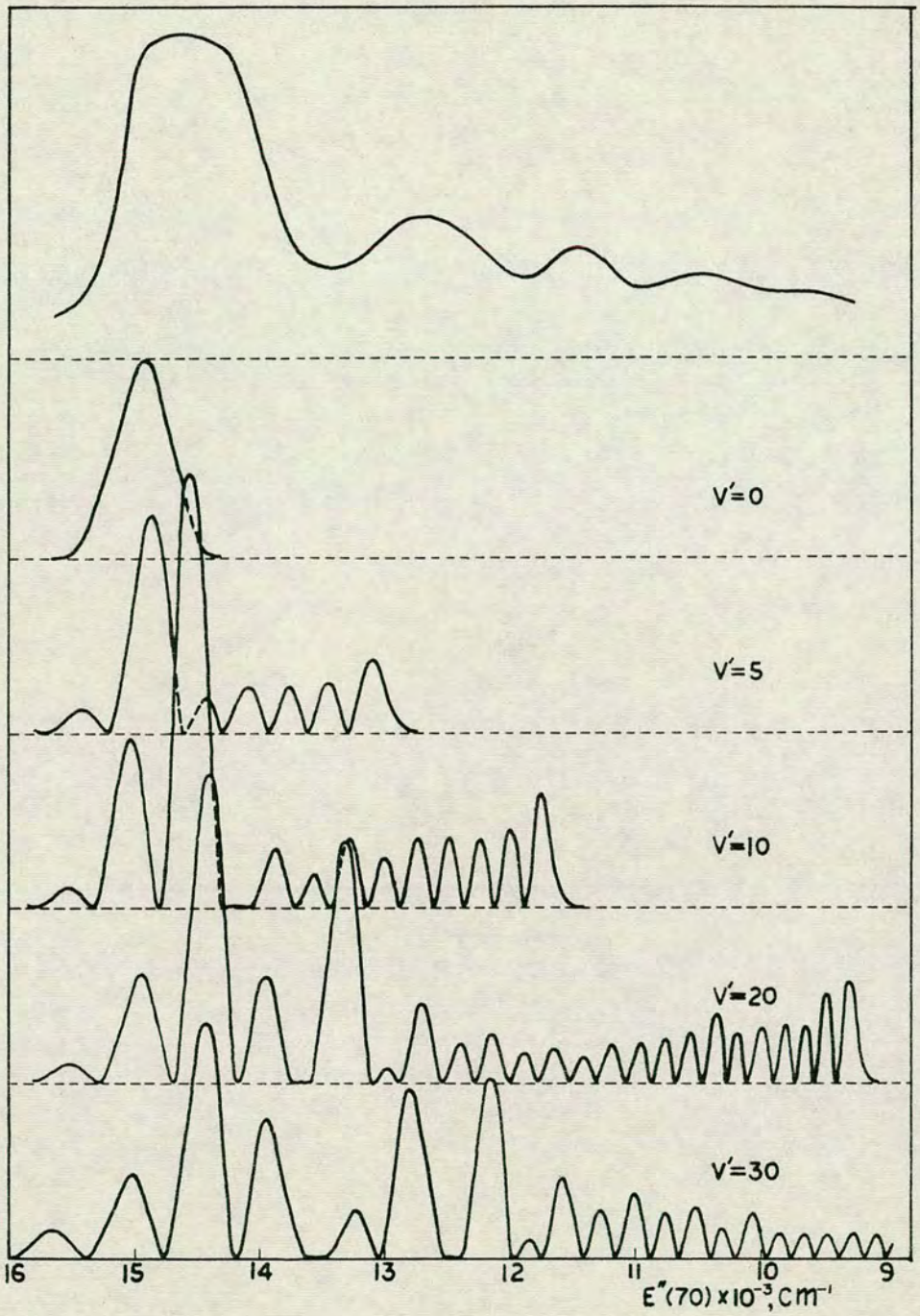

Fig. 5.37 Calculated spectrum (top) and vibrational contributions ($v' = 0,5,10,20,30$) (below) for transitions from U'_{cl} to U''_{cl} for μ_l = constant (μ_0). The spectrum was obtained by adding up all vibrational contributions for $v' = 0$-70 for even population distribution. The $v' = 10$, 20 and 30 contributions have been multiplied by equal population values but those for $v' = 0$ and 5 have been multiplied by lower population values. More vibrational contributions are shown in figure 5.38. $1 cm^{-1} = 11.963$ J mole^{-1}.

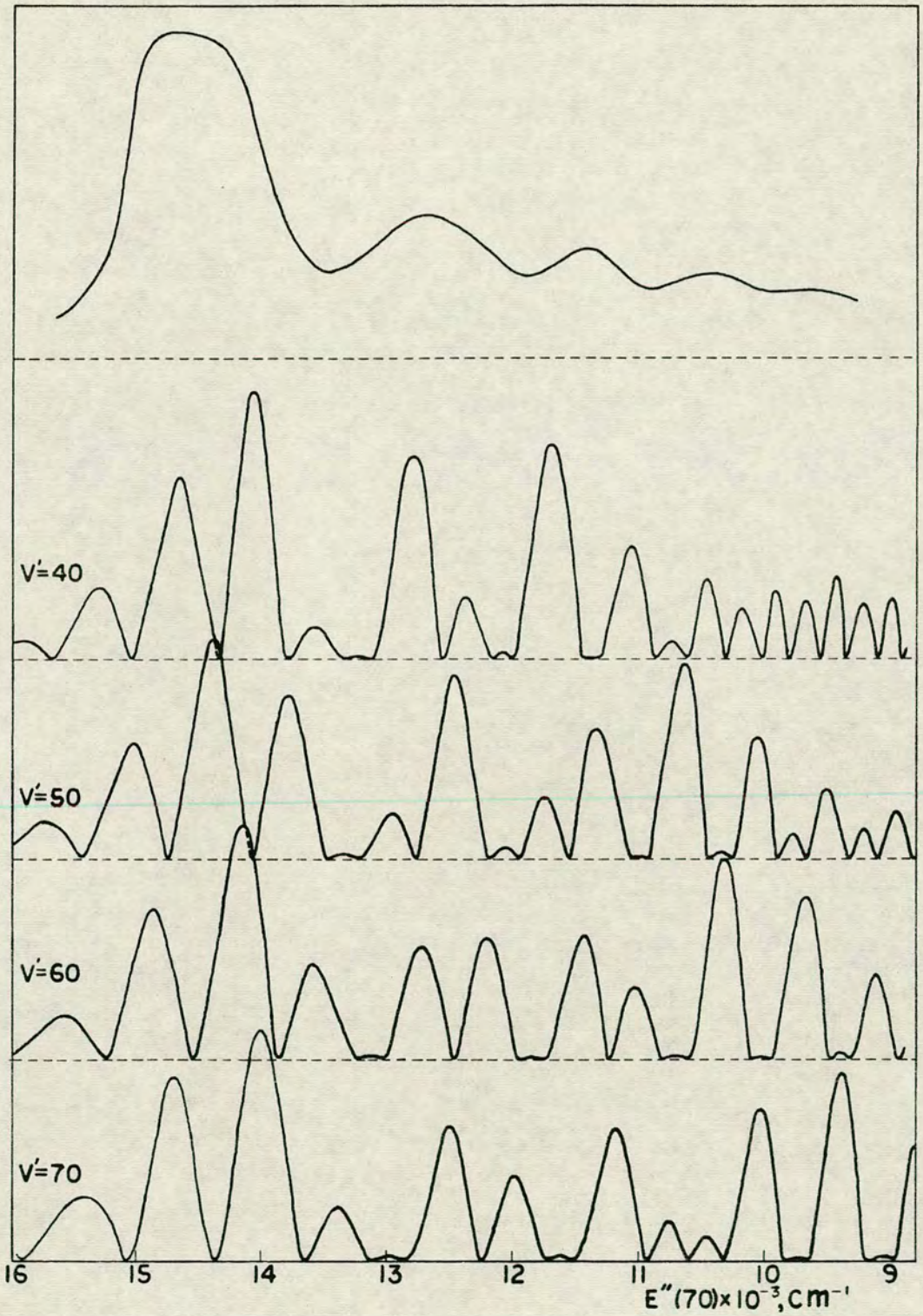

Fig. 5.38 Calculated spectrum (top) and vibrational contributions (v′=40, 50, 60, 70) (below) for transitions from U'_{cl} to U''_{cl} for μ_i=constant (μ_0) and even vibrational population distribution. The spectrum was obtained by adding up all vibrational contributions for v′= 0-70. More vibrational contributions are shown in figure 5.37.
$1 cm^{-1} = 11.963$ J mole^{-1}.

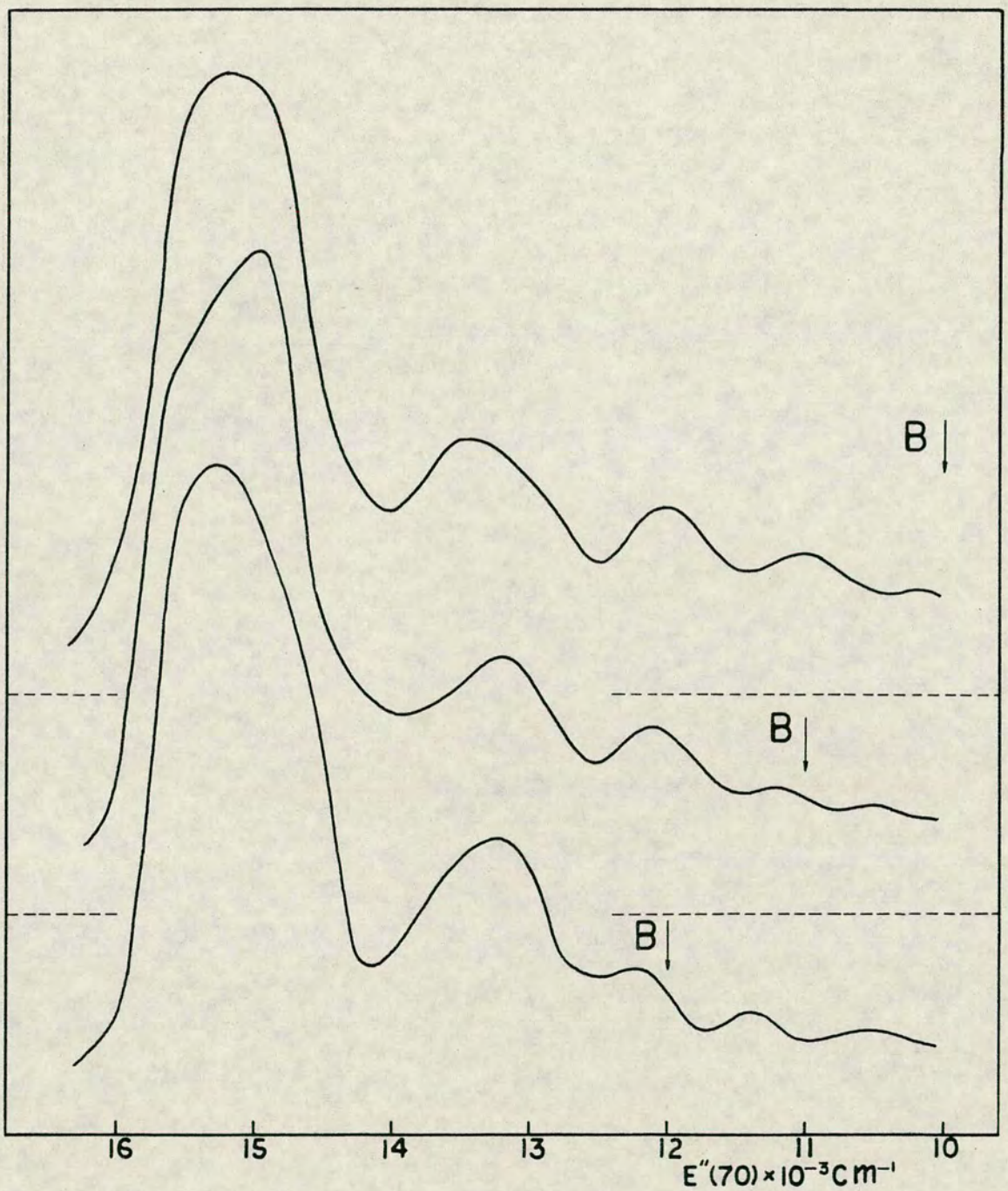

Fig. 5.39 Calculated spectra for transitions from U'_{c1}, $v'=0$-70 to U''_{ci} for $i = 2$ (top), 3 (middle) and 4 (bottom) for μ_i = constant (μ_0) and even vibrational population distribution. The arrows labeled B indicate the positions which correspond to the classical transitions from the inner turning point for U'_{c1}, $v'=70$. $1 cm^{-1} = 11.963$ J mole^{-1}.

The effect of using lower potentials with different slopes at short internuclear distance on the shape of the calculated spectra is shown in figure 5.39 for the three repulsive potentials, U''_{c2}, U''_{c3} and U''_{c4}, μ_i=constant and even population distribution for v'=0-70. Despite the fact that ΔAB and the range of the broad oscillatory structure of the v' contributions decreases as $U''_{c2} > U''_{c3} > U''_{c4}$ the structure of the calculated spectra was not found to change greatly. A slight shift of the intensity from low E'' to high E'' was observed as the B point was increased (figure 5.36 b). The position of the peaks on the high E'' side of B remains virtually unchanged.

5.22 Effect of changing the population distribution.

The effect on the calculated spectra of changing the population distribution will now be considered and a comparison of the calculated spectra with the experimental ones will be made.

The effect of changing v'_{max} is shown in figure 5.40, where calculated spectra are shown for U''_{c4}, μ_i=constant (μ_0) and even vibrational population distribution for v'= 0-v'_{max} where v'_{max}= 47,64 and 70. Peaks were found to shift to high E'' as v'_{max} was decreased due to the shift of the broad peaks in the contour spectra of the v' contributions with decreasing v' (figures 5.37 and 5.38). This is consistent with the observed shift of the peaks in the experimental ArCl spectra for the reactions of Ar^* with the different chlorine containing reagents with

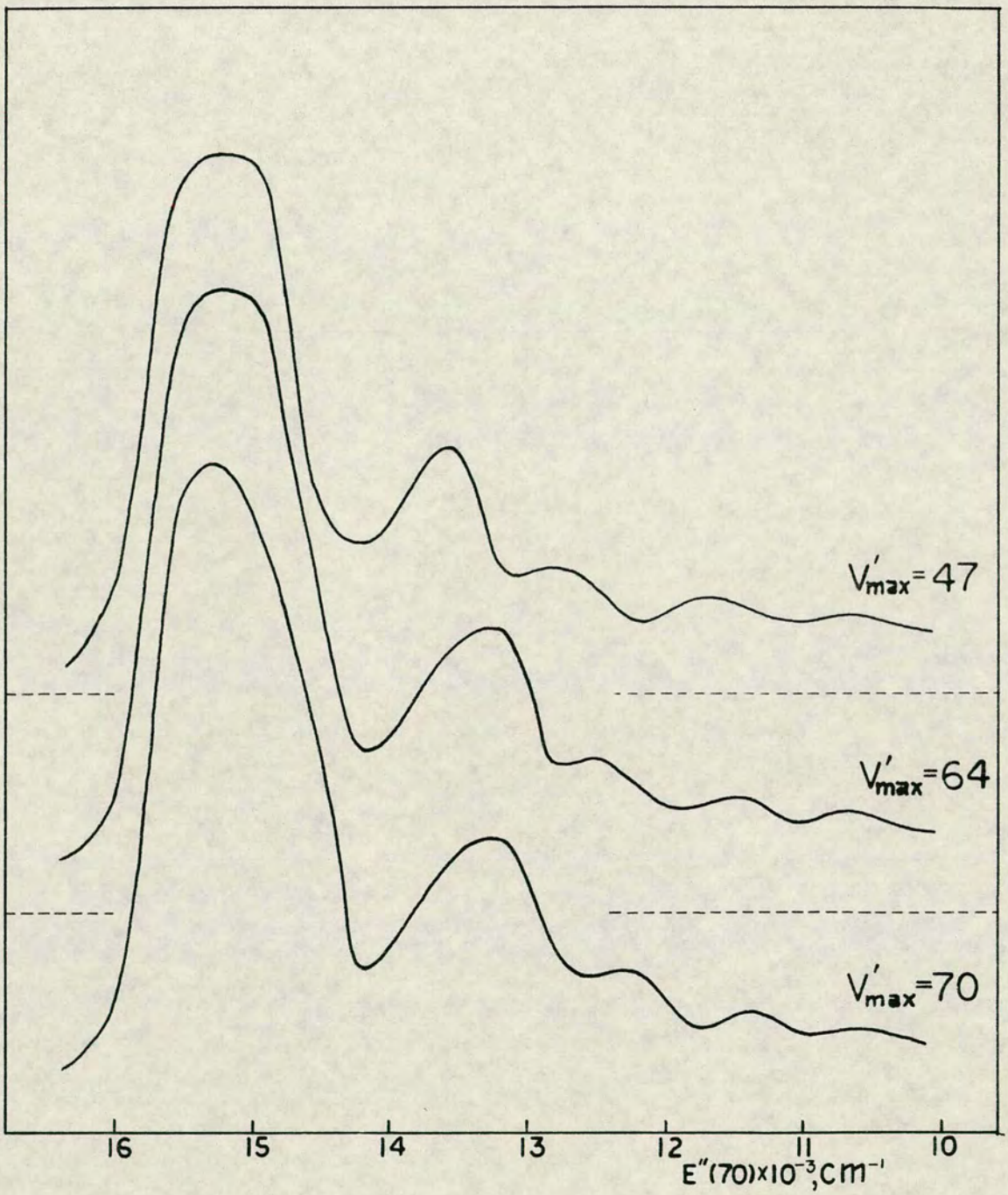

Fig. 5.40 Calculated spectra for transitions from U'_{c1}, to U''_{c4} for μ_i=constant (μ_0) and even vibrational population distribution for the vibrational levels $v'=0-v'_{max}$ for v'_{max}= 47 (top), 64 (middle) and 70 (bottom). $1cm^{-1}$= 11.963 J $mole^{-1}$.

different bond energies, since these spectra represent transitions from a range of v′ levels and different v'_{max} (different threshold energies). Such shifts have been observed by others and can be shown by comparing the spectra for Cl_2+Ar^* and CCl_4+Ar^* shown in figures 3.27 and 3.28. $v'_{max}= 47$ corresponds to the threshold energy for CCl_4+Ar^* and the spacing between the peaks in the corresponding calculated spectrum shown in figure 5.40 is close to that in the CCl_4+Ar^* spectrum.

Only a small difference was observed in the calculated spectra for $v'_{max}= 64$ and 70 as shown in figure 5.40. Therefore, the comparison of the calculated spectra for $v'_{max}= 70$ with the experimental Cl_2+Ar^* spectrum is equally useful as making a corresponding comparison of the calculated spectra for the more realistic case when $v'_{max}= 64$ (see section 5.21).

Population distributions were tried, where the population in the highest v′ levels is much greater than in the lowest levels, analogous to what is observed in the alkali halides[73-75] formed by reactions of the alkali atoms with the halogens. The population distribution shown in figure 5.41 a is qualitatively similar to that observed for KBr[139] ($\leftarrow K+Br_2$). The corresponding calculated spectrum for U''_{Cl}, $v'_{max}= 70$ and $\mu_i =$ constant shown in figure 5.41 a, shows little resemblance to that of the experimental spectrum for Cl_2+Ar^* (figure 3.27). Such a population distribution can therefore be ruled out.

As the population in the low levels was increased relative to that in the high levels, the intensity and the peaks shifted from low E'' to high E'', as shown in figure 5.41 b. The shape of the spectrum changes so that the intensity of the troughs relative to the peaks increases and the minimum at E''(70) = 14600 cm^{-1} in the spectrum in figure 5.41 a disappears and a single broad peak analogous to that observed in the experimental spectrum was formed. These characteristic changes are analogous to the changes which were observed in the experimental spectrum with increase in pressure (figure 3.27), which suggests that these are basically due to vibrational relaxation. The calculated spectra resemble more closely the experimental ones if the population in the lowest levels is relatively high, i.e. relatively higher than typically found in the alkali halide systems.

Various such calculated spectra for different population distributions were obtained and compared with the experimental spectra for Cl_2+Ar^* over the range where the broad structure was observed. These showed too deep a trough at about E''(70) = 13500 cm^{-1} (161500 J $mole^{-1}$) relative to the height of the strongest peak and a relatively too high intensity to lower E'', such as the one shown in figure 5.41 c with the experimental spectrum from figure 2.4 corrected for spectral response. The relatively too low calculated intensity between the two outermost peaks might be corrected for to some extend if account was taken of

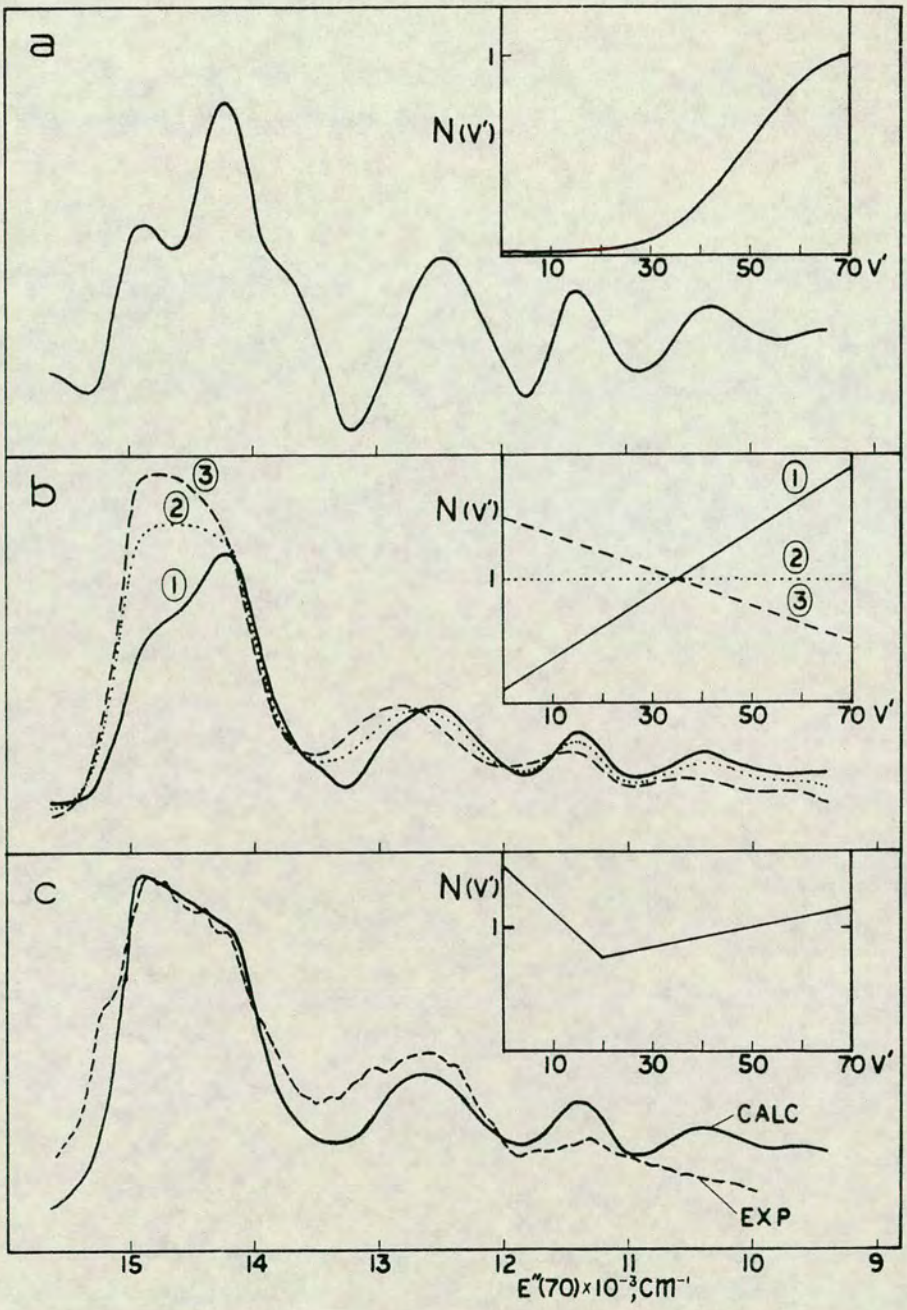

Fig. 5.41 Calculated spectra for transitions from U'_{Cl}, $v' = 0\text{-}70$ to U''_{Cl} for μ_i=constant (μ_0) and various vibrational population distributions shown graphically as $N(v')$ vs v'. a: Calculated spectrum for an inverse population distribution
b: Calculated spectra for linear population distributions. c: Calculated spectrum and the corresponding population distribution (solid curve) and experimental ArCl, MC spectrum (dashed curve) generated by $Ar^* + Cl_2$, 1.56 torr (208 Nm^{-2}), 500 μm slit width. $1 cm^{-1} = 11.963$ J $mole^{-1}$.

an underlying C-A(3/2) spectrum in this region while the percent contribution of such an underlying emission would presumably be greater in that region than at the position of the strongest peak. The relatively too low calculated intensity at low E'' can be accounted for by inclusion of a μ_i function which decreases with an increasing internuclear distance. A use of such functions was found to show a decrease in the calculated intensity with decreasing E''.

Calculated spectra for U''_{c2}, μ_i = constant, $v'_{max} - 47$ and different linear population distributions are shown in figure 5.42 a as well as a low pressure experimental spectrum (0.6 torr; 80 Nm^{-2}) for $CCl_4 + Ar^*$. Analogous to the above mentioned spectral calculations it was found that in order to obtain a calculated spectrum with a resonably comparable shape to the experimental spectrum it was necessary to weigh the population in the lowest levels relatively highly compared to that in the highest v' levels. Thus, in the calculation presented in figure 5.42 a, a linearly decreasing population with increasing vibrational level quantum number was found to give the best fit of a number of such linear population distribution functions.

By using the same potentials and the μ_o function, as in the simulation calculations for $CCl_4 + Ar^*$ MC, it was found that the shape and spectral range of the ArCl MC observed from $HCl + Ar^*$ (figure 3.29) is consistent with transitions from the very lowest vibrational levels

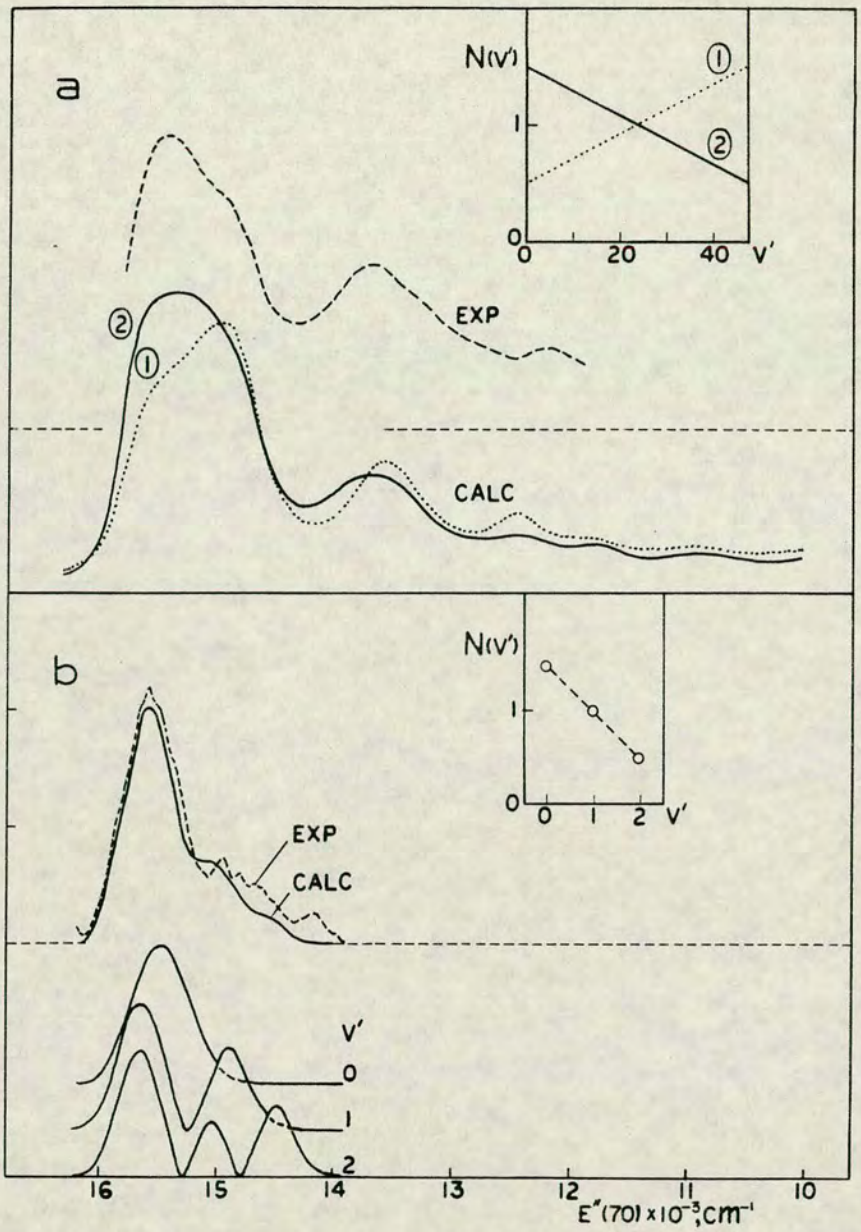

Fig. 5.42 Calculated spectra and experimental ArCl, MC spectra. The calculated spectra were obtained for transitions from U'_{cl} to U''_{c2} for μ_i=constant (μ_0). a: Calculated spectra (① and ②) and corresponding linear vibrational population distributions (N(v′) vs v′) for v′=0-47. The dashed curve is an ArCl, MC spectrum generated by $Ar^* + CCl_4$, 0.6 torr (80 Nm^{-2}), 500 μm slit width. b: Calculated spectrum and vibrational contributions for v′= 0, 1 and 2 (solid curves) and experimental ArCl, MC spectrum generated by Ar^*+HCl, 500 μm slit width (dashed curve). The calculated spectrum was obtained for a linear population distribution. $1cm^{-1}$= 11.963 J $mole^{-1}$.

with $v'_{max} = 2$ as shown in figure 5.42 b. The population distribution is found to be decreasing with increasing v′ level. It should be noted, however, that the presence of an HCl emission at the same frequency makes this analysis difficult.

5.23 Discussion.

The population distributions obtained for $ArCl^*(B)$ from the reaction of Cl_2+Ar^* is found to differ from that obtained for the potassium halides from the reactions of the halogens with K in not showing a greatly inversed population distribution. This may be due to the fact that other reaction mechanisms are also responsible for the formation of $ArCl^*(B)$ than the stripping mechanism, which has been used to explain the high efficiency of conversion of the exothermicity into vibrational excitation for the reactions of the halogens with the alkali atoms.

Comparison of the results for the population distribution in $ArCl^*$ for CCl_4+Ar^* and Cl_2+Ar^* suggests that relatively less fraction of the total energy available goes into vibrational energy for CCl_4+Ar^* than for Cl_2+Ar^*. This fact is consistent with what is found for the analogous reactions of potassium with CCl_4 and Cl_2 respectively.[73,74] The latter of these reactions is thought to occur by the stripping mechanism to form vibrationally excited KCl while for the former one the yield and other properties are intermediate between

those for the prototype rebound and stripping cases,[73] with relatively less energy going into vibration.

Liu and Olsen have performed ab initio calculations[141] on the ground state of ArCl. The calculated potential has a slight Van der Waals minimum at long internuclear distance (~ 0.48 nm). It is lower in energy in the region of r_e for U'_{cl} than any of the lower state potential curves which were used in the simulation calculations. The potential curve U''_{cl} is closest to the calculated one of these (see figure 5.43).

The nature of analytical potentials on the form $a/(r-b)^2$ is such that they all approach the asymptotic zero energy limit relatively slowly and are very steep to shorter wavelength, so it is even difficult to obtain closer fit than that shown in figure 5.43. A Morse potential with a slight minimum might be more useful for that purpose.

If the analytical potentials are substituted by the calculated potential the upper state potential will have to be lowered by about 200-300 cm^{-1} (2390-3590 J $mole^{-1}$) in order to make the calculated spectra lie in a correct position on the absolute frequency scale. This lowering is comparable to the lowering which was made for the U'_{bl} potential (section 5.132). Since both the potentials U'_{bl} and U'_{cl}, which were obtained by the same method, described in section 5.11, will have to be lowered, the conclusion is reached that this method leads to potentials of too high energy or too small

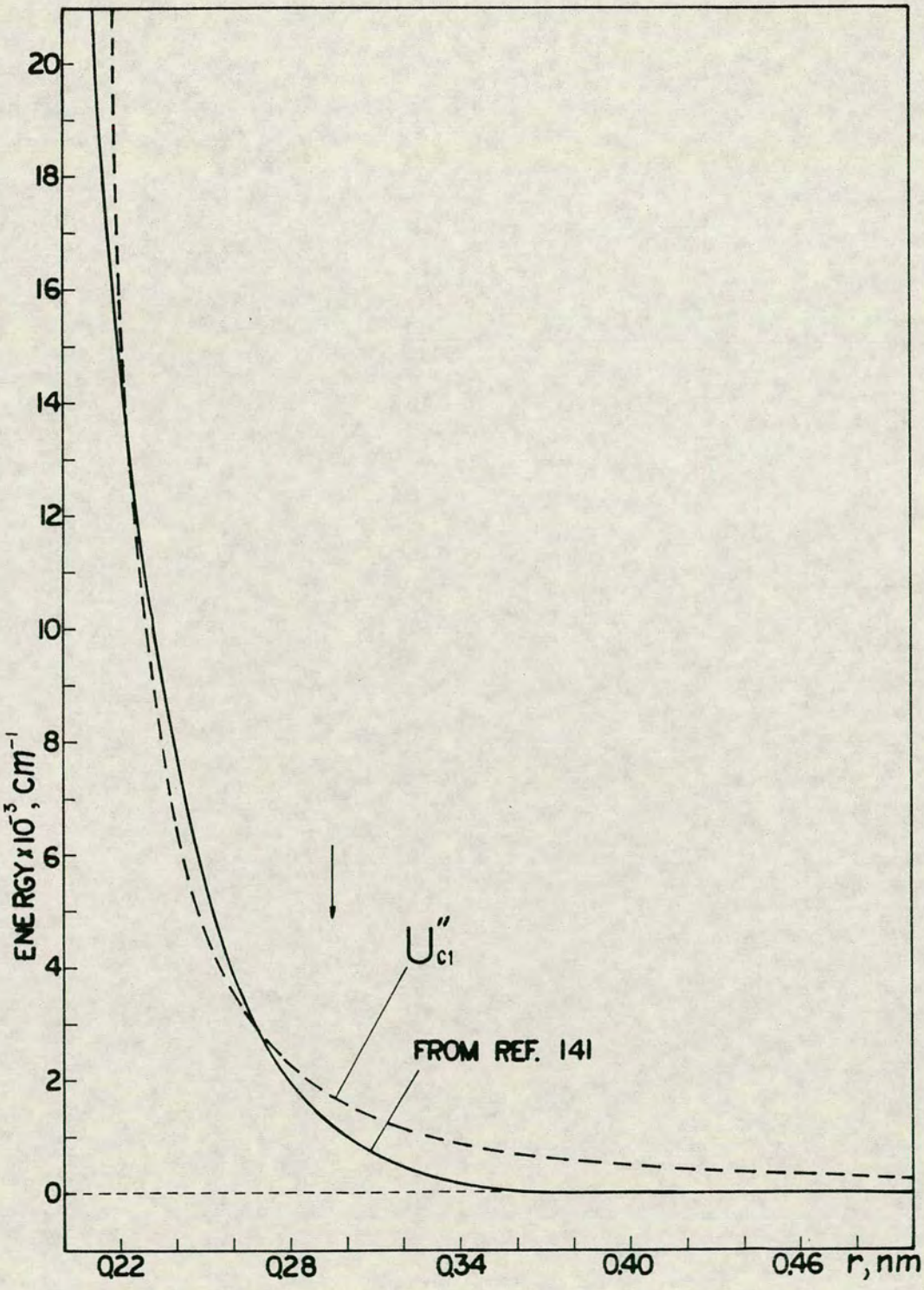

Fig. 5.43 Repulsive potential curves for the ArCl, X - state obtained from ab initio calculations[141] (solid curve) and U''_{Cl}, which was used in the simulation calculations for the ArCl, MC spectrum generated by $Ar^* + Cl_2$. The arrow indicates the equilibrium internuclear distance for the U'_{Cl} potential. $1 cm^{-1} = 11.963$ J mole^{-1}.

bond strength. On the other hand, the fact that U'_{Cl} was found to give calculated v′ contributions and spectra with the spacing between broad peaks close to that observed in the experimental spectra, suggests that the shape and the vibrational frequency of these potentials is close to that of the B-state. The spacing between broad peaks in the contour spectra has been found to be significantly dependent on the vibrational frequency.[9,21]

Due to the great overlap of transitions from a number of v′ levels in spectra like those obtained for Cl_2+Ar^* and CCl_4+Ar^* these are more difficult to analyse and obtain significant information from, than spectra where fewer v′ levels are emitting such as in the ArBr spectra. It is therefore of importance to select chlorine containing reagents which give relatively low threshold energy and few v′ levels populated, for the purpose of studying the ArCl system. While the reagents HCl, DCl and CNCl which were tried satisfy this requirement none of these are ideal for the purpose of studying the ArCl spectra. The ArCl spectra for HCl and DCl overlap with HCl and DCl spectra and the ArCl spectrum for CNCl is very weak, possibly due to a more favourable formation of $ArCN^*$ rather than $ArCl^*$, judging from somewhat analogous reactions such as the reactions of the alkaline earth atoms with CNBr [150] which mainly result in the formation of the alkaline earth monocyanides. On the other hand spectra obtained for systems with low threshold energies do not show

any chlorine atomic lines, which makes these spectra less useful than the ArBr spectra. One of the great advantages of using the ArBr spectra for the purpose of studying the noble gas halide system is the appearance of the bromine atomic lines which could be used as an internal standard against which changes in the relative intensities could be studied. In most of the noble gas halide systems the situation is analogous to that found for the ArCl system, and either no halogen atomic emission is observed or it is observed as well as complicated noble gas halide spectra. In other systems only halogen atomic emission is observed as for $RI+Ar^{*}$. This suggests that the ArBr spectra are the most useful spectra for studying the noble gas halide systems.

APPENDIX 1

Publications.

The paper: "Emission Spectra of the Noble-gas halides: The B(1/2)-A(1/2) System". Chem. Phys. Lett. 59 51 (1978) deals with some of my results as well as results obtained by Dr. M.F. Golde and M.P. Casassa and is listed below.

In addition, two papers by Dr. M.F. Golde and myself on the subjects:

I The Emission Spectrum of ArBr.

II Potential Curves of ArBr and Population Distributions in the B(1/2) and C(3/2) Electronic States,

are now in preparation and will be published soon.

Volume 59, number 1 CHEMICAL PHYSICS LETTERS 1 November 1978

EMISSION SPECTRA OF THE NOBLE-GAS HALIDES: THE B(1/2)–A(1/2) SYSTEM

M.P. CASASSA, M.F. GOLDE and A. KVARAN‡
Department of Chemistry, University of Pittsburgh, Pittsburgh, Pennsylvania 15260, USA

Received 28 July 1978

The B(1/2)–A(1/2) transition has been detected in the emission spectra of ArBr, KrBr, KrI and XeI at low pressure. Comparison with the well-known "B–X" continua implies that, in many cases, the latter is heavily overlapped by C(3/2)–A(3/2) emission.

1. Introduction

The diatomic noble-gas halides were recently discovered through their chemiluminescence arising from the reactions of electronically-excited Ar, Kr and Xe ($^3P_{0,2}$) atoms with a variety of halogen-containing molecules [1,2]. These reactions are of great interest in that the excited atoms show certain properties similiar to those of ground state alkali atoms and the noble-gas halides have acquired importance as the basis of a group of high-power near-UV and vacuum-UV lasers.

The properties of the noble-gas halides have been studied theoretically and also through their absorption and emission spectra. Ab initio calculations [3–5] show that three close-lying excited states, B(Ω = 1/2), C(3/2) and D(1/2) can emit by $\Delta\Omega = 0$ transitions to the lower states, X(1/2), A(3/2) and A(1/2) (see schematic potential curves, fig. 1). Of these, the B–X, C–A(3/2) and D–X systems have been observed [6,7].

Interpretation of the experimental spectra has been most successful for XeF and XeCl where vibrational and, for XeF, rotational analysis of the B–X and D–X spectra have given information about the bound upper and lower electronic states [8,9]. In the other molecules, where the lower states are largely unbound, the emission spectra are continuous and assumptions concerning the assignments of the various features in the spectra have been necessary in order to allow analysis of the spectra [10].

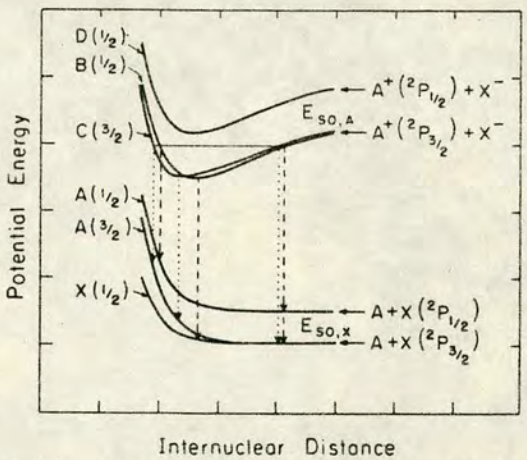

Fig. 1. Schematic potential curves for the noble-gas halides, AX. $E_{SO,A}$ (cm^{-1}): Ar: 1432; Kr: 5371; Xe: 10537. $E_{SO,X}$ (cm^{-1}): Br: 3685; I: 7603. – – – Transitions from B(1/2), . . . transitions from C(3/2).

In the present work, we report observation of B(1/2)–A(1/2) emission spectra in ArBr, KrBr, KrI and XeI. By comparing this new emission with the B–X and C–A(3/2) continua, we obtain evidence for appreciable overlap of B–X and C–A(3/2) emission in the "main continuum" of the spectrum.

2. Experimental

Spectra were generated in a discharge-flow apparatus by the reaction of metastable Ar, Kr and Xe

‡ Also Department of Chemistry, University of Edinburgh, Edinburgh, UK.

atoms ($A^{*3}P_{0,2}$) with bromine- and iodine-containing molecules (RX):

$$A^* + RX \rightarrow AX^* + R, \quad (1)$$

$$AX^* \rightarrow A + X + h\nu. \quad (2)$$

The metastable excited atoms were produced by flowing prepurified Ar, pure or with small admixtures of Kr or Xe, through a weak dc discharge at a total pressure of 0.5 to 12 torr. This flow was mixed with a small flow of reagent molecules, emerging from a concentric tube and the emission from the mixing zone was monitored with a vacuum monochromator (Hilger E766 one-meter normal incidence or Minuteman 305 MV 1/2-meter Czerny–Turner) and photomultipliers (EMR 542G for wavelengths less than 185 nm and EMI 9789QB for the range 150 to 500 nm).

The spectral responses of the detection systems were measured using band and continuous spectra of known spectral distribution. For the vacuum-UV, the ArCl B–X continuum ($Ar^* + Cl_2$, CCl_4), and the $H_2(B\,^1\Sigma_u^+ - X\,^1\Sigma_g^+)$, $N_2(a\,^1\Pi_g - X\,^1\Sigma_g^+)$ and $CO(A\,^1\Pi - X\,^1\Sigma^+)$ band systems were used and, for the near UV, $NO(A\,^2\Sigma^+ - X\,^2\Pi)$, $N_2(C\,^3\Pi_u - B\,^3\Pi_g)$ and $CO(a\,^3\Pi - X\,^1\Sigma^+)$. The spectra presented here have been corrected, where necessary, for spectral response.

Gaseous reagents, HBr and HI (Matheson), were trapped at 77 K and pumped on to remove volatile impurities, then were passed through a cooled, 195 K, trap at low pressure to remove condensable impurities. $CHBr_3$, CBr_4, CH_3I and CH_2I_2 (Aldrich Chemical Co.) and Br_2 and I_2 (Mallinckrodt Inc.) were used without purification.

3. Results

The reactions of Ar, Kr and Xe metastable ($^3P_{0,2}$) atoms with Br_2, I_2, HBr, HI, CH_2Br_2, $CHBr_3$, CBr_4, CH_3I and CH_2I_2 were studied. The dominant component of the gas was always Ar, the other components normally comprising at most a few percent of the flow. Low pressure spectra are presented in figs. 2 to 5; these include the first published spectra of KrI and ArBr.

The emission spectra arising from the reactions of Ar* with all the iodides and of Kr* with I_2 and CH_2I_2 consisted only of atomic lines from energetically-accessible excited states of iodine, populated by dissociative excitation of the reagent molecule. Kr* + HI, however, gave three distinct regions of continuous emission, as shown in fig. 2, which are referred to, from low to high wavelength, as the main continuum (MC), secondary continuum (SC) and third continuum (TC) and were assigned as principally B(1/2)–X(1/2), C(3/2)–A(3/2) and B(1/2)–A(1/2) respectively. The very intense $I(6s\,^4P_{5/2} - {}^2P_{3/2})$ line at 183 nm provided the low wavelength limit of this spectrum; other much weaker I lines

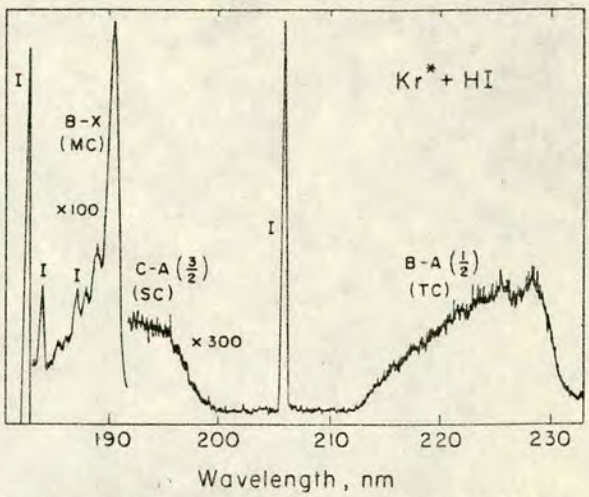

Fig. 2. KrI* spectrum generated by Kr* + HI at 2.1 torr total pressure. Iodine lines at 184.5, 187.6 and 206.2 nm arise from Ar* + HI.

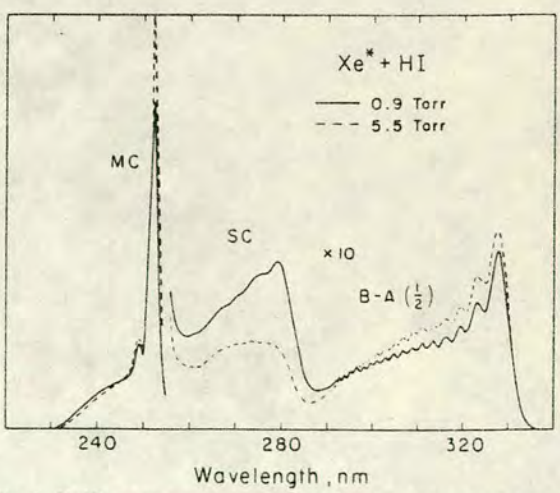

Fig. 3. XeI* spectra generated by Xe* + HI. Integrated intensities at the two pressures are equal.

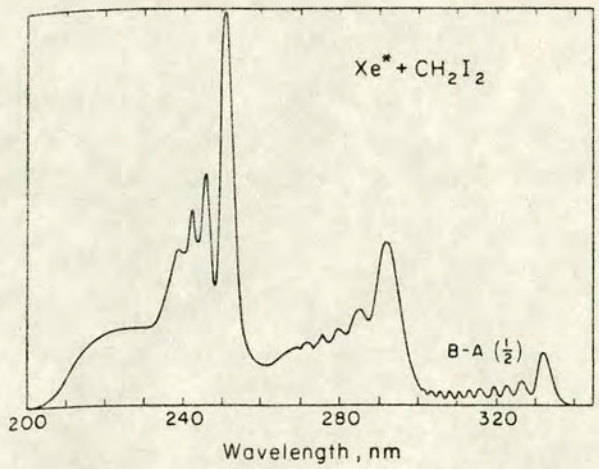

Fig. 4. XeI* spectrum generated by Xe* + CH_2I_2. Total pressure: 0.8 torr.

arise from the reaction of HI with residual traces of Ar*.

Spectra of Xe* with CH_3I, CH_2I_2 and HI showed no I* emission; again, the three XeI continua could be clearly distinguished (figs. 3 and 4).

For the reactions of Kr* with HBr and the bromomethanes, the MC and SC of KrBr were clearly resolved, but the B–A(1/2) system appeared as a shoulder at the long wavelength end of the C–A(3/2) continuum; structure, in the form of a separate peak at 228 nm, was apparent only in the case of Kr* + HBr.

The spectra of ArBr in fig. 5 are composites of

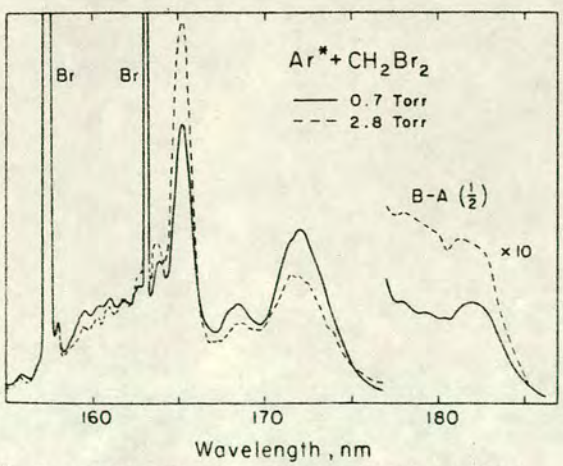

Fig. 5. ArBr* spectra generated by Ar* + CH_2Br_2. The integrated intensities at the two pressures are equal.

data obtained with both detection systems used in this study: the B–A(1/2) continuum is only partially resolved from the strong SC in the Ar* + CH_2Br_2 and HBr spectra. In the spectrum from Ar* + HBr, a further weak continuum was observed, extending from the tail of the B–A(1/2) system at 185 nm to at least 330 nm. The considerable structure in the ArBr continua will be discussed in a separate publication.

The dependence of the form of the spectra on total Ar pressure was investigated in order to confirm the B–A(1/2) assignments. For Xe* + HI, the ratio of the integrated XeI MC intensity to that of the B–A(1/2) continuum varied little with increasing pressure (fig. 6), while the SC intensity dropped markedly relative to that of the MC, due to electronic quenching of the C state.

Fig. 5 shows spectra of the Ar* + CH_2Br_2 reaction at 0.7 and 2.8 torr, the spectra being normalized to yield equal total integrated intensities. Both the B–A(1/2) region and MC peak show a positive pressure dependence, while the whole SC drops in intensity as the pressure is raised. Further data in table 1

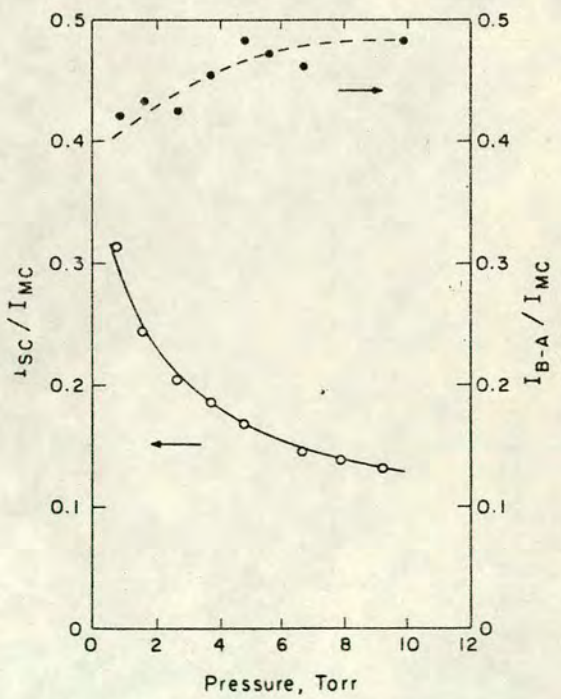

Fig. 6. Pressure dependence of the main continuum, secondary continuum and third continuum (B–A(1/2)) in XeI* (Xe* + HI). • I_{B-A}/I_{MC}; ○ I_{SC}/I_{MC}.

Table 1
Pressure dependence of the C–A(3/2) and B–A(1/2) continua relative to the main continuum in ArBr* from the reaction of Ar* with CH_2Br_2

p (torr)	$\frac{I(172.0\text{ nm})}{I(165.2\text{ nm})}$	$\frac{I(179.0\text{ nm})}{I(165.2\text{ nm})}$	$\frac{I(182.0\text{ nm})}{I(165.2\text{ nm})}$
0.45	0.78	0.027	0.030
0.77	0.59	0.029	0.031(5)
1.33	0.45	0.033	0.033
1.78	0.37	0.034(5)	0.033
2.34	0.31	0.038	0.034
3.06	0.25	0.040	0.035
3.75	–	0.042	0.035

confirm that the pressure dependence at 182 nm in the third continuum is closely similar to that of the B–X peak at 165.2 nm. No strong pressure dependence of the form of the KrI spectrum was observed over the range 1 to 4 torr, but the other systems studied showed behavior comparable to that of Xe* + HI and ArBr.

4. Discussion

4.1. Assignment of the B–A(1/2) system

Ab initio calculations [3–5] have provided much of the present knowledge concerning the electronic states of the noble-gas halides. The potential curves of the excited B(1/2) and C(3/2) states are predicted to be similar in shape and position but there is as yet no definite experimental information as to their relative positions. Calculations and experiments [7] find that the D(1/2) state is displaced to higher energy by approximately the spin–orbit splitting of the noble-gas positive ion.

Calculations and experiment further agree that the A(3/2) state is considerably more repulsive than the X(1/2) ground state [5,10,11]. The A(1/2) state lies above the A(3/2) state by the halogen atom spin–orbit splitting at large internuclear distance; an atoms-in-molecule model calculation for KrF [3] found the A(1/2) and A(3/2) components to converge slowly at smaller internuclear distances to a limiting energy separation of two-thirds of that in the free atom.

The schematic potential curves, fig. 1, constructed on the basis of the above, imply that the B–A(1/2) bound–free continuum is expected to resemble that of the C–A(3/2) system in shape but to be shifted to long wavelength by approximately the halogen spin–orbit splitting. As shown in fig. 1, the limiting low and high wavelength regions of these continua should involve transitions close to the outer and inner turning-points respectively from the highest populated vibrational levels of the emitting states.

Applying these principles to the experimental spectra, in KrI (fig. 2), the highest emitting levels are determined by predissociation of the B and C states by states correlating with $Kr(^1S_0) + I^*(^4P_{5/2})$ (not shown in fig. 1). The threshold of the C–A(3/2) system is thus defined approximately by the wavelength, 183.0 nm, of the $I(^4P_{5/2}–^2P_{3/2})$ line. The low wavelength threshold of the B–A(1/2) continuum is 213.3 ± 0.2 nm, a displacement of 7750 ± 40 cm^{-1} from the iodine line. This value is close to the spin–orbit splitting of the I atom, 7603 cm^{-1}.

Similarly, in the Xe* + HI spectrum, the predicted B–A(1/2) threshold is at 280.8 ± 0.6 nm, close to the lowest wavelength, 285 nm, at which B–A(1/2) emission can be resolved from the overlapping C–A(3/2) system.

In all the other noble-gas halides, the B–A(1/2) low wavelength threshold lies in the region of strong C–A(3/2) or B–X emission.

The long wavelength limits of the KrI B–A(1/2) and C–A(3/2) continua are similarly separated by an energy close to the iodine spin–orbit splitting. For XeI, KrBr and ArBr, however, this separation, although not accessible to precise measurement, is always somewhat smaller than the halogen spin–orbit splitting. We ascribe this to small differences in the B- and C-state potentials and in the A(3/2) and A(1/2) potentials, as discussed above (see fig. 1).

In conclusion, the wavelength ranges of the third continua are consistent with either B- or C-state emission to the A(1/2) state and the pressure dependences of the spectra (figs. 5 and 6 and table 1) establish the emitting state as the B(1/2) state.

The structure in the "third continua" is also consistent with this assignment. The broad oscillations in the ArBr and Xe* + CH_2I_2 spectra and at the long wavelength end of the Xe* + HI spectrum are quantum oscillations analogous to those in the C–A(3/2) spectrum [10], arising from the overlap of upper and lower state wavefunctions near the inner turning

points of the potential curves. The structure in the low wavelength region of the Xe* + HI B–A(1/2) spectrum is due to emission near the outer turning-point; each emitting vibrational level gives rise effectively to a separate peak and the spacing, approximately 110 cm^{-1}, between peaks is close to the vibration frequency of the analogous alkali halide, CsI.

The branching ratio for B-state emission to the X and A(1/2) states can be estimated from the Kr*, Xe* + HI spectra, showing that the B–A(1/2) system accounts for approximately 20% of the B-state emission in KrI and XeI.

For the bromides, the B–A(1/2) continuum is best resolved in ArBr; the resolved portion in the Ar* + HBr spectrum accounts for over 10% of the total B-state emission.

The iodides and bromides thus show very different behavior to KrF, for which calculations predict the B–A(1/2) system to be weaker than the B–X by a factor of about 30 [3].

4.2. Composition of the main continuum

Analysis of the noble-gas halide spectra is of interest for two reasons: to obtain potential curves for these novel species and to determine the vibrational distributions in the emitting states. This is especially important for spectra at low pressure ($\ll$1 torr), where the unrelaxed distributions give information concerning the dynamics of the formation reactions (1). The present results have an impact on both these aspects, in providing the first instance, in the noble-gas halides, of two band systems arising from a single excited electronic state.

Previous analyses of the MC of KrF at low pressure [10] and of several other noble-gas halides at high pressure [12] have assumed that the entire emission within this region can be assigned to the B–X system. A surprising result of the present study of ArBr and XeI was that the ratio of the B–A(1/2) intensity to that of the MC shows a small but definite positive pressure dependence. For Xe* + HI (fig. 6), where integrated intensities in the MC and B–A(1/2) continua were measured, the change in the ratio is about 20% between 1 and 5 torr.

For ArBr (Ar* + CH_2Br_2), the enhancement with pressure of the resolved B–A(1/2) emission relative to the peak of the MC, which itself shows a strong positive pressure dependence, is very striking (fig. 5 and table 1); the ratio of the B–A(1/2) intensity at 179 nm to the MC peak rises by more than 50% between 0.45 and 3.75 torr.

These results are consistent with a significant contribution of C state emission to the MC region. This is not unexpected as the C–A(3/2) low-wavelength threshold coincides with that of the B–X system (see fig. 1) and the spectra for Xe* + CH_2I_2 and Ar* + CH_2Br_2 (figs. 4 and 5) show strong C–A(3/2) emission right up to the long wavelength edge of the strong peak of the MC.

That the C–A(3/2) emission extends strongly to low wavelength under the MC can be deduced from the two Xe* + HI spectra in fig. 3, referring to 0.8 and 5.6 torr. The decrease in C–A(3/2) emission intensity as the pressure is increased is due to electronic quenching of the C(3/2) to the B(1/2) state. This is seen to result in an intensity enhancement of almost the whole B–A(1/2) spectrum, consistent with enhanced population of all but the highest emitting levels of the B state (which may be depleted by vibrational relaxation). In contrast, only the long wavelength peak of the MC shows a comparable enhancement, showing that at lower wavelength, particularly in the range 240–250 nm, quenching of contributing C-state emission is offsetting most of the enhancement of B–X emission.

In terms of the potential curves of fig. 1, this portion of C–A(3/2) emission arises from transitions near the outer turning-point of the C-state potential curve. Strong emission may result, despite the fact that the electronic transition moment for C–A(3/2) has been calculated to decrease sharply with increasing internuclear distance [3,5], because of the strong ν^5 dependence of intensity on transition frequency, ν, when the spectra are plotted, as here, on a wavelength scale. For high vibrational levels, the outer turning-point in the C state occurs at very large internuclear distances; in these cases (e.g. Xe* + CH_2I_2), the low wavelength region probably also includes C–X emission, whose transition moment may exceed that of C–A(3/2) in this region [3].

We have calculated C–A(3/2), X spectra for KrF, for which calculated molecular properties are available; these show that emission from high vibrational levels in fact reaches a separate intensity maximum at

low wavelength, in the region of the MC. This behavior is supported by the observed spectra of several noble-gas halides, in which strong C–A(3/2) emission in the SC is accompanied by a pronounced hump or shoulder in the low-wavelength region of the MC. Examples include $Xe^* + CH_2I_2$ (fig. 4), $Kr^* + CBr_4$ and $CHBr_3$, and $Ar^* + CCl_4$.

The possible presence of appreciable C-state emission particularly at low pressures must be considered when analyzing the MC in terms of the dominant B–X system. For the low-pressure ArBr spectrum produced by $Ar^* + CH_2Br_2$, for instance, the MC cannot be simulated in terms of B–X transitions alone. However, in other cases such fits to the MC may be possible but will give erroneous results for the B and X state potential curves and the B state vibrational distribution unless the C–A(3/2) contribution is allowed for.

Additionally, in deriving vibrational distributions in the B state, both the B–X and B–A(1/2) continua must be analyzed; because of the strong and very different dependence of transition moments on internuclear distance for these two transitions [3], the partitioning of emission between the B–X and B–A(1/2) systems may change markedly with vibrational quantum number.

Acknowledgement

We acknowledge the Donors of the Petroleum Research Fund, administered by the American Chemical Society, the Research Corporation and the Royal Society for support of this research. We are also indebted to Dr. R.J. Donovan for the loan of a monochromator for experiments performed at the University of Edinburgh.

References

[1] M.F. Golde and B.A. Thrush, Chem. Phys. Letters 29 (1974) 486.
[2] J.E. Velazco and D.W. Setser, J. Chem. Phys. 62 (1975) 1990.
[3] P.J. Hay and T.H. Dunning, J. Chem. Phys. 66 (1977) 1306.
[4] M. Krauss, J. Chem. Phys. 67 (1977) 1712.
[5] E.W. McDaniel, M.R. Flannery, H.W. Ellis, F.L. Eisele, W. Pope and T.G. Roberts, Compilation of Data Relevant to Rare Gas–Rare Gas and Rare Gas–Monohalide Excimer Lasers, Technical Rept H-78-1, U.S. Army Missile Research and Development Command (1977) Vol. 1.
[6] J. Tellinghuisen, G.C. Tisone, J.M. Hoffman and A.K. Hays, J. Chem. Phys. 64 (1976) 4796.
[7] J.E. Velazco, J.H. Kolts and D.W. Setser, J. Chem. Phys. 65 (1976) 3468.
[8] J. Tellinghuisen, J.M. Hoffman, G.C. Tisone and A.K. Hays, J. Chem. Phys. 64 (1976) 2484.
[9] P.C. Tellinghuisen, J. Tellinghuisen, J.A. Coxon, J.E. Velazco and D.W. Setser, J. Chem. Phys. 68 (1978) 5187.
[10] K. Tamagake and D.W. Setser, J. Chem. Phys. 67 (1977) 4370.
[11] M.F. Golde, J. Mol. Spectry. 58 (1975) 261.
[12] J. Tellinghuisen, A.K. Hays, J.M. Hoffman and G.C. Tisone, J. Chem. Phys. 65 (1976) 4473.

APPENDIX 2.

Computer Program.

Computer program (FORTRAN IV) to calculate vibrational contributions and spectra for bound-free transitions for:

1. The bound potential U'_{b1}.
2. Exponential repulsive potential
   $U'' = a \exp(-r/b))$ (a = APAR, b = BPAR).
3. Certain range of energy levels in U'' between EN and EM.
4. μ_i = constant and three linear μ_i functions $(= a_i \cdot r + b_i)$ for a_i = ALF1, ALF2, ALF3 and b_i = BET1, BET2, BET3.
5. Certain number of vibrational levels ($v'_{max} = S-1$).
6. Certain population distribution values (N(v') = VEC11(J)).

The calculations are based on the methods described in chapter 4. The wavefunctions used are uniform WKB wavefunctions. The subroutine: C05AA5(A,B,C,D,E) which is used is not included. It is a standard subroutine to calculate a zero of a function by the binomial bisection method.

```
C
C
C
      DOUBLE PRECISION ATSE,MMBSJ1,SAFI
      DIMENSION VEC6(50),VEC7(50),VEC8(50),VEC9(50)
      DIMENSION XT(3),YT(3)
      DIMENSION SBJ(150)
      DIMENSION AM(50,50)
      DIMENSION VEC10(50),VEC11(50)
      DIMENSION VEC20(50),VEC21(50),VEC22(50),VEC23(50)
      DIMENSION VEC24(50),VEC25(50),VEC26(50),VEC27(50),VEC28(50)
      DIMENSION BM(50,50),CM(50,50),DM(50,50)
      DIMENSION VEC5(100)
      DIMENSION VEC1(100),VEC2(100),VEC3(100),VEC4(100)
      DIMENSION VEC16(50),VEC17(50),VEC18(50)
      DIMENSION VEC12(50),VEC13(50),VEC14(50),VEC15(50)
      DIMENSION VEC30(50),VEC31(50)
      COMMON /D/ARR,APAR,BPAR
      COMMON /E/CA1,CA2,CB1,CB2,CC1,CD3,CE4
      COMMON /C/DFR,DAN1,DAN2
      NON=0
      DO 436 J=1,50
      DO 437 I=1,10
      BM(I,J)=0
      CM(I,J)=0
      DM(I,J)=0
      AM(I,J)=0
  437 CONTINUE
  436 CONTINUE

C INPUT:
      READ(5,735) EN,EM
C EN & EM ARE THE MAXIMUM AND MINIMUM ENERGIES RESPECTIVELY
C AT WHICH THE LOWER STATE WAVEFUNCTIONS ARE EVALUATED
      READ(5,735) APAR,BPAR
C APAR & BPAR ARE CONSTANTS IN THE EXPONENTIAL REPULSIVE
C POTENTIAL, U"=APAR*EXP(-R(NM)/BPAR)
      READ(5.735) ALF1,BET1
      READ(5,735) ALF2,BET2
      READ(5,735) ALF3,BET3
C ALFI & BETI (I=1,2,3) ARE SLOPES AND INTERSECTS
C RESPECTIVELY, FOR LINEAR TRANSITION MOMENT FUNCTIONS
      READ(5,736) S
C S IS THE TOTAL NUMBER OF EMITTING VIBRATIONAL LEVELS
C (S<8FOR ARBR)
  735 FORMAT(2G)
  736 FORMAT(G)

      II=S
      IS=S
```

```
C CONSTANTS CHARACTERISTIC FOR THE UPPER STATE POTENTIAL
C WHICH IS USED
      DO 733 J=1,II
  733 READ(7,734) VEC31(J) *
  734 FORMAT(G)
C THE VEC31(J)-VALUES ARE NORMALIZATION FACTORS
C FOR THE UPPER STATE WAVEFUNCTIONS
      CA1=1144.259568E4
      CA2=0.3746623
      CB1=5.94444358E6
      CB2=0.45136066
      CC1=116055.75
      CD3=156287.98
      CE4=327857.47
C THE ABOVE CONSTANTS,CA1-CE4,ARE CHARACTERISTIC CONSTANTS
C FOR EVALUATING THE UPPER STATE POTENTIAL CURVE WHICH IS
C EXPRESSED AS:
C U'=CA1*EXP(-R(A)/CA2)+CB1*EXP(-R(A)/CB2)
C     -CC1/R(A)-CD3/(R(A)**3)-CE4/(R(A)**4)
      DFR=193.8215021
      DAN1=0.5599828087
      DAN2=-0.0020458953
C DFR,DAN1,DAN2 ARE CONSTANTS IN AN EXPRESSION FOR THE
C ENERGY OF THE VIBRATIONAL LEVELS:
C G(V')=DFR*(V'+0.5)-DAN1*((V'+0.5)**2)+DAN2*((V'+0.5)**3)

      ULL=EN
   51 CONTINUE
      ULL=ULL-80.
C FEQUENCY DIFFERENCE BETWEEN CALCULATED POINTS IS 80 CM-1
      EN=ULL
      SUMMA=0
      SUMMB=0
      SUMMC=0
      SUMMD=0
      XU=2.66
C XU=2.66 IS THE MINIMUM INTERNUCLEAR DISTANCE(R)
      KINA=0
      XUU=XU
      E1=35710.25088
      TA=3.56
C TA=3.56 IS THE MAXIMUM INTERNUCLEAR DISTANCE(R)
    1 CONTINUE
      ASUM=0
      AKA=0
      AKB=0
      AKC=0
      TA=TA-0.03
C TA(MAX R) IS LOWERED
      K=0
      I=0
      S=S-1.
      IRK=0
```

```
*
      VEC31(1)=0.6059147
      VEC31(2)=0.4269020
      VEC31(3)=0.2125622
      VEC31(4)=0.8651362E-1
      VEC31(5)=0.3041684E-1
      VEC31(6)=0.9610008E-2
      VEC31(7)=0.2758732E-2
      VEC31(8)=0.7345812E-3
```

```
C UPPER STATE WAVEFUNCTION CALCULATED AT AT THE INTER-
C NUCLEAR DISTANCE XU(A)
   40 XU=XU+0.005
      II=S

C ENERGY OF VIBRATIONAL LEVEL WITH VIBRATIONAL QUANTUM
C NUMBER S EVALUATED
      EXTERNAL FCT
      COMMON E
      IRK=IRK+1
      F11=S+0.5
      F1=F11*DFR
      F21=F11*F11
      F2=-DAN1*F21
      F31=F21*F11
      F3=-DAN2*F31
      F=F1+F2+F3
      E=37131.55-F
C 37131.55 IS THE ENERGY DIFFERENCE BETWEEN V'=7 AND THE
C AS-YMPTOTIC ENERGY FOR THE B-STATE.--=>THE CALCUL-
C ATED SPECTRA WILL BE ON THE E"(7)-SCALE.
      DEE=E-E1
      EN=EN-DEE
C CALCULATION OF THE ENERGY OF THE V'-LEVEL ENDED

      IF(EN-0) 50,50,52
   52 CONTINUE

C TURNING POINTS CALCULATED
      E1=E
      A=2.75
      B=3.048
      XL=XY(S,A,B)
      A=3.048
      B=3.43
      RU=XY(S,A,B)
C TURNING POINT CALCULATION ENDED
```

```
C S(R) CALCULATED S(R)=X1, R=XU
      CALL QG4(XL,RU,FCT,Y)
      BB=(2.*Y)/3.141592654
      B=SQRT(BB)
      A=-B
      IF(XU-XL) 5,6,8
    6 Y=0
      X1=A
      GO TO 7
    5 CONTINUE
      RR1=XU
      RR2=XL
      CALL QG2(RR1,RR2,FCT,Y)
      Y1=Y
      A=B
      X1=XX(Y1,A)
      X1=-X1
      GO TO 7
    8 CONTINUE
      IF(XU-RU) 2,4,3
    2 CONTINUE
      CALL QG4(XL,XU,FCT,Y)
      X1=XW(Y,A,B)
      GO TO 7
    3 XL=RU
      CALL QG2(XL,XU,FCT,Y)
      Y1=Y
      A=B
      X1=XX(Y1,A)
      GO TO 7
    4 X1=B
      Y=BB
    7 CONTINUE
C S(R) CALCULATION ENDED, S(R)=X1,R=XU

C P(R) CALCULATED
      W11=-(XU/CA2)
      W12=EXP(W11)
      W1=CA1*W12
      W21=-(XU/CB2)
      W22=EXP(W21)
      W2=CB1*W22
      W3=-(CC1/XU)
      W41=XU*XU*XU
      W4=-(CD3/W41)
      W51=W41*XU
      W5=-(CE4/W51)
      W=W1+W2+W3+W4+W5
      P2=-E1-W
      P1=ABS(P2)
      P=SQRT(P1)
C P(R) CALCULATION ENDED

C SQRT(C*C - S*S) CALCULATED
      DEN1=X1*X1
      DEN3=BB-DEN1
      DEN2=ABS(DEN3)
      DEN=SQRT(DEN2)
C SQRT(C*C -S*S) CALCULATION ENDED
```

```
      DRDS=DEN/P
      SDRDS=SQRT(DRDS)

C HERMITE POLYNOMIA CALCULATED
      VAR=1.1211372*X1
      IT=II+1
      IF(II-0) 23,23,24
   23 CONTINUE
      AH=1.00E-25
      GO TO 30
   24 IF(II-1) 25,25,26
   25 CONTINUE
      AH=2.81.00E-25*VAR
      GO TO 30
   26 CONTINUE
      VEC30(1)=1.00E-25
      VEC30(2)=2.*1.00E-25*VAR
      DO 27 J=3,IT
      ES=J-2
      IES=J-2
      IET=J-1
      TRU=-(2.*ES*VEC30(IES))
      BEL=2.*ES*VEC30(IES))
      BEL=2.*VAR*VEC30(IET)
   27 VEC30(J)=TRU+BEL
      AH=VEC30(IT)
   30 CONTINUE
C HERMITE POLYNOMIA CALCULATION ENDED

C EXP TERM. CALCULATED
      EX1=-0.62847435*DEN1
      EX=EXP(EX1)
C EXP TERM CALCULATION ENDED

      AN=VEC31(IT)
      YWAVE=EX*AH*AN
      UWAVE=SDRDS*YWAVE
C CALCULATION OF UPPER STATE WAVEFUNCTION ENDED


C WAVEFUNCTION FOR LOWER STATE(U'') CALCULATED
      ZONA=EN/(APAR)
      ZONB=ALOG(ZONA)
      Z1=-BPAR*ZONB
      IF(XU-Z1) 70,71,72
   72 RXX=Z1
      RYY=XU
      ARR=EN
      EXTERNAL FOSS
      COMMON ARR
      CALL QG3(RXX,RYY,FOSS,YKK)
      ARS=(0.7413876215*YKK)+0.6889902831
      BRS=(1.0125*YKK)+4.
      FOS=ZK(YKK,ARS,BRS)
      GO TO 73
   71 FOS=0.6889902831
      GO TO 73
```

```
   70 CONTINUE
      RXX=XU
      RYY=Z1
      ARR=EN
      EXTERNAL FOSS
      COMMON ARR
      CALL QG3(RXX,RYY,FOSS,YKK)
      AQER=0.4747076102
      BRS=SQRT(AQER)
      ARS=1.00D-19
      FOS=ZM(YKK,ARS,BRS)
   73 CONTINUE
      RX1=FOS
      RX2=1.2569164*RX1
      SAFI=RX2
      ATSE=MMBSJ1(SAFI,IER)
      RY=SQRT(RX2)
      BX=RY*ATSE
      D11=-(XU/BPAR)
      D12=EXP(D11)
      D1=APAR*D12
      PX=EN-D1
      PZ=ABS(PX)
      PY=SQRT(PZ)
      QL=-(0.4747076102/(FOS*FOS))
      QM=1.+QL
      QK=ABS(QM)
      QN=SQRT(QK)
      VELT=QN/PY
      VELTS=SQRT(VELT)
      B1=VELTS*BX
      IF(IRK-3) 632,633,633
  633 CONTINUE
      WRITE(6,631) XU,XM,VELTS,BX,B1
  631 FORMAT(5G)
      IRK=0
      GO TO 632
C CALCULATION FOR WAVEFUNCTION IN U'' ENDED

C TRANSITION MOMENT FUNCTIONS CALCULATED
      DA=(ALF1*XU)+BET1
      DB=(ALF2*XU)+BET2
      DC=(ALF3*XU)+BET3
C CALCULATION OF TRANSITION MOMENT FUNCTIONS ENDED

C FC-FACTOR CALCULATED
  632 CONTINUE
      FRA=B1*UWAVE*1.0E+3
      AFRA=DA*FRA
      BFRA=DB*FRA
      CFRA=DC*FRA
      AKA=AKA+AFRA
      AKB=AKB+BFRA
      AKC=AKC+CFRA
      ASUM=ASUM+FRA
C FC-FACTOR CALCULATION ENDED
```

```
      IF(XU-TA) 40,40,41
   41 CONTINUE
      BSUM=ASUM*ASUM
      KINA=KINA+1
      VEC5(KINA)=BSUM
      SUMMA=SUMMA+BSUM
      VEC20(KINA)=AKA*AKA
      SUMMB=SUMMB+VEC20(KINA)
      VEC21(KINA)=AKB*AKB
      SUMMC=SUMMC+VEC21(KINA)
      VEC22(KINA)=AKC*AKC
      SUMMD=SUMMD+VEC22(KINA)
      XUU=XUU+0.06
C MINIMUM INTERNUCLEAR DISTANCE INCREASED
      XU=XUU
      IF(S-0) 50,50,1
   50 CONTINUE
      WRITE(6,144)
  144 FORMAT(4X,11HV'MAX-V'MIN)
      WRITE(6,145)
  145 FORMAT(4X,7HE''A(7))
      WRITE(6,820) ULL
  820 FORMAT(G)
      WRITE(6,143)
  143 FORMAT(5X,29HL5*S2(W1*MI*W2) FOR I=0,4,5,6)
      WRITE(6,851) (VEC5(J),J=1,KINA)
      WRITE(6,851) (VEC20(J),J=1,KINA)
      WRITE(6,851) (VEC21(J),J=1,KINA)
      WRITE(6,851) (VEC22(J),J=1,KINA)
      NON=NON+1
      VEC10(NON)=ULL
      DO 60 J=1,KINA
      BM(J,NON)=VEC20(J)
      CM(J,NON)=VEC21(J)
      DM(J,NON)=VEC22(J)
   60 AM(J,NON)=VEC5(J)
      IF(ULL-EM) 61,51,51
   61 CONTINUE
   64 READ(5,851) (VEC11(J),J=1,IS)
C POPULATION DISTRIBUTION VALUES (=VEC11(J))
      DO 62 J=1,NON
      TSS=0
      TRR=0
      TTT=0
      TVV=0
      DO 63 I=1,IS
      VEC23(I)=VEC11(I)*BM(I,J)
      VEC24(I)=VEC11(I)*CM(I,J)
      VEC25(I)=VEC11(I)*DM(I,J)
      TRR=TRR+VEC23(I)
      TTT=TTT+VEC24(I)
      TVV=TVV+VEC25(I)
      VEC7(I)=VEC11(I)*AM(I,J)
   63 TSS=TSS+VEC7(I)
```

```
      VEC26(J)=TRR
      VEC27(J)=TTT
      VEC28(J)=TVV
   62 VEC6(J)=TSS
      WRITE(6,140)
  140 FORMAT(4X,23HPOPULATION DISTRIBUTION)
      WRITE (6,851)(VEC11(J),J=1,IS)
      WRITE(6,141)
  141 FORMAT(4X,9HINTENSITY)
      WRITE(6,146)
  146 FORMAT(4X,3HM0:)
      WRITE(6,851) (VEC6(J),J=1,NON)
      WRITE(6,147)
  147 FORMAT(4X,3HM4:)
      WRITE(6,851) (VEC26(J),J=1,NON)
      WRITE(6,148)
  148 FORMAT(4X,3HM5:)
      WRITE(6,851) (VEC27(J),J=1,NON)
      WRITE(6,149)
  149 FORMAT(4X,3HM6:)
      WRITE(6,851) (VEC28(J),J=1,NON)
      WRITE(6,142)
  142 FORMAT(4X,7HE''A(7))
      WRITE(6,851) (VEC10(J),J=1,NON)
      GO TO 64
  850 FORMAT(G)
  851 FORMAT(8G)
      END


C SUBPROGRAMS (SUBROUTINES,FUNCTIONS):
C

      SUBROUTINE QG3(RXX,RYY,FOSS,YKK)
      A=0.5*(RXX+RYY)
      B=RYY-RXX
      Y=0.2886751*B
      YKK=0.5*B*(FOSS(A+Y)+FOSS(A-Y))
      RETURN
      END


      FUNCTION FOSS(X)
      COMMON /D/ARR,APAR,BPAR
      BT1=-(X/BPAR)
      BT2=EXP(BT1)
      BT=APAR*BT2
      BS=ARR-BT
      BS1=ABS(BS)
      FOSS=SQRT(BS1)
      RETURN
      END
```

```
SUBROUTINE QG4(XL,XU,FCT,Y)
A=0.5*(XU+XL)
B=XU-XL
C1=0.430568155*B
C2=0.16999052*B
Y1=FCT(A-C1)*0.173927425
Y2=FCT(A-C2)*0.326072575
Y3=FCT(A+C2)*0.326072575
Y4=FCT(A+C1)*0.173927425
Y=B*(Y1+Y2+Y3+Y4)
RETURN
END

SUBROUTINE QG2(XL,XU,FCT,Y)
A=0.5*(XU+XL)
B=XU-XL
Y=0.2886751*B
Y=0.5*B*(FCT(A+Y)+FCT(A-Y))
RETURN
END

FUNCTION FCT(X)
COMMON E
COMMON /E/CA1,CA2,CB1,CB2,CC1,CD3,CE4
V11=-(X/CA2)
V12=EXP(V11)
V1=CA1*V12
V21=-(X/CB1)
V22=EXP(V21)
V2=CB1*V22
V3=-(CC1/X)
V41=X*X*X
V4=-(CD3/V41)
V51=V41*X
V5=-(CE4/V51)
V=V1+V2+V3+V4+V5
FCT2=-V-E
FCT1=ABS(FCT2)
FCT=SQRT(FCT1)
RETURN
END

FUNCTION XW(Y,A,B)
COMMON /A/CON,CX,CCX
EXTERNAL G
CON=Y
CX=B
CCX=B*B
EPS=1.00E-7
ETA=1.00E-7
IFAIL=1
CALL C05AAF(A,B,EPS,G,XW)
RETURN
END
```

```
      FUNCTION G(XW)
      COMMON /A/CON,CX,CCX
      G11=XW*XW
      G12=CCX-G11
      G13=SQRT(G12)
      G1=XW*G13/2.
      G21=XW/CX
      G22=ASIN(G21)
      G2=CCX*G22/2.
      G3=3.141592654*CCX/4.
      G=G1+G2+G3-CON
      RETURN
      END

      FUNCTION XX(Y1,A)
      COMMON /B/CON1,C,CC
      EXTERNAL GI
      CON1=Y1
      B=6.
      C=A
      CC=A*A
      EPS=1.00E-7
      ETA=1.00E-7
      IFAIL=1
      CALL C05AAF(A,B,EPS,GI,XX)
      RETURN
      END

      FUNCTION GI(XX)
      COMMON /B/CON1,C,CC
      G11=XX*XX
      G12=G11-CC
      G13=SQRT(G12)
      G1=XX*G13/2.
      G21=XX+G13
      G22=ALOG(G21)
      G2=-(CC*G22/2.)
      G31=C
      G32=ALOG(G31)
      G3=CC*G32/2.
      GI=G1+G2+G3-CON1
      RETURN
      END
```

```
FUNCTION XY(S,A,B)
COMMON E2
COMMON /C/DFR,DAN1,DAN2
EXTERNAL FUN
F11=S+0.5
F1=F11*DFR
F21=F11*F11
F2=-DAN1*F21
F31=F21*F11
F3=-DAN2*F31
F=F1+F2+F3
E2=37131.55-F
EP=1.00E-7
ET=1.00E-7
IFAIL=1
CALL C05AAF(A,B,EP,FUN,XY)
RETURN
END

FUNCTION FUN(XY)
COMMON E2
COMMON /E/CA1,CA2,CB1,CB2,CC1,CD3,CE4
V1=-(CC1/XY)
V21=XY*XY*XY
V2=-(CD3/V21)
V51=-(XY/CB1)
V52=EXP(V21)
V5=CB1*V22
V31=V21*XY
V3=-(CE4/V31)
V41=-(XY/CA2)
V42=EXP(V41)
V4=CA1*V42
V=V1+V2+V3+V4+V5
FUN=V+E2
RETURN
END


FUNCTION ZK(YKK,ARS,BRS)
COMMON EKKO
EXTERNAL FOP
EKKO=YKK
EP=1.00E-7
ET=1.00E-7
IFAIL=1
CALL C05AAF(ARS,BRS,EP,FOP,ZK)
RETURN
END
```

```
FUNCTION FOP(ZK)
COMMON EKKO
TI1=ZK*ZK
TI2=TI1-0.4747076102
TI=SQRT(TI2)
SVART=0.4747076102
TII1=SQRT(SVART)
TII2=-TII1/ZK
TII3=ASIN(TII2)
TII=-TII1*TII3
TIII1A=-1.
TIII1=ASIN(TIII1A)
TIII=TII1*TIII1
TO=TI+TII+TIII
FOP=TO-EKKO
RETURN
END

FUNCTION ZM(YKK,ARS,BRS)
COMMON ELLO
EXTERNAL FIL
ELLO=YKK
EP=1.00E-7
ET=1.00E-7
IFAIL=1
CALL C05AAF(ARS,BRS,EP,FIL,ZM)
RETURN
END

FUNCTION FIL(ZM)
COMMON ELLO
BLAR=0.4747076102
U11=SQRT(BLAR)
U12=ZM*ZM
U13=0.4747076102-U12
U14=SQRT(U13)
U15=2.*U11*U14
U16=2.*0.4747076102
U17=(U15+U16)/ZM
U18=ALOG(U17)
U1=U11*U18
U21=2.*U11
U22=ALOG(U21)
U2=-U11*U22
U3=-U14
UO=U1+U2+U3
FIL=UO-ELLO
RETURN
END
```

References.

1. a) R.J. Donovan, "Reactive, Inelastic and Radiative Processes Involving Electronically Excited Atoms", review, (to be published).
   b) R.J. Donovan and D. Husain, Chem. Rev. 70, 489 (1970).
2. M.F. Golde, in "Energy Transfer", ed. R.J. Donovan (Specialist Periodical Reports), The Chemical Society, London 1976, Vol. 2.
3. D.H. Stedman and D.W. Setser, Progr. Reaction Kinetics 6, 194 (1971).
4. E.J. Robinson, J. Levine and B.Bederson, Phys. Rev. 146, 95 (1966).
5. R.W. Molof, H.L. Schwartz, T.M. Miller and B. Bederson, Phys. Rev. A 10, 1131 (1974).
6. D.H. Winicur, J.L. Fraites and F.A. Stackhouse, Chem. Phys. Lett. 23, 123 (1973).
7. D.H. Winicur and J.L. Fraites, J. Chem. Phys. 61, 1548 (1974).
8. M.F. Golde and B.A. Thrush, Chem. Phys. Lett. 29, 486 (1974).
9. M.F. Golde, J. Mol. Spectrosc. 58, 261 (1975).
10. M.F. Golde, A. Kvaran and M.P. Casassa, Chem. Phys. Lett. 59, 51 (1978).
11. M.F. Golde and B.A. Thrush, Proc. R. Soc. Lond. A 330, 109 (1972).
12. M.F. Golde, "Vacuum UV Emission from Active Nitrogen", Theses, Cambridge, 1971.

13. D.W. Setser and J.E. Velazco, "Quenching Studies of Xe ($^3P_2$) metastable atoms", in 4th conference in chemical and molecular lasers, St. Louis, October 1974.

14. D.W. Setser and J.E. Velazco, J. Chem. Phys. 62, 1990 (1975).

15. D.W. Setser, L.A. Gundel, M.A.A. Clyne, J.A. Coxon and W. Nip, J. Chem. Phys. 64, 4390 (1976).

16. D.W. Setser, J.E. Velazco and J.H. Kolts, J. Chem Phys, 65, 3468 (1976).

17. D.W. Setser, D.L. King and L. G. Piper, J.C.S. Faraday II, 73, 177 (1977).

18. D.W. Setser and J. H. Kolts, J. Appl. Phys. 48, 409 (1977).

19. D.W. Setser, H.C. Brashears jr. and D. Desmartean, Chem. Phys. Lett. 48, 84 (1977).

20. D.W. Setser, J.E. Velazco and J. H. Kolts Chem. Phys. Lett. 46, 99 (1977).

21. D.W. Setser and K. Tamagake, J. Chem. Phys. 67, 4370 (1977).

22. D.W. Setser and J. H. Kolts, J. Chem. Phys. 68, 4848 (1978).

23. D.W. Setser, J. Tellinghuisen, P.C. Tellinghuisen, J.A. Coxon and J.E. Velazco, J. Chem. Phys. 68, 5187 (1978).

24. D.W. Setser and G.W. Taylor, Chem. Phys. Lett. 8, 51 (1971).

25. D.W. Setser and J.H. Kolts, J. Phys. Chem. 82, 1766 (1978).

26. D.W. Setser and H.C. Brashears jr. Appl. Phys. Lett. 33, 821 (1978).

27. J.J. Weing and C.A. Brau, J. Chem. Phys. 63, 4640 (1975).

28. J.J. Ewing and C.A. Brau, Phys. Rev. A 12, 129 (1975).

29. J.J. Ewing and C.A. Brau, Appl. Phys. Lett. 27, 350 (1975).

30. J.J. Weing and C.A. Brau, Appl. Phys. Lett. 27, 435 (1975).

31. J.J. Ewing, Seventh Winter Colloquium on Quantum Electronics, (Park City, Utah, 1977).

32. J.M. Hoffman, A.K. Hays and G.C. Tisone, Appl. Phys. Lett. 28, 538 (1976).

33. R.W. Waynant, Appl. Phys. Lett. 30, 234 (1977).

34. J.R. Murray and H.T. Powell, Appl. Phys. Lett. 29, 252 (1976).

35. S.K. Searles and G.A. Hart, Appl. Phys. Lett. 27, 243 (1975).

36. J. Tellinghuisen, Chem. Phys. Lett. 29, 359 (1974).

37. J. Tellinghuisen, Phys. Rev. Lett. 34, 1137 (1975).

38. J. Tellinghuisen, J.M. Hoffman, G.C. Tisone and A.K. Hays, J. Chem. Phys. 64, 2484 (1976).

39. J. Tellinghuisen, G.C. Tisone, J.M. Hoffman and A.K. Hays, J. Chem. Phys. 64, 4796 (1976).

40. J. Tellinghuisen, A.K. Hays, J.M. Hoffman and G.C. Tisone, J. Chem. Phys. 65, 4473 (1976).

41. J. Tellinghuisen, P.C. Tellinghuisen, G.C. Tisone, J.M. Hoffman and A.K. Hays, J. Chem. Phys. 68, 5177 (1978).

42. A.L. Smith and P.C. Cobrinsky, J. Mol Spectrosc. 69, 1 (1978).

43. B.D. Ault and L. Andrews, J. Chem. Phys. 64, 3075 (1976).

44. J. Goodman and L.E. Brus, J. Chem. Phys. 65, 3808 (1976).

45. B.S. Ault and L. Andrews, J. Chem Phys. 65, 4192 (1976).

46. B.S. Ault, L. Andrews, D.W. Green and G.T. Reedy, J. Chem. Phys. 66, 2786 (1977).

47. F.J. Adrian and V.A. Bowers, J. Chem. Phys. 65, 4316 (1976).

48. M.R. Levy, C.T. Rettner and J.P. Simons, Chem. Phys. Lett. 54, 120 (1978).

49. J.G. Eden and S.K. Searles, Appl. Phys. Lett. 30, 287 (1977).

50. R. Burnham and N.W. Harris, J. Chem Phys. 66, 2742 (1977).

51. C.H. Fisher and R.E. Center, J. Chem. Phys. 69, 2011 (1978).

52. T.H. Dunning jr. and P.J. Hay, Appl. Phys. Lett. 28, 649 (1976).

53. T.H. Dunning jr. and P.J. Hay, J. Chem. Phys. 66, 1306 (1977).

54. T.H. Dunning jr. and P.J. Hay, J. Chem. Phys. 69, 134 (1978).

55. T.H. Dunning jr. and P.J. Hay, J. Chem. Phys. 69, 2209 (1978).

56. E.W. McDaniel, M.R. Flammery, H.W. Ellis, F.L. Eisele, W. Pope and T.G. Roberts, "Compilation of data relevant to rare gas - rare gas and rare gas monohalide excimer lasers", Technical Rept. H - 78 - 1 U.S. Army Missile Research and Development Command 1977, Vol. 1.

57. N.W. Winter, C.F. Bender and T.N. Rescigno, J. Chem. Phys. 67, 3122 (1977).

58. M.J. Clugston and R.G. Gordon, J. Chem. Phys. 66, 239 (1977).

59. M. Krauss, J. Chem. Phys. 67, 1712 (1978).

60. M. Krauss and B. Liu, Chem. Phys. Lett. 44, 257 (1976).

61. R.G. Gordon and Y.S. Kim, J. Chem. Phys. 56, 3122 (1972).

62. J.R. Morton and W.E. Falconer, J. Chem. Phys. 39, 427 (1963).

63. W.E. Falconer, J.R. Morton and A.G. Streng, J. Chem. Phys. 41, 902 (1964).

64. L.A. Kuznetsova, Y.Y. Kuzyakow, V.A. Shapanskii and V.M. Khutorelskii, Vestn. Mosk. Univ. Ser. II Khim. 19, 19 (1964).

65. B. Liu and H.F. Schaefer, J. Chem. Phys. 55, 2369 (1971).

66. D.H. Liskow, H.F. Schaefer, P.S. Bagus and B. Liu, J. Am. Chem. Soc. 95, 4056 (1973).

67. H. Scheingraber and C.R. Vidal, J. Chem.Phys. 66, 3694 (1977).

68. F.H. Mies and A.L. Smith, J. Chem. Phys. 45, 994 (1966).

69. G.E. Gibson, O.K. Rice and N.S Bayliss, Phys. Rev. 44, 193 (1933).

70. T. Kleindienst and E.J. Bair, Chem. Phys. Lett. 49, 338 (1977).

71. J.A. Beswick, M. Shapiro and R. Sharon, J. Chem. Phys. 67, 4045 (1977).

72. K. Sakurai and H.P. Broida, J. Chem. Phys. 65, 1138 (1976).

73. D.R. Herschbach, Advan. Chem. Phys. 10, 319 (1966).

74. J.L. Kinsey, in "MTP International Review of Science", ed. J.C. Polanyi, Butterworth, London 1972, Vol. 9, p. 173.

75. R.D. Levine and R.B. Bernstein, "Molecular Reaction Dynamics", Oxford University Press, New York, 1974.

76. J.L. Magee, J. Chem. Phys. 8, 687 (1940).

77. S. Glasstone, K.J. Laidler and H. Eyring, "Theory of Rate Processes", McGraw Hill, New York, 1941.

78. J.A.R. Samson, "Techniques of Vacuum Ultraviolet Spectroscopy", John Wiley and Sons, Inc., New York, 1967, p. 181.

79. D. Wallach and C.B. Moore, J. Chem. Phys. 56, 3608 (1972).

80. A.C. Allison and A. Dalgarno, Atomic Data 1, 289 (1970).

81. M.J. Mumma, E.J. Stone and E.C. Zipf, J. Chem. Phys. 54, 2627 (1971).

82. W.C. Fernelius, ed., "Inorganic Syntheses", Vol. 2, p. 90, McGraw Hill Book Company.

83. E. Wigner and E.E. Witmer, Z. Physik, 51, 859 (1928).

84. J.M. Cook, T.A. Miller and V.E. Bondybey, J. Chem. Phys. 68, 2001 (1978).

85. C.E. Moore, ed., National Bureau of Standards, Circular 467, "Atomic Energy Levels", Vol. 1 - 3, U.S. Government Printing Office, Washington, D.C., 1958.

86. G.M. Lawrence, The Astrophysical Journal, 148, 261 (1967).

87. "JANAF Thermochemical Tables", 2nd ed., NSRDS - NBS 37, 1971.

88. A.G. Gaydon, "Dissociation Energies", 3rd ed., Chapman and Hall, London, 1968.

89. R.C. Weast, ed., "Handbook of Chemistry and Physics", Chemical Rubber Co., Cleveland, 1972.

90. A. Kant, J. Chem. Phys. 49, 5144 (1968).

91. A. Lord, C.A. Goy and H.O. Pritchard, J. Phys. Chem. 71, 2705 (1967).

92. L.V. Gurvich, G.V. Karachevtsev, V.N. Kondrat'yev, Yu.A. Lebedev, V.A. Medvedev, V.K. Potapov and Yu.S. Khodeev, "Bond Energies, Ionization Potentials and Electron Affinities", Nauka, Moscow, 1974.

93. G.D. Blue, J.W. Green, R.G. Bautista and J.L. Margrave, J. Phys. Chem. 67, 877 (1963).

94. M. Lavollée and A. Tramer, Chem. Phys. Lett. 47, 523 (1977).

95. F. Lahmani, J. Phys. Chem. 80, 2623 (1976),

96. J.D. Cox and G. Pitcher, "Thermochemistry of organic and organometallic compounds", Academic Press, London, 1970.

97. D.D. Davis and H. Okabe, J. Chem. Phys. 49, 5526 (1968).

98. J.G. Edwards, H.F. Franklin and P.W. Gilles, J. Chem. Phys. 54, 545 (1971).

99. B. Rosen, ed., "Spectroscopic data relative to diatomic molecules", Oxford, New York, Pergamon Press, 1970.

100. J.I. Steinfeld, in "Molecular Spectroscopy: Modern Research", ed. Rao and Mathews, Academic press, New York and London, 1972.

101. R.F. Barrow and J.K. Jacques, Proc. Phys. Soc. 73, 538 (1959).

102. J.A. Myer and J.A.R. Samson, J. Chem. Phys. 52, 266 (1970).

103. E. Boursey, J. Chem. Phys. 62, 3353 (1975).

104. S.G. Tilford, M.L. Ginter and J.T. Vanderslice, J. Mol. Spectrosc. 33, 505 (1970).

105. A.E. Douglas and F.R. Greening, 29th Symposium of Molecular Structure and Spectroscopy, Columbus, Oh. 1974.

106. G. Herzberg, "Molecular Spectra and Molecular Structure, I. Spectra of Diatomic Molecules, Van Nostrand, New York, 1950.

107. R.S. Mulliken, J. Chem. Phys. 55, 288 (1971).

108. R.S. Mulliken, J. Chem. Phys. 55, 309 (1971).

109. A. Einstein, Verh. D. Deutsch. Phys. Ges. 18, 318 (1916).

110. A. Einstein, Phys. Z. 18, 121 (1917).

111. L. Pauling and E.B. Wilson, "Introduction to Quantum Mechanics", McGraw - Hill, New York, 1935.

112. M. Born and R. Oppenheimer, Ann. Phys. 84, 457 (1927).

113. G.E. Gibson, O.K. Rice and N.S. Bayliss, Phys. Rev. 44, 193 (1933).

114. S.M. Adler and J.R. Wiesenfeld, J. Mol. Spectrosc. 66, 357 (1977).

115. S. Flüge, "Practical Quantum Mechanics", Springer Verlag, New York, Heidelberg, Berlin 1974.

116. Whittaker and Watson, "Modern Analysis", fourth edition, Cambridge, 1927.

117. E.S. Rittner, J. Chem. Phys. 19, 1030 (1951).

118. J.W. Cooley, Mathematics of Computation, 15, 363 (1961).

119. J.K. Cashion, J. Chem. Phys. 39, 1872 (1963).

120. R.N. Zare and J.K. Cashion, University of California Lawrence Radiation Laboratory, Technical Report UCRL - 10881, July 1963.

121. B.R. Johnson, J. Chem. Phys. 67, 4086 (1977).

122. G. Wentzel, Zeitschr. f. Ph. 38, 518 (1926).

123. H.A. Kramers, Zeitschr. f. Ph. 39, 828 (1926).

124. L. Brillouin, C.R. 183, 24 (1926).

125. R.E. Langer, Phys. Rev. 51, 669 (1937).

126. E.C.G. Stuckelberg, Phys. Rev. 42, 518 (1932).

127. S.C. Miller jr. and R.H. Good jr. Phys. Rev. 91, 174 (1953).

128. Ung In Cho and Byung Chan Eu, Journal for the Korean Chemical Society, 18, 307 (1974).

129. F. H. Mies, J. Chem. Phys. 48, 482 (1968).

130. L.D. Landau and E.M. Lifshitz, "Quantum Mechanics", Pergamon press, 1958.

131. Messiah, "Quantum Mechanics", North Holland Publ. Comp., Vol 1, 1970.

132. B.K. Agarwal, "Quantum Mechanics and Field Theory," Asia Publishing House, London, 1977.

133. S.D. Conte and C. de Boor, "Elementary Numerical Analysis", McGraw - Hill, 1972.

134. Z. Kopal, "Numerical Analysis", Chapman and Hall, London, 1961.

135. T.M. Apastol, "Calculus", Vol 2.

136. P.M. Hunt and M.S. Child, Chem. Phys. Lett. 58,202 (1978).

137. R.J. Exton, W.L. Snow and M.E. Hillard, J. Quant. Spectrosc. Radiat. Transfer, 20, 235 (1978).

138. P.R. Bevington, "Data Reduction and Error Analysis for the Physical Sciences", McGraw Hill Book Company, New York, 1969.

139. J.H. Birely and D.R. Herschbach, J. Chem. Phys. 44, 1690 (1966).

140. P. Brumer and M. Karplus, J. Chem. Phys. 58, 3903 (1973).

141. R.E. Olsen and B. Liu, Phys. Rev. A 17, 1568 (1978).

142. K.T. Gillen, C. Riley and R.B. Bernstein, J. Chem. Phys. 50,4019 (1969).

143. A. van der Meulen, A.M. Rulis and A.E. de Vries, Chem. Phys. 7, 1 (1975).

144. E.A. Entemann, J. Chem. Phys. 55, 4872 (1971).

145. M.F.R. Mulcahy, "Gas Kinetics, Studies in Modern Chemistry", Nelson, 1973.

146. A.P. Thorne, "Spectrophysics", Chapman and Hall and Science Paperbacks, London, 1974.

147. J.E.Adams and W.H. Miller, J. Chem. Phys. 67, 5775 (1978).

148. P.M. Hunt and M.S. Child, Chem. Phys. Lett. 58, 202 (1978).

149. M.A.D. Fluendy and K.P. Lawley, "Chemical Applications of Molecular Beam Scattering", Chapman and Hall, London, 1973.

150. L. Pasternack and P.J. Dagdigian, J. Chem. Phys. 65, 1320 (1976).

COURSES ATTENDED.

During the years of my graduate studies I attended a number of lectures and courses on the following subjects:

At the University of Edinburgh:

1. Molecular Spectroscopy.
2. Quantum Mechanics.
3. Reaction Dynamics.
4. Atmospheric Chemistry.
5. Spectroscopy of Dyes.
6. NMR.
7. Electrochemistry.
8. Computer Programming (FORTRAN IV).

At the University of Pittsburgh:

9. Chemical Kinetic (lectures given by professor F. Kaufmann).

In addition I attended a number of seminars and research group meetings.